Universitat Politècnica de València
Departamento de Máquinas y Motores Térmicos

Analysis of the combustion process and soot formation in a single cylinder optical engine fueled with e-fuels and using different piston geometries

Doctoral Thesis
Presented by:
D. Felipe De Vargas Lewiski
Directed by:
Prof. José Vicente Pastor Soriano
Prof. Antonio García Martínez

Valencia, November 2021

Doctoral Thesis

Analysis of the combustion process and soot formation in a single cylinder optical engine fueled with e-fuels and using different piston geometries

Presented by: D.Felipe De Vargas Lewiski
Directed by: Prof. José Vicente Pastor Soriano
Prof. Antonio García Martínez

Evaluation Board:

President: Prof. Raúl Payri Marín
Secretary: Dr. María del Pilar Dorado Pérez
Examiner: Dr. Silvana Di Lorio

External examiners:

Dr. Silvana Di Lorio
Dr. Michele Bardi
Dr. Juan José Hernández Adrover

Valencia, November 2021

Resumen

La reducción de emisiones en motores de combustión interna (MCI) es uno de los mayores desafíos técnicos de la sociedad. Aunque están surgiendo nuevas tecnologías para la movilidad, el ICE seguirá teniendo un papel clave en el transporte durante las próximas décadas. Los motores diesel son un desafío en términos de emisiones contaminantes, en particular óxidos de nitrógeno (NO_X) y hollín. De hecho, el último representa el 50 % de las emisiones totales de este tipo de motores. En este contexto, las nuevas tecnologías de hardware y los nuevos combustibles renovables han mostrado un gran potencial para reducir las emisiones de hollín sin afectar la eficiencia del motor (emisiones de CO_2). Por esta razón, los impactos del uso de e-fuels (OME_X y FT-diesel) y diferentes geometrías del bowl del pistón (reentrante, labio escalonado y labio escalonado con ondas) en la formación de hollín y el desarrollo de la combustión han sido analizados en un motor óptico monocilindrico diesel. Primero, se realizó una caracterización del flujo en el cilindro utilizando un pistón de geometria real (Reentrante)y aplicando la técnica de velocimetría de imagenes por partículas (PIV). Posteriormente, se analizó el movimiento de la llama, el proceso de combustión y la formación de hollín para diferentes geometrías de pistón mediante diversas técnicas ópticas como la velocimetría de imagen por combustión (CIV), luminosidad natural, quimioluminiscencia OH * y pirometría de 2 colores. Finalmente, se estudió el proceso de combustión y la formación de hollín al utilizar diferentes e-fuels aplicando las mismas técnicas ópticas utilizadas anteriormente. Además, para esta parte del estudio, se incluyó una técnica óptica específica denominada espectroscopia de alta velocidad para el análisis de hollín. Con respecto a la evaluación de las distintas geometrías del bowl, el labio escalonado y el labio escalonado con ondas presentaron una oxidación tardía del hollín qué ha sido mas rápida en comparación con la geometría reentrante. En condiciones extremas de hollín, también se observaron diferencias entre el labio escalonado y el labio escalonado con ondas. Se observó una oxidación más rápida del hollín para el segundo. Los e-fuels mostraron una notable reducción en la formación de hollín (especialmente OME_X) en comparación con el diesel fósil. A partir del análisis de espectroscopía, es posible afirmar la ausencia de hollín durante la combustión de OME_X puro. En general, tanto la aplicación de nuevos hardwares(geometrías de bowls) como nuevos tipos de combustibles (e-fuels) en motores diesel han presentado un gran potencial para disminuir las emisiones de hollín.

Resum

La reducció d'emissions en motors de combustió interna (MCI) es un dels majors reptes tècnics de la societat. Encara que estan sorgint noves tecnologies per a la mobilitat, el ICE seguirà tenint un paper clau en el transport durant les pròximes dècades. Els motors diesel son un dels reptes en termes d'emissió de contaminants, en particular òxids de nitrogen (NO_X) i sutge. De fet, l'últim representa el 50% de les emissions totals d'aquest tipus de motor. Dins aquest context, les noves tecnologies de hardware y de nous combustibles renovables han mostrat un gran potencial per reduir les emissions de sutge sense afectar l'eficiència del motor (emissions de CO_2). Per aquesta raó, els impactes sobre l'ús de e-fuels (OME_X i FT-diesel) i diferents geometries de bowl del pistó (re-entrant, llavi escalonat i llavi escalonat amb ones) en la formació de sutge i el desenvolupament de la combustió, han estat analitzats en un motor òptic mono-cilíndric diesel. Primer, es va realitzar una caracterització de flux en el cilindre utilitzant un pistó amb geometria real (re-entrant) i aplicant la tècnica de velocimetria de imatges per partícules (PIV). Posteriorment, es va analitzar el moviment de la flama, el procés de combustió i la formació de sutge per a diferents geometries de pistó mitjançant diverses tècniques òptiques com per exemple la de velocimetria de imatge per combustió (CIV), lluminositat natural, quimioluminescència de OH* i pirometria de 2 colors. Finalment, es va estudiar el procés de combustió i la formació de sutge utilitzant diferents e-fuels aplicant les mateixes tècniques òptiques utilitzades anteriorment. A més, per aquesta part de l'estudi, es va implementar una tècnica òptica específica denominada espectroscòpia d'alta velocitat per a l'anàlisi del sutge. Respecte a l'avaluació de les distintes geometries de bowl, els llavis escalonats i els escalonats amb ones presentaren una oxidació tardana del sutge que ha estat més ràpida en comparació amb la de geometria re-entrant. En condicions extremes de sutge, també es varen observar diferencies entre la geometria de llavi escalonat y la de llavi escalonat amb ones. Es va observar una oxidació més ràpida del sutge per al segon. Els e-fuels mostraren una reducció més ràpida del sutge (especialment l'OME_X) en comparació amb el diesel fóssil. A partir de l'anàlisi d'espectroscòpia, es possible afirmar l'absència de sutge durant la combustió de l'OME_X pur. En general, tant l'aplicació de nous hardwares (geometries de bowl) com nous tipus de combustibles (e-fuels) en motors diesel han presentat un gran potencial per a la reducció d'emissions de sutge.

Abstract The emissions reduction in internal combustion engines (ICE) is one of the greatest technical challenges of society. Although new technologies for mobility are emerging, the ICE will still have a key role in transport over the next decades. Diesel engines are challenging in terms of pollutant emissions, in particular nitrogen oxides (NOX) and particles. In fact, the last one represents 50 % of total emissions of this kind of engine. In this context, new hardware technologies as well as new renewable fuels have shown great potential to reduce soot emissions without affecting engine efficiency (CO_2) emissions. For this reason, the impacts of using e-fuels (OME_X and FT-diesel) and different piston bowl geometries (re-entrant, stepped lip and stepped lip-wave bowl) on soot formation and combustion development were analyzed in a single cylinder optical diesel engine. First, an in-cylinder flow characterization when using a real bowl shape was performed by applying particle image velocimetry (PIV) technique. Subsequently, the flame movement, combustion process and soot formation were analyzed for different piston geometries through several optical techniques such as combustion image velocimetry (CIV), natural luminosity, OH* chemiluminescence and 2 color pyrometry. Finally, the combustion process and soot formation when using different e-fuels were studied by applying the same optical techniques used previously. In addition, for this part of the study, it was included a specific optical technique named high-speed spectroscopy for the soot analysis. Regarding the bowl geometries evaluation, the stepped lip and wave-stepped lip presented a faster late soot oxidation in comparison with the re-entrant geometry. Under extreme soot conditions, differences were also observed between the wave-stepped lip and the stepped lip. A faster soot oxidation was observed for the first one. The e-fuels showed a remarkable reduction in soot formation (especially OME_X) when compared with fossil diesel. From the spectroscopy analysis, it is possible to state the absence of soot during the combustion of pure OME_X. In general, the application of new hardware (bowl geometries) as well as new kind of fuels in diesel engines have presented a great potential in order to diminish the soot emissions.

The road to wisdom? Well, it's plain And simple to express: Err and err and err again, but less and less and less. Piet Hein

aos meus pais, Rui e Delci
aos meus irmãos, Daniel e Eduardo
à memória de meu avô, Adalberto Pires de Vargas

Acknowledgements

It has been four years since I started my PhD studies and there are several peoples that have been involved in this long journey who I would like to express my sincere gratitude.

First, I would like to thank CMT-Motores Térmicos Direction Board, Francisco Payri, José María Desantes, Jesus Benajes and Vicente Macián, for giving me the opportunity to be part of this prestigious research center and for providing all tools necessary to perform my investigation. I would like to extend my gratitude to all the administration staff (Amparo, Haby, Elvira, Carmina and Elena).

In addition, I am extremely grateful to my supervisors, Dr. José Vicente Pastor and Dr. Antonio García for all support, orientation, and advice during these last four years, always pushing me and encouraging me to move on, even in hard moments. Their immense knowledge and plentiful experience have encouraged me in all the time of my academic research and daily life. I started my PhD having two directors of thesis and I am leaving with two friends. Xevi (Dr. José Vicente Pastor), thank you for introducing me to the fantastic optical diagnosis world and showing me that cameras can provide much more than beautiful pictures of places or landscapes. Toni (Dr. Antonio García), thank you for not only teaching me a lot about engines but also for making me believe that was possible to publish my experiment results in excellent journals. I would also like to extend my gratitude to Dr. Carlos Micó for his tireless help during my PhD. You are one of the major responsible in the development of this work. I cannot forget to thank Dr. José María García for always giving me excellent advice during this journey.

I would like to thank all the work done and help received by the technical staff of the department. My most sincere gratitude to the technician Daniel Lérida for all the time spent together in front of the optical engine, solving issues, recording moves, and measuring points. Thank you for the talks about football and interesting things as well. Besides, I also need to thank all the CMT technician staff. Especially, José Henrique and Omar for all the support during my experiments.

My gratitude to GM/Punch Group for funding the work in this thesis. Thanks to Alberto Vassallo and Francesco Concetto for following closely the different projects that we have developed together during all these years. It was a pleasure to be part of this investigation together with you.

To reach the end of this journey, it is essential to be surrounded by good friends and I am sure that I have the best ones. Santiago, Rafael, Cássio, Vítor, Jácson, André, Augusto and Douglas, thank you all for the beers, talks and time we spent together. "Parzas", you made my life easier during this period. I also must extend my thanks to my office colleagues and CMT friends Alba, Léo, Frank, Daiana, Andrés, Antonio Jimenez, Santiago Cardona, Tomas, and Brayan. Thank you for the good times together working and discussing as well as enjoying the time. My last words in this section were saved for my family. Without their tremendous understanding and

encouragement in the past few years, it would be impossible for me to complete my study. I will take the liberty of writing in Portuguese, my native language.

Família, vocês são os principais responsáveis de tudo isso ter sido possível. Não tenho palavras que possam expressar a gratidão eterna que terei por vocês. Apesar da distância durante esses últimos 4 anos, foram vocês as pessoas que sempre me ajudaram a seguir em frente, vencer os momentos difíceis e nunca desistir. Pai e Mãe, a vocês eu somente posso dizer obrigado. Obrigado pelo amor, incentivo e apoio incondicionais. Obrigado por sonharem junto comigo e acreditarem que era possível. Dani e Dudu, obrigado por todo apoio e aconselhamento. Vocês são os melhores irmãos que eu poderia ter.

This work was partially funded by Generalitat Valenciana through the Programa Santiago Grisolía (GRISOLIAP/2018/142) program.

Table of Contents

Index of Figures

Index of Tables

Nomenclature

Initials and acronyms

A/F	Air-fuel ratio
P	Pressure
ICE	Internal Combustion Engine
CI	Compression Ignition
$RoHR$	Rate of Heat Release
SOI	Start of injection
PAH	Polycyclic aromatic hydrocarbons
LOL	Lift-off Length
LDV	Laser Doppler Velocimetry
RMZ	Radial Mixing Zone
HVO	Hydrogenated Vegetable Oil
LPG	Liquid Petroleum Gas
PM	Particulate Matter
SOE	Start of energizing
IVC	Inlet Valve Closing
$IMEP$	Indicated Mean Effective Pressure
ET	Energizing Time
$aTDC$	After Top Dead Center
PIV	Particle Image Velocimetry
DBI	Diffused Back Illumination
TKE	Turbulent Kinetic Energy
CAD	Crank Angle Degree
PID	Proportional Integral Derivative
NL	Natural Luminosity
$FT-diesel$	Fischer-Tropsch diesel

EGR	Exhaust Gas Recirculation
LHV	Lower Heating Value
UV	Ultraviolet
KL	Optical Thickness
$2C$	Two color pyrometry
$CA50$	Crank Angle at 50% mass fraction burned
FPS	Frames per second
rpm	Engine speed
$O100$	Pure OME_X
$D100$	Pure diesel
$O50D50$	50% OME_X and 50% diesel
$O90D100$	90% OME_X and 10% diesel
$O80D20$	80% OME_X and 20% diesel
$O70D20$	70% OME_X and 30% diesel
OEM	original equipment manufacturer

Greek

ω	Angular Velocity
λ	Wavelength
ϵ	Absorption coefficient
δ	Variation
η	Efficiency
μ	Micro

Subscripts

C_r	Compression Ratio
$Pinj$	Injection pressure
$Pint$	Intake pressure
$Tcol$	Coolant Temperature
$Tint$	Intake Temperature
$Toil$	Oil Temperature

Latin

NO_X	Nitrogen Oxides
CO	Carbon Monoxide
HC	Hydrocarbons

OME_X	Oxymethylene dimethyl ether
OH	Hydroxil radical
$O_{æ2}$	Oxygen
T	Temperature
m	mass
$\dot{m}$	Mass flow
$\bar{h}$	Enthalpy
p	Pressure
u	Internal energy
V	Volume
H_2O	Water

Chapter 1

Introduction

Contents

1.1 Introduction

The present chapter presents an overview of the work and research performed in this thesis in the framework of the internal combustion engines for transport. The first part shows the global context of the thesis in the current transport scenario and the issues of the internal combustion engines that have motivated this study. In addition, a brief discussion is performed about the new technologies which have been recently developed for keeping the ICE's alive. Finally, the objectives of the thesis and the general structure of this document are addressed, highlighting the novelties of this work.

1.2 General Context and Motivations of the Study

1.2.1 The future of transport: Challenges and projections

The constant growth of the world population as well as the industrial activity have increased significantly the energy demand during the last decades. Since around 1900, the fossil source have been the main alternative for supply the global energy demand [1]. In figure 1.1 it is possible to appreciate the energy consumption increase during the human life evolution. Until 2019, the figure shows that the oil, coal and gas were still the main source of energy. Nowadays, around 70% of fossil oil is used for running IC engines [2]. Internal combustion engines using liquid fuels have been considered the main responsible for powering the global transport. The dynamism of the society life have been allowed thanks to the ICE. Around 99.8% of the current transport is powered by ICE's [3]. In addition, the liquid fuels from petroleum are responsible for providing 94% of the energy used for the transport sector [4].

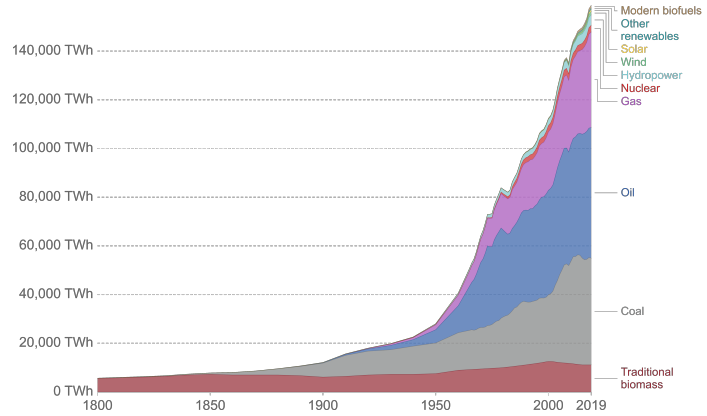

Figure 1.1. *Global direct primary energy consumption. Source [1].*

In contrast, recently, different sectors such as transport, industry and agriculture have faced the severe emission legislation imposed by the government. Although mass media commonly point out the ICE as the main contributor to the greenhouse gas emission, data reveal that only 16% [5] of the total GHG comes from the transport, as shown in figure 1.2. The energy used for buildings and industry represent a higher percentage of GHG emission when compared with the transport sector.

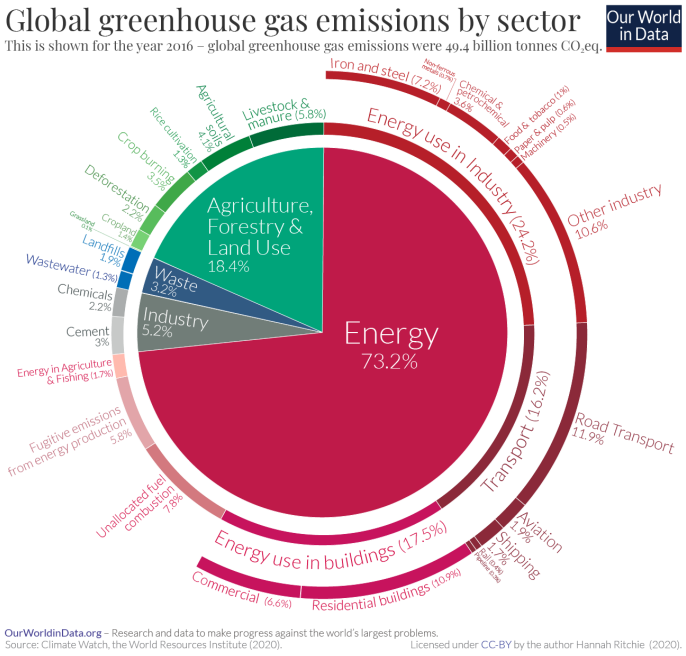

Figure 1.2. *Global greenhouse gas emissions by sector. Source: https://ourworldindata.org/ghg-emissions-by-sector.*

In this sense, one the main objectives of the automotive industry has been searching ways for reducing the percentage of contribution of the transport sector in the GHG emissions. For this purpose, during the last years, different new technologies for the internal combustion engines replacement have been massively reported by the media. The most attractive are the electrification and hybridization of the transport sector. The electric motors can be extremely efficient and electric vehicles have the capacity of recovering energy during the deceleration. The battery electric vehicles (BEV) have been considering as the new zero-emission cars due to they do not have any associated tailpipe emissions or local emissions. However, when the energy source for electric generation and battery manufacture are considered in the life-cycle analysis of GHG emissions, these statements could not be really true. Currently, the fossil fuels are still the main source for the global electricity production (around 60%). The renewable sources represent less than 10% of the global energy mix [6]. This fact reinforces the necessity of decarbonization and air pollutant reduction in all sectors. One single solution will not be enough for stopping the global warming. Another limitation of the BEV is related with the freight transport, where the dynamism is one

the main requirements in this sector. The most part of the trucks do not return for the base in the end of the day, making the battery recharging difficult. The fast charging, which could be a solution for this problem, creates a very high grid cost. Besides that, heavy-duty vehicles have very long drive cycle, which requires a high autonomy of the battery. Several alternative solutions have been pointed out by companies and research centres. The solution that is planned from the European commission is the utilization of BEV for the passenger cars and Fuel Cell Electric Vehicles (FCEV) for heavy-duty vehicles [7]. However, none of them have consolidated yet in the vehicle market. The future of transportation is still uncertain and indicates long life for the ICE.

In fact, the current scenario requires new technology solutions for the ICE. During the last few years, the ICE technology has been continuously improved, resulting in cleaner and more efficient engines. Focusing in compression ignition (CI) engines, several different technologies have mainly been implemented during the last decade. Efficient after treatment systems, new combustion modes [8] and new injection systems [9] have contributed for producing cleaner diesel engines. In the same way that the pollutant emissions have been reduced, the cost of diesel engine production have increased considerably as shown in figure 1.3. As the emissions legislation became stricter and the particulate emissions were reduced, the costs with after-treatment systems have increased significantly [10]. The treatment of pollutants outside of combustion chamber demands a plenty of different devices such as DOC, DPF and SCR, where the price of raw materials are elevated. In contrast, the reduction of in-cylinder pollutant emissions has been considered an important alternative.

Besides the new combustion modes, as already mentioned above, alternative fuels and innovative piston geometries appear with great potential for achieving the emissions target by promoting the pollutant reduction inside the combustion chamber. In diesel engines, the piston geometry takes a significant role on the flame movement, spray-wall interaction and fuel/air mixing process, which impacts directly on the in-cylinder pollutant formation and efficiency [11]. Different piston geometries have been tested for both light/medium-duty and heavy-duty engines. The re-entrant geometry is usual for high swirl light-duty CI engines. Recently, the inclusion of a stepped lip in standard re-entrant piston has been studied and tested by different companies. Besides that, for heavy-duty CI engines, Volvo group developed a new piston design called "wave piston", which is formed by wave protrusions distributed around the bowl circumference.

In the same way, the renewable fuels have also been considered an alternative for both fossil fuels replacement and pollutant emissions reduction. Among these renewable fuels, the synthetic fuels, more specifically the e-fuels, have demonstrated a great potential for reducing the in-cylinder pollutant formation as well as the fossil fuel dependence.

For a deeper understanding of the in-cylinder phenomena when using different pistons geometries and alternative fuels, the utilization of optical engines is crucial. Thanks to the development of new optical techniques, the direct visualization of the combustion process is able for explaining the phenomena which cannot be explained in tests using metal engines.

In addition, the combination of several optical techniques allow the quantitative and qualitative analysis of mixing, combustion and pollutant formation processes that take place inside the combustion chamber.

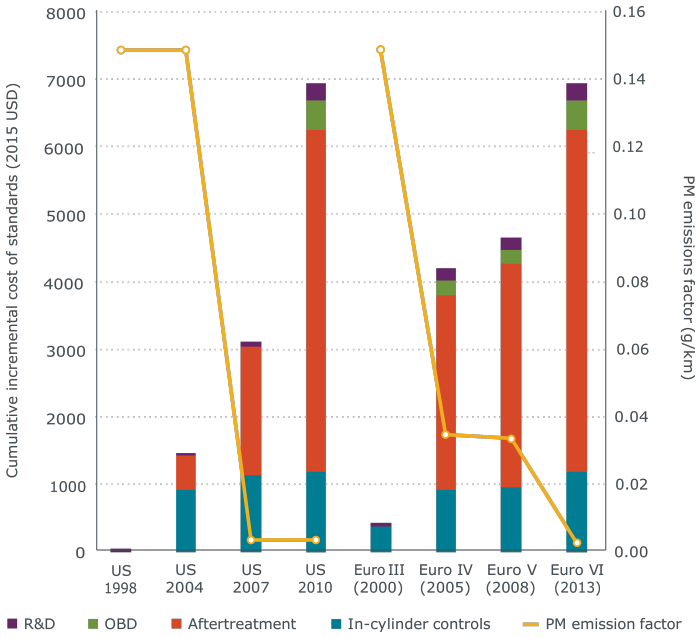

Figure 1.3. *Cumulative increment of diesel engine costs for each regulatory stage. Source [10].*

1.3 Objectives of the Study

In order to keep the improvements in engine technologies always growing up with less pollutant and more efficient engines, the present thesis aims to improve understanding on the effect that piston bowl geometry can play on combustion efficiency and soot production, linked to the use of clean e-fuels with low soot potential and net well-to-wheel low CO_2 emissions. To achieve this, there are some specific objectives that have to be followed:

- To characterize the in-cylinder flow pattern of a optical engine by using a real piston geometry (re-entrant).
- To identify the differences in terms of flame movement inside the combustion chamber using three different piston bowl geometries.
- To analyse the combustion process and quantify the soot formation in these three different piston geometries by using specific optical techniques.
- To evaluate the influence of e-fuels on the combustion process development and soot formation.
- To evaluate the soot formation when using different substitution rates of diesel in OME_X.

To fulfil these objectives, experiments will be performed in a single cylinder optical diesel engine operating with different transparent (quartz) piston geometries and e-fuels. A variety of optical techniques will be employed for a better comprehension of the different phenomena involved in each study.

1.4 Outline of the work

The present document is organized in 7 chapters. This is the first one (chapter 1), where it is presented a short introduction providing a general overview about the future of transport and also the alternatives available for keeping the internal combustion engines alive.
Chapter 2 presents a general description about the conventional diesel combustion process, focusing on the formation of air-fuel mixture and soot formation process. In addition, this chapter includes a bibliographic review about the effects of the in-cylinder movement, specifically the movement

generated by different piston geometries, in these air-fuel mixture and soot formation process. Besides that, the section also describes the potential of the replacement of fossil fuel by alternative fuels in diesel engines as well as their recent applications in CI engines.

Chapter 3 shows the tools and methodology applied for developing the current thesis. The optical engine used for the experiments, the test matrix and the optical techniques are explained in detail. The different fuels and the theoretical tools applied in the study are also discussed in this chapter.
Chapter 4, the results of an in-cylinder air-flow motion inside of a real bowl shape (re-entrant) are presented. The velocity field was measured by applying the Particle Image Velocimetry-PIV. From the velocity maps, it was possible to get the turbulent kinetic energy distribution inside the piston bowl. The main objective of this chapter was analyse the effect of the fuel spray on the velocity field and TKE distribution. This chapter allowed also a good comprehension about the limitations of optical techniques when using real bowl shapes. Different methodologies for image processing were developed for this analysis.

Chapter 5 is focused on the analysis of soot reduction by using new hardware systems in internal combustion engines. In this case, the chapter presents the main results obtained with the study of the impact of different piston geometries on soot formation and combustion behaviour. Three quartz pistons with different geometries were tested in a light-duty optical diesel engine. One of them is a completely new design proposed by General Motors. For the optical analysis, three optical techniques were applied simultaneously: 2 color pyrometry, OH* chemiluminescence and natural luminosity. Different engine operating conditions were used for understanding the differences of the three piston geometries and also for testing their potential in terms of in-cylinder soot reduction and soot oxidation improvement.

Chapter 6 is focused on soot reduction by using alternative fuels. The chapter discuss the potential of using e-fuels for the replacement of the fossil diesel. E-fuels are basically synthetic fuels, where the energy used for their production comes from renewable energies. Two different e-fuels were tested in a single cylinder optical diesel engine: fischer-tropsch diesel and oxymethylene dimethyl ether (OME_X). The previous methodology of chapter 5 was used again and a new spectral analysis has been included to analyse the soot propensity when using different e-fuels.

Chapter 7 summarizes the main results obtained in this thesis. In addition, some suggestions for future works, which could not be discussed in this thesis but present a strong potential for improving the work, are also proposed in this chapter.

Bibliography

[1] Ritchie Hannah. "Energy". *Our World in Data*, 2014. https://ourworldindata.org/energy.

[2] Reitz R. D., Ogawa H., Payri R., Fansler T., Kokjohn S., Moriyoshi Y., Agarwal A. K., Arcoumanis D., Assanis D., Bae C., Boulouchos K., Canakci M., Curran S., Denbratt I., Gavaises M., Guenthner M., Hasse C., Huang Z., Ishiyama T., Johansson B., Johnson T. V., Kalghatgi G., Koike M., Kong S. C., Leipertz A., Miles P., Novella R., Onorati A., Richter M., Shuai S., Siebers D., Su W., Trujillo M., Uchida N., Vaglieco B. M., Wagner R. M. and Zhao H. "IJER editorial: The future of the internal combustion engine". *International Journal of Engine Research*, Vol. 21 n^o 1, pp. 3–10, 2020.

[3] Leach Felix, Kalghatgi Gautam, Stone Richard and Miles Paul. "The scope for improving the efficiency and environmental impact of internal combustion engines". *Transportation Engineering*, Vol. 1 n^o April, pp. 100005, 2020.

[4] Kalghatgi Gautam. "Is it really the end of internal combustion engines and petroleum in transport?". *Applied Energy*, Vol. 225 n^o April, pp. 965–974, 2018.

[5] Ritchie Hannah. "Sector by sector: where do global greenhouse gas emissions come from?", 2020.

[6] Serrano José Ramón, Novella Ricardo and Piqueras Pedro. "Why the development of internal combustion engines is still necessary to fight against global climate change from the perspective of transportation". *Applied Sciences (Switzerland)*, Vol. 9 n^o 21, 2019.

[7] European Co. "European Partnership under Horizon Europe Towards zero emission road transport". Technical Report May, European Comission, 2020.

[8] Benajes Jesús, García Antonio, Monsalve-Serrano Javier and Lago Sari Rafael. "Fuel consumption and engine-out emissions estimations of a light-duty engine running in dual-mode RCCI/CDC with different fuels and driving cycles". *Energy*, Vol. 157, pp. 19–30, 2018.

[9] Boccardo Giulio, Millo Federico, Piano Andrea, Arnone Luigi, Manelli Stefano, Fagg Simon, Gatti Paolo, Herrmann Olaf Erik, Queck Dirk and Weber Jost. "Experimental investigation on a 3000 bar fuel injection system for a SCR-free non-road diesel engine". *Fuel*, Vol. 243 n^o October 2018, pp. 342–351, 2019.

[10] Posada Francisco, Chambliss Sarah and Blumberg Kate. "Costs of Emission Reduction Technologies for Heavy-Duty Diesel Vehicles". *The International Council of Clean Transportation (ICCT)*, Vol. 1 n^o February, pp. 39, 2016.

[11] Zhang Tankai, Eismark Jan, Munch Karin and Denbratt Ingemar. "Effects of a wave-shaped piston bowl geometry on the performance of heavy duty Diesel engines fueled with alcohols and biodiesel blends". *Renewable Energy*, Vol. 148 n^o x, pp. 512–522, 2020.

Chapter 2

Alternative technologies and fuels for soot reduction in compression ignition engines

Contents

2.1 Introduction

As the diesel engines have been faced big challenges regarding pollutant emissions, the industry and research centers have been trying to find new alternatives that can minimize or eliminate this problem. The in-cylinder pollutant reduction is one of these alternatives that has been widely explored. In this case, the utilization of less pollutant fuels or new geometries of piston have been considered promising solutions.

Therefore, in this chapter is carried out a literature review, focused on describing the issues involved in the conventional diesel combustion and the alternatives that have been employed for solving them. First, a general description of the diesel combustion phases is presented. Then, the in-cylinder flow movement in CI engines is described, highlighting the differences in terms of flow pattern for different engine sizes. After this, a review regarding piston geometries and its effect on the combustion process and soot formation is included in the chapter. Finally, a literature review of the the alternative fuels that have been considered as a potential for reducing the soot formation is presented.

2.2 Overview of diesel combustion process

2.2.1 Combustion phases

The combustion process in diesel engines can be classified as a combination of both premixed and diffusion combustion, where the diffusion phase is dominant, except at very low loads. It is a non-homogeneous combustion, with spontaneous ignition in different regions of the combustion chamber. Typically, the analysis of the diesel combustion is performed by means of rate of heat release (RoHR) trace, as represented in figure 2.1. It is obtained by the direct measurement of the in-cylinder pressure referenced with the crank shaft and the application of the First Law of Thermodynamics during the close cycle (intake and exhaust vales are closed) [1, 2].

Considering the RoHR trace and the start of injection (SOI), the literature usually splits the diesel combustion in three different stages, as follows:

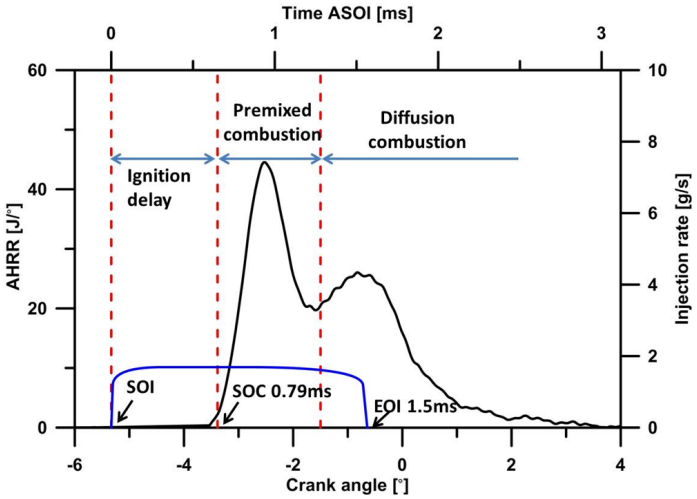

Figure 2.1. *Rate of heat release (black line) and injection rate (blue). Source [3].*

- **Ignition Delay**: In general, the ignition delay is defined as the time elapsed from the start of injection (SOI) up to the start of combustion (SOC). It is an important parameter for efficiency, pollutant emission, combustion noise and component load [4]. Once the fuel is injected in the combustion chamber, both physical and chemical processes take place during the ignition delay phase. Physical ignition delay involves the processes of primary and secondary breakup, evaporation and the formation of a reactive mixture. The chemical ignition delay corresponds to the period where pre-reactions occur and create appropriate conditions for triggering the spontaneous ignition.

- **Premixed combustion**: All fuel injected that had enough time for mixing with the air and forming an ignitable mixture during the ignition delay, is rapidly burned. It is a stage that generates a high-temperature combustion and a rapid and intense heat release. An abrupt heat release characterizes this phase, marked by the highest RoHR peak in figure 2.1. The end of the premixed phase occurs when the RoHR drops to relatively low values. During this phase, some soot precursors, as well as, final species such as CO_2 and H_2O are formed. In addition, the NO_X formation is usually linked with the quantity of fuel burned during the premixed phase as represented in figure 2.2. As higher is the RoHR peak, higher it will be the temperature and consequently the NO_X formation [4].

- **Diffusion phase**: Once the fuel and air premixed during the ignition delay are completely burned, the mixing-controlled process takes place. The RoHR is controlled by the rate that the *air* mixture becomes available for burning. Considering an injection that is long enough, the diesel jet achieves stationary conditions, keeping more or less the same flame structure until the end of injection. At the moment that the injection ends, the mixture formation is driven by the remaining turbulence inside the combustion chamber. The NO_X formed during the first phases is negligibly reduced during this stage, as can be seen in figure 2.2. The soot formation also begins when the energy starts to be released. However, the most part of the soot is formed during the diffusion phase although it is almost all oxidized during the expansion phase.

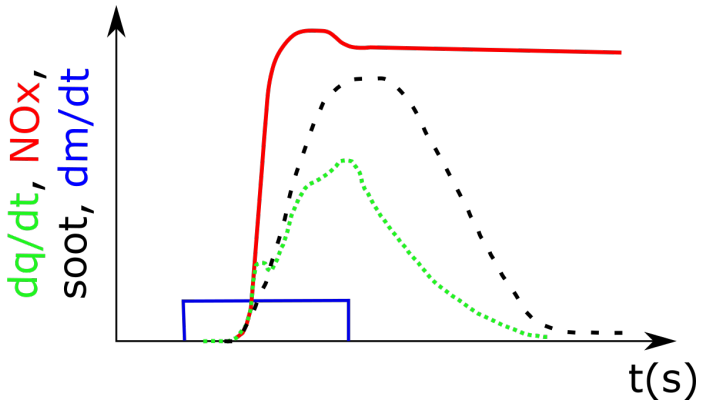

Figure 2.2. *NO_X and soot concentrations in a combustion chamber as function of time. Source [4].*

2.2.2 Formation of air-fuel mixture

Diesel engines are known to be an engine with internal mixture formation and "auto ignition". This is the reason that highly ignitable fuels need to be used and high temperatures have to be guaranteed. In this kind of engines, the energy conversion is controlled by the speed of the mixture formation, as well as, the injection rate. In this way, the air-fuel mixture process takes an important role for the combustion quality and emission formation in CI engines.

Considering that the mixture formation is internal and the injection of fuel inside the combustion chamber occurs just some degrees before starting the combustion, different air/fuel (λ) gradients are produced. Regions located in the core of the spray usually are extremely rich, where $\lambda \approx 0$. In contrast, the regions located at the periphery of the spray present $\lambda \approx \infty$, with pure air. These λ gradient also generates temperature differences inside the combustion chamber. Due to the short time available for getting a completely homogeneous mixture, the existence of rich regions makes impossible to avoid the soot formation. In the modern diesel engines, up to 95% of the generated soot is oxidized mainly during the expansion stroke.

In a normal way, the air movement inside the combustion chamber, which will be explained in detail later, as well as, the injection process have a direct impact in the mixture formation. In particular, the injection is one of the dominant parameter in the air-fuel mixing process. In this way, the injection system has to be capable of providing a spray which propagates for whole combustion chamber, forming small droplets that vaporise and mix with the ambient air. This entire process can be split in specific events known as atomization (primary and secondary breakup) and evaporation:

2.2.2.1 Atomization and Evaporation

This phase starts when a high-pressure liquid fuel is discharged inside the combustion chamber from the injector nozzle. During this process, there is a first phase, which is called primary breakup, where the liquid spray is converted in a cloud of droplets due to increase of the interaction between the liquid phase (fuel) and air. [3]. At this instant, deformations occurs in the liquid phase as a consequence of inertial instabilities, surface tension, cavitation, turbulence, etc.

These big droplets formed during the primary breakup can be unstable and they may further be fragmented into smaller droplets. The process occurs repeatedly until the droplets become stable [5]. This process is known as the secondary breakup, where the droplets obtained are much smaller than the nozzle diameter [1]. Aerodynamics interactions between fuel and air are the dominant phenomena during the secondary breakup. The process of getting small droplets is extremely important and necessary for the fast heating and evaporation, directly impacting on the ignition delay.

Besides the spray break-up process, the evaporation of the fuel also takes an important role on pollutant formation and combustion. Once the spray is atomized and the droplets are completely surrounded by the hot air present

in the combustion chamber, the process of heat transfer from the air to the droplets is intensified.

This process is directly influenced by kinetic energy of the fuel spray. The high velocity between the droplets and the air helps the mass transport and heat transfer. In this way, the droplet temperature is increased, causing the increase of its vapour pressure and the amount of evaporated fuel. By means of the evaporation process, the droplets decrease in size continuously, until they are completely evaporated

When the fuel injection and evaporation rate are equal, the liquid phase of the spray stops to penetrate. The distance from the nozzle exit to the tip of the liquid region is known as liquid length. It is an important parameter in the combustion process of engines. Longer liquid length could generate impingement inside the piston bowl and it leads to a higher formation of emissions.

2.2.3 Autoignition

The autoignition process occurs in regions where thermodynamic conditions in the combustion chamber, local temperatures and concentration of vapour are proper for promoting the chemical reactions. At this point, intermediate species are formed and energy is released, becoming the rate of heat release (RoHR) positive. The chain of processes during the autoignition were classified by *Higgins* [6] in three different stages: phisical induction, first stage ignition and second stage ignition/premixed-burn period.

- **Physical Induction Period**: This period is mainly driven by the physical process involved during the spray break-up. The fuel vaporization process absorbs heat, causing a rapid temperature decrease inside the combustion chamber. During this point, any kind of chemical reaction is impeded of occurring. Once the *air* mixture temperature starts to increase again and the conditions are appropriated, there is a simultaneous increase in pressure and chemiluminescence. This marks the end of the physical induction period and the beginning of the first stage of ignition.

- **First Stage Ignition Period**: It is the period characterized from the time where a small pressure rise and chemiluminescence can be detected, until the beginning of a rapid heat release. At this instant, the fuel is consumed due to the chain-branching reactions under rich conditions of *air* mixture. These reactions induce the production of radicals and

the release of small quantities of energy, increasing the temperature and pressure. Different authors have classified this period as low-temperature ignition process or cool flame [7, 8].

- **Second Stage Ignition Period**: It is marked by a significant heat release with a sudden increase of the premixed-burn pressure. The increase of the temperature due to the heat released during the first stage is responsible for promoting the hydrogen peroxide dissociation reactions, which leads to the production of the OH radicals [9]. These reactions release considerable amount of heat and they trigger the premixed burn. The transition of this radical from the excited to the ground state releases the typical OH^* chemiluminescence of this period.

2.2.4 Diffusion combustion phase

Once the premixed phase ends, the diffusion combustion phase starts, which extends until all the fuel injected is consumed. The diffusion combustion is classified as a process where the mixing rate controls the burning rate and the fuel and oxygen are not previously mixed. In this way, the fuel consumption rate is determined by the rate that fuel and oxidizer are mixed in appropriate portions for burning [10, 11]. Diffusion flames present a wider region than premixed flames, where the composition changes and chemical reactions take place. During this phase, the flame front establishes and it is sustained by the convective and diffusive transport of fuel and oxygen. The momentum induced by the spray makes the convection a dominant process during the injection event. Once the injection ends, the diffusion process becomes more relevant. In addition, some authors, such as Hsu [2] and Heywood [1], consider the existence of an independent phase, which begins after the injection ends. It is called late combustion phase.

The soot is formed in zones where the mixture is rich, with temperatures above 1600 K. These rich regions are located mainly in the spray core as well as in the piston bowl walls, where the spray is blocked. The high soot formation impacts in poor combustion and low efficiency of diesel engines. In addition, soot emissions are considered extremely harmful for both human health and environment. In modern diesel engines, most part of the soot formed (around 95 %) is oxidized during the expansion stroke. In general, the soot produced during the end of combustion is less susceptible to be oxidized due to the low temperature and pressure inside the combustion chamber. The existence of intense turbulence during the final stage of the combustion guarantees the late cycle soot oxidation.

In figure 2.3, the most widespread and well-accepted diffusion flame model proposed by Dec [11] is presented. The distance from the injector tip to the most upstream location of the lifted flame is known as lift-off length (LOL). The equivalence ratio at this fuel-rich zone is between 2-4. The oxygen that entrained previously in this region is consumed, increasing the temperature. The quantity of oxygen that is present in the premixed combustion is directly related to the LOL of the flame. The typical diffusion flame structure is formed downstream the LOL, where the internal volume is occupied by intermediate combustion products, unburned fuel and soot precursors (blue region). The diffusion flame front (orange) is formed by a thin layer stoichiometric surface with high amount of oxygen available [12]. The partial products of the combustion are oxidized when they reach the flame front. At this region most part of the fuel chemical energy is released. In addition, the existence of oxygen in the outer region of the spray (green) leads to lean mixtures and high temperature, promoting the NO_X formation.

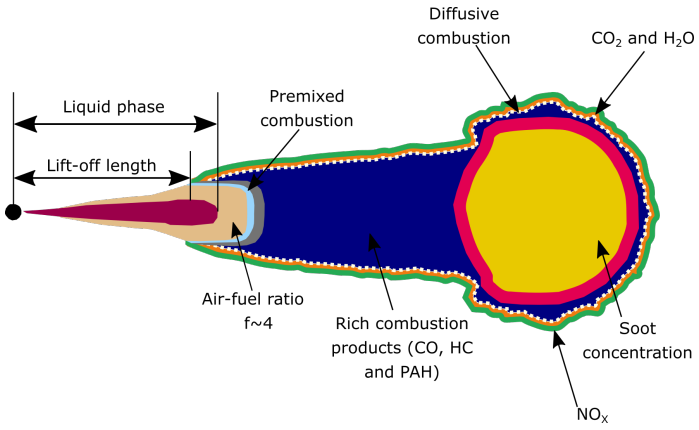

Figure 2.3. *Diffusion flame structure. Source [11].*

2.2.5 Soot Formation

Soot can be considered as a solid substance, which is mostly composed by carbon. It appears when the fuel molecules lose hydrogen atoms and carbon atoms combine and agglomerate to create the complex soot structures following the complex process. The transition from liquid or vapor hydrocarbons to solid particles mainly implies six processes: pyrolysis, nucleation, coalescence, surface growth, agglomeration, and oxidation [13]. The schematic of the different processes is represented in figure 2.4.

The pyrolysis is the process that comprehends the modification of the molecular structure of organic compounds under high temperature conditions. During the pyrolysis, the oxidation process is not notable. The fuel pyrolysis produces some species responsible for forming the soot precursors. In general, all fuels produce the same kind of species during the pyrolysis process, such as polycyclic aromatic hydrocarbons (PAH), polyacetylenes, unsaturated hydrocarbons and acetylene. Following the events in figure 2.4, the next process is the nucleation, where the soot particles are formed from the gas phase reactants. The beginning of the nucleation process is considered when it is formed the first aromatic ring by the combination of two propynyl radicals (C_3H_3). The process requires temperatures between 1300 and 1600 K, and it occurs in the radical-rich regions. This first aromatic ring adds alkyl groups and it is converted into a PAH structure. The presence of acetylene and different vapor-phase precursors makes the PAH structure grow [13, 14].

The surface growth is the next process in the evolution of the soot particles. It happens simultaneously with the nucleation process, without a clear difference between the end of nucleation and the beginning of surface growth. During this phase, mass is added to the surface of the soot particle formed during the nucleation. The hydrocarbons in gas-phase (usually acetylenes) are captured by the hot surface of soot particles, increasing the soot mass, while the particle numbers keep the same.

The last step comprehends both coalescence and agglomeration processes, where the particles combine. During the coalescence, the particles collide, reducing the number of particles, but keeping constant the mass of the combination of two particles. When primary particles stick together to form large groups of primary particles, the process is called agglomeration. Among these different processes for the soot formation, there is also the oxidation. It can occur at any time during the different soot processes, converting hydrocarbons to CO, CO_2 and H_2O.

During the last years, several optical diagnostics have been applied for a better understanding of the soot formation in diesel combustion. One of them is the 2-colour pyrometry [15–17]. It is based on the detection of the soot thermal radiation at two different wavelengths, which allows to obtain not only the 2D soot distribution, but also, the corresponding temperature. It will be one of the techniques used in the experiments for the soot studies in the optical engine performed in this thesis and it is presented in the following chapters.

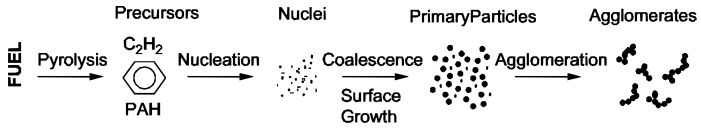

Figure 2.4. *Schematic of soot formation process. Source [13].*

2.3 In-cylinder flow movement in CI engines

The air movement inside the cylinder is one of the factors that impact directly the fuel-air mixing, soot formation and combustion process in internal combustion engines. In addition, the heat transfer is also affected by the air movement [1]. During the intake stroke, the incoming air interacts with the cylinder walls and moving piston, generating flow structures with large-scale turbulent motions within the cylinder [18].The flow through the cylinder head is very complex due to the high velocity of the gas, strong effects of the curvature in the inlets ducts and strong flow separation in the valve area [19]. In general, in-cylinder flow structures can be considered as organized or disorganized structures. Organized structures such as swirl and tumble, can be initially prepared during the intake process [20]. In direct injection (DI) diesel engines, the swirl flow takes an important role while tumble is more important in SI engines. These structures are shaped by the intake port design, cylinder-head geometry, intake valve design and valve timing. In addition, the squish flow is another in-cylinder motion extremely important in diesel engines, affecting directly the swirl in the bowl.

2.3.1 Swirl flow

Swirl is basically a organized "rotatory flow of solids" around the axis of the cylinder [1, 4]. The main function of the air swirl is to break up the compact fuel air spray and mix the air located between the sprays with the fuel. Obviously, there is a balance between the number of nozzle holes and swirl. As the holes number increases, the necessity of swirl decreases. In diesel engines, where the design is bowl-in-piston combustion chamber, the rotational movement created during the intake stroke is modified during the compression stroke. There are two way for producing swirl flow inside the cylinder. In the first one, the flow is discharged tangentially into the cylinder toward the cylinder wall and the swirl can be easily generated. In contrast,this approach induces high charge losses, which can impact on the combustion efficiency and emissions. The second and better suitable alternative is the utilization

of helical intake ports. The swirl is generated within the inlet port and the air is forced to rotate around the valve axis before entering the cylinder as represented in figure 2.5.

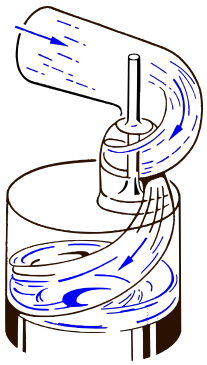

Figure 2.5. *Helical intake port design for swirl generation. Source [4].*

It can guarantee a good comprise between the necessary level of swirl and acceptable loss of volumetric efficiency. A constant ratio of swirl speed to engine speed can be obtained with this configuration. The swirl ratio can be mathematically defined as the equation 2.1, where the ω_{swirl} is the angular velocity around the cylinder centre axis and ω_{engine} is the engine crankshaft angular velocity.

$$SR = \frac{\omega_{swirl}}{\omega_{engine}} \tag{2.1}$$

2.3.2 Squish flow

The squish area is located on the outer radius of the piston. It is defined as a radial inward or transverse gas motion that occurs during the final stage of the compression stroke. [1]. The amount of air located between the piston crown and the cylinder head is pushed into the piston bowl, generating the typical squish flow. The fuel spray propagation is counteracted by the squish flow that supports the exchange of momentum between the injection spray and combustion chamber air [4]. Furthermore, the swirl and squish flow interaction has a strong effect in the turbulence generated inside the piston bowl. As the swirling flow is compressed into bowl, the moment of inertia decreases and rotational velocity increases (conservation of angular momentum). The squish flow disturbs the radial distribution of the swirl velocity and creates vertical

structures in the r-z plane that depend on the swirl level and bowl geometry [21]. In Light Duty (LD) engines with low SR, the squish flow enters the bowl horizontally and it creates a rotating vortex. However, for high SR, the squish goes down into the piston, following the bowl geometry [22, 23]. This effect can be seen in figure 2.6.

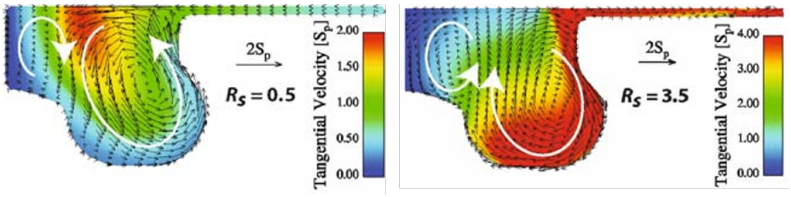

Figure 2.6. *Squish flow behaviour at different SR. Source [22].*

2.3.3 Cylinder head and intake port design

The port shape is responsible for the charge motion, where favourably shaped vortices reduce energy dissipation, and it influences the amount of air that gets into the combustion chamber [24]. Different intake port designs have been studied and tested during last years. In conventional light diesel cylinder heads with 4 valves, the swirl flow is promoted by the typical combination of two different intake port geometries: tangential and helical ports. The tangential design makes the intake flow enter the cylinder with a strong tangential velocity component, while the helical port creates a more spatially uniform flow, reducing the induction losses [25]. A butterfly valve is employed in variable swirl systems, where the swirl magnitude is set by the different positions of the throttle. For medium duty diesel engines, the intake port layout is more commonly used with two tangential ports (dual tangential). The figure 2.7 shows both tangential-helical port and dual tangential port layouts.

Depending on the engine size, different swirl levels are required. The twin and siamese ports, which are shown in figure 2.8, are typically used for heavy duty diesel engines. Twin port has advantages due to ease of manufacturing but it makes the design complicated because any change at one valve side can affect the other. The siamese intake port is composed by two separated ducts, allowing to get a better fluid pattern in isolation. It is used for reducing, as much as possible, the swirl flow inside the cylinder [26].

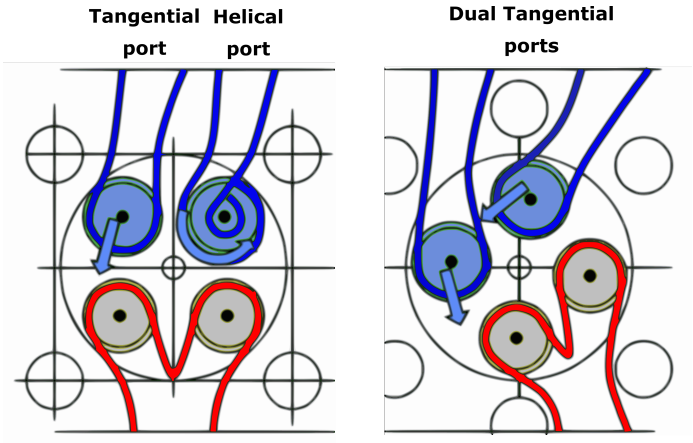

Figure 2.7. *Typical intake port layout for light and medium duty diesel engines.*

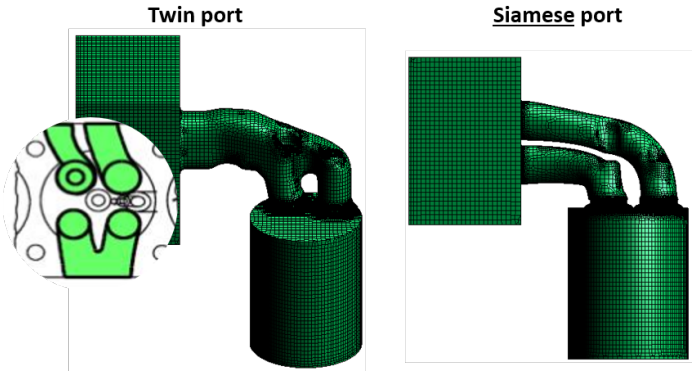

Figure 2.8. *Typical layout for heavy-duty diesel engines. Source [26].*

During the last years, a great variety of works have been developed focusing on the optimization of the intake ports. Most studies aim to develop a port layout that provides a high swirl ratio at low engine load, guaranteeing a good air-fuel mixing process, but low swirl ratio at high engine load to meet the intake air requirements. The CFD simulations in combination with experiments have been used for developing and validating new arrangements of intake ports.

Wang et al [27] optimized the intake port volute radius and the inlet and outlet section dimensions of helical intake port in a controllable intake swirl diesel engine. The swirl ratio and flow coefficient increased 16% and 4% respectively. Tikar et al. [28] also used the combination of CFD and

experiments for improving the combustion process and reducing pollutant emissions in IC engine for off-highway applications, where fuel injection systems are mechanical. In this kind of engines, the intake air process and the swirl generation take a vital role for achieving the target of emissions regulations. Optical techniques have also been used as an important tool for studying these new intake port designs and their effect on the different in-cylinder flow patterns. Regarding instantaneous planar techniques, Particle Image Velocitmetry (PIV) measurements are typically used in optical engines at motored and firing conditions [25, 29, 30]. For single point measurements, Laser Doppler Velocimetry (LDV) is also a laser diagnostic technique used for identifying the different in-cylinder flow structures and the turbulence properties [31–33]. Although the in-cylinder large scale flow structures are mainly dominated by the intake ports and cylinder head geometries, the combustion chamber geometry and fuel spray also affect the flow behaviour. In general, it is necessary a perfect matching of fuel spray, air motion and combustion chamber design in order to get a proper in-cylinder fuel/air mixing. Different works [29, 30, 34] have been studied the effect of different injection strategies on the in-cylinder flow pattern, turbulent kinetic energy distribution and heat transfer. Regarding combustion chamber geometry effects, several authors have reported works involving the utilization of different combustion chamber designs and their impacts on the in-cylinder flow [25, 35, 36]. The topic of combustion chamber geometries will be discussed in detail in next section.

2.4 Piston bowl geometry effects on the combustion process in CI engines

Currently, DI engines are the most common diesel engines used in the transport sector. This kind of engine typically has a piston with a bowl or cup machined into them, where the fuel is injected into.

In largest bore size engines, where the swirl is almost non-existent and the requirements of air-fuel mixing rate are lower, the combustion chamber is usually quiescent [37] with a shallow piston cavity.

For these systems, the energy and momentum of the spray injection is enough for getting a proper fuel distribution and efficient air-fuel mixing [1]. The injection pressure is high, between 2000 and 3000 bar. The injector is a multi-hole and it is located in the center of the combustion chamber. It is a combustion system known for operating at relative low engine speed

and having high thermal efficiency. In addition, the air can be accomplished without the need for air motion [38]. Heywood [1] classifies as a quiescent combustion system the engines with piston bore from 150 to 900 mm and engine speeds between 120 and 2100 rpm.

For smaller engines, in which the engine speed increases and the piston bore decreases, a faster air-fuel mixing rate, as well as, a higher swirl ratio are necessary. As already presented previously, the swirl flow is promoted by the intake port design and directly influenced by the geometry of the bowl and engine's stroke. The intake ports that generate swirl are designed as helical ports or tangential ports. Both variants may be used in four-valve technology, which is the most typical cylinder head configuration used today. In this way, the piston geometry for swirl assisted-DI engines is usually based on narrow and deep (re-entrant) piston bowls [4].

In general, these engines have high efficiency and moderate injection pressures, between 1600 and 2000 bar, with a multi-hole injector. The piston bore size considered for swirl-assisted DI engines is between 70 and 150 mm, comprising from light duty to heavy duty vehicles. In figure 2.9 is represented the geometry design variations and swirl intensity as the piston bore increases.

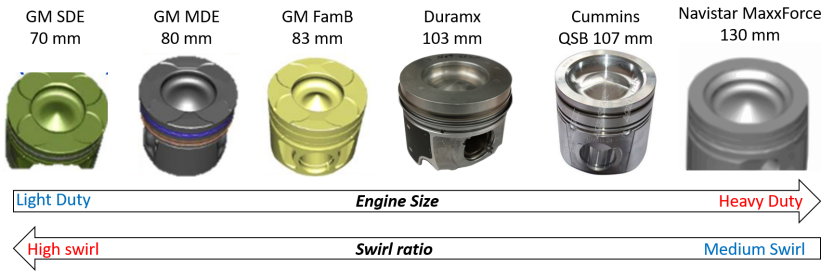

Figure 2.9. *Typical bowl designs according to different engine sizes.*

For four-valve high-speed direct-injection (HSDI) diesel engines, usually light and medium duty vehicles, the axisymmetric bowl-in-piston geometry with an injector located on the axis of combustion chamber is widely used. In this kind of geometry, the combustion chamber is defined as the volume existent in the squish region and piston bowl surface. The bowl has a concave recess shape for accommodating the spray that penetrates radially. This recess shape is crucial for swirl-assisted engines, due to the swirl is amplified when the air located in the squish region is compressed into the bowl. This movement results in a decrease in moment of inertia for the chamber charge, but in an

increase of the bore-scale angular velocity, with the purpose of conserving the angular momentum [39]. In addition, this kind of bowl shape also facilitates the interaction with the spray. The re-entrant piston (or ω shaped bowl), is the most common geometry used in light and medium duty HSDI engines.

In addition to swirl amplification, the re-entrancy also impacts in several factors. Firstly, it increases the turbulence levels and mixing rates within the bowl. Secondly, it preserves the kinetic energy of the fuel sprays re-directing them toward the cylinder center. Thirdly, it impacts the strength of the flow from the squish volume into the bowl. Fourthly and finally, it connects the bowl lip to the inner bowl. The bowl lip, highlighted in figure 2.10, controls spray penetration into squish and enhances the air utilization. The bowl pip re-directs the fuel jets and avoid stagnation of fuel-rich mixtures in the central region of the bowl. It also maintains the desired compression ratio.

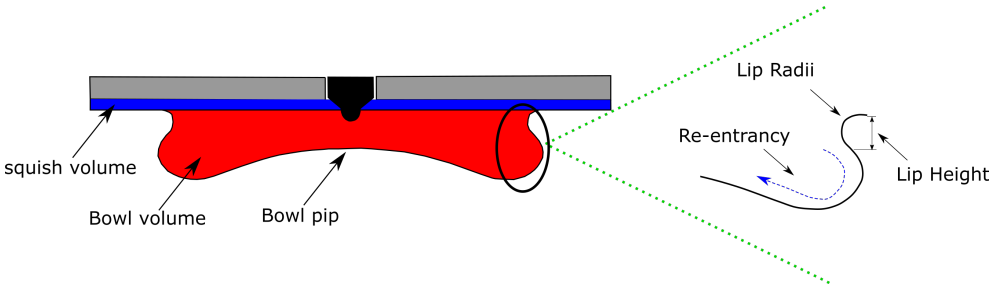

Figure 2.10. *Different areas of a typical four-valve HSDI diesel engine piston.*

The k-factor is a parameter very important to define the proportion of available air that participates in the combustion process [36]. The k-factor, represented in equation 2.2, is the ratio of the bowl volume and the total volume of the combustion chamber. Higher k-factor implies better air utilization. As the engine displacement is reduced, the relative k-factor decreases, leading to a deterioration of the combustion process.

$$K_{factor} = \frac{Volume_{bowl}}{Volume_{total}} \, at \, TDC \tag{2.2}$$

The surface to volume ratio, which is represented in equation 2.3, is the ratio between the total surface area and the volume of the chamber at TDC. Higher surface to volume ratio (S/V) implies higher heat losses. Larger chamber surface tends to increase heat transfer as the heat transfer area is bigger.

$$S/V = \frac{Surface Area}{Volume} \; at \; TDC \tag{2.3}$$

In general, the piston bowl design follows some basic rules. The maximum bowl diameter is typically around 60 % of the bore diameter and 3-4 times the maximum bowl depth. Currently, the industry is trending towards wider and shallower piston bowls in combination with higher injection pressure, lower compression ratio and higher k-factor. In addition, it is considered greater tolerance to variation in spray targeting (injection timing). The variations in the re-entrant piston geometries as well as different k-factors for different companies are shown in figure 2.11. It can be observed that, although the piston diameter is different, the k-factor is very similar for all pistons. In comparison with a heavy-duty piston, also represented in figure 2.11, it is possible to perceive that as the bore increases, the piston tends to be shallower. The best solution has to be balanced with the engine requirements such as efficiency, emissions and packaging.

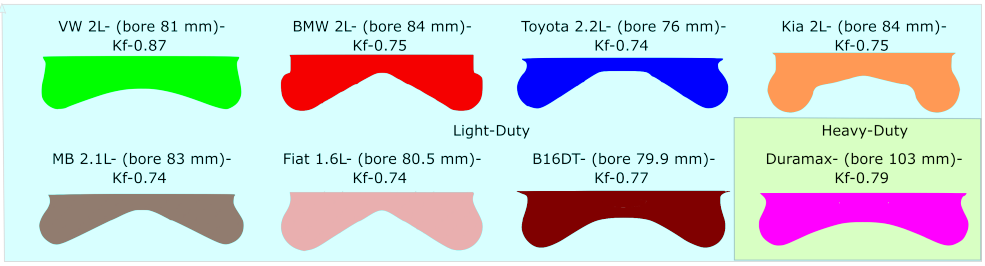

Figure 2.11. *Geometry variations of the re-entrant piston.*

2.4.0.1 Role of the piston geometry in the soot formation

The spray-wall interaction is a phenomenon that occurs in all diesel engines. Once the fuel spray is injected into the piston bowl, it collides with the walls and spreads out over the wall of the combustion chamber [9]. The flame-wall interaction occurs during most part of the combustion process. The interaction of the spray and piston at the lip of the piston has a significant influence on local air-fuel ratios in both the squish region and the bowl. It impacts directly the in-cylinder soot formation as well as the engine thermal efficiency [35].

In general, the net soot emission is linked with two main factors: the in-cylinder soot formation and in-cylinder soot oxidation. Generally, the rate of

these two processes is in the same order of magnitude. Thus, there are two ways for reducing the engine-out soot emissions: reducing the soot formation or increasing the soot oxidation efficiency. In this regard, the bowl geometry could affect both factors. The geometric parameters like the piston bowl throat diameter, depth of the bowl, central pip area and toroidal radius are extensively studied and optimized in order to get low soot formation and efficient soot oxidation as well as high thermal efficiency [40].

When the spray collides with the piston lip, the formation of a fuel film on the cavity wall occurs and rich mixtures are formed near the cavity wall [41]. These regions are the main source of soot formation. Depending on how the spray is spread inside the combustion chamber, more air entrainment can be obtained and consequently better air-fuel mixing and lower soot formation [42–44]. For the typical re-entrant piston, the bowl redirects the flame down into the bowl and then towards the center of the bowl. A small portion of the spray is conducted to the squish region for using the oxygen available in that region. A strong squish and reverse squish flow are provided by the narrow throat of the bowl, enhancing the fuel-air mixing.

The strong interaction between squish flow and swirl results in strong mixing during the final phase of the combustion, improving the late soot oxidation [45]. Zhu et al. [40] analysed by means of CFD, the effect of using reentrant pistons with different toroidal radii on the soot formation. The different geometries and also the soot distribution inside of each bowl geometry are presented in figure 2.12, where mod 1 and mod 2 are the modified geometries. The first important thing that can be highlighted in this image is that the highest soot concentration for this kind of bowl geometry is located at the periphery of the bowl. This is the region where strong flame/wall and flame-flame interactions happen, which generates fuel rich zones. The second important thing to highlight here is the effect of varying geometric parameters of the bowl on the soot formation and distribution. In this case, the authors have concluded that mod 1 presents larger soot concentration in comparison with the other two geometries. In contrast, mod 2 presents the smallest soot concentration area. This is an example which confirms that piston bowl can directly affect the soot formation in a diesel engine and how important is the correct development of the piston geometry for a specific engine. Depending on the engine size, swirl intensity and number of injector orifices, it will exist different optimum combustion chambers.

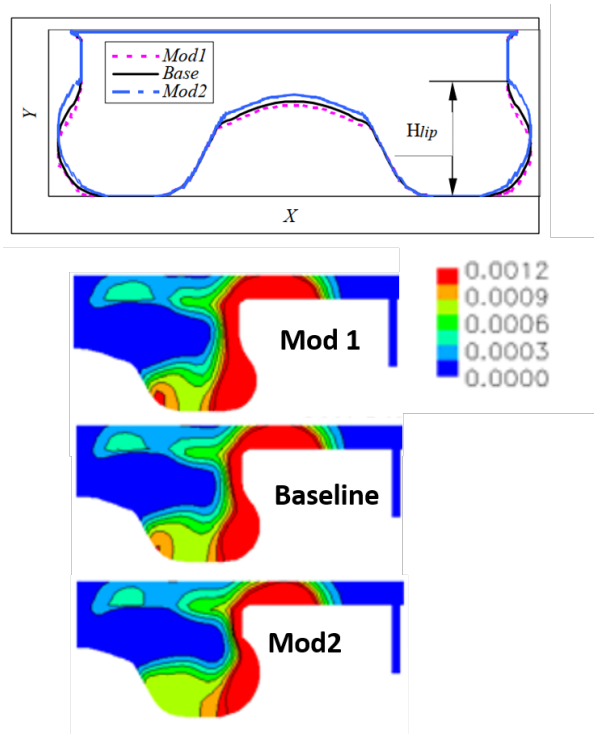

Figure 2.12. *Soot distribution in different toroidal radii of reentrant pistons. Source [40].*

2.4.1 Recent applications in new piston bowl templates

During the last years, different new piston designs have been developed for both high (light duty) and low (heavy duty) swirl supported diesel engines. Regarding the high swirl engines, the different variations and optimization are based on the re-entrant geometry. Zha et al. [39] made a review in timeline format, showing the evolution and modifications of the re-entrant geometry over the years. Figure 2.13 shows the different geometries tested and developed by different authors [45–53]. The inclusion of a stepped or chamfered lip instead of the protruding lip was a milestone in the new designs of re-entrant bowls. The literature indicates that a better air-fuel mixing and more complete combustion is achieved at the point where the spray is targeted when the steeped lip is used [54]. Several authors have also demonstrated that stepped or ramped lip can improve the fuel consumption as well as reduce the CO and soot emissions in comparison with the conventional re-entrant bowl shape [36, 55, 56].

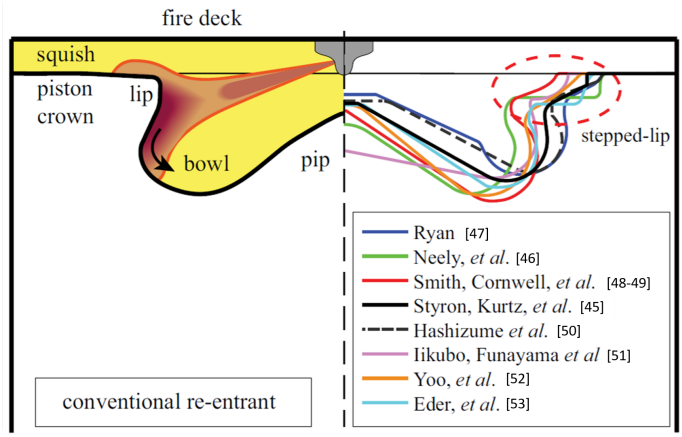

Figure 2.13. *Re-entrant piston variations developed over the years. Source [39].*

Nelly et al. [46] studied a kind of stepped lip bowl geometry called two-stage chamber. It was developed by Honda and tested in a 2.2 L 4-cylinder diesel engine. An improvement in fuel consumption for high engine loads was reported by the authors. The local equivalence ratio was reduced significantly, producing an important reduction of soot emissions. A bowl geometry called "twin vortex", which includes the stepped lip design, was developed, patented [49] and tested [48] by Ricardo UK company. The tests were performed in JCB off-highway diesel engines, where the Tier 4 interim/Stage 3B legislation was complied without the necessity of using any kind of after treatment systems. The fuel consumption was also improved [48]. Another variation of the stepped lip geometry was tested by Dockoon et al. [52]. The piston is called ULPC (ultra-low particulate emissions) and it was developed to be used in light-duty and off-road applications. The authors have reported a reduction of soot above 60 % and an improvement in the soot-NO_X trade-off.

In figure 2.14, Busch et al. highlighted the differences between the re-entrant and stepped lip geometry in terms of fuel splitting, jet impingement and vortex dynamics. In the conventional bowl, once the fuel collides with the lip, around 50 % of the spray is redirected downward. In contrast, when using the stepped lip bowl, around 60 % of vapor fuel is directed toward the squish zone after it impinges the piston step. In addition, for the stepped lip bowl, the fuel which is directed upward impinges on the cylinder head and spreads inward and outward. This recirculation enhances the air utilization and the late-cycle turbulent mixing. The upper toroidal vortex transports the

mixture toward the cylinder center, away from the mixture in the outer squish region [35, 57].

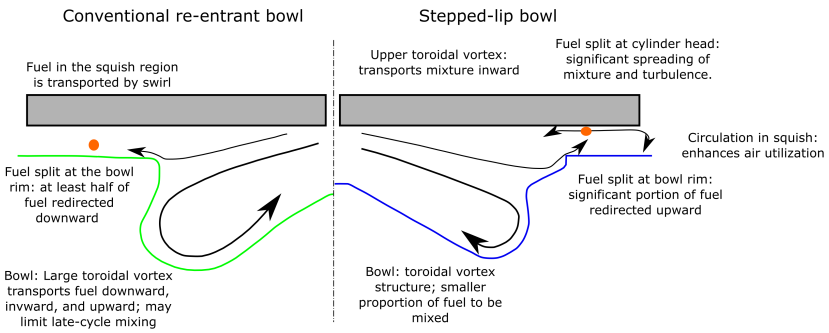

Figure 2.14. *Scheme for comparing the differences of a conventional re-entrant bowl and a stepped lip bowl. Source [36].*

Regarding the new templates for low-swirl heavy-duty engines, recently Volvo has launched a new piston named "wave piston" [58]. These waves are located around the circumference of the outer bowl, as it is represented in figure 2.15. The late cycle oxidation was studied by Eismark et al. [59] using this wave geometry.

Figure 2.15. *Wave piston developed by Volvo for truck engines. Source: [59].*

The tests were performed in both a single cylinder engine and a high pressure/temperature vessel. The soot emissions had a reduction of up to 80 %, as well as, a strong reduction of soot-NO_X trade-off. The images taken in the vessel have shown an improvement of the soot oxidation and a faster soot burn-out. In this case, the protrusions direct the flame toward the bowl center, where fresh oxygen is available. After the collision of the flame with the piston walls has occurred, the tangential flame movement generates flame-flame collisions in an unfavourable angle (180◦ near the wall). During this strong flame-flame interaction, the useful kinetic energy of the spray is wasted, creating stagnation zones, where rich combustion products are mixed. At this stagnation zones, the oxidation rate of both fuel and soot are reduced [59].

The protrusions have the objective of providing a more smooth flame-flame collision, as can be seen in figure 2.16, creating a more efficient transport of spray kinetic energy and less stagnation areas (regions represented by letter P) inside the combustion chamber. As the collision between flames is smoother, more kinetic energy becomes available for creating important vortices.

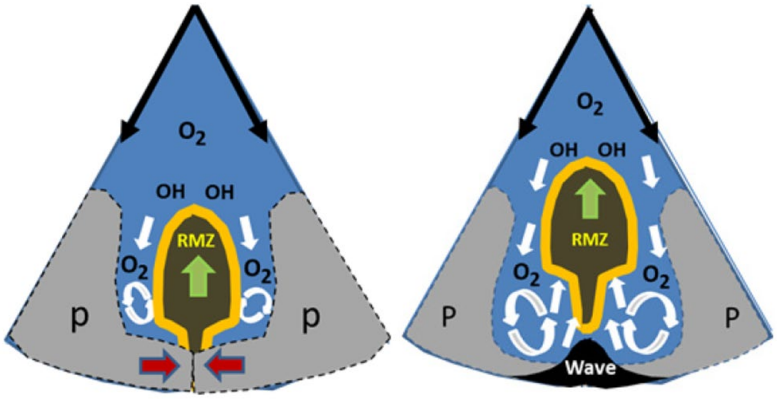

Figure 2.16. *Scheme of the late-cycle mixing in low-swirl combustion. Source: [59].*

A radial mixing zone (RMZ) is generated in the wave piston, as can be seen in figure 2.16. It is responsible for moving the flame and combustion products toward the center of bowl, where there is oxygen available. This movement enhances the oxidation process. Later, when the injection event finishes, this RMZ, which is still active, is detached from the piston wall. An optical study developed by [60] captured this effect, as can be seen in figure 2.17. A time series of instantaneous natural luminosity images illustrates the movement of the RMZ and how its trailing edge detaches from the wall and goes toward the center. This trailing edge contains soot that is oxidized thanks to the

energy provided by the side vortices (white arrows). The authors have stated that the oxidation of this trailing edge can be considered the main reason for the significant enhancement of the late-cycle oxidation process when using the wave piston.

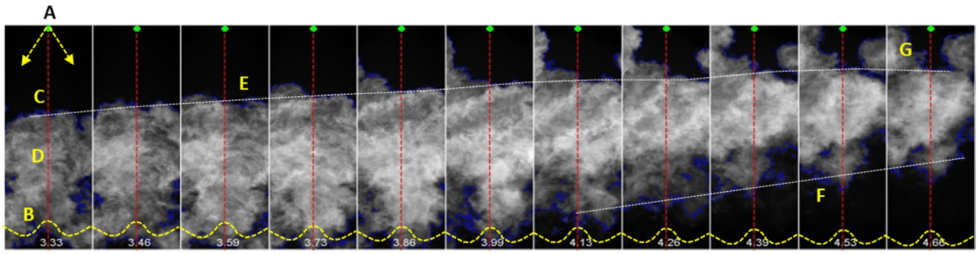

Figure 2.17. *NL images of the effect of wave protrusions on the flame movement. The green dot and yellow arrows indicate the nozzle location and original spray axes, respectively. Source: [60].*

2.5 Alternative fuels for CI engines

The constant increasing of the global energy consumption, the climate concerns due to the burning of fossil fuels and the possibility of their depletion, makes the alternative fuels become a potential solution, in combination with new combustion concepts and hardware, for reducing the pollutant emissions in ICE [61, 62]. Alternative fuels can be classified as all those other than conventional gasoline and diesel fuels, having a big variety of different final forms and production sources. Among this vast variety of non-conventional fuels are alcohols, natural gas, biodiesel and hydrogen [63]. In addition, for the complete defossilization of the transport sector, the production of fuels from renewable sources, using mainly renewable electricity and biomass, is extremely important for a sustainable supply of fuel [64]. The utilization of this renewable biofuels can create a CO_2 life cycle, contributing to mitigate the net CO_2 emissions. Figure 2.18 represents the energy demand previous until 2040 for the transport sector. The heavy duty vehicles, which probably will still be mainly propelled by ICE, will demand a significant quantity of energy. In this sense, the utilization of alternative fuels is expected to increase around 70 % for medium-duty and 20 % for heavy-duty vehicles [65].

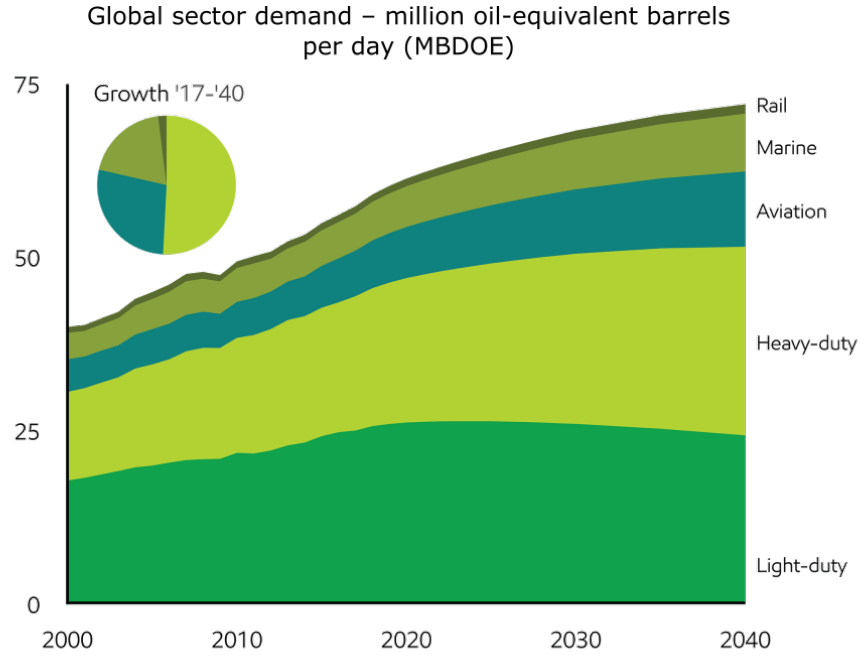

Figure 2.18. *Transportation energy demand growth driven by commerce. Source: [65].*

2.5.1 Potential of replacement of fossil diesel by alternative fuels

Currently, there is a great variety of alternative fuels that have the potential to be used in diesel engines. Among them, biofuels and e-fuels have been considered as promising alternatives for achieving a cleaner combustion and reducing the fossil diesel dependency. Biofuels are produced from the biomass or organic matter. E-fuels are synthetic fuels, which are produced using renewable energy.

Among the biofuels that could be used in diesel engines, hydro-treated vegetable oil (HVO) is a promising drop-in fuel with low impact on CO_2 emissions. Moreover, the production of syngas, bio-oil and biochair from non-food biomass via fast pyrolysis are also considered interesting biofuels for replacing the diesel. Regarding biodiesel, which is the biofuel most consolidated in the CI engines market, there are some types that are more than 70 % net-carbon neutral today.

On the other hand, the synthetic fuels derived from waste biomass and renewable electric energy have also been proposed to produce an electro-fuel (e-fuel) with net zero CO_2 emissions [66]. The figure 2.19 shows different synthetic fuels that can be produced from renewable electric energy, clean hydrogen and carbon capture [67]. In general, the green hydrogen, which is used for obtaining the e-fuels, is generated by using renewable electrical energy (wind, mini-hydro, solar thermal, photovoltaic, etc) and electrolysis to split water. Therefore, methanol or syngas can be obtained by the combination of the captured CO_2 and hydrogen through the direct methanol synthesis or reverse water gas shift. From syngas and applying the fischer-tropsch (FT) process, it is possible to obtain the synthetic diesel. From the methanol it is possible to obtain the Oxymethylene dimethyl ether (OME_X). The last one is a very promising fuel for obtaining cleaner diesel engines. In the same way, the same renewable fuels cited above can be obtained by generating the blue hydrogen instead of the green one. In this case, the hydrogen is obtained through the steam methane reforming (SMR) by using the natural gas.

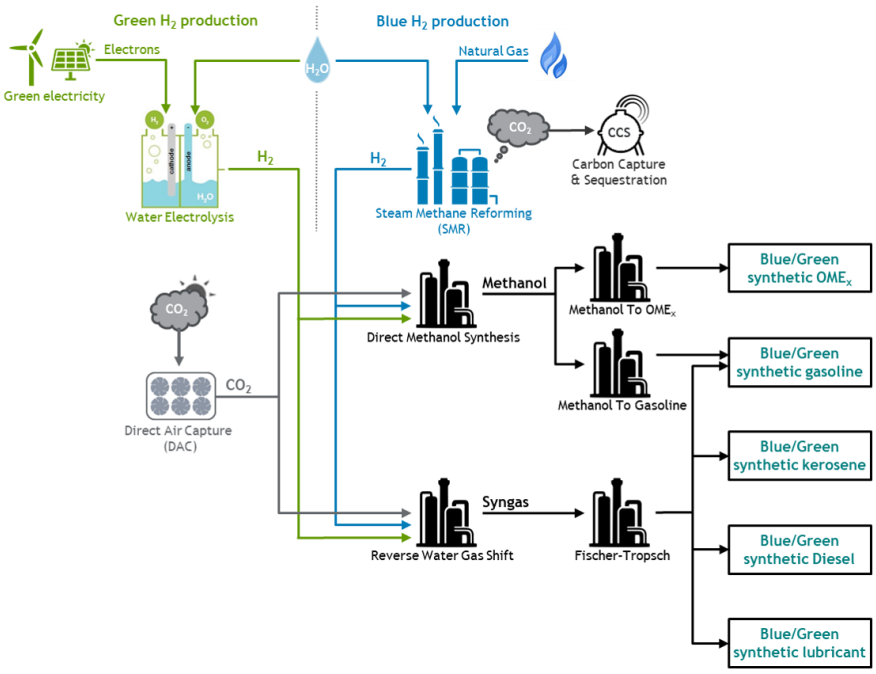

Figure 2.19. *Different fuel production pathway for synthetic fuels. Source: [67].*

In general, there are some critical considerations for considering alternative fuels in CI engines, which are pointed out by Bae and Kim [63]:

- **Lower heating value (LHV)**: Alternative fuels with similar level of LHV to conventional diesel fuel is an important factor, where low LHV's can affect directly the fuel consumption.

- **Physical properties**: The mixture formation is also dependent of the physical properties of the fuel. Density, viscosity and flash point are some parameters that impact the quality of the air-fuel mixture and the spray behavior. The cetane number is another important property which drives the combustion evolution process in CI engines.

- **Material compatibility**: The direct utilization of alternative fuels in the current engine hardware and injection system technologies is another point that determines if a new fuel has the potential, or not, of replacing the conventional diesel fuel. Extra costs involving engine modifications stop the penetration of these alternative fuels in the automotive market.

- **Manufacturing costs**: This issue is related with both manufactures and costumers. The price of alternative fuels production has to be competitive with the conventional diesel. Over the years, the price of alternative fuels production has reduced as the technology employed has improved. However, the production price is still high in comparison with the fossil diesel.

2.5.2 Recent applications of alternative fuels in CI engines

Many recent studies have been focused on the utilization of HVO and e-fuels in CI engines. HVO is a mixture of paraffinic hydrocarbons without sulphur and aromatic contents, which are processed from vegetable oils through an alternative process to esterification called hydrotreating [68]. In general, HVOs present similar chemical properties to conventional diesel, but lower density and higher cetane number. Different tests have been performed in both diesel engines and high pressure and high temperature vessels. Dimitriadis et al. [69] used HVO produced by Neste Oil in a light-duty diesel engine applying different injection strategies. The authors have compared the performance of the engine operating with HVO to conventional diesel fuel. The objective was to achieve soot and NO_X reduction without penalizing the thermal efficiency and fuel consumption. In general, the results showed a soot reduction of 40 % as well as a HC reduction of 45 % in comparison with diesel. NO_X emissions were similar or sightly higher than diesel. However, the authors stated that, as the soot emissions decrease significantly, a proper engine re-adjustment has a big potential of reducing the NO_X emissions. Pastor et al. [70] analysed the combustion ignition and behaviour of blend of HVO and liquid Petroleum Gas (LPG)in a high pressure and high temperature vessel by means of optical techniques. The authors found that ignition delay increases as LPG percentage increases in the blend. Furthermore, it was concluded that the natural luminosity of the flame decreases as LPG is added in the blend, indicating less soot formation. A study using pure HVO and blends with diesel was carried out by Bortel et al. [71]. They used a passenger car size single cylinder diesel engine for the tests. Significant reduction of HC and CO and soot emissions (64.3 %, 61.8 %, 80.2 % respectively) was found by the authors. Unlike most studies, the authors reported a small decrease of NO_X emissions, which opens new possibilities to optimize the ECU strategy for diminishing the NO_x-PM trade-off.

Among the alternative fuels that are on the up in the moment, it is possible to highlight the e-fuels. They are synthetic fuels produced with renewable energy and do not compete with foodstuffs, as they use CO_2 as raw material and can be both gaseous or liquid fuels [72]. Diesel produced by Fischer-tropsch(FT) process is among the different e-fuels with high potential for replacing the fossil diesel. It is a composition of different n-alkanes and can be produced from several natural resources e.g. biomass [73]. Furthermore, FT diesel also presents properties very similar to diesel such as viscosity, lubricity,

flash temperature, cold-flow properties and boiling temperature, covering the most part of diesel specifications.

Regarding the spray structure, Kook and Picket [74] analysed the vapor penetration and liquid length in a constant volume chamber using fischer-tropsch as the fuel and conventional diesel. For the analysis, the authors have applied two different optical techniques: Schlieren and Mie-scattering. The vapor penetration was similar for both fuels tested, but shorter liquid length was observed for the FT-diesel, indicating an improvement of air-fuel mixing. By testing this kind of fuels, several studies have demonstrated the reduction of soot, HC and CO emissions [75–77]. However, the results regarding NO_X emissions have not converged toward a common point, since different studies have presented different conclusions. Blends of methanol-FT diesel-biodiesel-diesel were tested and compared with fossil diesel at different altitudes by Jiao et al. [78]. The particulate matter (PM) emissions decreased for all altitudes tested, while NO_X emissions were slightly higher in comparison with conventional diesel. Contrary to this, there are some studies where the decrease of NO_X, as well as, the improvement of soot-NO_X trade-off were reported when using adequate blending and EGR rate [76, 79, 80]. An investigation in an optical engine was performed by Schaberg et al. [81]. The authors used Two colour pyrometry and OH* chemiluminescence for the analysis. The results showed a reduction of the soot radiation when using FT-diesel instead of conventional diesel.

The oxymethylene dimethyl ethers (OME_X), which also belong to the family of e-fuels, are another interesting alternative widely discussed today. OME_X is a chemical structure formed by a CH_3-O-$(CH_2$-O$)_x$-CH_3, where the x can be in the range of 1 to 5 [82]. It is produced by using formaldehyde and methanol [83]. The absence of C-C bonds and the high quantity of oxygen atoms make the OME_X combustion process practically free of soot emissions. The simplest chemical structure of OME_X is known as OME_1 and presents problems with the storage and handling because of the very low boiling point. A modification of the injection is necessary for operating with the OME_1 in order to avoid the problems with vapour lock [82, 83]. Chemical structures of OME_X with longer chains (x=3,4,5) present characteristics more similar to diesel, being more appropriate for using in the current injection systems [84]. A significant soot, HC and CO reductions have been reported in several studies involving the utilization of OME_X in diesel engines [85, 86]. Some optical studies regarding soot formation using blends of OME_X and diesel have been developed in constant volume vessels [82, 87]. A remarkable soot reduction (around 68 %) was found by Ma et al. [87] in an experiment using up to 30 % of OME_X blended with diesel and without the necessity of any modification

in the injection system. Ianuzzi et al. [82] also reported a massive reduction of the soot formation when increasing the oxygenated fraction (OME_X) in the blend. Regarding NO_X emissions, the authors have reported contradictory results. Lump et al. [88] found that the NOx emissions decreased when 20 % of OME_{3-4} was blended with diesel. In contrast, Liu et al. [89] reported an increase of NO_X emissions as the OME_{3-4} quantity was increased in the OME_{3-4}/diesel blend. However, it is important to highlight that taking into account the high amount of oxygen in the fuel, high EGR rate can be applied without penalizing the soot emissions [83, 84].

2.6 Summary & conclusions

As it could be seen throughout this chapter, different alternatives for both soot reduction and fossil diesel replacing in CI engines have been applied in the last years. In this sense, the review highlighted the potential of two of them: innovative piston geometries and e-fuels. Although some studies were already carried out with these technologies, there are still some topics that could be explored and they are summarized as follows:

- In the case of wave protrusion, they demonstrated a significant soot reduction when applied in heavy-duty engines. However, what could be the effect of this geometry in light diesel engines?
- The flame behaviour when it interacts with the wave protrusions was analyzed just by CFD simulations and optical studies in a high pressure and high temperaure vessel. The utilization of this geometry in an optical engine operating under real condition can provide important insights regarding the flame movement and the soot production.
- As OME_X is a e-fuel that started to be studied recently, there are several things about the combustion process that still cannot be explained. In this way, the application of simultaneous optical techniques for studying pure OME_X combustion in an optical engine can improve the comprehension about this fuel and provide important results.

Bibliography

[1] HEYWOOD J. B. *Internal Combustion Engine Fundamentals.* McGraw-Hill, New York, 1 edition, 1988.

[2] Hsu Bertrand. *Practical Diesel-Engine Combustion Analysis*. SAE International, oct 2002.

[3] Xuan Tiemin. *Optical investigations on diesel spray dynamics and in-flame soot formation*. Doctoral Thesis, Universitat Politècnica de València, 2017.

[4] Mollenhauer Klaus and Tschöke Helmut. *Handbook of Diesel Engines*. Springer, Berlim, 2010.

[5] Dumouchel Christophe. "On the experimental investigation on primary atomization of liquid streams". *Experiments in Fluids*, Vol. 45 n^o 3, pp. 371–422, 2008.

[6] Higgins Brian, Siebers Dennis and Aradi Allen. "SAE TECHNICAL Diesel-Spray Ignition and Premixed-Burn Behavior". n^o 724, 2014.

[7] Skeen Scott, Manin Julien and Pickett Lyle M. "Visualization of Ignition Processes in High-Pressure Sprays with Multiple Injections of n-Dodecane". *SAE International Journal of Engines*, Vol. 8 n^o 2, pp. 696–715, 2015.

[8] Pickett Lyle M. "Visualization of diesel spray penetration, cool-flame, ignition, high-temperature combustion, and soot formation using highspeed imaging". *Western States Section/Combustion Institute Fall Meeting 2007*, Vol. 2 n^o 1, pp. 867–879, 2007.

[9] Pickett Lyle M., Siebers Dennis L. and Idicheria Cherian A. "Relationship between ignition processes and the lift-off length of diesel fuel jets". *SAE Technical Papers*, n^o 724, 2005.

[10] Glassman Irvin and Yetter Richard A. *Combustion*. Elsevier Inc., Burlington, fourth edition edition, 2008.

[11] Dec John E. "A conceptual model of di diesel combustion based on laser-sheet imaging". *SAE Technical Papers*, 1997.

[12] Dec John E. and Coy Edward B. "OH radical imaging in a di diesel engine and the structure of the early diffusion flame". *SAE Technical Papers*, n^o 412, 1996.

[13] Tree Dale and I. Svensson Kenth. "Soot processes in compression ignition engines". *Progress in Energy and Combustion Science*, Vol. 33, pp. 272–309, jun 2007.

[14] Bockhorn Henning. "Soot formation in Combustion", 1994.

[15] Yan Jingde and Borman Gary L. "Analysis and In-Cylinder Measurement of Particulate Radiant Emissions and Temperature in a Direct Injection Diesel Engine". sep 1988.

[16] Quoc Hoang Xuan, Vignon Jean Marc and Brun Maurice. "A new approach of the two-color method for determining local instantaneous soot concentration and temperature in a D.I. Diesel combustion chamber". *SAE Technical Papers*, 1991.

[17] Zhao H. and Ladommatos N. "Optical diagnostics for soot and temperature measurement in diesel engines". *Progress in Energy and Combustion Science*, Vol. 24 n^o 3, pp. 221–255, 1998.

[18] Basha Syed Ameer and Raja Gopal K. "In-cylinder fluid flow, turbulence and spray models-A review". *Renewable and Sustainable Energy Reviews*, Vol. 13 n^o 6-7, pp. 1620–1627, 2009.

[19] Kaario Ossi, Lendormy Eric, Sarjovaara Teemu, Larmi Martti and Rantanen Pekka. "In-cylinder flow field of a diesel engine". *SAE Technical Papers*, n^o 724, 2007.

[20] Binjuwair Saud, Ibrahim Salah, Wigley Graham and Pitcher Graham. "In-Cylinder Flow Structure Analysis by Particle Image Velocimetry Under Steady State Condition". *SAE Technical Paper Series*, Vol. 1 n^o Ic, 2012.

[21] Pastor Jose V., Garcia Antonio, Micó Carlos, Lewiski Felipe, Vassallo Alberto and Pesce Francesco Concetto. "PIV and DBI Experimental Characterization of Air Flow-Spray Interaction and Soot Formation in a Single Cylinder Optical Diesel Engine Using a Real Bowl Geometry Piston". *SAE Technical Paper Series*, Vol. 1 n^o Ld, pp. 1–14, 2019.

[22] Miles Paul C. *Turbulent Flow Structure in Direct-Injection, Swirl-Supported Diesel Engines*, pp. 173–256. Springer Berlin Heidelberg, Berlin, Heidelberg, 2009.

[23] Dembinski Henrik W R. *In-cylinder Flow Characterisation of Heavy Duty Diesel Engines Using Combustion Image Velocimetry*. Doctoral Thesis, 2013.

[24] CAESES. "Intake Port Design", 2018.

[25] Senecal P. K., Miles Paul C., Mitra Saurav, Busch Stephen, Wijeyakulasuriya Sameera and Zha Kan. "Characterization of Flow Asymmetry During the Compression Stroke Using Swirl-Plane PIV in a Light-Duty Optical Diesel Engine with the Re-entrant Piston Bowl Geometry". *SAE International Journal of Engines*, Vol. 8 n^o 4, 2015.

[26] Pourfallah Mohsen. "Optimization of Intake port shape in a DI Diesel Engine Using CFD Flow Simulation". n^o June 2010, 2018.

[27] Wang Guixin, Yu Wenbin, Li Xiaobo and Yang Rui. "Influence of fuel injection and intake port on combustion characteristics of controllable intake swirl diesel engine". *Fuel*, Vol. 262 n^o November 2019, pp. 116548, 2020.

[28] Tikar Sameer, Malkhede Dileep and Nandgaonkar Milankumar. "Design and Development of Intake Ports for 2-Valve & 4-Valve Configurations for Heavy Duty Off-Highway Diesel Engine". *SAE Technical Papers*, n^o October, 2019.

[29] Garcia-Oliver Jose M, Garcia Antonio, Gil Antonio and Pachano Leonardo. "Study of Air Flow Interaction with Pilot Injections in a Diesel Engine by Means of PIV Measurements". *SAE International Journal of Engines*, Vol. 10 n^o 3, 2017.

[30] Wang Zhenkan, Tanov Slavey, Wang Hua, Richter Mattias, Johansson Bengt and Alden Marcus. "High-Speed Particle Image Velocimetry Measurement of Partially Premixed Combustion (PPC) in a Light Duty Engine for Different Injection Strategies". 2015.

[31] Albrecht H.-E, Borys M., Damaschke N. and Tropea Cameron. *Laser Doppler and Phase Doppler Measurement Techniques*. 01 2003.

[32] Johansson Bengt. "Influence of the velocity near the spark plug on early flame development". *SAE Technical Papers*, 1993.

[33] Miles Paul, Megerle Marcus, Sick Volker, Richards Keith, Nagel Zac and Reitz Rolf. "The evolution of flow structures and turbulence in a fired HSDI diesel engine". *SAE Technical Papers*, n^o 724, 2001.

[34] Tanov Slavey, Johansson Bengt, Richter Mattias, Wang Zhenkan and Wang Hua. "Effects of Injection Strategies on Fluid Flow and Turbulence in Partially Premixed Combustion (PPC) in a Light Duty Engine". *SAE Technical Paper Series*, Vol. 1 n^o Ldv, 2015.

[35] Busch Stephen, Zha Kan, Perini Federico, Reitz Rolf, Kurtz Eric, Warey Alok and Peterson Richard. "Bowl Geometry Effects on Turbulent Flow Structure in a Direct Injection Diesel Engine". *SAE Technical Papers*, Vol. 2018-Septe, 2018.

[36] Busch Steve, Zha Kan, Perini Federico and Reitz Rolf. *Piston Bowl Geometry Impacts on Late-Cycle Flow and Mixing in a Small-Bore Diesel Engine Outline â¢ Overview : piston bowl geometry project â¢ Computational study : bowl geometry impacts on late-cycle flow structure and turbulent mixing â¢ Results â¢ Bowl geo*. 2017.

[37] Cartellieri Wolfgang P. and Herzog Peter L. "Swirl supported or quiescent combustion for 1990's heavy-duty di diesel engines - An analysis". In *SAE Technical Papers*, feb 1988.

[38] Suppes Galen J. and Storvick Truman S. "The New Electric Vehicle Society". *Sustainable Power Technologies and Infrastructure*, pp. 161–190, 2016.

[39] Zha Kan, Busch Stephen, Warey Alok, Peterson Richard C. and Kurtz Eric. "A Study of Piston Geometry Effects on Late-Stage Combustion in a Light-Duty Optical Diesel Engine Using Combustion Image Velocimetry". *SAE International Journal of Engines*, Vol. 11 n^o 6, pp. 783–804, 2018.

[40] Zhu Y., Zhao H., Melas D. A. and Ladommatos N. "Computational study of the effects of the re-entrant lip shape and toroidal radii of piston bowl on a HSDI diesel engine's performance and emissions". *SAE Technical Papers*, Vol. 2004 n^o 724, 2004.

[41] Montajir Rahman M., Tsunemoto H., Ishitani H. and Minami T. "Fuel spray behavior in a small di diesel engine: Effect of combustion chamber geometry". *SAE Technical Papers*, n^o 724, 2000.

[42] Lee Jongyoon, Lee Sangyul, Kim Jungho and Kim Duksang. "Bowl Shape Design Optimization for Engine-Out PM Reduction in Heavy Duty Diesel Engine". *SAE Technical Papers*, Vol. 2015-April n^o April, 2015.

[43] Wickman D. D., Senecal P. K. and Reitz R. D. "Diesel engine combustion chamber geometry optimization using genetic algorithms and multi-dimensional spray and combustion modeling". *SAE Technical Papers*, Vol. 2001 n^o 724, 2001.

[44] Bianchi G M and Pelloni P. "Numerical Study of the Combustion Chamber Shape for Common Rail H . S . D . I . Diesel Engines". *Society*, n^o 724, 2010.

[45] Kurtz Eric M. and Styron Joshua. "An Assessment of Two Piston Bowl Concepts in a Medium-Duty Diesel Engine". *SAE International Journal of Engines*, Vol. 5 n^o 2, pp. 344–352, 2012.

[46] Neely Gary D., Sasaki Shizuo and Sono Hiroshi. "Investigation of alternative combustion crossing stoichiometric air fuel ratio for clean diesels". *SAE Technical Papers*, 2007.

[47] Ryan Tom. "Combustion Targets for Low Emissions and High Efficiency". In *Diesel Engine Emissions Reduction (DEER) Conference*, 2005.

[48] Smith Anthony. "Ricardo low emissions combustion technology helps JCB create the off-highway industry ' s cleanest engine". *Ricardo Press Release*, n^o 222915, pp. 4–6, 2010.

[49] Cornwell Richard and Conicella Fabrizio. "DIRECT INJECTION DIESEL ENGINES", 2011.

[50] Nishida Kentaro, Hashizume Takeshi, Hasegawa Ryo and Ogawa Takashi. "Low Cooling Losses and Low Emission Analysis of Small Bore Diesel Engine Combustion". *SAE Technical Papers*, Vol. 2015-September n^o September, pp. 1–7, 2015.

[51] Iikubo Shotaro, Adachi Yusuke and Shimokawa Kiyohiro. "COMBUSTION CHAMBER STRUCTURE FOR DIRECT NUECTION DESEL ENGINE", 2012.

[52] Yoo Dockoon, Kim Duksang, Jung Wook, Kim Nagin and Lee Dongin. "Optimization of diesel combustion system for reducing PM to meet tier4-final emission regulation without diesel particulate filter". *SAE Technical Papers*, Vol. 11 n^o October 2013, 2013.

[53] Eder Torsten, Lückert Peter, Kemmner Markus and Sass Heiko. "OM 654 â Launch of a New Engine Family by Mercedes-Benz". *MTZ worldwide*, Vol. 77 n^o 3, pp. 60–67, 2016.

[54] Leach Felix, Ismail Riyaz, Davy Martin, Weall Adam and Cooper Brian. "The e ff ect of a stepped lip piston design on performance and emissions from a high-speed diesel engine". *Applied Energy*, Vol. 215 n^o November 2017, pp. 679–689, 2018.

[55] Dahlstrom Jessica, Andersson Oivind, Tuner Martin and Persson Håkan. "Experimental Comparison of Heat Losses in Stepped-Bowl and Re-Entrant Combustion Chambers in a Light Duty Diesel Engine". *SAE Technical Papers*, 2016.

[56] Dolak Jonathan George, Shi Yu and Reitz Rolf. "A computational investigation of stepped-bowl piston geometry for a light duty engine operating at low load". *SAE Technical Papers*, 2010.

[57] Busch Stephen, Zha Kan, Kurtz Eric, Warey Alok and Peterson Richard. "Experimental and Numerical Studies of Bowl Geometry Impacts on Thermal Efficiency in a Light-Duty Diesel Engine". *SAE Technical Paper Series*, Vol. 1, pp. 1–12, 2018.

[58] Eismark Jan and Balthasar Michael. "Device for reducing emissions in a vehicle combustion engine", 2013.

[59] Eismark Jan, Christensen Magnus, Andersson Mats, Karlsson Anders and Denbratt Ingemar. "Role of fuel properties and piston shape in influencing soot oxidation in heavy-duty low swirl diesel engine combustion". *Fuel*, Vol. 254 n^o December 2018, pp. 115568, 2019.

[60] Eismark Jan, Andersson Mats, Christensen Magnus, Karlsson Anders and Denbratt Ingemar. "Role of Piston Bowl Shape to Enhance Late-Cycle Soot Oxidation in Low-Swirl Diesel Combustion". *SAE International Journal of Engines*, Vol. 12, apr 2019.

[61] Schemme Steffen, Samsun Remzi Can, Peters Ralf and Stolten Detlef. "Power-to-fuel as a key to sustainable transport systems â An analysis of diesel fuels produced from CO 2 and renewable electricity". *Fuel*, Vol. 205, pp. 198–221, 2017.

[62] Abdul Karim Z. A. and Khan Mohammed Yahaya. "Water-in-Diesel EmulsionsâFuel Characteristics". pp. 53–64. Springer, 2018.

[63] Bae Choongsik and Kim Jaeheun. "Alternative fuels for internal combustion engines". *Proceedings of the Combustion Institute*, Vol. 36 n^o 3, pp. 3389–3413, 2017.

[64] König Andrea, Marquardt Wolfgang, Mitsos Alexander, Viell Jörn and Dahmen Manuel. "Integrated design of renewable fuels and their production processes: recent advances and challenges". *Current Opinion in Chemical Engineering*, Vol. 27, pp. 45–50, 2020.

[65] "2018 Outlook for Energy: a view to 2040". Vol. 49 n^o 11-12, pp. 23–25, 2018.

[66] Reitz R. D., Ogawa H., Payri R., Fansler T., Kokjohn S., Moriyoshi Y., Agarwal A. K., Arcoumanis D., Assanis D., Bae C., Boulouchos K., Canakci M., Curran S., Denbratt I., Gavaises M., Guenthner M., Hasse C., Huang Z., Ishiyama T., Johansson B., Johnson T. V., Kalghatgi G., Koike M., Kong S. C., Leipertz A., Miles P., Novella R., Onorati A., Richter M., Shuai S., Siebers D., Su W., Trujillo M., Uchida N., Vaglieco B. M., Wagner R. M. and Zhao H. "IJER editorial: The future of the internal combustion engine". *International Journal of Engine Research*, Vol. 21 n^o 1, pp. 3–10, 2020.

[67] Poussin Olivier, Gaillard Patrick, Garcia Antonio, Monsalve-Serrano Javier and Martinez-Boggio S.D. "Dual-Fuel RCCI Diesel-Gasoline Hybrid Truck Concept to Achieve the Future Emissions Targets". *10th Aachen Colloquium China Sustainable Mobility 2020*, n^o Ci, 2020.

[68] Bohl Thomas, Smallbone Andrew, Tian Guohong and Roskilly Anthony P. "Particulate number and NOx trade-off comparisons between HVO and mineral diesel in HD applications". *Fuel*, Vol. 215 n^o March 2016, pp. 90–101, 2018.

[69] Dimitriadis Athanasios, Seljak Tine, Vihar Rok, Žvar Baškovič Urban, Dimaratos Athanasios, Bezergianni Stella, Samaras Zissis and Katrašnik Tomaž. "Improving PM-NOx trade-off with paraffinic fuels: A study towards diesel engine optimization with HVO". *Fuel*, Vol. 265 n^o December 2019, 2020.

[70] Pastor José V., García A., Micó C. and García-Carrero Alba A. "Experimental study of influence of Liquefied Petroleum Gas addition in Hydrotreated Vegetable Oil fuel on ignition delay, flame lift off length and soot emission under diesel-like conditions". *Fuel*, Vol. 260 n^o October 2019, pp. 116377, 2020.

[71] Bortel Ivan, Vávra JiÅí and Takáts Michal. "Effect of HVO fuel mixtures on emissions and performance of a passenger car size diesel engine". *Renewable Energy*, Vol. 140, pp. 680–691, 2019.

[72] Siegemund Stefan, Trommler Marcus, Kolb Ole, Zinnecker Valentin, Schmidt Patrick, Weindorf Werner, Zittel Werner, Raksha Tetyana and Zerhusen Jan. "E-Fuels study. The potential of electricity-based fuels for low-emission transport in the EU". *Deutsche Energie-Agentur GmbH (dena)*, 2017.

[73] Hao Bin, Song Chonglin, Lv Gang, Li Bo, Liu Xiaofang, Wang Kan and Liu Yaowu. "Evaluation of the reduction in carbonyl emissions from a diesel engine using Fischer-Tropsch fuel synthesized from coal". *Fuel*, Vol. 133, pp. 115–122, 2014.

[74] Kook Sanghoon and Pickett Lyle M. "Liquid length and vapor penetration of conventional, Fischer-Tropsch, coal-derived, and surrogate fuel sprays at high-temperature and high-pressure ambient conditions". *Fuel*, Vol. 93, pp. 539–548, 2012.

[75] Rimkus Alfredas, Žaglinskis Justas, Rapalis Paulius and Skačkauskas Paulius. "Research on the combustion, energy and emission parameters of diesel fuel and a biomass-to-liquid (BTL) fuel blend in a compression-ignition engine". *Energy Conversion and Management*, Vol. 106, pp. 1109–1117, 2015.

[76] Lapuerta Magín, Armas Octavio, Hernández Juan José and Tsolakis Athanasios. "Potential for reducing emissions in a diesel engine by fuelling with conventional biodiesel and Fischer-Tropsch diesel". *Fuel*, Vol. 89 n^o 10, pp. 3106–3113, 2010.

[77] Gill S. S., Tsolakis A., Dearn K. D. and Rodríguez-Fernández J. "Combustion characteristics and emissions of Fischer-Tropsch diesel fuels in IC engines". *Progress in Energy and Combustion Science*, Vol. 37 n^o 4, pp. 503–523, 2011.

[78] Jiao Yufei, Liu Ruilin, Zhang Zhongjie, Yang Chunhao, Zhou Guangmeng, Dong Surong and Liu Wuquan. "Comparison of combustion and emission characteristics of a diesel engine fueled with diesel and methanol-Fischer-Tropsch diesel-biodiesel-diesel blends at various altitudes". *Fuel*, Vol. 243 n^o July 2018, pp. 52–59, 2019.

[79] Abu-Jrai A., Tsolakis A., Theinnoi K., Cracknell R., Megaritis A., Wyszynski M. L. and Golunski S. E. "Effect of gas-to-liquid diesel fuels on combustion characteristics, engine emissions, and exhaust gas fuel reforming. Comparative study". *Energy and Fuels*, Vol. 20 n^o 6, pp. 2377–2384, 2006.

[80] Rounce P., Tsolakis A., Rodríguez-Fernández J., York A. P. E., Cracknell R. F. and Clark R. H. "Diesel Engine Performance and Emissions when First Generation Meets Next Generation Biodiesel". *SAE Technical Paper Series*, Vol. 1, pp. 1–10, 2010.

[81] Schaberg Paul, Botha Johan, Schnell Mark, Hermann Hans Otto, Pelz Norbert and Maly Rudolf. "Emissions performance of GTL diesel fuel and blends with optimized engine calibrations". *SAE Technical Papers*, 2005.

[82] Iannuzzi Stefano Emanuele, Barro Christophe, Boulouchos Konstantinos and Burger Jakob. "Combustion behavior and soot formation/oxidation of oxygenated fuels in a cylindrical constant volume chamber". *Fuel*, Vol. 167, pp. 49–59, 2016.

[83] Pellegrini Leonardo, Marchionna Mario, Patrini Renata, Beatrice Carlo, Del Giacomo Nicola and Guido Chiara. "Combustion Behaviour and Emission Performance of Neat and Blended Polyoxymethylene Dimethyl Ethers in a Light-Duty Diesel Engine". *SAE Technical Paper Series*, Vol. 1, 2012.

[84] Härtl Martin, Seidenspinner Philipp, Jacob Eberhard and Wachtmeister Georg. "Oxygenate screening on a heavy-duty diesel engine and emission characteristics of highly oxygenated oxymethylene ether fuel OME1". *Fuel*, Vol. 153, pp. 328–335, 2015.

[85] Liu Haoye, Wang Zhi, Li Yanfei, Zheng Yanyan, He Tanjin and Wang Jianxin. "Recent progress in the application in compression ignition engines and the synthesis technologies of polyoxymethylene dimethyl ethers". *Applied Energy*, Vol. 233-234 n^o October 2018, pp. 599–611, 2019.

[86] Omari Ahmad, Heuser Benedikt and Pischinger Stefan. "Potential of oxymethylenether-diesel blends for ultra-low emission engines". *Fuel*, Vol. 209 n^o May, pp. 232–237, 2017.

[87] Ma Xiao, Ma Yue, Sun Shuaishuai, Shuai Shi-Jin, Wang Zhi and Wang Jian-Xin. "PLII-LEM and OH* Chemiluminescence Study on Soot Formation in Spray Combustion of PODEn-Diesel Blend Fuels in a Constant Volume Vessel". *SAE Technical Paper Series*, Vol. 1 n^o 2329, 2017.

[88] Lumpp Björn, Rothe Dieter, Pastötter Christian, Lämmermann Reinhard and Jacob Eberhard. "OXYMETHYLENE ETHERS AS DIESEL FUEL ADDITIVES OF THE FUTURE". *MTZ worldwide eMagazine*, Vol. 72 n^o 3, pp. 34–38, 2011.

[89] Liu Haoye, Wang Zhi, Zhang Jun, Wang Jianxin and Shuai Shijin. "Study on combustion and emission characteristics of Polyoxymethylene Dimethyl Ethers/diesel blends in light-duty and heavy-duty diesel engines". *Applied Energy*, Vol. 185, pp. 1393–1402, 2017.

Chapter 3

Tools and Methodology

Contents

The main objective of the present thesis is to analyse two different ways for reducing the soot formation inside the combustion chamber. On one side by using different piston templates; on the other side, by testing the potential of different e-fuels for replacing the fossil diesel. In order to carry out this work, a variety of experimental and theoretical tools and methodologies were applied and they are presented and explained in detail in this chapter.

All the experiments were developed in a 1.6 L GM optical diesel engine, always keeping the same in-cylinder conditions used in a metal diesel engine and making extensive use of a variety of optical techniques. In this sense, the chapter begins with a general description of the optical engine, the geometric details and the explanation of its subsystems (injection, cooling and lubrication systems). The description of the test cell, its instrumentation and the theoretical tools for getting the thermodynamic engine characterization were also included in this first part of the chapter. Following this, the different optical techniques used for the study of in-cylinder flow induced by real bowl geometries as well as the effects of both piston geometries and e-fuels upon in-cylinder soot production are presented. Then, two specific sections present the tools used for analysing the different bowl templates and e-fuels. The first section includes the geometry details of the quartz piston bowls used in the study together with the peculiarities of the processing tools developed to enhance the effects of bowl geometry on combustion. In the second section, it is presented the tools used for the experiments involving the utilization of promising alternative fuels which are called e-fuels. In this part, the details of the physical and chemical fuel properties are provided as well as the processing methodology applied for analysing the results of this part.

3.1 Optical engine test cell

For the whole development of this current thesis, a single cylinder optical diesel engine based on a commercial GM 1.6L diesel engine, with displacement of 400 cm^3 per cylinder was used. The optical engine was developed with the Bowditch design, where the cylinder head is lifted up and an extensor is used in the metal piston. A 45◦ mirror is placed in the bottom of the hollow piston extension to allow the visualization of the combustion chamber, as it is shown in figure 3.1.

The original GM cylinder head composed by 4 valves and a centrally located injector with 8 holes was assembled in the optical engine. The bore

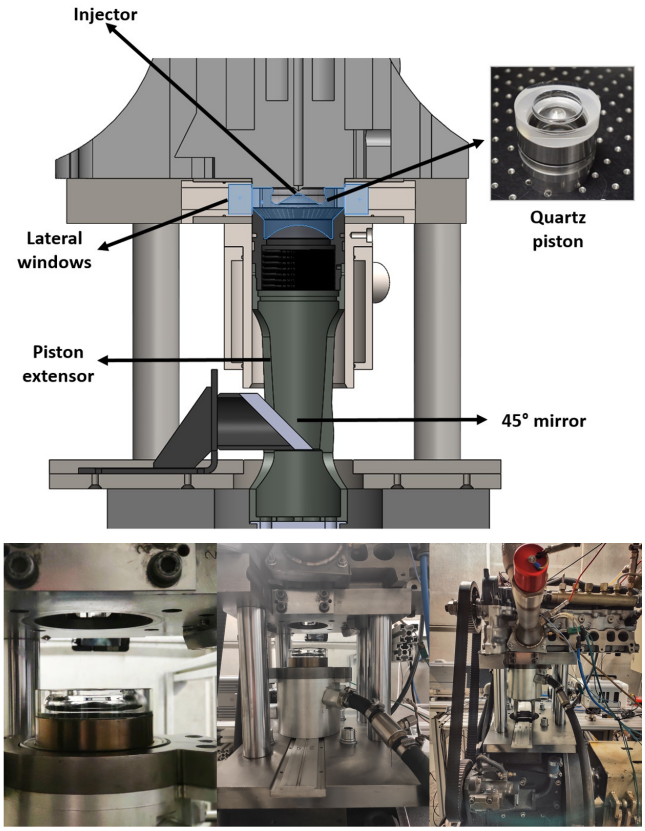

Figure 3.1. *GM 1.6L optical diesel engine.*

and stroke were kept the same as the original 1.6L GM diesel engine. Two optical accesses to the combustion chamber are available in the optical engine. The first one is from the side of the engine trough the cylinder liner. The second access is through the piston bottom, where a full-quartz piston allows the visualization of the combustion chamber. The swirl ratio was provided by GM. The geometric information is summarized in table 3.1.

The air leakages (blow-by) are minimized by using special piston rings made of a synthetic material called Rulon J, which expands with temperature. The positions of the rings are lower than in the original piston with the objective of avoiding them passing the joint between the steel and the glass window part. This fact contributes to reduce the engine compression ratio.

Engine characteristics	4 stroke, direct injection
Number of cylinders [-]	1
Valves [-]	4
Stroke [mm]	80.1
Bore [mm]	80
Rod length [mm]	152
Swirl number	2.2-3.5
Maximum in-cylinder pressure [bar]	165
Injector nozzle	8x340x155
Hole diameter [μ m]	116
Injection system	Common-rail (up to 2000 bar)
Displacement [l]	0.402

Table 3.1. *Optical engine parameters.*

3.1.1 Injection system

The injection system is managed by a DRIVVEN Engine Control System (ECS). ECS is a research engine controller based on the powerful PXI platform from National Instruments. It includes an open-source LabVIEW software project that serves as both a steady-state engine control application and a template for more advanced control applications. By means of this device is possible to command piezoelectric or solenoid direct injectors and port fuel injectors. The device allows set all parameters regarding the injection duration, injection timing, number of injections per cycle, etc. In addition, it is possible to define the number of cycles at firing conditions (skip fire mode), which is extremely necessary in optical engines for preserving the optical parts. A conventional high pressure fuel pump with common rail is employed in the injection system. A pressure control valve mounted in the pressure rail, in combination with a PID control, maintains constant the desired pressure. The system allows to achieve injection pressures of up to 2000 bar.

3.1.2 Lubrication and cooling system

In the case of a single cylinder optical engine, the heat generated by a single cylinder operating under skip fire conditions is very low, becoming extremely difficult to warm up the coolant and the lubricant fluid until reaching the appropriate working temperature.

In this sense, the optical engine has an independent cooling system, as represented in figure 3.2, for keeping the liner temperature low and preserving the piston rings. Between the inner liner (in contact with the piston rings) and the outer liner, there is a spiral pipe where the coolant enters on one side, circulates around the liner and leaves the pipes on the other side. The coolant used is glycol and it is kept between 15◦ C and 25◦ C by using a refrigeration machine controlled by a PID regulator. In this way, the same temperature conditions are achieved in the cylinder walls for all operating points.

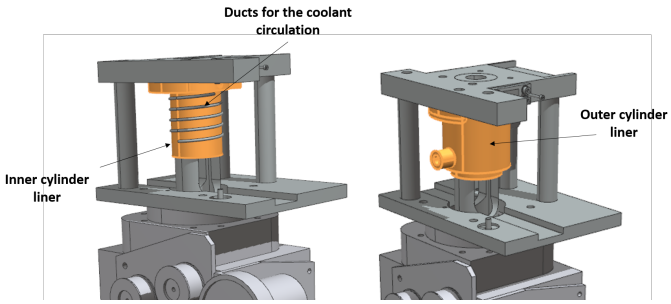

Figure 3.2. *Cooling system of the optical engine.*

Regarding the lubrication system, it consists of two circuits, which guarantee the proper lubrication of the engine metal parts such as crankshaft, valve train, etc. In the first one, an external pump leads the oil to the engine, working as a coolant fluid as well. In the second circuit, the oil flows to a heat exchanger with the objective of decreasing the oil temperature. The oil temperature (60°C) and oil pressure (3 bar) are kept constant for all tests performed in this thesis.

3.1.3 Air supply and exhaust system

It is very important to highlight that the intake and exhaust system explained below can be only found in the single-cylinder engine test cells, where the intake and exhaust system are external. In this way, the desired

intake air conditions can be obtained in an efficient way and with higher flexibility.

The air supply system can be appreciated in the scheme of figure 3.3. A screw compressor supplies the intake air at the required pressure up to 30 bar of pressure and a maximum flow rate of 400 kg/h for each test condition. The air is directed into the filter for removing particles that could damage the engine elements during the combustion process. The intake air is prepared by using a dryer and a heat exchanger. After this, the air enters in a settling chamber of 500 liters in order to equalize the flow and attenuate the pressure waves. The air temperature needed for the different engine conditions is achieved by employing an air heater governed by a PID control, which is located just before the intake port.

In the same way as the intake system, the exhaust system is also external. This system aims to eliminate the exhaust gases generated during the combustion process. A settling chamber is also present in the exhaust system in order to avoid the pressure pulses. Furthermore, an exhaust backpressure valve is used with the objective of controlling the exhaust pressure and to simulate similar conditions to the turbine backpressure of a conventional turbocharged compression ignition engine. The exhaust pressure was always kept 0.2 bar higher than the intake pressure.

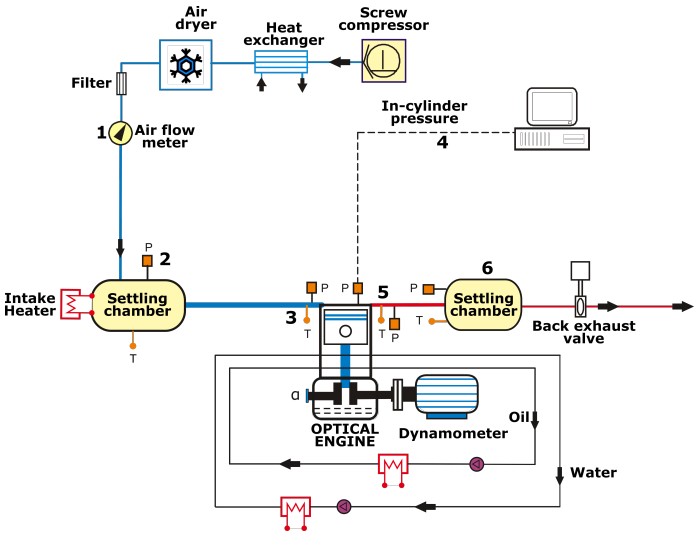

Figure 3.3. *Test cell scheme.*

3.1.4 Injection rate

The mass flow rate measurement was performed by a device named Injection Rate Discharge Curve Indicator (IRDCI) from IAV. The measurement uses the Bosch method [1, 2], where the principle is based on the theory of pressure wave propagation in a liquid column.

The injector is placed in the cavity at the mass flow rate meter, so that when injecting it fills with fuel the total volume. A pressure wave is generated when the fuel is injected into the measurement tube. This wave moves at the sound speed through the long tube that goes around the device, up to the reservoir where it is dampened. Then, the fuel enters through a filter into the equalizing piston, which is pressurized on the other side by nitrogen set at the desired discharge pressure, sealing the outlet. A piezoelectric sensor capture the pressure variation caused by the wave. The signal that is generated during this event is used for calculating the instantaneous mass flow rate by applying the equation 3.1.

$$\dot{m} = \frac{A_t}{a}.\Delta P \tag{3.1}$$

Where A_t represents the cross-sectional area of the tube, a is the speed of sound of the fluid and ΔP the pressure difference induced by the wave. In addition, a procedure described by Payri et al. is also used for obtaining a more accurate injection rate. The fuel mass flow signal is adjusted by making coincident the measured fuel mass injected in one injection event with the integer of the fuel flow mass signal. Fuel mass is obtained by using a fuel balance meter located downstream the fuel flow rate meter.

3.1.5 Instrumentation and Measuring Equipment

This subsection is dedicated to describe the sensors and different equipments that have been used to carry out the tests presented in this thesis. The principles and uncertainties these devices are discussed to provide informations about the reliability of the measurements.

3.1.5.1 Torque and engine speed measurement

Although the optical engine is motored by the dynamometer and it operates at skip-fire conditions, the torque and speed measurement are extremely important to operate the engine safely. The dynamometer actuates

as an engine when it drives the engine (no combustion operation) or as a generator when it is driven by the engine (during combustion operation). The torque measurement is performed by torque flanges as well as load cells which are coupled to the dynamometer. Load cells are usually used at steady-state applications. It provides the highest sensibility to load variations by means of a strain-gauge inside a specific metal shape. A calibration curve has to be provided to the acquisition system, where the output voltage from the load cell is related with a calibrated weight. For the current thesis, a Schenck dynamometer equipped with a load cell is used to perform the tests. The main characteristics of the dynamometer can be visualized in the table 3.2.

Type	dynamometer
Manufacturer	Schenck
Nominal Power [kW]	2200
Nominal Torque [Nm]	562
Max. Speed [rpm]	9000
Min. Speed [rpm]	250

Table 3.2. *Dynamometer characteristics .*

For the engine speed measurements, different sensors can be employed. In general, Hall and inductive effect sensors placed near to a toothed wheel provide engine speed measurements. However, for the heat release analysis, the toothed wheel has limitations due to the low number of pulse per stroke (60-2). In this way, an additional optical encoder AVL 364, with a resolution of 0.2 CAD, was installed on the crankshaft of the optical engine. The presence of three output signals (A, B, and C) are typical in this kind of encoder. The signal A is related with the pulses generated per stroke. B is a phased A, which allows to determine the direction of rotation. Finally, the signal C is the trigger used to reference the piston position with respect to the start of acquisition.

3.1.5.2 Average pressure and temperature measurement

The average pressure and temperature measurements are used for monitoring and control different systems and subsystems of the optical engines, as well as, getting quantitative information of important engine parameters, where the signal dynamics are low. In the test cell, the average pressure have been measured by using a PMA P40 model piezoresistive pressure transducer.

The range of measurement is from 0 to 10 bar with 25 mbar of accuracy. The average pressure sensor is installed in different parts of the optical engine such as intake and exhaust systems, cooling circuit and lubricant circuit.

Regarding temperature measurements, they are performed by using thermocouples type K and thermo resistive sensors. The thermocouples have a range of measurement from 0 to 1100 ◦C and an accuracy of 2.5 ◦C. The water and oil temperatures were measured with the thermo resistive sensors, where temperatures from -200 to +850 ◦C and a accuracy of 0.3 ◦C can be registered.

3.1.5.3 Instantaneous pressure transducer

The most combustion analysis in ICE can be performed thanks the utilization of instantaneous pressure measurements. This kind of measurements are extremely complex and they require special instrumentations, where the signal from the transducer has to be with low thermal shock and support high pressure values. For the in-cylinder pressure measurements, where the conditions of pressure and temperature are severe, an AVL/GH13P glow-plug piezoelectric transducer [3] was mounted in the cylinder head. Piezoelectric sensors measure relative pressure and they are appropriate for both high temperature and high pressure. The transducer allows measuring range from 0 to 250 bar, with a operating temperature range from -40 to 400 °C. The accuracy is 1.25 bar. In addition, no additional cooling system is required by this sensor, simplifying installation on the cylinder head. The signal from the sensor was conditioned by a Kistler 4603B10 charge amplifier before to be acquired by the acquisition system. For the intake and exhaust pressure measurements, besides the average pressure values, the instantaneous one were also registered. For this purpose, a Kistler 4045A10 piezoresistive sensor [4] was mounted in both intake and exhaust manifolds, just before the ports. This sensor can measure a range of pressure from 0 to 10 bar, allowing a maximum temperature of 120 °C. Piezoresistive sensors measure absolute pressure and can be used when the temperature and pressure conditions are not extremely high.

3.1.5.4 Mass flow measurement

The measurement of air mass flow is extremely important for ICE studies, since from this parameter is possible to calculate derived parameters such as equivalence ratio or volumetric efficiency. In addition, for the thermodynamic

characterization of optical engines, which are affected by blow-by and heat transfer, the correct measurement of the mass flow is mandatory for the purpose of this thesis. For the air mass flow rate measurement, a Sensyflow from Sensycom company, is employed. This device uses a hot wire anemometer to perform the measurements, where the measuring range is from 0 to 400 Kg/h and the accuracy of 1% over the measured value [5].

The fuel mass injected into the combustion chamber for each different operating conditions is measured separately, during the fuel mass flow measurement previously explained. The instantaneous measurement during the tests by using a gravimetric principle balance was not possible to be performed. As the quantity of injected fuel is low due to the skip fire mode, the fuel mass flow rate is below the lower limit that the balance can register.

3.1.6 Computational tools

The results obtained with the experimental facilities have been post-treated by using different computational tools, which helped a better comprehension and understanding about the different phenomena involved in the combustion process of different bowl templates and fuels. In this way, the different software that have been used for post-processing the experimental data will be briefly described in this section.

3.1.7 Combustion diagnosis model-Calmec

The thermodynamic diagnostic in CI engines is necessary in order to get the heat release information. In this sense, CALMEC is a OD diagnostic model developed in CMT- Motores Térmicos that allows to perform heat release calculations. The model uses the experimental data as the input for performing the in-cylinder thermodynamic analysis, such as the instantaneous in-cylinder pressure and averaged values of mass flow consumption (air and fuel), as well as intake and exhaust average temperature and pressure. It is based on an one zone model and applies the first law of thermodynamic between the intake valve closing and exhaust valve opening. Heat transfer, mechanical deformations and blow-by are taken into account in the model.

As the model is 0-D, it does not provide spatial resolution, assuming that in-cylinder pressure and temperature are spatially uniform inside the chamber. In addition, a homogeneous mixture of air, fuel and burned products are considered as the in-cylinder gas. Assuming this set of hypotheses, the CALMEC model proposes the resolution of the first principle

of thermodynamics applied to open systems. In this way, the equation 3.2 is solved in calculation intervals determined by the angular resolution of the instantaneous pressure measurement.

$$\Delta RoHR = m_{cyl} \cdot \Delta U_{cyl} + AQ_w + p \cdot \Delta v - \left(\bar{h}_{f,inj} - u_{f,g}\right) \cdot \Delta m_{f,evap} + R_{cyl} \cdot T_{cyl} \cdot \Delta m_{bb} \tag{3.2}$$

where the different terms of the equation can be described as following:

- $\Delta RoHR$ corresponds to the the thermal energy released during the combustion of the fuel injected at a given CAD, assuming constant heat power throughout the combustion process.
- $m_{cyl} \cdot \Delta U_{cyl}$ is the internal energy variation of the mass trapped enclosed in the control volume
- AQ_w is the heat transferred from the gas to the surfaces of the piston, the cylinder, the cylinder head and the valves. The heat transfer is calculated with the modified Woschni-like model [6].
- $p \cdot \Delta v$ is the total work produced by the gas within the control volume during the calculation interval. This instantaneous volume is calculated as the the sum of the combustion chamber volume, the volume displaced by the piston (function of crank angle), and the volume changes caused by the mechanical deformations. The mechanical deformations take into account both the pressure force exerted by the gas on the piston head and the inertial forces generated by the reciprocating masses.
- $(\bar{h}_{f,inj} - u_{f,g}) \cdot \Delta m_{f,evap}$ refers to the energy balance in the injection process.
- $R_{cyl} \cdot T_{cyl} \cdot \Delta m_{bb}$ is associated with the mass that is lost by the control volume due to the blow-by process.

From the heat release analysis is possible to get important informations about the evolution of the burning process inside the cylinder. This analysis allows to define different combustion parameters such as the ignition delay (0-2 % of MFB), CA 10, CA50 and CA 90 (crank angle degrees where 10, 50 and 90 % of the mass fraction is burned) or the combustion duration, generally defined as CA90-CA10. These parameters are useful when comparing different piston geometries and fuels for example.

3.1.8 GT power

This package consists in multi domain approach combining the 1-D discretization of the conservation equations by finite volumes method with 0-D phenomenological model and experimental data to properly describe the engine operation. Generally, these equations are solved explicitly in time, i.e., considering the solution field from the last iteration during the integration and specifying a proper time step to guarantee solver stability calling the Courant condition [7].

A specific method available in this package and called three pressure analysis-TPA was applied for this current thesis. Basically, when using this method, the model requires the three measured pressures: intake, cylinder, and exhaust to analyse gas exchange and combustion. It is a simulation based method to analyse test cell data to determine quantities that are difficult to measure directly.

3.2 Optical techniques

The present section is dedicated to show and explain the different optical techniques used for developing this thesis. The section is basically split into two main parts. The first one related with air motion and in-cylinder flow characterization. The second part is focused on the application of optical techniques that are useful for the study of combustion development and soot production.

3.2.1 Air motion analysis - PIV

The in-cylinder flow field measurements are extremely useful and necessary for CFD validations, studies of fundamental in-cylinder flow processes and for the verification of innovative systems in ICE. The measurement and characterization of in-cylinder flow are usually performed by using optical laser diagnostic techniques. They can be base either on single-point time-resolved measurements, such as laser Doppler velocimetry (LDV) [8], or on instantaneous spatially-resolved techniques, such as particle image velocimetry (PIV). In the current thesis, the worked have been focused on the PIV technique in order to characterize the in-cylinder flow. In this way, just the PIV details and explanation will be addressed in this section.

The principle of PIV measurement consists of calculating the velocity vector from the displacement of an element of fluid in a specific time interval

which is known. For the application of the PIV technique, a thin slice of the flow field has to be illuminated by a laser sheet. The laser illuminates the particles present in the flow. This light is scattered by the particles and detected by a camera located at a right angle to the light. Laser sheet illumination is provided by a double-pulse laser; i.e. two laser pulses are fired in rapid succession, separated by a known time δt. The camera is synchronized with the laser, where first frame of the camera records the initial particle positions during the first pulse. Following this process, the camera exposures the second frame in order to register the light scattered by the particles during the second laser pulse illumination. In this way, two images are captured for representing the flow field movement, the first one showing the initial positions of the particles and the second one the final positions of the particles.

The measurement region comprehends the intersection between the field of view of the optical system and the region illuminated by the laser sheet. This measurement region can be divided in small areas, which are known as interrogation area (IA). The cross-correlation function is applied between the interrogation areas from each image frame, I1 and I2, pixel by pixel.

The flow velocity u and v are determined by the particle displacement in the object plane Δx and Δy and the time between the two laser pulses Δt as represented in equation 3.3. A simple calibration is performed in order to know the magnification of the imaging optics.

$$u = \frac{\Delta x}{\Delta t} \quad \text{and} \quad v = \frac{\Delta y}{\Delta t} \tag{3.3}$$

The CCD (Charge-Coupled Device) cameras are usual for the PIV measurements. They permit to record in two separate frames. The images of particles are generated by two consecutive laser pulses. This kind of camera sensor converts photons to an electric charge based on the photoelectric effect. The CCD sensor consists of many individual sensors that are arranged in a rectangular array [9]. There is a specific storage site for each active pixel, with a progressive scan [8]. The exposed entire image can be transferred within a few microseconds into the adjoining storage site, as shown in figure 3.4 . In this way, two consecutive singles exposed images can be captured at a time delay slightly longer than the transfer time. Each pixel has a size on the order of 10x10 μm. Their repetition rate in PIV double frame mode is on the order of 10 Hz. Although the time elapsed between the frame 1 and 2 is very short and it is possible to control the exposure time of the frame 1, the frame 2 presents a longer exposure time than frame 1. This is due to the process of transferring the frame 1 from the cell storage to the output shift register takes

time. For this reason, the frame 2 cannot be transferred to the storage cells until the frame 1 to be completely transferred to the output shift register. In order to avoid frame 2 over exposure exposure, it is common to use a narrow band pass filter in the same wavelength of the laser.

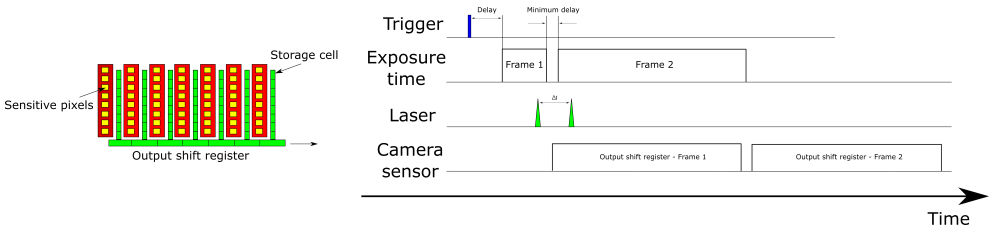

Figure 3.4. *The working principle of CCD cameras.*

Lasers are the suitable source of light for the PIV measurements since they provide the light in a collimated and intense form. The high power illumination is another decisive factor in the choice of light source for the PIV measurements, due to the necessity of illuminating an extended area. In addition, a short pulse width is mandatory for freezing the flow [8]. The most commonly used laser is the twin oscillator, twin-amplifier frequency-doubled (532 nm) Nd-YAG laser. This type of laser can trigger the two oscillators and amplifiers separately, allowing different possibilities of control of the laser pulse separation and individual pulse energy. Pulse duration is typically 5-10 ns, and repetition rate is on the order of 10 Hz [9].

In PIV measurements, the laser beam has to be transformed in a thin light sheet within the flow. For this purpose, a specific arrangement of cylindrical and spherical lenses is used. By means of cylindrical lenses is possible to expand and collimate the laser beam into a sheet. The spherical lenses allow to focus the laser beam in order to get the required light sheet thickness. The typical arrangement is shown in figure 3.5.

3.2.2 Combustion development and soot production analysis

For the current thesis, four different optical techniques (natural luminosity, OH* chemiluminescence, 2 color pyrometry and spectroscopy) were applied in order to study and analyse the combustion behaviour and combustion evolution, as well as, the soot formation by using three different bowl geometries and two different e-fuels. By applying these different optical techniques, the information about flame movement pattern, high temperature zones and soot concentration could be obtained.

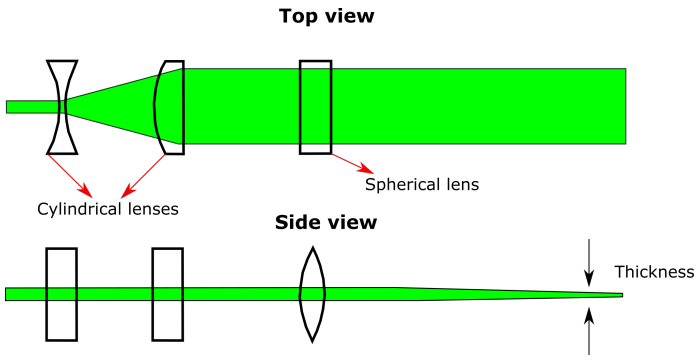

Figure 3.5. *Typical arrangement of lenses for PIV measurements.*

3.2.2.1 High-speed Natural Luminosity imaging

This method was used with the objective of obtaining the general information about the combustion process evolution, as well as, the flame movement and flame structure for both piston geometries and e-fuels analysis. In addition, the NL images were also used for applying the Combustion Image Velocimetry (CIV) analysis. The utilization of NL images have proven to be an important technique for a first approach in the characterization of in-cylinder combustion processes when using new engine hardware (pistons geometries, injection system), new fuels and new combustion modes [10–12].

The NL signal is mainly composed by two typical components: the first one comes from the soot incandescence and the second one from the chemiluminescence. Regarding soot incandescence, the hot soot particles emits broadband thermal radiation, which is the dominant luminosity source during the diffusion combustion. The chemiluminescence is the term used for the spontaneous no-thermal radiation emitted by molecules when they go from its excited energy state to the ground state during chemical reactions. There are several intermediate species which emit light in this form over relatively narrow spectral ranges during the diesel combustion [13].

The NL images were registered by using the optical access through the piston bottom and high-speed CMOS cameras. The images were registered from the start of energizing of the first pilot injection until the end of combustion.

3.2.2.2 OH* chemiluminescence

The OH* chemiluminescence was applied in this current thesis with the objective of getting spatial information about the near-stoichiometric high temperature combustion zones where combustion is taking place and soot oxidation is promoted inside the piston, when testing either different piston geometries or different e-fuels. The energetic reactions and high temperatures that occur during stoichiometric combustion of typical hydrocarbon fuels form excited state species that include excited state OH (OH*). Once the OH* is formed, it returns to its ground state and loses energy through either spontaneous fluorescence (chemiluminescence) or physical quenching (collisions). Additionally the OH* radiation mainly exists in the UV region from 280 to 350 nm with a peak at 308 nm. The emissions due to other species (mainly associated with CO2*) are comparatively weak in the UV region, about 3.5 % of the OH* radiation intensity [14, 15].

The OH* images were recorded by using an Andor Solis iStar DH334T-18H-83 ICCD intensified camera. The camera is equipped with an Bernhard-Halle UV objective with a 100 mm focal length f/2 lens and a 310 nm $\pm$ 10 nm bandpass filter camera. Considering the maximum framerate that the camera allows, one image was recorded per injection event. Different crank angle positions were recorded by using different time delays in relation to the injection pulse.

3.2.2.3 2 color pyrometry

The radiation from the diesel flame is dominated by the soot incandescence, where the soot particles inside of the flame and the surrounded gas have almost the same temperature. This makes the soot particle to emit thermal radiation like any body at high temperature. Due to the range of temperature that appears inside the flame (700 K - 2800 K), this thermal radiation emitted by the soot is much more intense that the emissions of other species from the chemiluminescence phenomenon. In this way, the images taken during the diesel combustion process by using cameras in the range of visible wavelengths are basically composed by the soot radiation [16]. Taking this into account, the 2-Color Pyrometry (2C) is an optical thermometry technique that makes use of the presence of radiating soot inside the flame. The intensity of radiation emitted by soot particles I_{soot} is proportional to the radiation emitted by a black body at the same temperature (T).

The starting point of the Two-color method is the assumption that radiation from a sooting flame with uniform spatial temperature and soot

distributions depends on the wavelength, the temperature and the amount of soot within the flame. In general, considering that the flame emits like a blackbody, the soot radiation intensity at a certain wavelength can be expressed by the Planck's law as represented in equation 3.4.

$$I_b(T,\lambda) = \frac{C_1}{\lambda^5\left[e^{\frac{C_2}{\lambda T}} - 1\right]} \tag{3.4}$$

Where I_b is the radiance emitted by the blackbody. $C_1 = 1.1910439X10^{-16}$ Wm^2/sr is the first Planck's constant, $C_2 = 1.4388X10^{-2}mk$ is the second Planck's constant and λ is the wavelength. However, the soot is a grey body with an emissivity ε below 1. Thus, the emission of the flame can be expressed as the equation 3.5.

$$I(T,\lambda) = \varepsilon I_b(T,\lambda) \tag{3.5}$$

Where the emissivity ε is the fraction of a blackbody radiation emitted by a surface at wavelength λ. In this sense, $I(T,\lambda)$ is the emissive of a nonblackbody and $I_b(T,\lambda)$ is the emissive of a blackbody, where both are at same temperature (T) and wavelength λ. For the two-color technique an apparent temperature T_a is considered in the calculation, which is defined as the blackbody temperature that emits the same radiation intensity as a nonblackbody at temperature T. Taking into the definition of T_a, it is possible assume that $I(T,\lambda) = I_b(T,\lambda)$. From this assumption and combining with the equation 3.4, it is possible to express the equation 3.6.

$$\varepsilon(KL,\lambda) = \frac{e^{\left(\frac{C_2}{\lambda T}\right)} - 1}{e^{\left(\frac{C_2}{\lambda T_a}\right)} - 1} \tag{3.6}$$

By using the Hottel and Broughton (1932) empirical correlation [8], it is possible to express the emissivity as equation 3.7.

$$\varepsilon(KL,\lambda) = 1 - e^{-\left(\frac{KL}{\lambda^\alpha}\right)} \tag{3.7}$$

Where α is a parameter that depends on the soot properties (optical and physical). Zhao [17] reported that for the visible wavelength range, $\alpha = 1.39$ can be used for most fuels. The parameter KL_{2C} represents the dependence of emissivity with the amount of soot, and includes the total contribution of the

soot along the optical path, no matter either its distribution or geometrical size [18].

From the Equation 3.6 and 3.7, it is possible to get the KL_{2C} parameter, which is represented in equation 3.8.

$$KL = -\lambda^a ln\left[1 - \left(\frac{e^{\left(\frac{C_2}{\lambda T}\right)} - 1}{e^{\left(\frac{C_2}{\lambda T_a}\right)} - 1}\right)\right] \tag{3.8}$$

The equation can be rewritten by using two specific wavelengths λ_1 and λ_2, eliminating the unknown product KL. In this case, the temperature (T) can be obtained by applying the equation 3.9.

$$\left[1 - \left(\frac{e^{\frac{C_2}{\lambda_1 T}} - 1}{e^{\frac{C_2}{\lambda_1 T_{a1}}} - 1}\right)\right]^{\lambda_1^{\alpha_1}} = \left[1 - \left(\frac{e^{\frac{C_2}{\lambda_2 T}} - 1}{e^{\frac{C_2}{\lambda_2 T_{a2}}} - 1}\right)\right]^{\lambda_2^{\alpha_2}} \tag{3.9}$$

3.2.2.4 High-Speed spectroscopy

In general the combustion luminosity in diesel engines can be characterized like a very bright yellow-white flame. In a combustion process, the light emissions can be related with continuum thermal radiation of soot particles, as well as, the emissions of chemiluminescence from gas species. When the soot emission is not present in the flame, the chemiluminescence is responsible for the emission of the light between the regions of UV (ultraviolet) and IR (infrared). The strong light emissions of the combustion of some species like CH, OH, CH_2O, CO_2, C_2 and CHO, which are situated in the UV-visible range, are typical in ICE and widely used for studying the autoignition process in CI engines. The emissions of these band spectra can be measured and directly registered by using a spectrographic equipment, which allows to detect the presence of certain species during the combustion process inside the cylinder [8].

Following this theory, the spectroscopy technique can be applied. It consists of a device that measures the emission (fluorescence, phosphorescence, electroluminescence) of electromagnetic radiation from a sample, as well as the interaction (absorption) of electromagnetic radiation with a sample [19]. In the case of this thesis, the sample is the flame, and the spectrometer will measure the emission of electromagnetic radiation emitted by this flame. In figure 3.6 is represented a scheme of a spectrometer with the different components. The light, that is emitted by a source, i.e. flame, enters in the

device trough a slit. It determines the amount of light that is able to enter the instrument. After this, a mirror reflect the light rays toward a dispersive element that separates light into its constituent wavelengths. This element is known as a diffraction grating which is used for separating the incident polychromatic light. Once the light is split into a beam of its component colors in different wavelengths, a detector system 'all at once', which uses an array detector, collects this dispersed light. In the case of this thesis, a high-speed camera coupled to a high-speed intensifier is applied like the detector system. Thanks to this optical devices, the high speed spectroscopy can be carried out, allowing to get temporal resolution during the measurements. For the case of ICE, spectroscopy measurements with temporal resolution are extremely important because different species can be identified during the combustion process evolution.

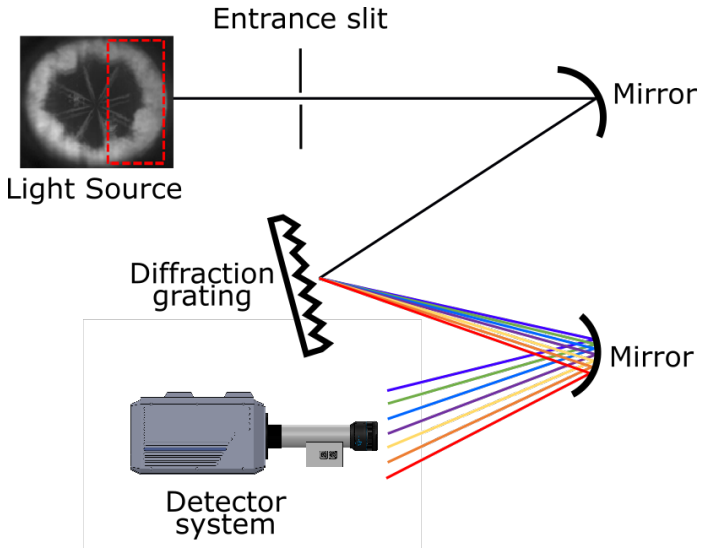

Figure 3.6. *Scheme of a spectrometer device with its different optical components.*

3.2.3 Processing methodology

Some specific image processing methodology were developed in order to extract the parameters and informations necessary from the measured combustion images. The general methodology to process and post-process de 2C images as well as getting the KL values is presented in the beginning of this section. In the case of the analysis of different bowl templates and e-fuels, post-processing image methodologies were created for diving the piston

in different regions (sectors and radial) and creating maps with temporal and spatial resolution for the soot evolution.

3.2.3.1 Methodology for 2D evolution map analysis

A single map was created in order to represent time and spatially resolved the KL values from the 2C measurements. For this purpose, the images of the combustion chamber were divided in zones by applying two different criteria: sector zones and radial zones. For the sector analysis, the whole image is divided in 5◦ angular sectors in the azimuth direction. For every sector, firstly the flame area is calculated by the sum of the total amount of pixels that compose the flame. In the following, the value of each pixel inside this sector (KL value) is also summed. Finally, the mean KL is obtained as represented in equation 3.10.

$$KL_{mean} = \frac{KL_{cumul,\varphi}}{A_{\varphi}} = \frac{\sum_{i=flame,\varphi} KL_i}{\sum_{i=flame,\varphi} pixel} \tag{3.10}$$

By using the same methodology, the radial zones were also obtained. Instead of sectors, the images are divided in rings of different diameter, from the center to the periphery of the bowl. For each ring, the difference between the internal and external radius is 0.5 mm. For each ring, the KL_{mean} is calculated from the ratio between the accumulated KL value (sum of the KL values of each pixel) and the flame area (total number of pixels) in this current ring as represented in equation 3.11. The figure 3.7 shows how the different zones were considered in the analysis of the soot images.

$$KL_{mean} = \frac{KL_{cumul,r}}{A_r} = \frac{\sum_{i=flame,r} KL_i}{\sum_{i=flame,r} pixel} \tag{3.11}$$

3.2.3.2 KL processing

For getting the KL value from the 2C images, firstly a perfect image overlapping between frames from camera 550 nm and camera 660 nm for the correction of the KL value is performed by using a image correction code (Matlab). A spatial transformation matrix is calculated, considering translation, rotation and scaling for a perfect matching (pixel by pixel) of both images. In addition, a segmentation of the background of the images is also used. When the images (green and red) are overlapped and the best

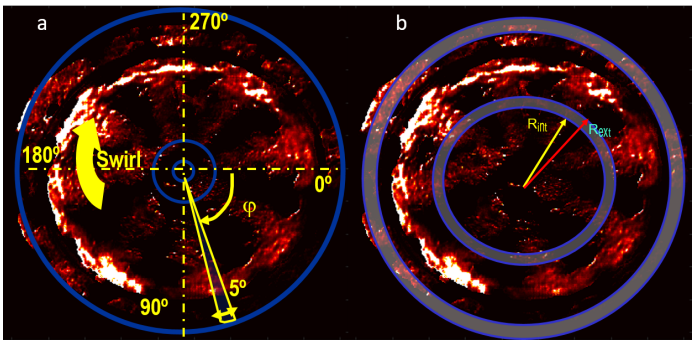

Figure 3.7. *Methodology for the sector analysis (a) and radial analysis b.*

possible match is obtained , the equation of 2C, previously explained, is applied for each wavelength, allowing to get both temperature and KL. An example of the composition of the instantaneous natural luminosity images from 550 nm and 660 nm, together with the results of the KL calculations and a map indicating the errors zones are shown in figure 3.8. The yellow color in the overlap of images 660 nm and 550 nm in figure 3.8, is the result of a perfect match between the two different wavelengths images. However, the dark zones represent the regions where the code could not found a good match. These zones can induce errors in the KL calculation due to different sources of uncertainties [20]. In the errors map, the zones with red colors are formed by pixels where the combination of the two wavelengths can lead to a radiation intensities which do not present physical solutions. In this case, the value of 3 is assigned for the KL.

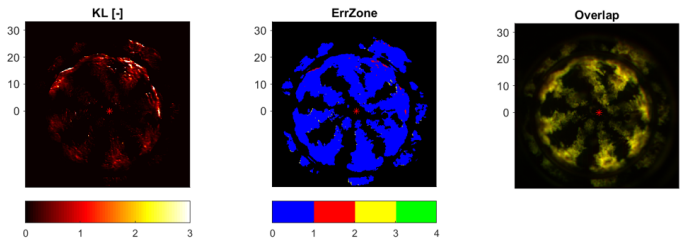

Figure 3.8. *Image overlapping and errors in the KL calculation.*

3.3 Tools for bowl template analysis

For the analysis involving the effect of different bowl templates on the soot production, some specific tools have been developed and applied in order to become possible the visualization of the combustion process as well as its correct interpretation and comprehension. This current section details the different piston bowls geometries that were employed in the present study and the different adaptations used for replicating real bowl shapes in quartz versions. The specific methodology for processing the images that was applied for this part of the study is also detailed.

3.3.1 Piston geometries

Three different piston geometries have been mounted, tested and analysed in the optical engine. These optical piston are made of quartz, where the piston top (bowl and squish region) are completely transparent. The material used for manufacturing the pistons is SUPRASIL 1 fused silica. SUPRASIL 1 is an optically isotropic 3D material. It is highly homogeneous and has no striations in all three dimensions. These properties are very important for multiple axis optics such as prisms, steep lenses, beam splitters or etalons [21]. Among the three geometries tested, the first one is the conventional re-entrant piston. In this case, it is used in the tests as the baseline piston. The geometry is the same as used in the metal version of the GM 1.6L. Due to the complexity of the geometry, some small modifications were necessary for the correct optical visualization and minimum optical distortion as represented in figure 3.9. The piston/vale cutouts, which are present in the metal piston, were removed in the optical version. However, the bowl geometry was kept the same, including the bowl volume, bowl pip, lip radii and lip height. Regarding the other two bowl geometries, they are new designs that have been developed and tested by General Motors for swirl supported light-duty diesel engines application. The first one is based on the stepped-lip geometry. As already explained in the previous section, it is a geometry that has been improved and applied in high-speed small diesel engines during the last decade in order to reduce the soot formation. The third geometry is the newest one, which consists of a combination of stepped-lip geometry and the waves purpose developed by Volvo. For the current thesis, a special hybrid optical piston was developed, where one half is composed only by the stepped-lip design and the other one by a merge between stepped lip and wave protrusions designs. The objective of developing a hybrid piston was to reduce, as much as possible, the uncertainties induced by the cycle-to-cycle variations, as well as, to allow a simultaneous

comparison between two geometries (stepped lip and stepped lip-wave) in terms of combustion process, soot formation and soot oxidation. Both quartz pistons, re-entrant and hybrid, are shown in figure 3.9.

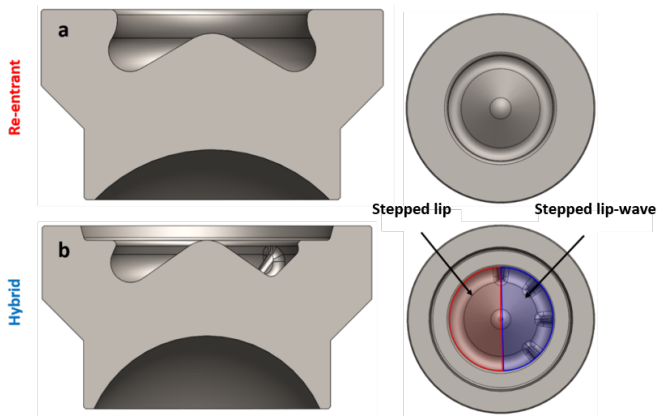

Figure 3.9. *Bowl geometries: (a) Re-entrant and (b) Hybrid.*

A manual procedure is necessary for glueing the quartz part inside the metal holder, as it is shown in figure 3.10. In this case, the thickness of the glue between the holder and the quartz part is not perfect the same for the different pistons. In addition, there are a small difference in terms of bowl volume between the two pistons used. These factors impact directly on the effective compression ratio. The effective compression ratio is obtained by using the thermodynamic characterization which is performed in CALMEC already explained in the previous section. The re-entrant piston has a effective compression ratio of 12.5, while for the hybrid piston is 11.5. This difference was compensated by tunning the in-cylinder pressure curve as well as the in-cylinder temperature evolution for both pistons through different intake pressures and temperatures. The details are explained in the chapter 5.

3.3.2 Processing methods for analysing the hybrid piston

A specific methodology was created for studying the hybrid piston, in order to analyse in isolation the two geometries. The two different bowl geometries that compose the hybrid piston, the stepped lip and stepped lip-wave, were isolated for the analysis by applying an additional methodology. In this sense, it was defined two sectors inside the hybrid bowl, where it was tried to separate them as much as possible, minimizing the crosstalk between the

Figure 3.10. *Quartz bowl and metal holder.*

two geometries. The bowl was divided into two zones with exactly the same size. The figure 3.11, shows the regions considered for analysing each one of the geometries. Considering that the bowl center (region of the bowl pip) induces high light reflections, it was excluded of the analysis. Moreover, the squish region was also not considered in the hybrid piston image processing due to the difficulty of isolating the impacts of the waves, which are located just inside the bowl. Taking into account that the flame location considered in the analysis is inside the piston bowl and close to the quartz surface, it was assumed that the optical distortion has not effect for the direct comparison between both pistons (re-entrant and hybrid). In addition, for the re-entrant piston, where the results of soot formation are compared with the hybrid piston, the same bowl region was considered for the re-entrant one. In contrast, for the analysis when using e-fuels, where it was used only the re-entrant piston, the analysis was performed for the entire piston bore, including the squish zone.

3.4 Tools for analyzing the effect of e-fuels

For the study of e-fuels, which is discussed in the chapter 6, the three fuels selected for the analysis present specific chemical and physical which are shown in this current section. The methodology applied for post-processing the spectroscopy results by using e-fuels is also explained in this section.

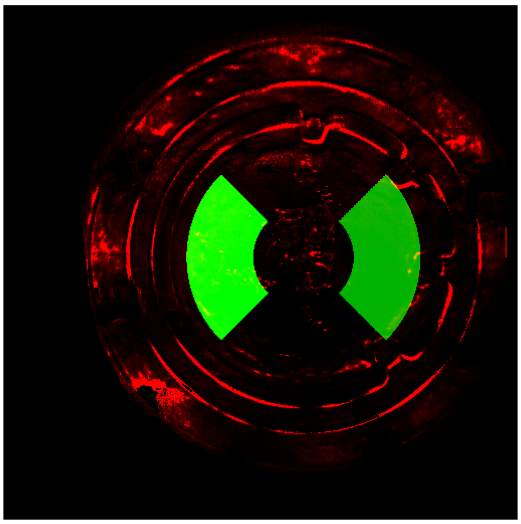

Figure 3.11. *The different zones considered for the analysis of the two bowl geometries.*

3.4.1 Fuels

The main properties of the fuels studied in this work are presented in Table 3.3. Commercial diesel (EN 590 diesel) was considered the reference fuel in this thesis. Fischer-Tropsch (FT) diesel was used in the pure form and Oxymethylene dimethyl ether (OME_X) was tested in the pure form, as well as, blended with different percentage of diesel. Cetane number for FT diesel and OME_X is clearly higher than for the commercial diesel, indicating that their ignitability is higher [22]. OME_X presents the lowest viscosity between the three tested fuels, which directly implies in an improvement of the spray atomization [23]. The main fuel properties are presented in Table 3.3.

3.4.2 Spectroscopy - Maps

For the spectroscopy analysis, a specific methodology of image processing was also developed for generating maps in order to represent the emission spectrum of the flame in the UV-Vis range for the different instants of the combustion (temporal resolution). The spectrum distribution for each instant of the combustion process was concatenated in a single map. In raw images

	EN 590 diesel	FT diesel	OME_X
Density [kg/m^3](T = 15◦C)	842	832	1067
Viscosity [mm^2/s](T = 40◦C)	2.929	3.25	1.18
Cetane number [-]	55.7	75.5	72.9
Carbon content [% m/m]	86.2	85.7	43.6
Hydrogen content [% m/m]	13.8	14.3	8.82
Oxygen content [% m/m]	0	0	47.1
Lower heating value [MJ/kg]	42.44	44.2	19.04

Table 3.3. *Fuel Properties.*

from the spectrometer, which are shown on the top of figure 3.12, the Y axis corresponds to the vertical location within the field of view. The X axis represents the spectrum distribution of the flame radiation when it is decomposed in the different wavelengths. In the first step, the pixels of the vertical axis (columns) are averaged in order to get an average intensity per wavelength. This is done for each image captured during the combustion, from the beginning to the end of the process. After this, the averaged spectrum for each instant is obtained, as can be seen in images located in the middle of figure 3.12. By joining the spectrum images, a single map can be generated. In this case, the Y axis is representing the temporal evolution of the combustion in CAD's and the X axis corresponds to the wavelength values of the spectrum.

3.5 Summary & conclusions

The experimental and theoretical tools as well as the optical apparatus used for developing the current thesis were presented and discussed in this chapter. In one side, the chapter starts presenting the main characteristics of the optical engine such as injection system, lubricating and cooling system and the different optical piston geometries. In addition, test cell and the different sensors used for its instrumentation which are used for obtaining the different data from the engine are also described. On the other side, the fundamentals of the optical techniques as well as the different optical devices which are involved in different studies of the thesis were explained in details. Finally, the theoretical tools used for getting the engine thermodynamic informations as well as the methodology applied for the image post-processing were presented and discussed.

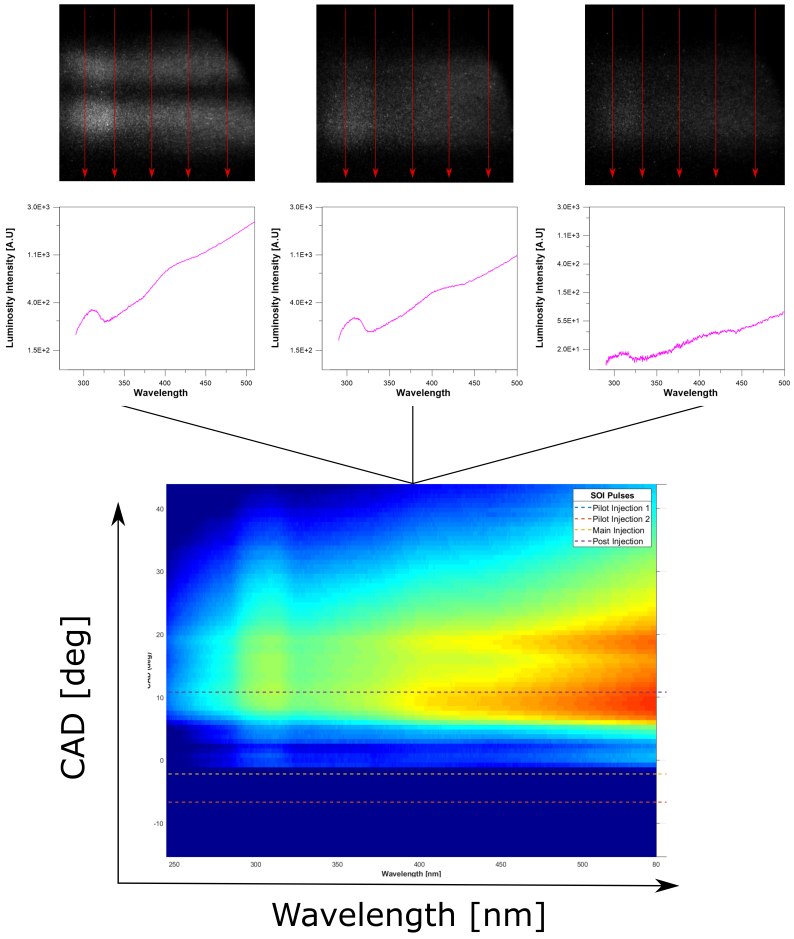

Figure 3.12. *Map of the flame radiation spectrum with temporal evolution.*

Bibliography

[1] Bosch Wilhelm. "The Fuel Rate Indicator: A New Measuring Instrument For Display of the Characteristics of Individual Injection", 1966.

[2] Payri R., Salvador F. J., Gimeno J. and Bracho G. "A new methodology for correcting the signal cumulative phenomenon on injection rate measurements". *Experimental Techniques*, Vol. 32 n^o 1, pp. 46–49, 2008.

[3] AVL. "Pressure sensor for combustion analysis". 2011.

[4] Group Kistler. "Piezoresistive Absolute Pressure Sensors". n^o 4053, pp. 1–7, 2009.

[5] ABB Automation Products GmbH and Analytics Measurement &. "Thermal Mass Flowmeter Sensyflow FMT700-P", 2017.

[6] Payri F., Margot X., Gil A. and Martin J. "Computational study of heat transfer to the walls of a di diesel engine". *SAE Technical Papers*, Vol. 2005 n^o 724, 2005.

[7] Gamma Technologies. "Engine Performance Application Manual". Technical report, 2016.

[8] Zhao H. *Laser Diagnostics and Optical Measurement Techniques in Internal Combustion Engines*. SAE International, 2012.

[9] Brossard C, Monnier J C, Barricau P, Vandernoot F X, Sant Y Le, Besnerais G Le, Brossard C, Monnier J C, Barricau P, Vandernoot F X and Sant Y Le. "Principles and applications of particle image velocimetry". *AerospaceLab*, pp. 1–11, 2009.

[10] Mueller Charles J. and Martin Glen C. "Effects of Oxygenated Compounds on Combustion and Soot Evolution in a DI Diesel Engine:Broadband Natural Luminosity Imaging". *SAE Technical Paper Series*, Vol. 1 n^o 724, 2002.

[11] Zha Kan, Busch Stephen, Warey Alok, Peterson Richard C. and Kurtz Eric. "A Study of Piston Geometry Effects on Late-Stage Combustion in a Light-Duty Optical Diesel Engine Using Combustion Image Velocimetry". *SAE International Journal of Engines*, Vol. 11 n^o 6, pp. 783–804, 2018.

[12] Dembinski Henrik W R. *In-cylinder Flow Characterisation of Heavy Duty Diesel Engines Using Combustion Image Velocimetry*. Doctoral Thesis, 2013.

[13] Gaydon A. G. *The Spectroscopy of Flames*, volume 53. Springer Netherlands, Dordrecht, 1974.

[14] Liu Yao, Tan Jianguo, Wan Minggang, Zhang Lang and Yao Xiao. "Quantitative Measurement of OHâ and CHâ Chemiluminescence in Jet Diffusion Flames". *ACS Omega*, Vol. 5 n^o 26, pp. 15922–15930, 2020.

[15] Zhao Mengmeng, Buttsworth David and Choudhury Rishabh. "Experimental and numerical study of OH* chemiluminescence in hydrogen diffusion flames". *Combustion and Flame*, Vol. 197, pp. 369–377, 2018.

[16] JOSÉ MARÍA GARCÍA OLIVER. *Aportaciones al estudio del proceso de combustión turbulenta de chorros en motores diesel de inyección directa*. Doctoral Thesis, 2004.

[17] Zhao H. and Ladommatos N. "Optical diagnostics for soot and temperature measurement in diesel engines". *Progress in Energy and Combustion Science*, Vol. 24 n^o 3, pp. 221–255, 1998.

[18] Pastor José V., García-Oliver José M., García Antonio, Micó Carlos and Möller Sebastian. "Application of optical diagnostics to the quantification of soot in n-alkane flames under diesel conditions". *Combustion and Flame*, Vol. 164, pp. 212–223, 2016.

[19] Edinburgh Instruments. “What is a Spectrometer?”.

[20] Musculus Mark P.B., Singh Satbir and Reitz Rolf D. “Gradient effects on two-color soot optical pyrometry in a heavy-duty DI diesel engine”. *Combustion and Flame*, Vol. 153 n^o 1-2, pp. 216–227, 2008.

[21] Heraeus-Quartzglass. “SUPRASIL 1, 2, 3 and SUPRASIL Standard 1.”.

[22] Liu Haoye, Wang Zhi, Wang Jianxin and He Xin. “Improvement of emission characteristics and thermal efficiency in diesel engines by fueling gasoline/diesel/PODEn blends”. *Energy*, Vol. 97, pp. 105–112, 2016.

[23] Chen Hao, Su Xin, Li Junhui and Zhong Xianglin. “Effects of gasoline and polyoxymethylene dimethyl ethers blending in diesel on the combustion and emission of a common rail diesel engine”. *Energy*, Vol. 171, pp. 981–999, 2019.

Chapter 4

In-cylinder flow characterization of the optical engine

Contents

4.1 Introduction

As it was described in chapter 2, the in-cylinder flow pattern directly affects the combustion process, fuel-air mixing and pollutant emissions of a diesel engine. In this sense, the characterization of the in-cylinder flow when using a real bowl shape piston (re-entrant) is extremely valuable and an important step for understanding the effects of these real geometries on the flow pattern

and its interaction with the fuel jets. In light-duty (LD) engines, the fuel jets interact with the air flow and bulk flow structures are formed by the jet deflection at the combustion chamber walls [1, 2]. These bulk flow structures are also very important because they generate turbulence that enhances small-scale mixing and increases the burning rate [3], as well as, affecting the wall heat transfer. Furthermore, the swirl and squish flow interaction has a strong effect in the turbulence generated inside the piston bowl, near the end of compression. For low swirl level, the squish flow penetrates close to the center of cylinder. As the swirl increases, the squish penetration into the piston bowl reduces due to the higher centrifugal forces [4]. In addition, this specific chapter is used as a baseline knowledge for applying in the studies developed in the chapter 5, when using different piston geometries and different optical techniques to study them.

The particle image velocimetry-(PIV) technique has been proposed to characterize the velocity field and TKE distribution inside of a re-entrant bowl shape. Moreover, the effect of the fuel jet on the velocity field has also been analysed. For this purpose, an optical single cylinder engine derived from the 1.6 commercial diesel engine (already presented previously in chapter 2) and equipped with a commercial re-entrant bowl piston was employed for the current study. The engine has been tested at motored and inert injection conditions (single injection).

The chapter begins with the description of the optical setup, as well as, the test matrix with the engine conditions used for carrying out the experiments. The details about the PIV technique were already explained in the chapter 3. Then, the following section presents the results obtained for both velocity field and TKE distribution. A detailed discussion regarding the different results at motored and injection conditions is described in the section.

4.2 Optical Setup

The measurements of instantaneous two-dimensional velocity fields were performed by using a standard PIV system. The source of light is a double-head 15 Hz pulsed Nd: YAG laser with 135mJ/pulse at 532 nm. A laser sheet was generated by means of a Plano-concave cylindrical lens. Furthermore, a set of Plano-concave spherical lenses was additionally used in order to adjust the laser sheet width and thickness. The width of the laser sheet was around 50 mm, which is the mirror width used to reflect the laser sheet toward the piston bottom. The thickness was kept around of 1 mm. The laser sheet was introduced through the bottom of the piston (vertical orientation) and it

was located just in the middle of the combustion chamber (aligned with the injector).

PIV seeding is performed with Aluminum Oxide (Al2O3) powder that have already been used in our previous PIV studies. Before choose Aluminum Oxide, different types of seeding particles were tested. Liquids particles were tested but it vaporizes at the compression stroke. In relation to the solid particles, Titanium Oxide particles were tested as well but it presents high tendency to agglomerate. In this way, a good behavior was found with Aluminum Oxide.

The particles were introduced and dispersed in the intake system by means of a cyclone that keeps particles in suspension by generating a continuous centrifugal movement with diameters higher than 5 microns. A positive pressure difference between the cyclone and the intake manifold system was maintained to ensure a continuous particle supply. To guarantee that the particles are able to follow the flow, the stoke number was computed according to the procedure described by Zha et al [5]. It was found that Stokes number in the CAD range when PIV measurements are performed is Sk ¡ 0.1. The evolution of this parameter with in-cylinder thermodynamic conditions for the particles used in this work is represented in figure 4.1. Based on these calculations, it is expected that the particles are able to provide reliable results. The particles were recovered with a specific filter in the exhaust pipe to avoid their dispersion in the atmosphere but they were not reused in the system.

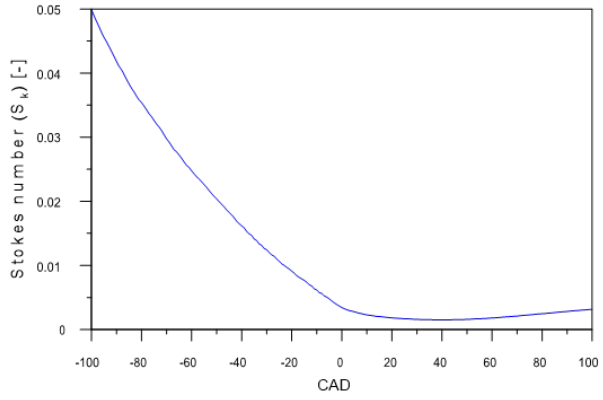

Figure 4.1. *Stokes number for checking the fidelity of seeding particles.*

A straddle CCD camera of 4 megapixels (Powerview Plus 4MP by TSI) was used to acquire the laser light scattered by the seeding particles. Time elapsed between the two consecutive laser shots was set between 10 μs and

15 μs. This time delay was set to fulfil the condition $\Delta T \leqslant \delta/4z$, where δ is the laser sheet thickness and z is the estimated out-of-plane velocity. This is described in the work performed by Danneman et al [6]. For PIV measurements in the r-z plane in small diesel engines supported by swirl, the out-of-plane (swirl) motion can induce errors in the results. When the viewing angle is large and with optical distortion, velocity errors are introduced by the projection of the tangential velocity onto the radial and axial velocity [7]. For the current study, the error induced by the out-of-plane (swirl) motion was neglected in the turbulent and kinetic energy obtained by means of PIV, as the optical set-up did not allow to characterize this effect. Different time intervals between laser pulses were tested in order to find an optimum configuration for the measured velocities inside the cylinder and to be able to perform the PIV cross correlation processing. They are synchronized with the frames grabbing by means of a synchronizer device (Laserpulse 610036 by TSI). A narrow band pass filter 532 nm was used to reduce the external light interference in the second frame that has a much higher exposure time than the first one (due to camera limitations). The schematics of PIV system assembly is presented in figure 4.2.

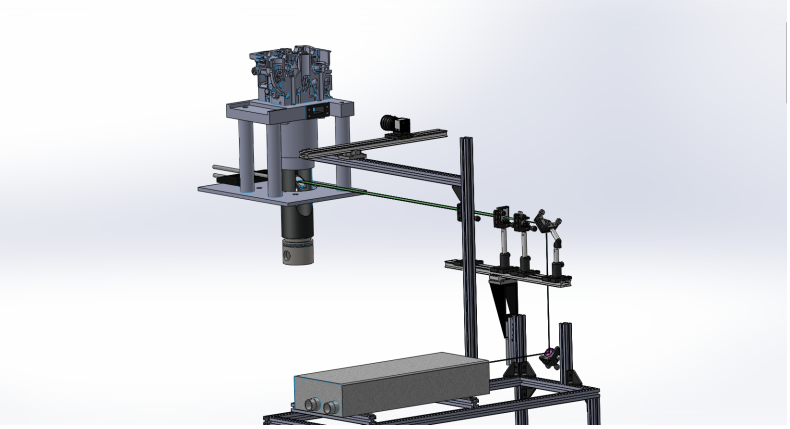

Figure 4.2. *PIV system.*

4.2.1 Ray-tracing analysis

For a better comprehension about the problems involved in the laser utilization with real piston geometries, a specific analysis by using ray tracing methodology was developed. The piston geometry was modeled in a Matlab

code and the directions of the rays were traced by using the simplified Snell's law, as represented in equation 4.1

$$n_1 \sin i_1 = n_2 \sin i_2 \tag{4.1}$$

The refraction index used for the glass piston was 1.46. The refraction index in the combustion chamber is considered 1 while pressure and temperature variations caused by the compression and combustion process have not been considered. Two examples of the ray tracing analysis are presented in figure 4.3. In the first image (a) the raw piston is shown without any optical improvement. The rays deviation caused by the piston geometry can be seen clearly. Most part of the light is directed to the center of the piston. Therefore, the bowl periphery, which is an important region for the current study, is poorly illuminated. In the second image (b) shows an improvement obtained by the addition of a divergent lens in the piston bottom. By using this lens, it was possible to diverge the laser rays and obtain a better illumination distribution, especially at the bowl periphery.

4.2.2 PIV data processing

4.2.2.1 Image processing

The number of repetitions per test condition was chosen in order to have statistically reliable results. A preliminary study was performed, to choose the optimum solution. Different sets were tested, varying the amount of cycles per test. The standard deviation for each set (different number of cycles measured) is presented in figure 4.4. Results indicate that differences between 50 and 200 cycles are negligible. Thus, all tests were formed by 50 engine cycles.

For the image processing, a couple of background images without seeding were taken before each test and a mean background image was obtained. Then, the background image was subtracted of the PIV images (with particles) in order to remove non-desired surface reflections. Since the piston used in the tests has a real bowl geometry, optical distortion in the radial and axial direction is caused by the bowl curvature. Furthermore, the side window also introduces an optical distortion in the radial direction. Therefore, for a correct analysis of the PIV measurements it is necessary to perform an image distortion correction. For this purpose, it was assumed that the optical distortion for the exploitable area inside the bowl, represented in figure 4.5, is the same for the range of piston positions considered in the tests.

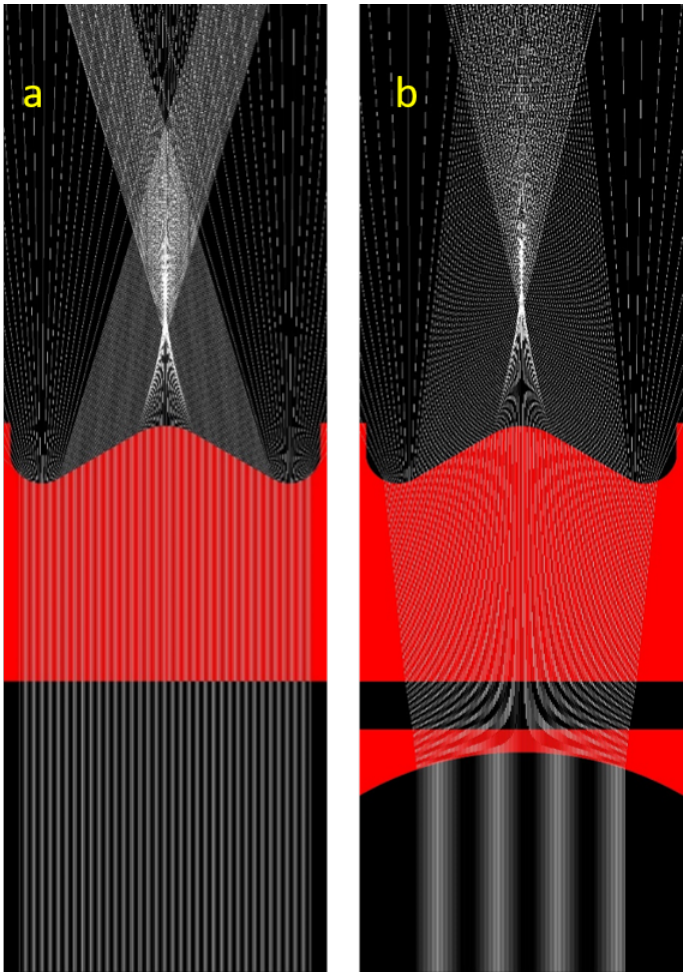

Figure 4.3. *Ray tracing results for the piston without improvement (a) and the improvement of the laser sheet by using a lens (b).*

A specific algorithm was applied to perform the image correction. Firstly, the contour bowl is identified and this area is extracted from the Figure 4.5. This step is made automatically being necessary only to manually select some control points in the original figure. In this way, it is possible to obtain only the part referent to the bowl region. It can be seen in Figure 4.5 as the code finds the bowl contour. Furthermore, it can be seen a huge distortion in the part just above the bowl contour. This area actually represents more or less 2 mm and the correction cannot be performed.

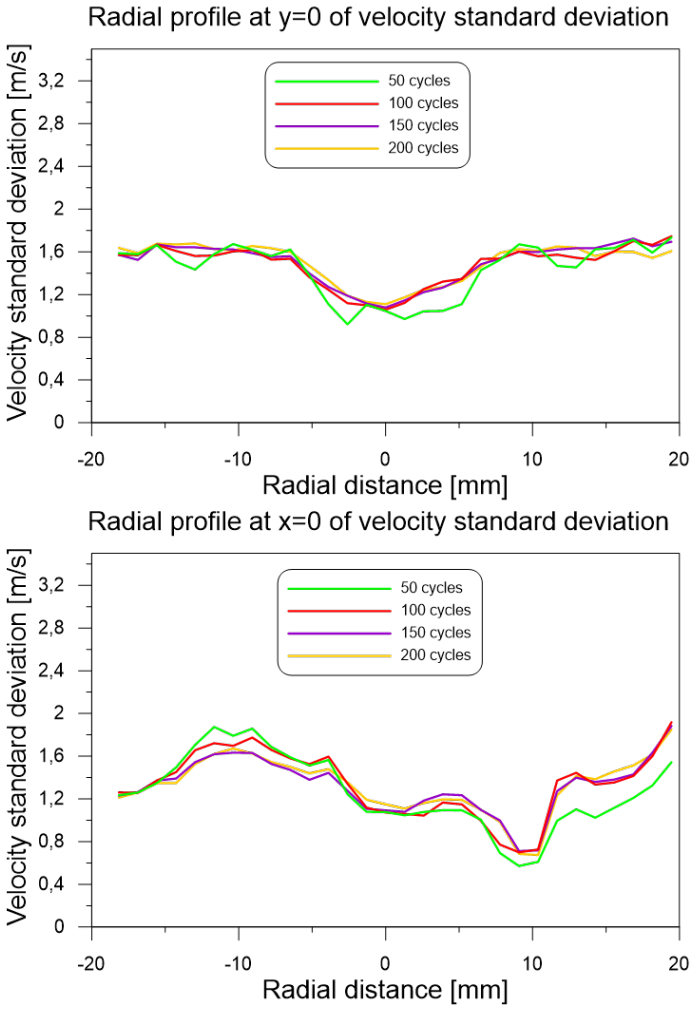

Figure 4.4. *Velocity standard deviation for different numbers of engines cycles.*

The correction was done feature matching between template images with and without distortion. A transformation matrix was generated using the above mentioned piece-wise linear transformation function, which was applied later to all processed images. In Figure 4.6 an example of a distorted calibration image and its correction is shown.

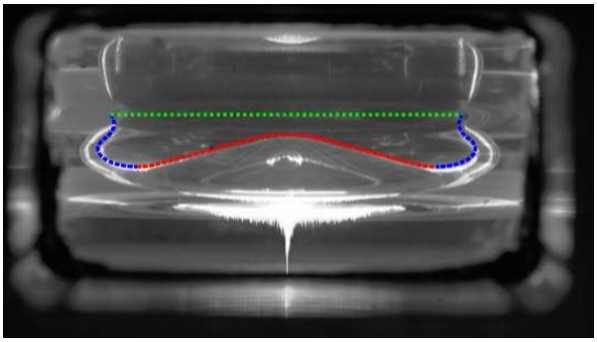

Figure 4.5. *Exploitable area identified by the algorithm.*

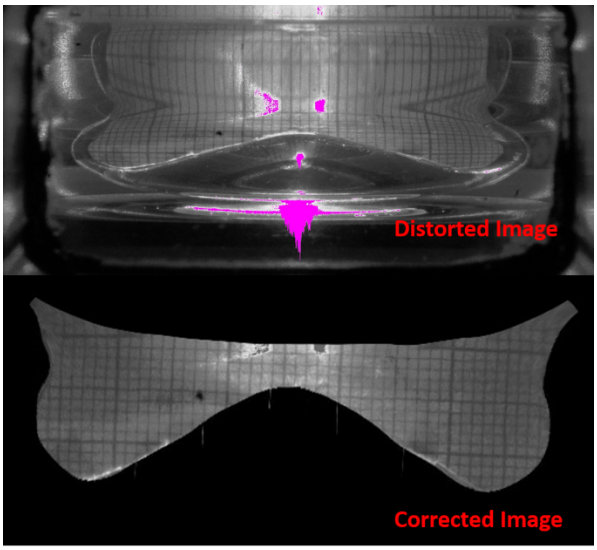

Figure 4.6. *Distorted image and corrected one.*

4.2.2.2 Velocity field processing

Images have been processed by a commercial PIV software package (Insight 3G by TSI). This tool uses a cross-correlation function, between two consecutively captured frames of particle-seeded air inside the cylinder. Velocity fields were computed based on the displacement of a particle group, which was found within a considered interrogation window. The magnification of the images was around 34 pix/mm with a maximum particle between consecutive images of 8.5 pixels (25 %). Considering the out-of-plane equation used previously, a pulse delay that guarantee sufficient pixel displacement and

the spatial resolution, it is expected to be able to resolve velocities of around 25 m/s. For this work, the interrogation window was varied from 88 x 88 pixels to 44 to 44 pixels. Velocity vector validation was performed in two steps. The first one is based on the Signal to Noise Ratio (SNR) of the cross-correlation performance [8]. The second step check the validity of each velocity vector based on a statistical analysis of the local velocity field. Any velocity vector out of this range was rejected and replaced by another one equal to the mean of its neighboring vectors.

4.2.2.3 Turbulent Kinetic Energy (TKE) analysis

For the TKE analysis, the weight of TKE in relation to the total energy of the fluid was quantified. The methodology used compares the flow pattern with and without injection. Firstly, the TKE was calculated using equation 4.2. This equation is based on the differences between the ensemble-averaged velocity field of the same CA position over different cycles and the instantaneous field:

$$TKE = \frac{1}{2}\frac{1}{N}\left(\sum_{j=1}^{N}\left((u_j - \bar{u})^2 + (v_j - \bar{v})^2\right)\right) \tag{4.2}$$

The ensemble-averaged u and v components were calculated by the equation 4.3, where N is the number of cycles considered.

$$\bar{u} = \frac{1}{N}\sum_{j=1}^{N} u_j \tag{4.3}$$

Additionally, the energy related with the mean velocity, i.e. the Mean Kinetic Energy (MKE), was calculated according to equation 4.4.

$$MKE = \frac{1}{2}\left(\overline{u}^2 + \overline{v}^2\right) \tag{4.4}$$

It was assumed that the total energy of the fluid is the addition of the energy related with the mean velocity (MKE) and the turbulence (TKE). From this, TKE is normalized (TKE^*) with respect to the total energy as expressed in equation 4.5. In this case, TKE^* is used in order to quantify the magnitude of turbulence in relation to the total energy of the fluid. When the velocities due to injection are lower, the flow kinetic energy is reduced resulting in leading lower TKE absolute values. Thus, it is very difficult to compare

this scenario with a motored cycle, in terms of the magnitude of turbulence. However, by normalizing and using TKE^*, it is possible to quantify the real percentage of the turbulence in relation to the total of energy present in the flow.

$$TKE^* = \frac{TKE}{TKE + MKE} \tag{4.5}$$

4.2.2.4 Analysis of the temporal and spatial evolution of TKE* and velocity field

For the analysis of results, the same methodology applied in the work developed by Tanov et al. [9] was followed here. A map was built in order to present the temporal and spatial evolution of the velocity field and $TKE*$ for the whole engine cycle. Each $TKE*$ and velocity field was averaged along the laser propagation direction, as it is represented in Figure 4.7.

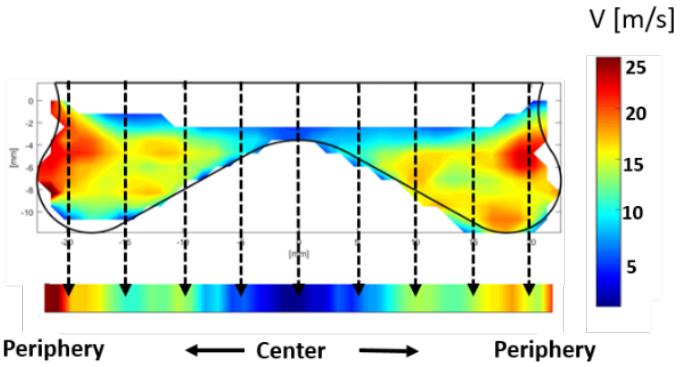

Figure 4.7. *Velocity under motored conditions.*

Then, averaged velocity and $TKE*$ fields were rearranged in columns, according to the CAD when the corresponding image was captured. An example is shown in Figure 4.8. Each column (colors bar) represents the spatial evolution of velocity or $TKE*$ at each CAD, which is the temporal evolution.

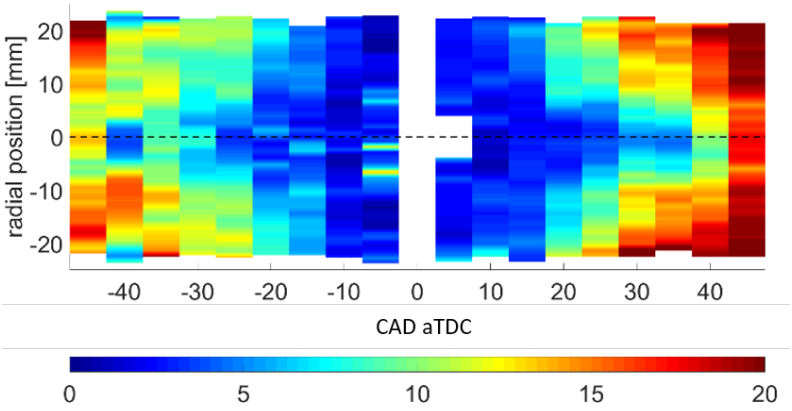

Figure 4.8. *Spatial and temporal evolution map of the ensemble average velocity.*

rpm	Pintake [bar]	T_Intake [$\circ C$]	Pinj [bar]	ET [us]	SOE [$\circ aTDC$]	PIV [CAD]
1200	1.5	50	400	700	-30	-25; -20; -15; +5; +10; +15

Table 4.1. *PIV measurement settings.*

4.2.3 Test matrix and engine operating conditions

All PIV tests were made at 1200 RPM, 1.5 bar of intake pressure and an exhaust pressure of 1.7 bar. Furthermore, the intake temperature was set to 50 $\circ C$. For this condition PIV measurements were performed at motored and injection conditions. The fuel was injected in a non-reactive environment. The injection pressure is 400 bar, an ET of 700 μs and a SOE of -30 $\circ aTDC$.

Table 4.1 shows the different laser timings which are tested at motored and injection conditions. Measurements at motored conditions are performed from -65 CAD to 65 CAD. Figure 4.9 shows the three laser timings used before TDC in reference to the fuel mass flow rate. Furthermore, in the same figure, the Natural Luminosity image represents where is located the eight sprays and the laser sheet (green line). In this case, the image is indicating that the laser sheet does not cross the spray anywhere.

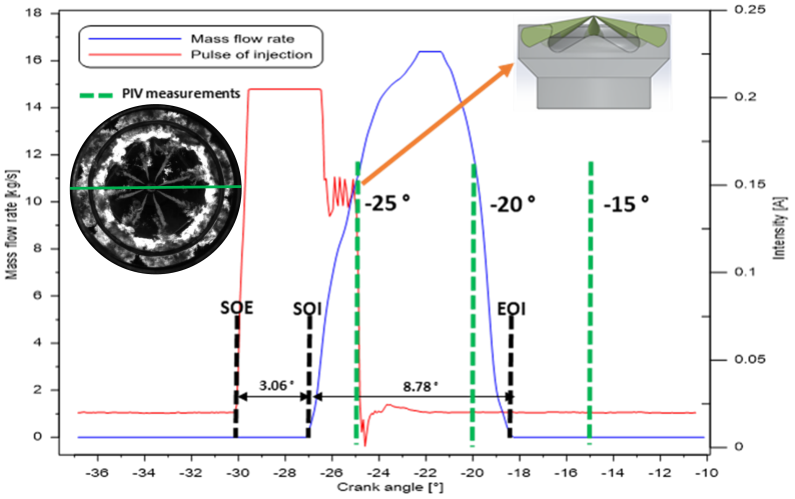

Figure 4.9. *Laser timings in reference to the fuel mass flow rate.*

4.3 Results and Discussions

4.3.1 Flow field for Motored Conditions

The analysis of the flow pattern and the $TKE*$ distribution starts in the squish zone, when the piston was still out of view. After that, velocities were evaluated inside the piston bowl from -40 CAD to +40 CAD, without fuel injection. In Figure 4.10, the in-cylinder flow evolution is shown for different crank angle degree. The distance from the cylinder head (CH) to the piston top is presented as well. It is possible to see measurements corresponding to the squish zone at -65 CAD, the flow moves upward together with the ascending piston movement. A deflection of the flow towards the center can be noted, indicating that the gases are being redirecting into the bowl.

The same flow deflection can be seen in the studied performed by Colban et al. [7]. The flow was not symmetric on the right side of the image is possible to see a recirculation with low velocities. However, on the left side, there are higher velocities and the flow is directed upwards. As the piston approaches to TDC, the velocities in the squish zone decrease.

From -40 CAD onwards the field of view allows visualizing the flow inside the piston bowl. It can be seen in the figure that the flow inside the bowl keeps going upward. Vectors in the periphery of the bowl are completely in the vertical orientation, indicating that squish flow into the bowl is still

negligible. This flow behavior is very similar to the results found by Wang et al. [10] and Tanov et al. [1] but the velocity field presented lower values than the results in this paper. The reason can be due to the higher engine speed and higher intake pressure used for the current study.

Velocities inside the bowl decrease as the piston approaches to TDC. This behavior can be found in others studies [9]. From -35 CAD some vectors begin to deflect on the center of the bowl, indicating the interaction with the squish zone. At -25 CAD, vectors located at the periphery of the bowl begin to deflect as well. From this point, the flow from the squish zone into the bowl in becoming more and more important. This same vector deflection is reported in the study of Tanov et al. [11], where before occurring the fuel injection, the vectors starts to decline at -30 CAD. The evolution of the figures in the current study show that the velocity magnitude in the bowl decreases from the center to the periphery. Similar behavior is noted in the results of Wang, et al. [10].

From -15 CAD the field of view is limited by the upper limit of the side window. Thus, when the piston approaches to TDC the measurement area diminishes as well. However, the bowl bottom can still be analyzed. At -10 CAD, the flow from squish zone is entering into the bowl resulting on a more horizontal flow movement inside the bowl. Considering that the optical engine used in the current tests has high swirl ratio (SR$\approx$2), from the maps at -20 CAD it is possible to observe the interaction of the swirl with the squish flow, as the highest velocities are concentrated in the periphery of the bowl. This behavior is related with the limited influence of the swirl flow, as it is not able to reach the cylinder center due to the higher centrifugal forces [12]. When the piston is almost in the TDC (-5 CAD), the flow velocity into the bowl is already very low.

After TDC (+5 CAD), the velocity field at the upper part of the bowl represents the air flowing out of the bowl into the squish volume. This movement is known as squish expansion [7]. From +20 CAD the flow increases the velocity as the piston goes downward and the flow is driven by the piston movement again. At +65 CAD, where the squish zone fills the field of view, it is possible to see just above the piston lip (right and left side) a flow recirculation and low velocities. Furthermore, the center of the squish zone is where the highest flow velocities are found. This flow recirculation above the piston was also found in previous studies [3, 13] but for these cases the velocities in the center of the squish zone are lower than the ones measured in the zones of flow recirculation.

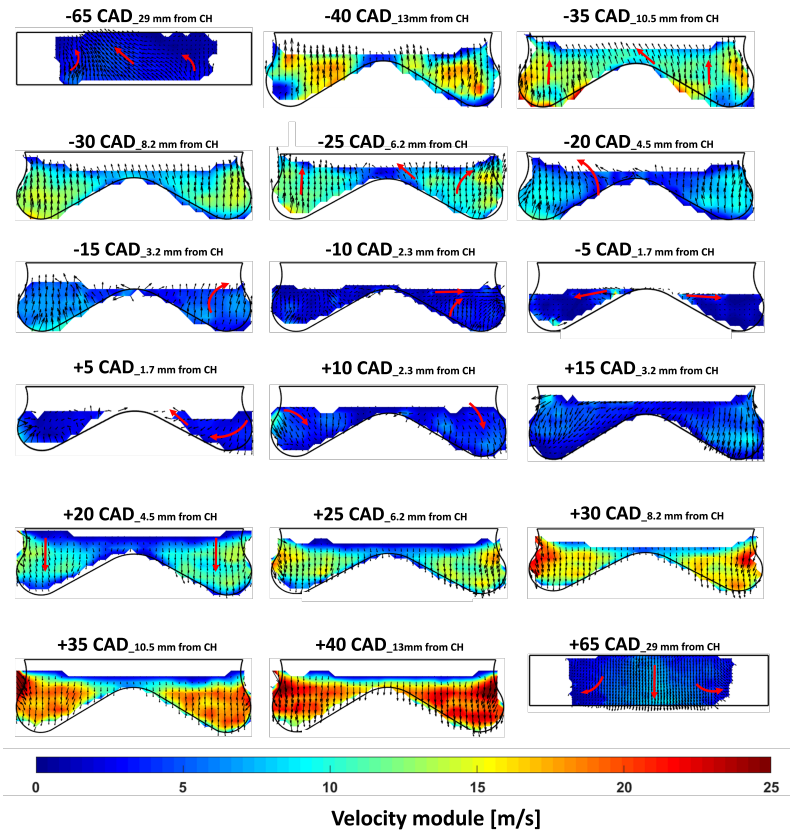

Figure 4.10. *In-cylinder flow velocity evolution at motored conditions.*

4.3.2 Effect of injection over flow field behavior at non-reactive conditions

When fuel injection is added, the flow filed is modified. Thus, the second part of the PIV analysis is performed injecting fuel during the cycle. In this case, measurements were performed at six different piston positions. Results obtained under these conditions can be compared with the motored condition. Thus, interaction of the flow with the injection is analysed. Early SOE (at -30 CAD) is chosen in order to make possible to perform PIV measurements after the injection while seeing the entire bowl. PIV acquisition starts at -25 CAD, when the injection has already started. In Figure 4.11, the results for the velocity field with injection and the position of the PIV measurement respect to the mass flow rate are shown.

At -25 CAD, the effect of the injection is already noticed in the upper part of the bowl. The sprays seem to cause a deceleration of the velocity field while injection event is still occurring. This effect continues until -20 CAD, where the region with low velocity is bigger. Furthermore, at -20 CAD the presence of a vortex can be observed. Probably the flow deceleration has been caused by the early injection timing which means that the spray is not entering directly inside the bowl. In Figure 4.12 is represented the spray footprint in the piston, indicating that the spray is not entering inside the bowl. One part of the spray is impacting on the piston squish region and the other one on the piston lip. This can be the explanation why the flow field does not present larger velocities or more vortices appear inside the bowl. The effect of the injection seems to be absent at -15 CAD and the velocity field increases slightly.

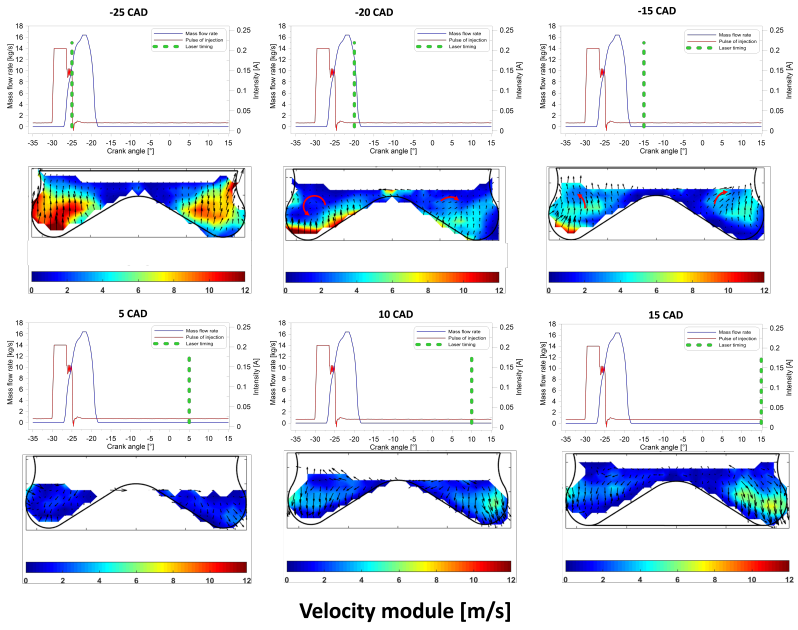

Figure 4.11. *In-cylinder flow velocity evolution with fuel injection at non-reactive condition.*

In Figure 4.13 maps with the temporal and spatial evolution of the velocity field are shown by using the methodology mentioned above. The map for the motored conditions contains all measured piston positions. The map corresponding to injection tests shows only the six positions measured. It is clear that the velocities decrease as the piston approaches to TDC from the

Figure 4.12. *Sprays impacting on the piston lip.*

center to the periphery of the bowl. Furthermore, looking for the same CAD positions in both maps, the velocities at injection conditions present lower velocities than at motored conditions.

4.3.3 TKE* analysis at motored and injection conditions

As mentioned above, TKE is normalized in relation to the total energy of the fluid ($TKE*$), which in this case is the sum of mean velocity kinetic energy (MKE) and turbulent kinetic energy. Figure 4.14 presents a comparison of $TKE*$ between motored and injection conditions.

The $TKE*$ distribution, in Figure 4.14, reveals that for the injection case, the turbulence represents a greater amount of the total fluid energy compared to the motored case. It means that despite the motored case presenting higher velocities, the weight of the TKE in relation to the total fluid energy is lower than for the injection case. Similar results were found by Tanov, et al. [1]. The turbulence for the single injection case is much higher than motored case. The effect of the injection is clear in the first two images, where the turbulence increases around the zone of the spray. This is the zone that the velocities are lower. After the injection ends, at -15 CAD, the $TKE*$ starts to dissipate inside the bowl.

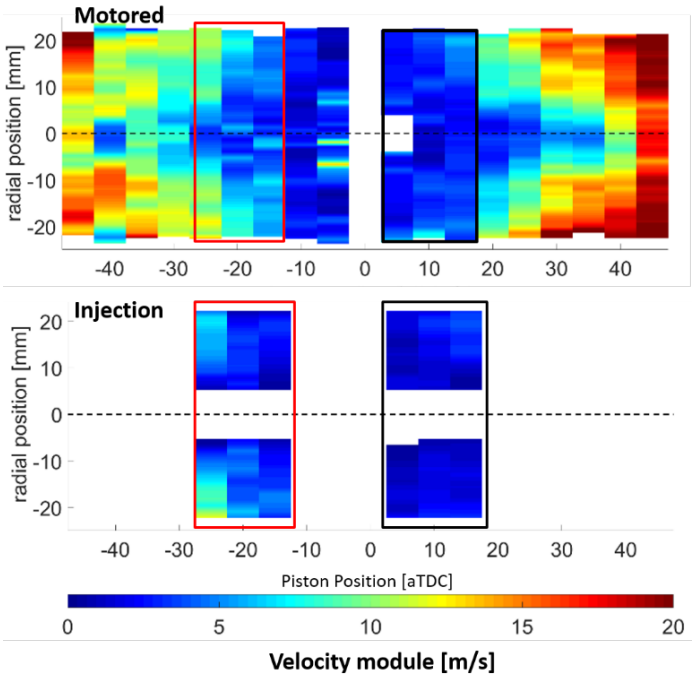

Figure 4.13. *Map of spatial and temporal flow velocity evolution at motored (upper map) and injection conditions (lower map).*

The maps to analyse the temporal and spatial evolution of $TKE*$ are represented in Figure 4.15. In a general way, the turbulence increases as the piston approaches to TDC, with the highest values close to TDC. It was also verified by Tanov et al. [9], where the highest values of TKE are from -8 CAD aTDC until 4 CAD aTDC. Furthermore, it seems to increase from the center to the periphery, despite it is not so clear due to the noise present in the processed data. At motored conditions, the sudden increase on the $TKE*$ at -10 CAD could be a consequence of the squish flow entering into the bowl due to the squish and swirl flow interaction [4]. After TDC, turbulence decreases very fast. Looking at the injection map, $TKE*$ increases from -25 CAD until -20 CAD, but at -15 CAD TKE has a slight decrease caused by the end of the injection.

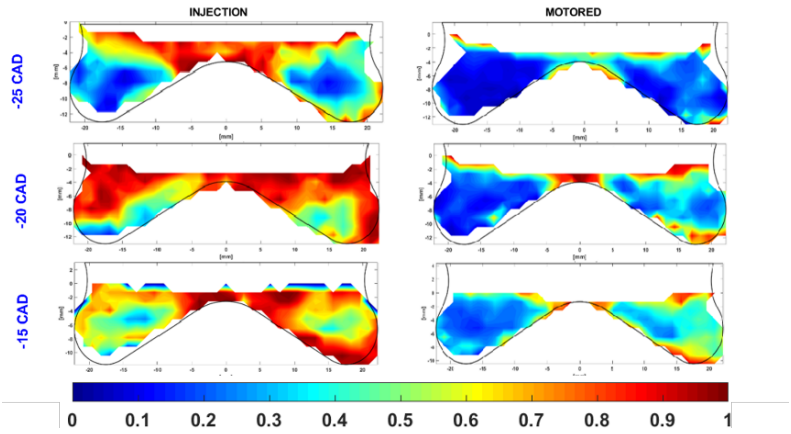

Figure 4.14. *$TKE*$ distribution inside the bowl at motored and injection conditions.*

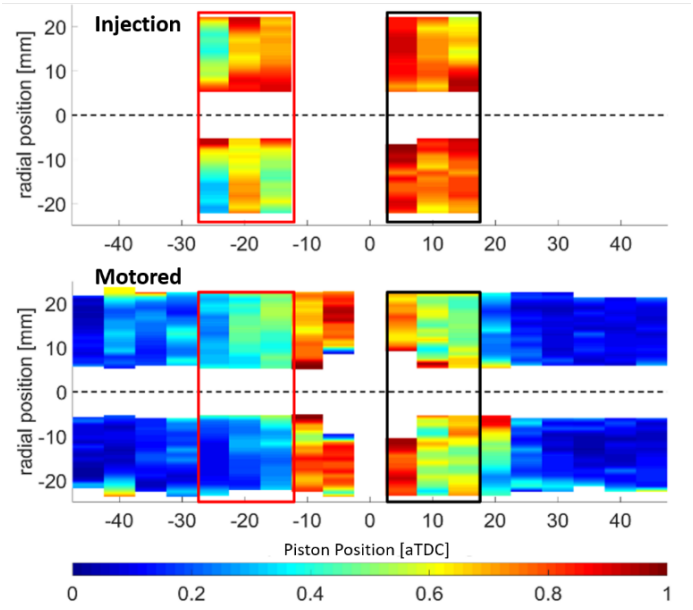

Figure 4.15. *Map of spatial and temporal evolution of $TKE*$ at motored (lower map) and injection conditions (upper map).*

4.4 Summary & conclusions

The current chapter has presented an in-cylinder flow analysis in a single cylinder optical diesel engine and its interaction with fuel spray. The in-cylinder velocity field was measured by using PIV in a vertical plane inside

the combustion chamber. TKE analysis was performed from the velocities field measurements. Main conclusions can be highlighted as follows:

In relation to the TKE^* at motored conditions:

- TKE^* increases as the piston approaches to TDC due to the squish flow which starts to enter into the piston bowl.
- The squish flow provokes a sudden increase of the TKE^* with the maximum effect observed at around -10 CAD aTDC.

Considering the comparison between the cases with and without fuel injection:

- TKE^* presents higher values in the injection cases than in motored ones, indicating that the turbulence caused by the injection event could help to improve the fuel air-mixing.
- When the injection event ends, a slight decrease of TKE^* can be seen inside the bowl. This reiterates the effect of the fuel injection on the in-cylinder flow.
- Bulk gas velocity and mean kinetic energy of the in-cylinder air decrease when the injection is occurring. This effect is evidenced when the injection ends and the velocity starts to increase again inside the bowl.

Bibliography

[1] Tanov Slavey, Johansson Bengt, Richter Mattias, Wang Zhenkan and Wang Hua. "Effects of Injection Strategies on Fluid Flow and Turbulence in Partially Premixed Combustion (PPC) in a Light Duty Engine". *SAE Technical Paper Series*, Vol. 1 n^o Ldv, 2015.

[2] da Costa Roberto Berlini Rodrigues, Gomes Carlos Alberto, Valle Ramon Molina, Franco Rafael Lara and Huebner Rudolf. "PIV Measurements of In-Cylinder Tumble Flow in a Motored Single Cylinder Optical Research Engine". *SAE Technical Paper Series*, Vol. 1, 2016.

[3] Miles Paul C., Collin Robert, Hildingsson Leif, Hultqvist Anders and Andersson Öivind. "Combined measurements of flow structure, partially oxidized fuel, and soot in a high-speed, direct-injection diesel engine". *Proceedings of the Combustion Institute*, Vol. 31 II n^o x, pp. 2963–2970, 2007.

[4] Miles Paul C. *Turbulent Flow Structure in Direct-Injection, Swirl-Supported Diesel Engines*, pp. 173–256. Springer Berlin Heidelberg, Berlin, Heidelberg, 2009.

[5] Senecal P. K., Miles Paul C., Mitra Saurav, Busch Stephen, Wijeyakulasuriya Sameera and Zha Kan. "Characterization of Flow Asymmetry During the Compression Stroke Using Swirl-Plane PIV in a Light-Duty Optical Diesel Engine with the Re-entrant Piston Bowl Geometry". *SAE International Journal of Engines*, Vol. 8 n^o 4, 2015.

[6] Dannemann J., Pielhop K., Klaas M. and Schröder W. "Cycle resolved multi-planar flow measurements in a four-valve combustion engine". *Experiments in Fluids*, Vol. 50 n^o 4, pp. 961–976, 2011.

[7] Colban W, Ekoto I, Kim D and Miles P C. "In-Cylinder PIV Measurements in an Optical Light-Duty Diesel at LTC Conditions". *THIESEL 2008 Conference on Thermo- and Fluid Dynamic Processes in Diesel Engines*, pp. 1–24, 2008.

[8] TSI Inc. "Particle Image Velocimetry INSIGHT 4G", 2011.

[9] Tanov Slavey, Pachano Leonardo, Andersson Öivind, Wang Zhenkan, Richter Mattias, Pastor José V., García-Oliver José M. and García Antonio. "Influence of spatial and temporal distribution of Turbulent Kinetic Energy on heat transfer coefficient in a light duty CI engine operating with Partially Premixed Combustion". *Applied Thermal Engineering*, Vol. 129, pp. 31–40, 2018.

[10] Wang Zhenkan, Tanov Slavey, Wang Hua, Richter Mattias, Johansson Bengt and Alden Marcus. "High-Speed Particle Image Velocimetry Measurement of Partially Premixed Combustion (PPC) in a Light Duty Engine for Different Injection Strategies". 2015.

[11] Najafabadi Izadi. "Analyzing of in-cylinder flow structures and cyclic variations of partially premixed combustion in a light duty engineIzadi". n^o 2016, 2017.

[12] Garcia-Oliver Jose M, Garcia Antonio, Gil Antonio and Pachano Leonardo. "Study of Air Flow Interaction with Pilot Injections in a Diesel Engine by Means of PIV Measurements". *SAE International Journal of Engines*, Vol. 10 n^o 3, 2017.

[13] Miles Paul C., Hildingsson Leif and Hultqvist Anders. "The influence of fuel injection and heat release on bulk flow structures in a direct-injection, swirl-supported diesel engine". *Experiments in Fluids*, Vol. 43 n^o 2-3, pp. 273–283, 2007.

Chapter 5

Combustion behaviour and soot formation analysis of the optical engine by using different bowl templates

Contents

5.1 Introduction

This chapter is focused on the comprehension of the combustion behaviour and soot formation when using different bowl templates. For this purpose, different optical techniques were combined to analyse the combustion evolution, flame movement, identify high-temperature zones where is occurring the soot oxidation and quantify the soot formation inside of each bowl geometry. The results and conclusions obtained in the previous chapter were also taken into account for studying and explaining the results from the optical techniques applied in this current chapter.

The soot measurements have received special attention in this chapter, as the soot reduction is the main objective of testing the different piston geometries. For this purpose, four optical techniques were applied in the analysis. The flame movement and combustion evolution were studied by using natural luminosity and combustion image velocimetry (CIV) techniques. The soot formation as well as the soot oxidation were analysed by applying OH* chemiluminescence and 2-color pyrometry. A specific optical setup was mounted in the optical engine in order to use simultaneously the four optical techniques.

The chapter begins with the description of the optical set-up as well as the calibration procedure used in the 2C pyrometry measurements. Following, the test matrix with the different engine loads and conditions is presented. The second part of the chapter is focused on the results and discussion obtained with the different techniques. Firstly, the results regarding the thermodynamic analysis of each bowl geometry are discussed, trying to highlight the differences found in each piston. Subsequently, the results from the flame movement and flow pattern analysis as well as the analysis for the combustion evolution are presented. Finally, the results and discussion regarding soot formation inside of each bowl geometry are shown and discussed. The chapter ends with a summary of the chapter and the main conclusions of the results.

5.2 Optical setup

For the current measurements, an optical setup, which allows the utilization of four optical technique simultanesouly was employed, as shown in Figure 5.1. For the OH* chemiluminescence measurements, the UV radiation was reflected by a dichroic mirror and recorded with an intensified camera, which was mounted in parallel with the engine's crankshaft. This element is transparent to the visible spectrum (up to 750nm) so light transmitted

was used for 2 color pyrometry measurements. Two high-speed cameras were mounted perpendicularly, each of them equipped with an interference filter, centered at 550 nm and 660 nm (10 FWHM) respectively. A beam splitter (50/50) was installed in order to transmit 50 % of the flame radiation to one of the cameras and reflect the other 50 % to the other camera. In this same optical assembly, the camera which is equipped with the filter of 660 nm was also used for recording the images for the natural luminosity and CIV analysis.

For the OH^* measurements an intensified camera (Andor Solis iStar DH334T-18H-83) with a Bernhard-Halle UV lens and a 310nm 6 10nm bandpass filter were used for the measurements. The spatial resolution of the images was 8.7 pixel/mm. Due to the maximum framerate of the camera, only one image per cycle was recorded. Two identical detection systems were used to register radiation at 550 and 660nm. In both cases, it was used a high-speed camera (Photron SA-5) in combination with a 100mm focal length and f/2 lens. The lenses were used with a wide-open aperture. The image was focused in the region closer the quartz surface with the piston at TDC. The acquisition rate was set to 25 kfps. A different exposure time was set for each camera, in order to maximize the dynamic range used for both of them: 6.65ms for 660nm and 10.05ms for 550 nm.

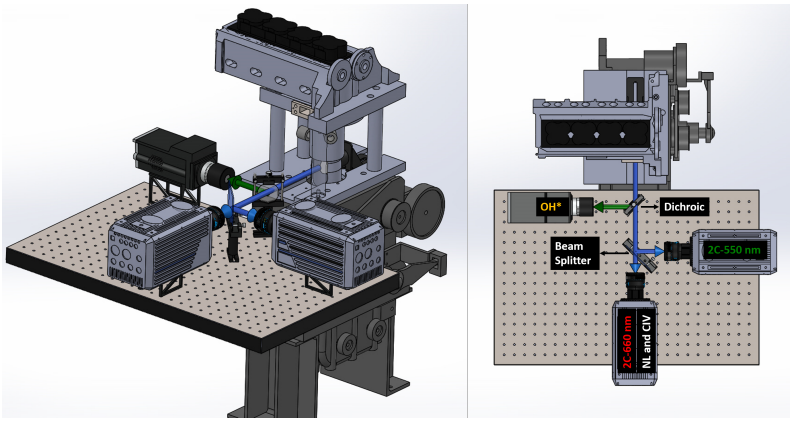

Figure 5.1. *Optical setup a) Isometric view - b) Top view.*

5.2.1 2 color calibration procedure

For the 2 color pyrometry measurements, the detection system was calibrated with a tungsten-ribbon calibration lamp (Osram Wi17G). The procedure followed was already applied in other studies [1, 2]. The calibration

lamp was located on top of the piston (flat area) and all the optical elements used in the tests were included (beam splitter, mirrors and filters) as shown in Figure 5.2 .

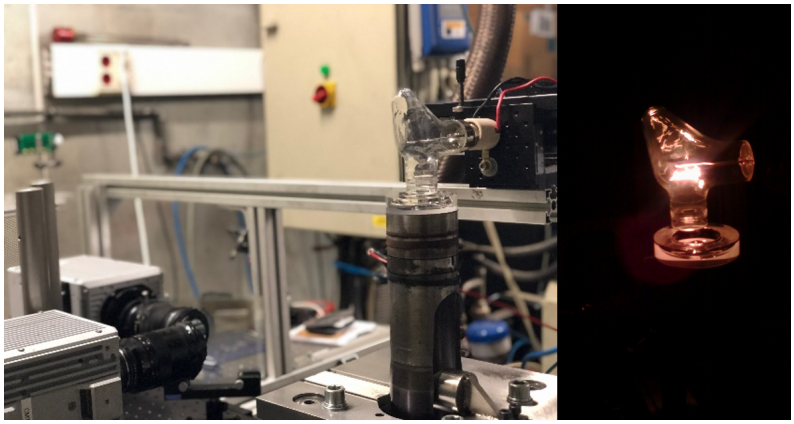

Figure 5.2. *Setup of calibration of 2 color pyrometry.*

It is known that 2 color method measures the apparent temperatures of the flame $Ta1$ and $Ta2$ at wavelengths λ_1 and λ_2. From this temperature it is possible to obtain the actual flame temperature by using the equation for KL calculation already presented in chapter 3. As the 2-color system will generate initially a specific digital level for each camera of the system (camera λ_1 and camera λ_2) which corresponds to the radiation from the flame at the two wavelenghts, the system can be calibrated by getting the apparent temperatures T_{A1} and T_{A2} correspondent to the digital level from camera λ_1 and camera λ_2, respectively. A calibration curve, where is represented the digital level against blackbody temperature, can be obtained for each wavelength. When the calibration is generated, the instantaneous digital levels can be converted to the apparent temperatures. In the case of this current thesis, a tungsten-ribbon calibration lamp is used like a blackbody source. The calibration was performed in a specific part of the squish zone, where the piston surface is flat. In addition, it was assumed that the light intensity registered in this flat zone is the same for whole piston. The lamp is powered by an electrical assembly, which consists of a voltage source and a variable resistor. The latter allows to control the electrical power supply with a precision of 0.1 A, exactly covering the working range of the lamp. Three different electric current, 9.1 A, 10.40 A and 11.7 A, were applied in the tungsten lamp for getting its spectral calibration. The radiance level of these three different lamp intensities are the ones expected in a diesel flame. This calibration allowed to know what is the

radiance emitted by the lamp through a specific area of 25 mm in diameter, which is located at the center of the lamp. The results of this calibration is shown in Figure 5.3. By means this curves it is possible to get the radiance from wavelengths of 550 nm and 660 nm.

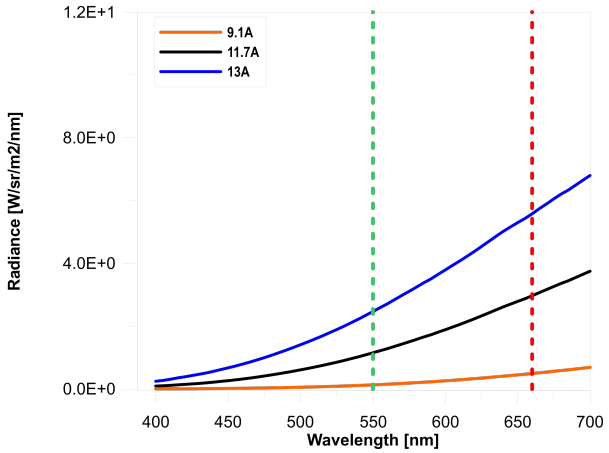

Figure 5.3. *Curves of the calibration lamp. The vertical lines mark the wavelengths used to apply the 2 color technique.*

The calibration process is performed exactly in the same optical system used to obtain the images in the optical engine, keeping the same distance from the lamp to the optical system and the flame to the optical system. Twenty images of the lamp filament were taken for each calibrated point (9.1A, 11.7A and 13A), as represented in Figure 5.4. The digital level of the pixels inside of the area of 25 mm in diameter are averaged and compared with the calibration values of the lamp. From this procedure, the calibration curve for each wavelength can be obtained.

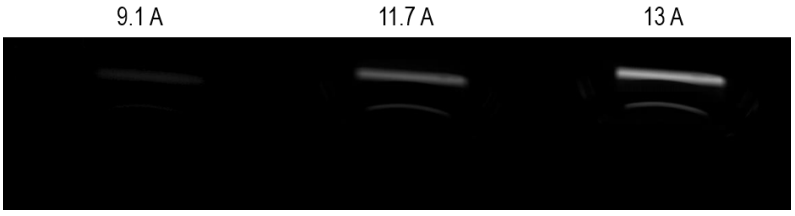

Figure 5.4. *Lamp filament images for different electrical currents.*

5.3 Test Matrix

The tests were performed with commercial diesel fuel. It was ensured the same in-cylinder conditions just before the pilot 1 ignition for the two combustion chambers. Taking into account that the two pistons have different compression ratio (Cr), in order to maintain the same IMEP, mass of fuel injected per cycle and maximum in-cylinder pressure were constant among geometries while different intake pressure and intake temperature were defined for each piston. An example of the intake thermodynamic adjustment between both pistons is represented in Figure 5.5, where it represents the intake conditions used for the tests at 4.5 bar IMEP. It was based on achieving the same P_{max} and density for motored cycles, which allows a direct comparison between both pistons. The same procedure was also applied for the different IMEP's tested in the optical engine. In order to simulate the exhaust back pressure, the intake pressure was set 0.2 bar lower than the exhaust pressure.

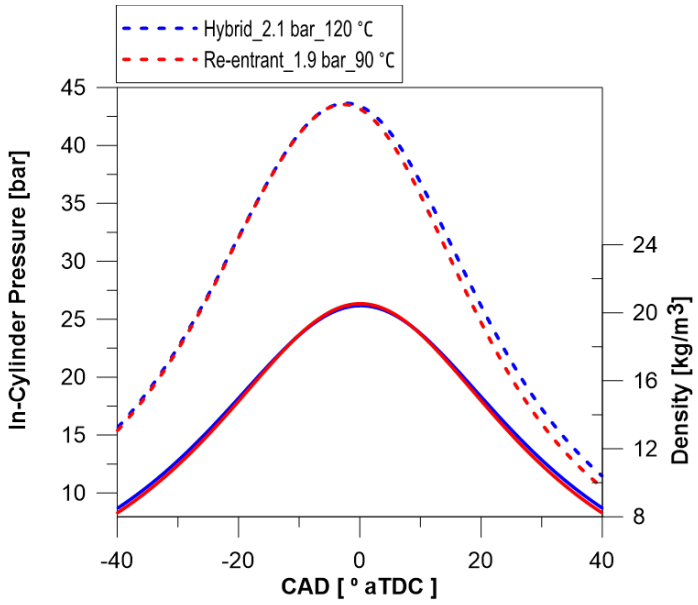

Figure 5.5. *Motored in-cylinder pressure and density used at 4.5 bar IMEP.*

The first part of this chapter, including the analysis of flame movement and combustion evolution was performed with the engine load of 7.5 bar IMEP. The second part, regarding the soot formation analysis, was performed under 4.5 bar and 8.9 bar IMEP. The test conditions are presented in table 5.1, where for the soot analysis, besides the reference cases (4.5 and 8.9 bar IMEP), a

sweep of SOE, post-injection timing and EGR were also performed at 8.9 bar IMEP. Four injections per cycle (pilot 1, pilot 2, main and post) were configured to mimic a commercial injection strategy. These injection settings were applied for both pistons.

Analysis	Case	Engine Speed	Piston	IMEP (bar)	Pinj (bar)	Pint (Bar)	Tint (◦C)	Toil (◦C)	Tcool (◦C).
Flame movement and Combustio evolution	**Ref**	1250	Re-entrant	7.5	800	2.15	90	60	15-25
			Hybrid			2.35	120		
Soot Formation	**Ref.**	1250	Re-entrant	4.5	670	1.9	90	60	15-25
			Hybrid			2.1	120		
			Re-entrant	8.9	800	2.15	100	60	15-26
			Hybrid			2.4	125		
	Sweep: SOE, Post and EGR	1250	Re-entrant	8.9	800	2.15	100	60	15-25
			Hybrid			2.4	125		

Table 5.1. *Engine operating conditions.*

5.4 Flame movement and combustion evolution

The current section of this chapter was focused on the description and analysis of the flame movement inside of each combustion chamber, trying to highlight the differences in terms of flow pattern which are induced by the different shapes tested. In addition, the diesel combustion phases (premixed, diffuse and late combustion) behaviour and the effects of each piston on the combustion evolution were also discussed in this section by means of a thermodynamic analysis and natural luminosity images. All data and analysis presented in this section were performed at 7.5 bar IMEP.

5.4.1 Thermodynamic analysis

Taking into account that the current study includes the utilization of three bowl shapes but just two pistons, as already previously explained, the thermodynamic analysis can only compare both pistons (re-entrant vs hybrid). Firstly, this kind of analysis allows to prove that a good agreement between both pistons was achieved regarding the in-cylinder pressure behaviour (maximum value and evolution), as can be seen in Figure 5.6. From this Figure, it is possible to state that in a general way, the piston are under similar in-cylinder conditions and the direct comparison between them can be carried out. Secondly, the RoHR analysis provides useful information in order to compare re-entrant piston against hybrid one. From the RoHR diagram of each piston, it is possible to see that both pistons present clearly the four injections, but some differences can be highlighted. The fuel injected during

the pilot 1 seems to burn faster for the hybrid piston than for the re-entrant piston, as the rate of energy released during this stage is higher. This is a typical effect of the stepped lip geometry, already reported by previous authors [3, 4], where the chamfered bowl permits a faster mixing process due to the better access of the air in the squish region. When looking for the end of the pilot 2, the same behaviour can be appreciated. Hybrid piston seems to burn fuel faster as the heat release rate suggests complete combustion. In this case, the rate of heat release for the hybrid piston achieves lower values than re-entrant one, close to 0 $J/\circ$, before the main injection starts.

In addition, a faster mixing occurs for the hybrid piston during the main injection, where the maximum RoHR is slightly higher in comparison with the re-entrant. In contrast, during the post-injection, a lower peak of the RoHR diagram can be appreciated for the hybrid piston, indicating that less residual of non-burned fuel from the main injection remains inside the combustion chamber. The late combustion phase after post-injection, which is represented in figure 5.6 by the grey area, is shorter when using the hybrid piston instead of the re-entrant, with a rapid decrease of the RoHR in the first case. This also indicates a shorter combustion duration that could be related with a better oxygen utilization inside the combustion chamber [5].

Regarding the hybrid piston, it is important to note that the stepped lip shape is present in both sides of the piston, indicating an important contribution of this geometry in the thermodynamic results presented and explained in this subsection. In this way, these results also agree with previous studies, where the authors found a faster decrease of the heat release during the late combustion cycle, as well as, a higher heat release rate (maximum peak) during the main part of the diffusion combustion with similar stepped lip geometries [3, 4, 6, 7]. These previous results corroborate with the RoHR shown in figure 5.6.

5.4.2 Flame movement and flow patterns

Figures 5.7 and 5.9 represent the detail of the flame movement and flow pattern at 7.5 bar IMEP. The right side of the figures make reference to the hybrid piston, where one side is composed only by the steeped lip shape and the other one by the stepped lip plus wave geometries. The left side of the figures indicate the results for the re-entrant piston. In figure 5.7, when the main injection is still occurring at 7.7 CAD, it is possible to appreciate that the spray interacts with the bowl wall. The red arrows are representing the flame movement during the flame-wall interaction and the yellow lines the wave

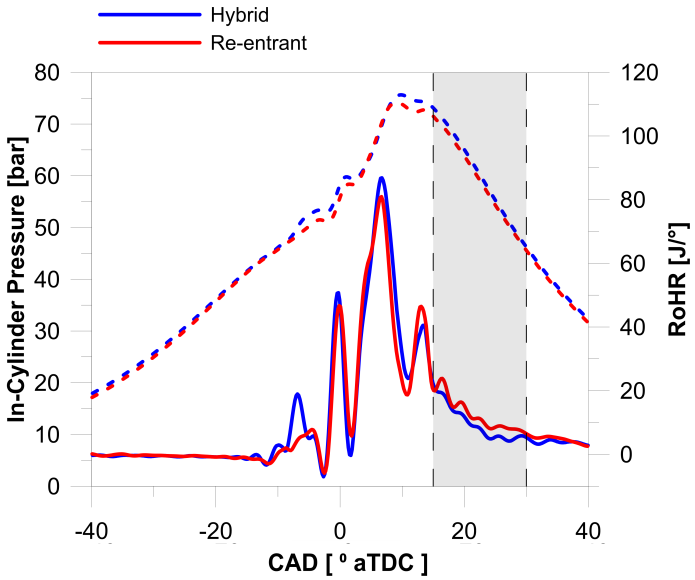

Figure 5.6. *In-cylinder pressure and RoHR at 7.5 bar IMEP.*

protrusions position in the piston. Important differences can be identified when the side composed by waves is compared with the other two geometries. When the sprays collide with the bowl wall, the wave protrusion redirects the flame toward the center of the bowl (red line area), avoiding the spreading of the flame in the tangential direction and reducing the collisions between the flames. This movement provides a pathway for the oxygen supply to flame front, generating less fuel rich zones. This improves the oxidation of soot pockets [8].

In contrast, the flame-flame collisions close to the bowl wall are evident when the waves are not present in the piston. In this regions, the fresh ambient gas cannot reach the fuel rich zones, resulting in much higher fuel/air ratio [9]. As the mixing of the products of combustion occurs, the turbulent kinetic energy of the jets is lost because of the collisions induced by the flame-flame interaction phenomenon. Thus, it leads to a creation of stagnation zones inside the bowl where low amount of oxygen is available.

At 11.9 CAD, when the main injection has already finished, different flame structures can be perceived for each side (geometry) of the hybrid piston. The flame occupies an area in the stepped lip side (orange line) much smaller than the stepped lip-wave side (red area). Therefore, it can be stated that the flame in the stepped lip side without waves seems to remain concentrated at

the periphery of the bowl. This behaviour has been related with the effect of the stepped lip, splitting the spray/flame into two parts (one inside the bowl and the other into the squish area) and reducing the momentum of the spray. Besides, the flame-flame collisions when not using wave protrusions and the resulting stagnations have been considered also a potential cause. In the case of the stepped lip-waves, the flame is forced by the reverse flow to move in direction to the bowl center. When looking for the re-entrant geometry, even though the flame goes toward the center due to higher spray momentum, the existence of strong flame-wall and flame-flame interaction can promote the formation of fuel rich zones. The same behaviour for the wave protrusions was reported by Eismark et al. [8, 9], where the wave piston has a smaller area of stagnation zones during the flame-flame collisions than the conventional piston.

The velocity field of the CIV analysis, which is shown in Figure 5.9, confirms the same behaviour previously commented. In addition, it was included the Figure 5.8 with the corresponding injection mass flow rate used during the CIV tests and the respective positions in CADs, where the CIV velocity maps images are being represented in Figure 5.9. For the hybrid piston, at the stepped lip-wave side, it is possible to see the effect of the waves on the flame movement.

A characteristic reverse flow is observed according to the vector's direction, as it has been already discussed. Thus, the zones with fresh oxygen at the center of the bowl can be reached by the flames. However, in the side without waves, it is clear that vectors are not directed toward the center and the velocities are lower than the other side. When comparing the wave side with the re-entrant bowl, a similar reverse flow to the one described before can be observed. As the re-entrant geometry does not split up the spray into two areas, all kinetic energy from the injection is kept inside the bowl. This produces a more intense velocity field than in the hybrid piston. At 9.5 CAD, it is possible to see that the re-entrant piston presents higher outward velocities in the squish region than the hybrid piston. In addition, the inward velocities are also weaker for this piston. This effect could be linked with the higher swirl amplification for the re-entrant piston as already reported and explained by Zha et al. [4]. Another difference that can be observed when comparing re-entrant and stepped lip-wave geometries is that, in the first case, a tangential flame movement inside the bowl is occurring. This is not observable in the hybrid piston, probably due to the presence of the wave protrusions and the reduction of the spray momentum inside the bowl.

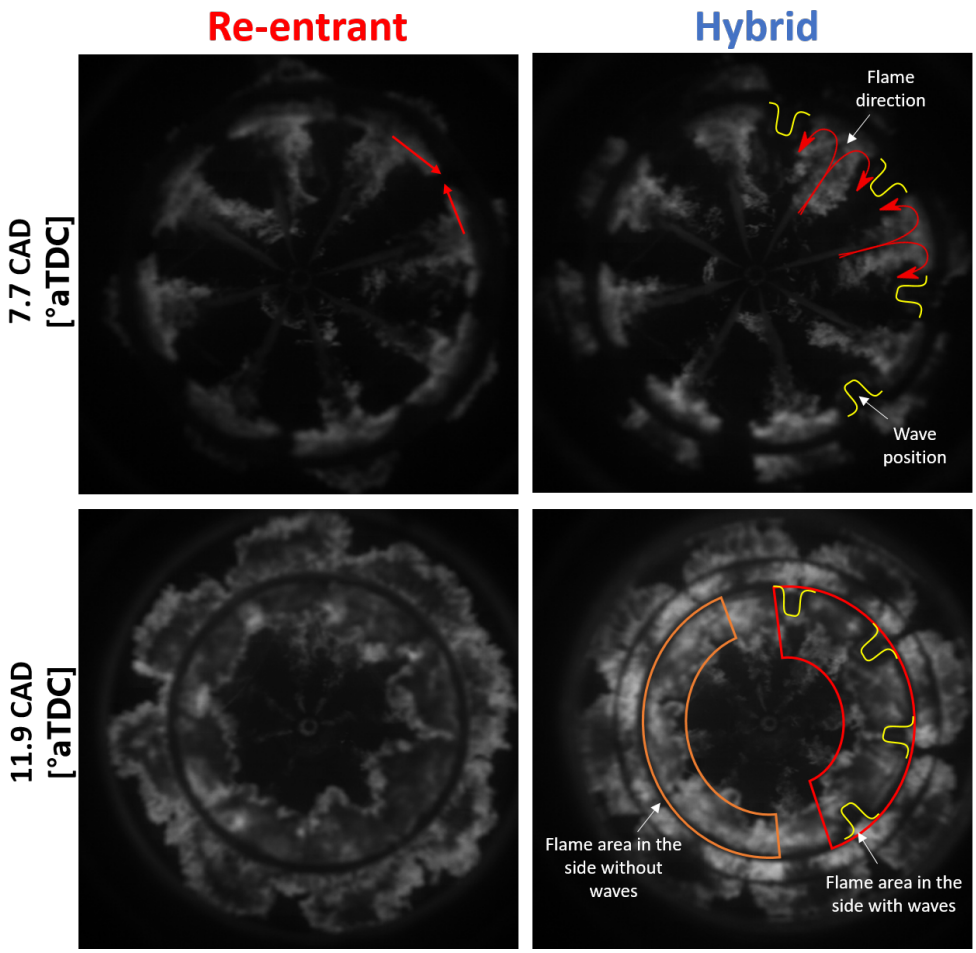

Figure 5.7. *Flame behaviour for the different bowl templates at 7.5 bar IMEP.*

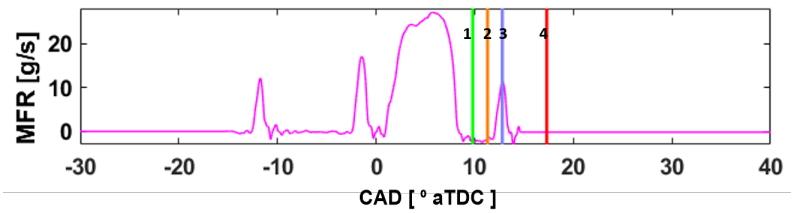

Figure 5.8. *Mass flow rate of injection for the CIV measurements.*

The velocity profile corresponding to a line crossing the center of each piston is also shown in Figure 5.9. This is represented by a green line drawn

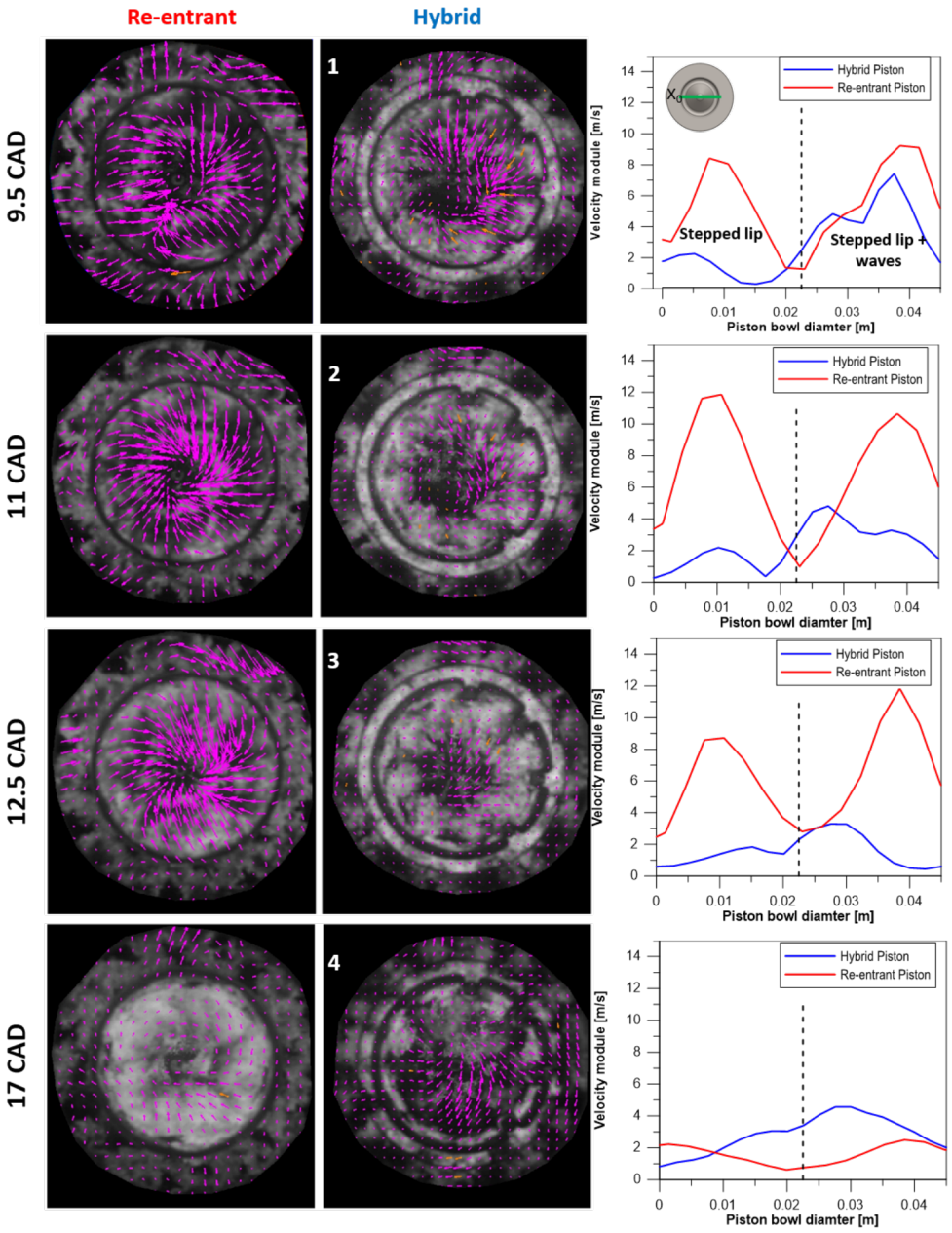

Figure 5.9. *Velocity field analysis for different CADs.*

in the piston sketch. Looking at the plots, the velocity profile shows that the side with wave protrusions promotes higher velocities inside the bowl than the

other side, without waves. In contrast, the velocity profile for the re-entrant piston seems to be very symmetric. At 11 CAD, the behaviour of each piston is different. The re-entrant piston presents high flame velocity but the flow of the hybrid piston starts to slow down, even though the wave side still shows slightly higher velocity values. At 17 CAD, just after the post injection, the re-entrant piston has a global reduction in the velocity and the vectors indicate that the flow seems to be driven only by the swirl motion. In the hybrid piston, the post injection accelerates the flow toward the periphery and the velocity field shows a small increment. For this piston, the typical swirl movement cannot be perceived as intense as for the re-entrant piston (especially in the wave protrusion side).

5.4.3 Combustion evolution

The combustion evolution for each geometry, at 7.5 bar IMEP, is represented in Figure 5.11 by means of NL and OH* chemiluminescence images. For clarification, the mass flow rate has been included again in Figure 5.10, indicating the CAD corresponding to the images shown. Starting at -4.15 CAD, early OH* chemiluminescence can be seen after the pilot 1 injection. The OH* intensity seems to be slightly higher for the hybrid piston and more distributed inside the bowl, corroborating with the RoHR curve presented previously that more intense reactions are taking place at this stage due to the mixing improvement and better air utilization [7]. In contrast, no NL is registered by the camera. At -0.4 CAD, just after the pilot 2, the flame structure for the hybrid piston is more uniform, burning faster (more intense signal) than for the re-entrant piston. Until this instant, no significant differences can be perceived between both sides of the hybrid piston.

After the main injection, at 10.11 CAD, some dark zones start appearing at the NL images of the re-entrant piston. This is just after the collision between the flames at the bowl's periphery. The absence of natural luminosity in these zones could indicate the existence of cold soot as reported in previous studies. The flame cooling, which could occur when the flame touches the cold bowl wall, eliminates hot soot sources in these regions. In addition, OH* chemiluminescence measurements present also a signal attenuation in these zones. The OH* attenuation could be linked with the soot presence which avoids the OH* signal to achieve the camera. At the same time, the higher OH* intensity for the hybrid piston evidences a more intense reaction. This can be related with a better fuel/air mixing process thanks to the flow patterns described previously.

For the hybrid piston, the wave side presents some dark zones too. They are smaller than in the re-entrant case but larger when compared to those observed in the side without waves. Although the flame movement in the wave side is toward the bowl center, the interaction with the colder piston wall could be reducing the flame temperature and consequently generating soot. The low OH* signal located in the same areas coincides with the dark zones present in the NL images. Furthermore, looking at the squish zone, the stepped lip region of the hybrid piston presents higher OH* intensity than the re-entrant piston. The stepped lip splits the spray into two parts. One of this part, and its kinetic energy, heads toward the squish of the piston promoting air-flow movement in this region and improving the air/fuel mixing. This upper portion of spray impinges on cylinder head and spreads toward the bowl and to the cylinder walls from the squish zone with a significant spreading of mixture and turbulence. This effect enhances the air utilization [10].

At 14.61 CAD, the NL intensity increase indicates that soot oxidation for the three geometries is accelerated. However, it is possible to see that the re-entrant geometry still presents dark zones as discussed previously, which corresponds with low OH* signal too. When this piston is compared with the hybrid one, differences in the OH* intensity are remarkable. This reinforces the idea that soot oxidation is occurring faster for both stepped lip and wave-stepped lip geometries. For the wave side, after the flame starts to move towards the center of the bowl, the rich zones with low OH* signal observable at 10.11 CAD disappear. This increase of the OH* intensity indicates that soot oxidation is accelerated. When comparing between the side with and without wave protrusions, it is possible to see that the waves seem to promote areas close to the bowl center with higher OH* signal intensity than the side without waves.

At 37.7 CAD almost no OH* signal is detected for the hybrid piston while a significant combustion process continues occurring in the re-entrant piston. In this sense, during the so-called late-cycle oxidation, both sides of the hybrid piston promote faster oxidation than the re-entrant geometry. This agrees with the conclusions extracted from the RoHR analysis [6, 10]. Furthermore, the OH* chemiluminesence measurements performed by Eismark et al. [9] reported the faster burn out for the wave piston than for the re-entrant one.

To evaluate the potential of the wave-stepped lip side in comparison with the stepped-lip side and the effect of the reverse flow in the combustion process, an extreme condition in terms of soot generation was also tested by applying a low average air/fuel ratio ($\lambda = 1.8$) and removing the post injection. The corresponding combustion evolution is presented in Figure 5.12. At this engine

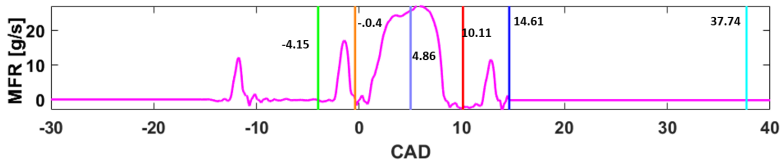

Figure 5.10. *Mass flow rate of the injection at 7.5 bar IMEP.*

condition, the phenomena already presented previously in the reference case were highlighted and new effects could be identified. The effect of reverse flow starts appearing after the spray reaches the bowl wall, where the flame is redirected toward the piston center. At 12.8 CAD, the flame front is closer to the center than in the side without wave protrusions. Eismark et al. [8] reported by using CFD calculations that the wave protrusions are responsible for moving the radial mixing zone, which is located between two adjacent sprays, toward available oxygen in the center of the bowl. A dark U-shaped area, which detaches from the wave protrusion/wall and continues going toward the center, can be observed in the zones highlighted with red lines. This U-shaped area, also reported by Eismark et al. [9], comes from the flame-flame interaction, which occurs later and closer to the bowl center in comparison to the side without waves. In these zones, the oxygen concentration is higher (as they are closer to the center) and the flame-flame collision occurs smoothly, with an incidence angle higher than 0 degrees. It is important to highlight that a portion of hot soot, which is located between the waves and attached to the wall, remains stagnant. In the late combustion cycle, most of the oxidation process has already occurred, and just specific areas show NL radiation. In this case, the side without wave protrusion seems to present a bigger area with flame in comparison with the side with the waves, indicating that the wave protrusions provide a faster burn out.

5.5 Soot formation analysis

For the soot formation analysis section, firstly an in-cylinder pressure analysis is presented for the different engine conditions: reference cases (4.5 and 8.5 bar IMEP) and the sweeps of SOE, post injection and EGR at 8.9 bar IMEP for both piston geometries. Following, an analysis and comparison between the re-entrant and hybrid piston by applying 2C pyrometry and OH*chemiluminescence will be performed only for the reference case at 4.5 bar IMEP. The second part of the results section will be focused only on the

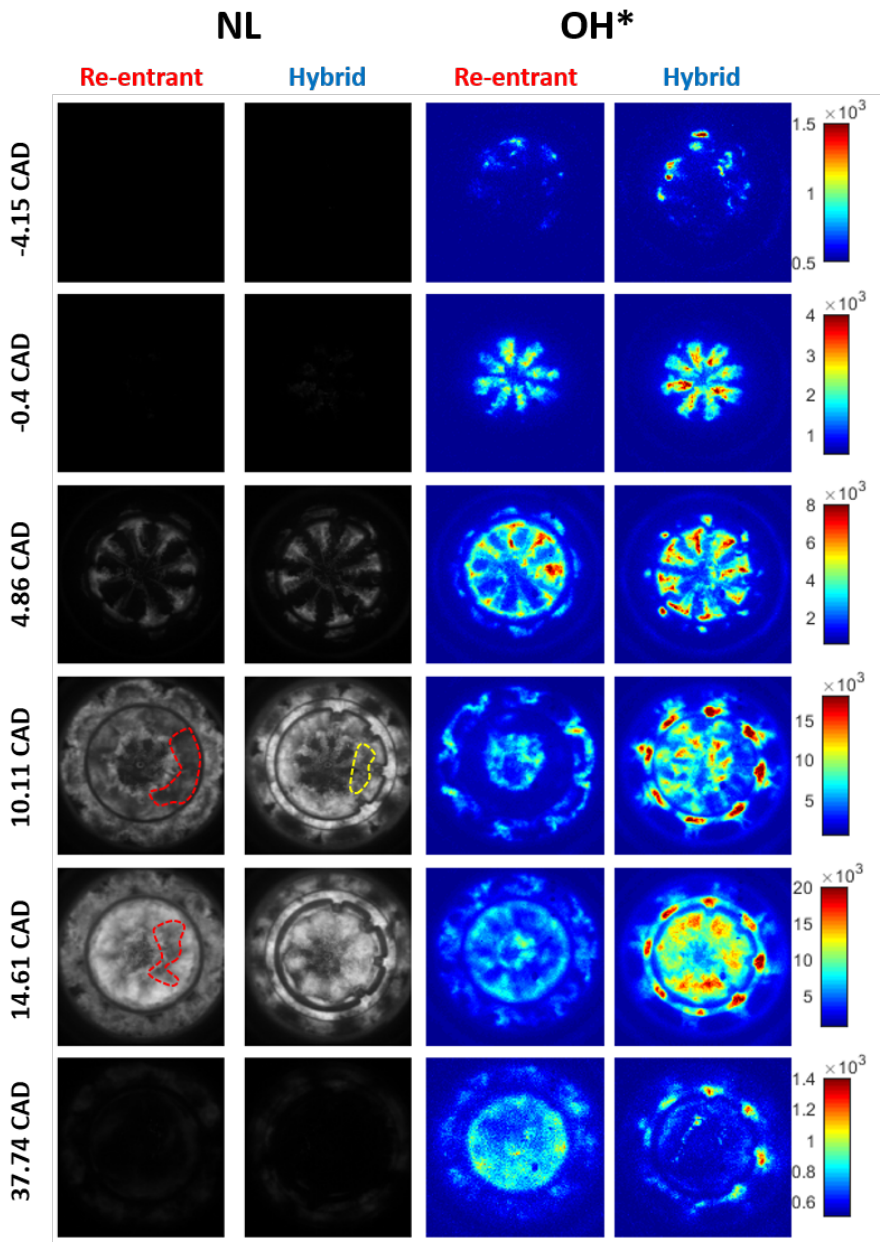

h!]

Figure 5.11. *Combustion evolution from natural luminosity and OH* chemiluminescence technique at 7.5 bar IMEP.*

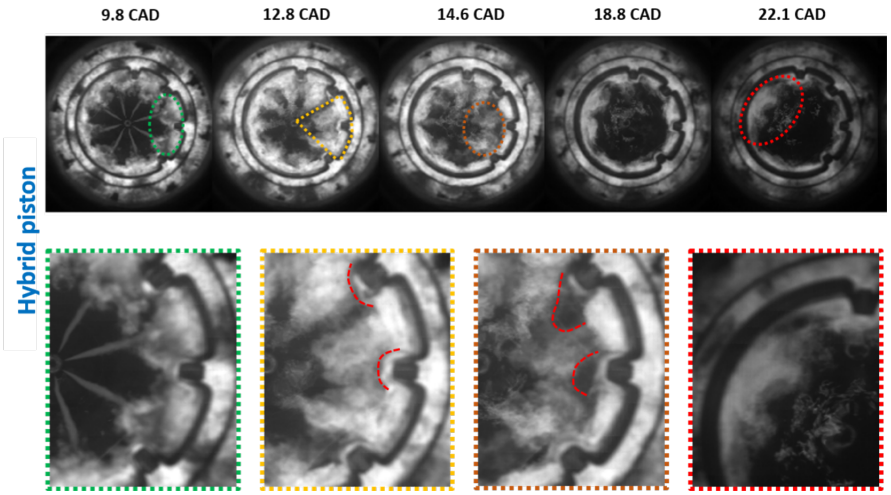

Figure 5.12. *Combustion images of the Stepped-wave lip piston under extreme conditions of soot generation.*

analysis of the hybrid piston, where the main differences due to the sweep of different conditions at 8.9 bar IMEP will be analyzed for stepped lip and stepped lip-wave bowl geometries.

5.5.1 Re-entrant vs Hybrid piston: In-cylinder pressure analysis

The in-cylinder pressure and RoHR for the reference condition as well as for the sweeps of SOE, post injection and EGR are presented in Figures from 5.13 to 5.15. As already shown in the section regarding the flame movement, a satisfactory agreement between the in-cylinder pressure and its evolution for both pistons can be appreciated. In general, the rate of heat release is similar for both pistons. However, still some differences can be detected, following the same trend appreciated in the previous section at 7.5 bar IMEP. For most of the cases, the hybrid piston burns the pilot 1 faster than the re-entrant one, as the RoHR at this stage is higher. However, this effect is not visible for the case of EGR. This suggests that the air-fuel mixing promotion created by the hybrid piston is more efficient with higher oxygen concentrations. Focusing on the main injection, it can be seen again that the corresponding peak is also higher for the hybrid piston. As already explained, this could be related with better air-fuel mixing, which impacts in higher heat released by the main injection. In addition, the RoHR peak for the post injection is lower for the

hybrid piston, indicating less residual of non-burned fuel during the main injection combustion. Finally, at the end of the combustion process, it is possible to see that the RoHR of the hybrid piston decreases faster than for the re-entrant one. This difference is more pronounced in cases without post injection (Figure 5.15, left and right). In these cases, where late oxidation is not accelerated, the higher effectiveness of the hybrid piston to produce late fuel and soot oxidation is visible.

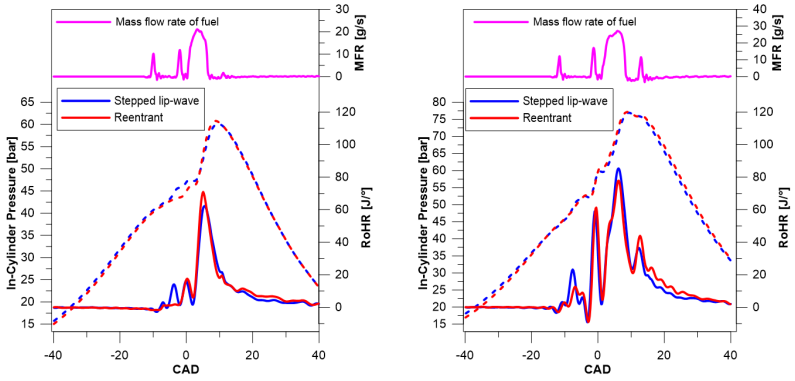

Figure 5.13. *Reference cases: Left: 4.5 bar IMEP and Right: 8.9 bar IMEP.*

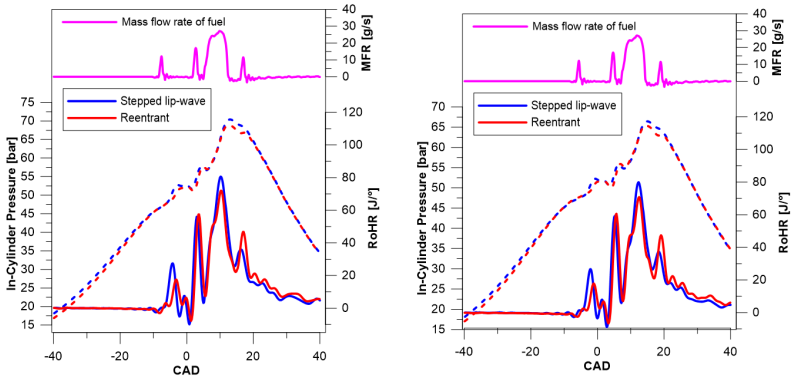

Figure 5.14. *Sweep of SOE at 8.9 bar IMEP: Left: SOE +4 CAD and Right: SOE +6 CAD.*

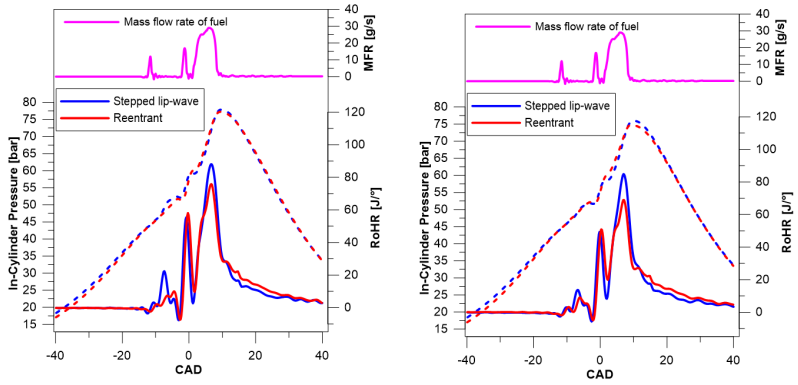

Figure 5.15. *EGR and post injection effect at 8.9 bar IMEP. Left: w/o post injection and Right: w/o post injection and 18 % of* O_2*.*

5.5.2 Re-entrant vs Hybrid piston: OH* chemiluminescence and soot KL analysis

The measurements of soot KL and OH^* chemiluminescence evolution at 4.5 bar IMEP can be seen in Figure 5.16. In general, results show that the soot formation is higher for the re-entrant piston. The high soot concentration on the periphery of the re-entrant bowl is linked with the high momentum induced by the spray injection. The spray reaches the lip and, after that, most of the fuel is directed toward the center and spreads tangentially, promoting strong flame-flame interaction. This leads to the creation of fuel rich zones, which are a key factor in the soot formation process. In contrast, with the hybrid piston, the sprays collide with the stepped lip and are split into two parts. One part of the fuel is sent to the squish region and the rest to the bowl [10]. This allows better air utilization and, as a consequence, reduces the soot pockets present in the late cycle oxidation.

The OH^* signal is an indicator of the high temperature oxidation reactions and its intensity provides qualitative information about the OH^* concentration. In general, the radiation registered for both pistons is similar. However, some differences can be observed. The first one appears at 11.71 CAD. At this instant, the re-entrant piston shows OH^* signal only at the center of the bowl and almost nothing at the periphery. However, the hybrid piston presents OH^* chemiluminescence all around. As the RoHR shows (Figure 5.13), there is still heat release at this stage. Besides, at 16.21 CAD signal is visible again. Therefore, the lack of signal for the re-entrant piston cannot be explained by a lack of oxidation. In fact, it has been related

with the soot content. The higher soot formation for the re-entrant piston causes OH^* signal attenuation within the bowl. Engine conditions, where the soot concentration is high, tend to foul the optical access and attenuate the OH^* signal. [11]. It is possible to see a correspondence between low chemiluminescence and high soot KL. For the hybrid piston, soot levels are lower and OH^* signal attenuation is not so severe.

At the end of the cycle (38.34 CAD) a more intense OH^* chemiluminescence is observed for the re-entrant piston. As soot KL at this stage is much lower or even negligible, no radiation absorption is taking place. Therefore, this difference proves that oxidation reactions are taking place later in the cycle than for the hybrid piston. This is coherent with the differences observed in terms of RoHR. In addition, the KL image shows for the re-entrant piston a soot area that has not yet finished to oxidize, which confirms that late oxidation is slower than for the hybrid piston.

The temporal evolution of the average KL and the accumulated flame radiation intensity registered by one of the high-speed cameras, at 4.5 bar IMEP is shown in Figure 5.17. In this Figure, hybrid piston KL has been split the two geometries and the average calculations were performed by using the same bowl regions shown previously in the methodology section. The same bowl region extension was considered for the re-entrant piston calculation. The curves show significantly higher soot formation for the re-entrant geometry. Besides, the oxidation phase is also slower than for any of the geometries of the hybrid piston, mainly during the late cycle burn-out phase (grey area). These results corroborate with the RoHR curve shown previously. Looking for the accumulated intensity behaviour, the slower oxidation process for the re-entrant piston can be seen even more clearly as the re-entrant piston shows a less steep curve. In addition, for this piston there is a delay between the maximum KL and the maximum intensity, which is caused by the soot self-attenuation. This is characteristic of high soot concentrations [12]. When comparing the stepped lip and stepped lip-wave, the peak KL values are similar. A different trend can be noted during the late cycle oxidation. In this case, the side with wave protrusions seems to oxidize faster than the side without lips.

The spatial and temporal evolution of the soot KL is shown in Figure 5.18. The development methodology of these 2D evolution maps was already explained in the methodology section. The start of energizing of the main injection is indicated by the red discontinuous line. In addition, the start of post injection energizing is represented by the black line. For the re-entrant piston, it can be seen that the KL value decreases smoothly, suggesting that

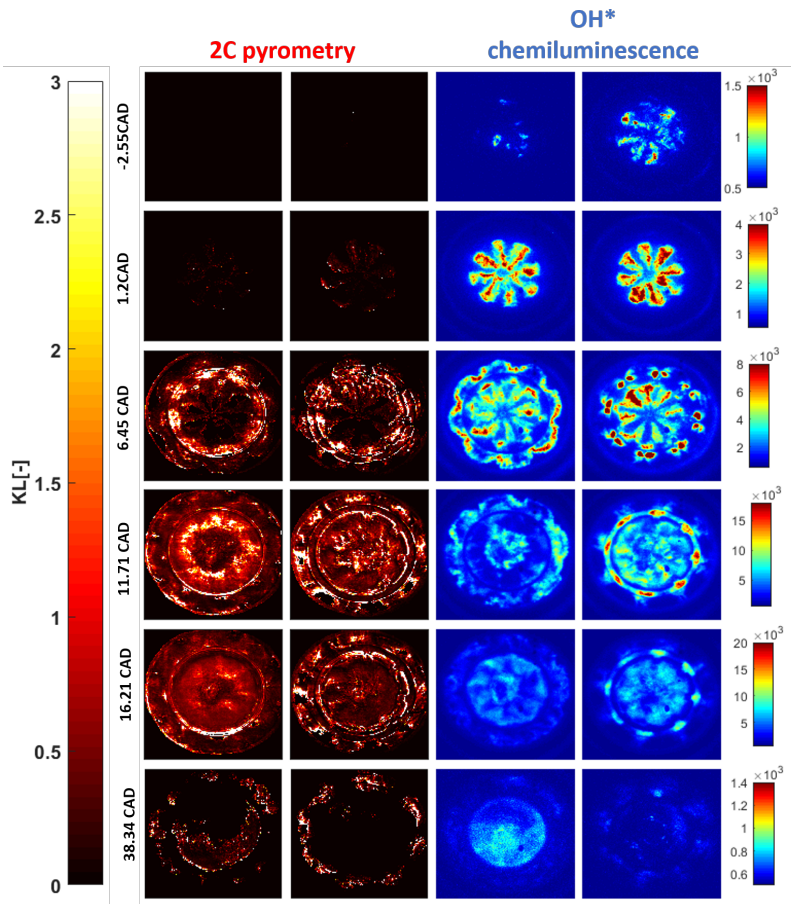

Figure 5.16. *KL and OH* chemiluminescence images at 4.5 bar IMEP.*

the soot oxidation process is slower. In this case, the soot formation goes from the bowl periphery toward the piston center and the areas with high soot concentration are much bigger than for the other two bowl geometries. As already explained previously, the re-entrant piston induces strong flame-flame interaction, promoting high soot formation during the first combustion stages. The swirl movement amplification, as well as, the movement of the flame toward the center occurs thanks to the bowl geometry, which guarantees the oxidation of the soot formed, even if slowly. The reduction of soot formation for the hybrid piston can be seen clearly in the maps. In addition, faster soot oxidation can be seen for both stepped lip and stepped lip-wave sides, which is indicated by abrupt transitions of the colors of the maps. This could be linked with the stepped lip effect as this feature is present at both sides of the

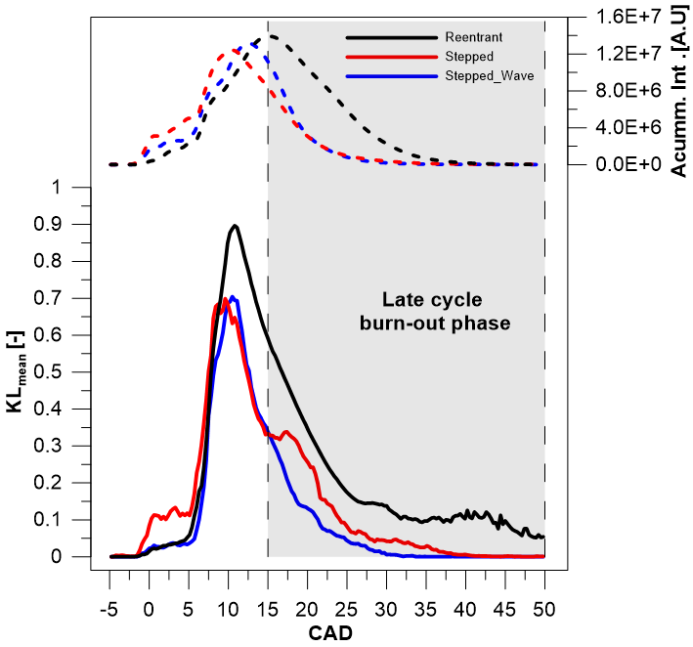

Figure 5.17. *Mean KL and accumulated intensity at 4.5 bar IMEP.*

hybrid piston. In contrast, the differences between stepped lip and stepped lip-wave geometries are less evident than when comparing with the re-entrant piston. The stepped lip bowl promotes fast oxidation during the first stages of the combustion and most of the soot is oxidized efficiently. However, as the combustion process evolves, the oxidation rate seems to decrease. From around 12 CAD to 20 CAD, a soot cloud remains inside the stepped lip bowl during some CADs until be completely oxidized. In contrast, for the stepped lip-wave, the soot is oxidized more efficiently during late-cycle burn out phase, with a faster transition from the high values of KL to the low values, as shown previously in the KL means curves.

5.5.3 Stepped lip vs Stepped lip-wave: soot KL analysis at different engine conditions

The benefits of the hybrid piston in comparison to the re-entrant one have been demonstrated in the previous section. Besides, it has been possible to identify certain differences between the stepped lip and the stepped lip-wave geometries. In the following paragraphs, a deeper analysis of both geometries

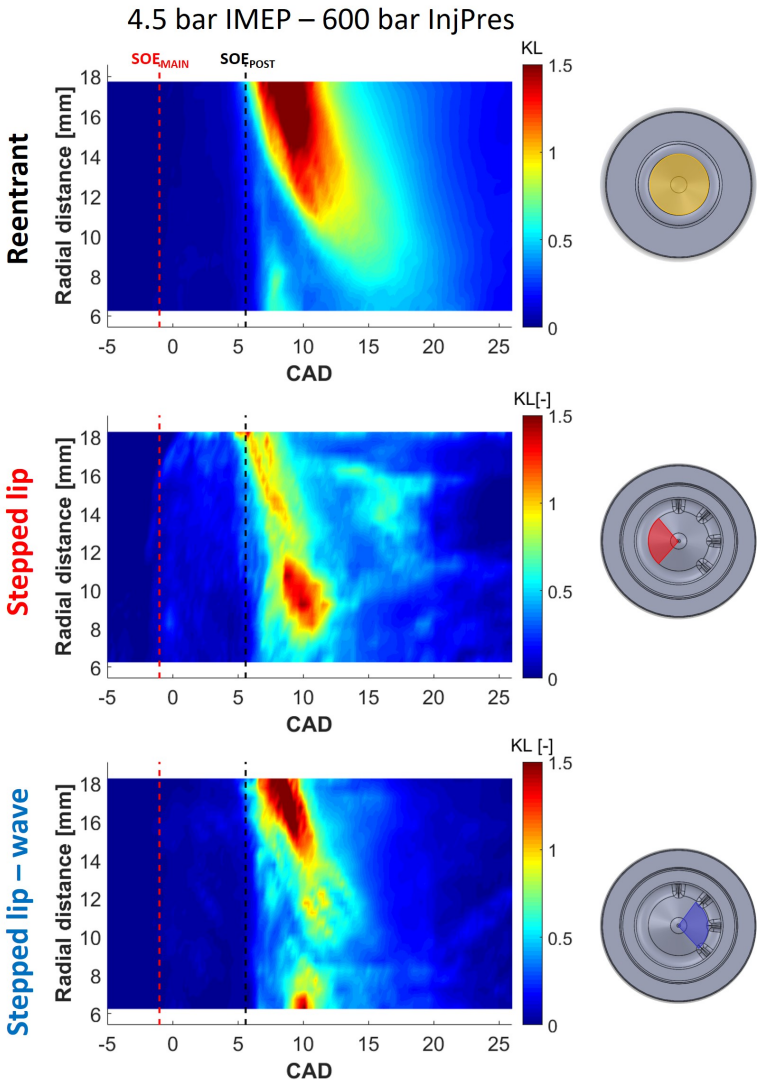

Figure 5.18. *2D evolution maps of KL at 4.5 bar IMEP.*

is performed in a variety of operating conditions where the soot formation is intensified.

5.5.3.1 Sweep of injection pulse train

In order to promote higher soot formation than the reference case and verify the potential of the waves in the soot oxidation process, the engine load was increased to 8.9 bar IMEP and injection pulses were delayed 4 and 6 CAD in relation to the case at 8.9 bar IMEP with similar Original Equipment Manufacturer-(OEM) calibration. The increase of IMEP had the objective to increase the soot formation. In addition, by delaying the fuel injection, in-cylinder pressure and temperature are reduced and consequently, also the mixture reactivity. The temporal evolution of the average KL and accumulated flame radiation intensity for both geometries are shown in Figures 5.19, 5.20 and 5.21, respectively. The maximum soot KL seems to be very similar for both sides of the hybrid piston. In contrast, during the oxidation phase, the stepped lip-wave side is clearly promoting faster soot oxidation, as it presents a steeper reduction. For the case without pulse delay Figure 5.19, this effect is not so evident. In contrast, the effect of the waves is more pronounced when the injection timing is delayed. The same behaviour can be appreciated in the accumulated intensity curves.

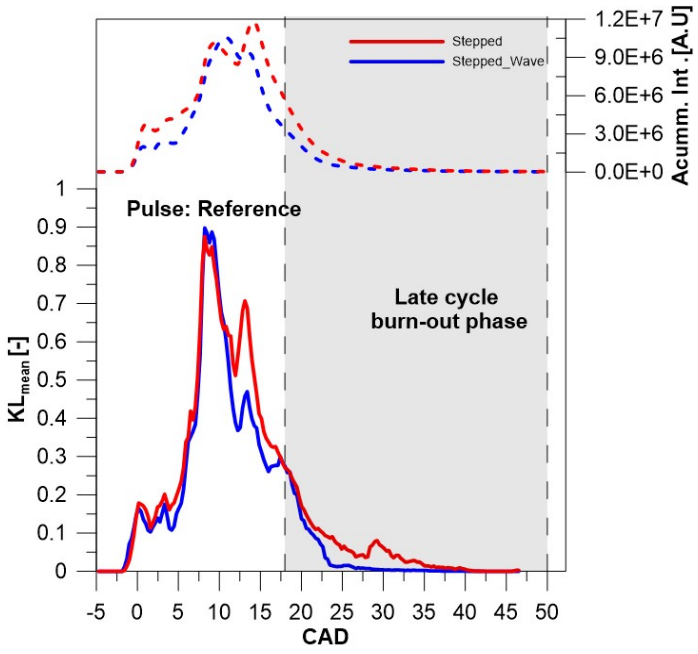

Figure 5.19. *Mean KL and accumulated intensity for reference pulse at 8.9 bar IMEP.*

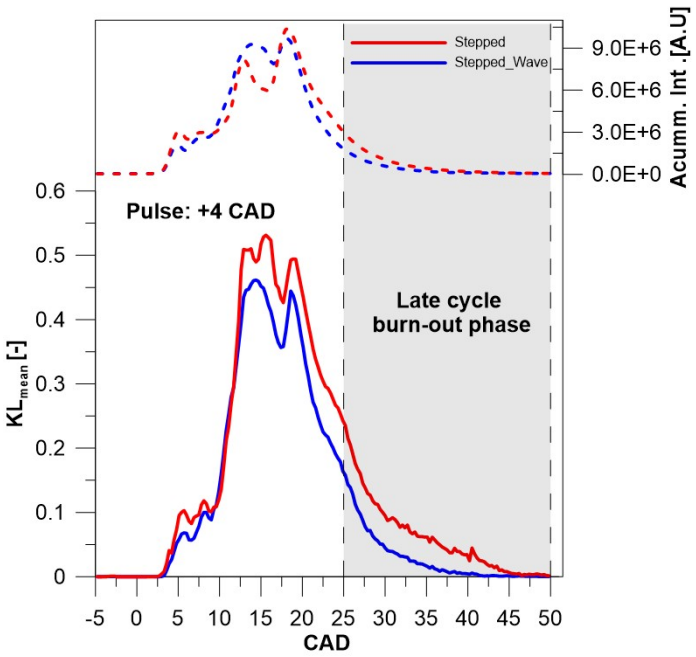

Figure 5.20. *Mean KL and accumulated intensity for 4 CAD of pulse delay at 8.9 bar IMEP.*

The Figure 5.22 shows soot KL evolution after the post injection has finished for the cases where the start of injection was delayed +4 and +6 CAD. In general, it is possible to see that the soot inside the bowl is slightly higher for the stepped lip side (left). In addition, the images show that the oxidation for the side without waves is slower. At 29.7 CAD, still a big soot area remains at the stepped lip side while much less soot is visible at the side of the waves (right).

The corresponding spatial and temporal evolution of soot KL for both sides of the hybrid piston is shown in Figure 5.23. They confirm the faster soot oxidation for the stepped lip-wave, as the KL values decrease faster along the corresponding part of the bowl. Besides, it can be highlighted, mainly for the injection delay cases that the stepped lip-wave side presents at first higher soot levels located at the bowl periphery. This could be related with the moment when the flame interacts with the waves and wall (cold surfaces), increasing momentarily the soot formation. However, the effect of redirecting the flame toward the center provides a rapid oxidation of this soot. As the flame is closer to the center, the KL value is lower. For the other side, without waves, the behaviour is different. The soot seems to be uniformly distributed inside

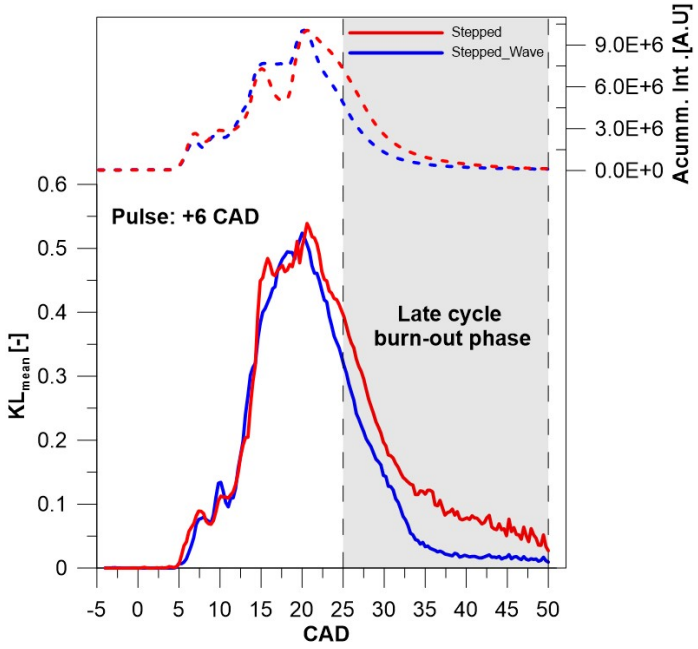

Figure 5.21. *Mean KL and accumulated intensity for 6 CAD of pulse delay at 8.9 bar IMEP.*

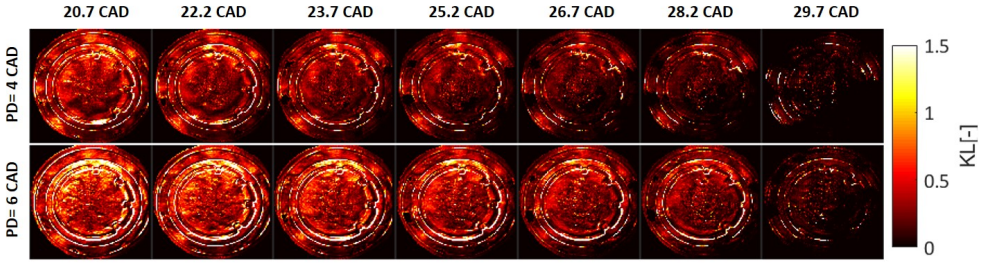

Figure 5.22. *KL images at 8.9 bar IMEP for 4 CAD and 6 CAD pulse delay.*

the combustion chamber, with higher values from the periphery to the bowl center. Thus, in this application the wave influence corroborates with previous results reported by Eismark et al [8]. These authors reported that the waves induced a change in the flame shape, which generates better oxygen supply for all flame regions. The same behaviour can be seen for both conditions tested.

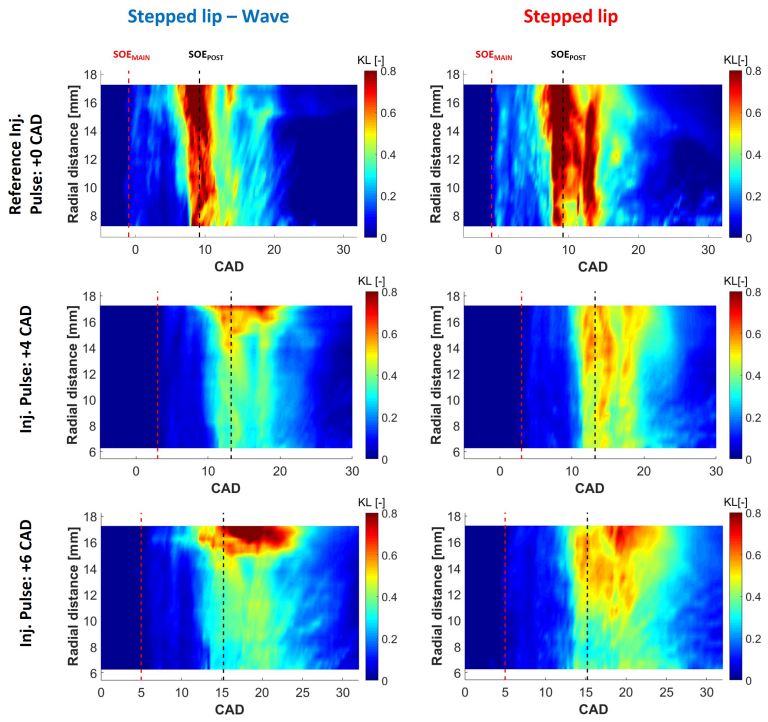

Figure 5.23. *2D evolution maps for SOE sweeps at 8.9 bar IMEP.*

5.5.3.2 Effect of piston geometries with EGR

All the operating conditions previously analyzed include the use of post injection. It is widely known that it improves the soot oxidation at the late stages of combustion. Besides, most of the commercial compression ignition engines use EGR. The main objective of this technology is to reduce the NOx formation, but it also reduces the soot oxidation. In this way, high sooting conditions were also reproduced by removing the post injection and using EGR. In Figures 5.24 and 5.25, the evolution of accumulated flame intensity and average KL are shown for 8.9 IMEP, with and without EGR respectively. In both cases, no post injection was used. Under these conditions, the stepped lip-wave side continued showing the same characteristics reported when the post injection is used. Both piston sides, with and without waves, present similar maximum KL peak during the diffusion combustion phase, when the main injection is still occurring. However, clear differences can be appreciated during the late cycle oxidation, with significantly faster oxidation for the stepped lip-wave side. In addition, at low oxygen concentration (EGR), the

stepped lip side showed a higher difficulty to promote the oxidation of soot formed during the first combustion phase. In both cases, when the injection event ends and the KL values start to decrease, the stepped lip KL curves seems to change its slope, reducing the rate of soot oxidation.

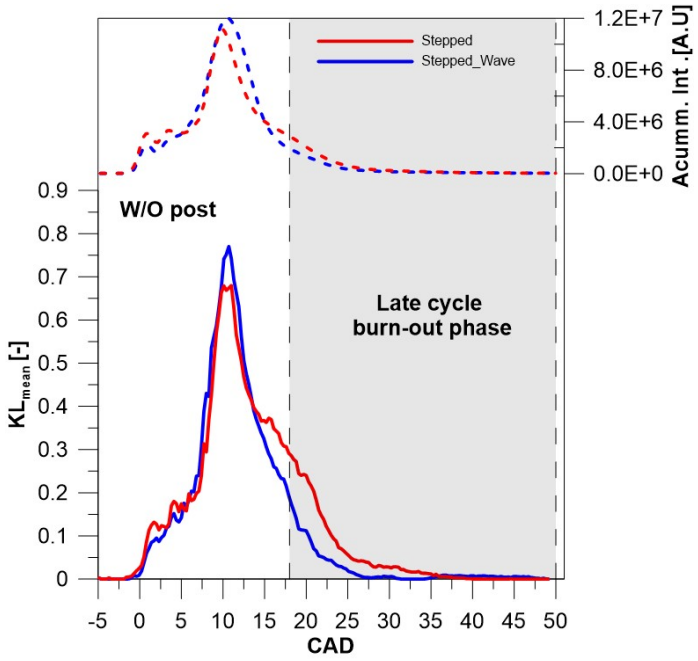

Figure 5.24. *Mean KL and accumulated intensity for the case w/o post injection.*

The Figure 5.26 shows the KL spatial distribution for both conditions (with and without EGR) after the main injection ends. The benefits of the wave protrusions are visible, even under high soot conditions. For both cases, the stepped lip-wave (right bowl side) always presents less area covered by soot than the side without waves (left bowl side). What is more, it is possible to state that differences between both geometries are bigger when the oxygen concentration is reduced using EGR.

When looking at the 2D maps in Figure 5.27, where the temporal and spatial evolution of these two conditions are represented, it is clear that initially a higher soot formation occurs for the side with waves. However, this higher concentration of soot, which is probably caused by the interaction between flame and the waves protrusions, is rapidly oxidized. This indicates that the waves are assisting the flame in finding fresh oxygen zones in an

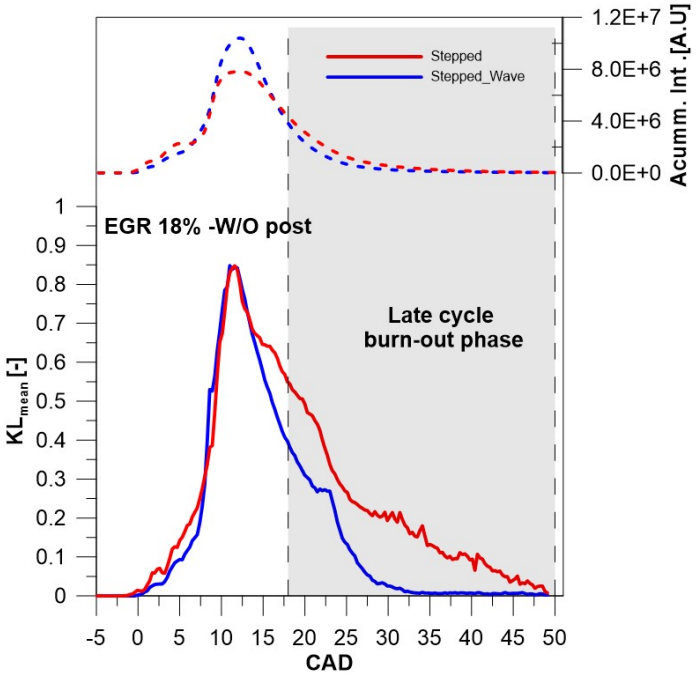

Figure 5.25. *Mean KL and accumulated intensity for the case with EGR and w/o post injection.*

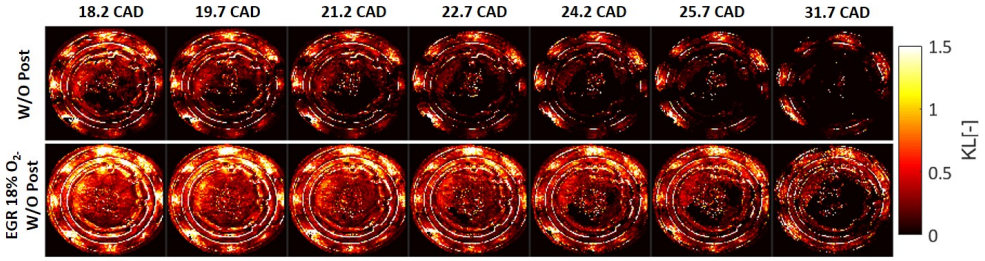

Figure 5.26. *KL images at 8.9 bar IMEP for the case w/o post injection and for the case with EGR.*

efficient way, improving the oxidation process. As the combustion evolves, it is possible to see that the area of the map covered by the soot cloud is higher for the side without waves.

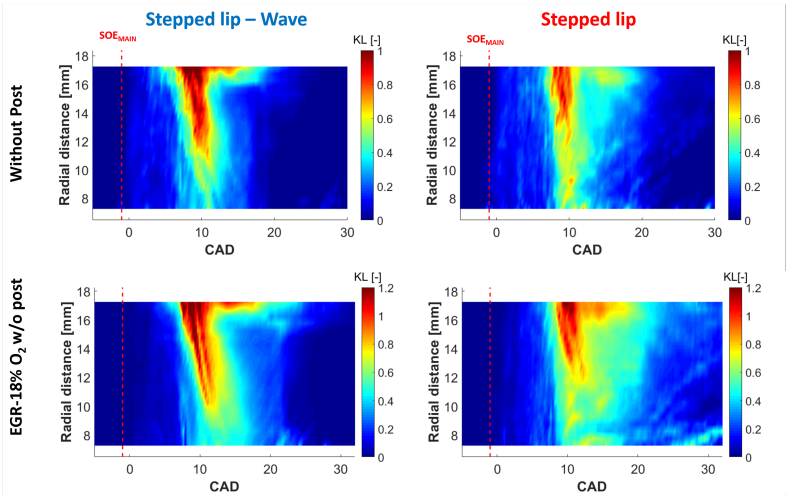

Figure 5.27. *2D evolution maps for the case w/o post injection and for the case with EGR.*

5.6 Summary & conclusions

The current chapter had the objective of evaluating the combustion process and soot formation in three different bowl templates (re-entrant, stepped lip and stepped lip-wave) in an optical light-duty diesel engine. For supporting the analysis, it was employed a variety of optical techniques. The natural luminosity as well as the CIV technique were applied with the intention of characterizing the flame movement in each piston and identifying the main differences between them. The OH^* chemiluminescence helped in identifying the high temperature and near-stoichiometric zones of the flame inside of each bowl piston. Finally, the 2-color pyrometry was employed for quantifying the soot formation and understanding how is the oxidation process in each piston geometry tested. In addition, an in-cylinder pressure analysis was performed for getting the thermodynamic information about the combustion process. The main findings are summarized as follows.

Regarding the analysis of the flame movement, it can be stated that:

- The thermodynamic analysis shows that the hybrid piston causes a faster fuel burn, especially visible for the pilot injections, and faster late soot oxidation. However, almost no differences are visible during the main injection and combustion event.

- The wave protrusions induce a reverse flow of the flames towards the bowl center. For the side without waves, the flames seem to stay at the periphery of the bowl contributing to the existence of rich fuel zones. Besides, the flame-flame collision is smoothed when the flame is driven by this geometry, avoiding frontal collision as it happens in the side without the protrusions and re-entrant piston.

- The velocity field in the re-entrant geometry presents higher velocity values than both sides of the hybrid piston. In the first case, the kinetic energy of the spray is kept inside the bowl. In the second case, spray (and its kinetic energy) is split as in the wave-stepped lip piston.

- The wave protrusions direct the flames towards the bowl center, as it is represented by the velocity fields obtained for this geometry. Besides, this effect results in higher velocity values for the wave-stepped lip side than for the side without them.

- The wave-stepped lip geometry shows higher $OH*$ signal than the re-entrant geometry at this stage. This indicates the presence of larger near-stoichiometric zones, resulting in a faster soot oxidation. Additionally, OH^* signal extinguishes earlier which confirms the end of chemical reactions. When comparing both geometries of the hybrid piston, during late oxidation, the side with waves seems to promote areas close to the bowl center with higher OH^* signal intensity than the side without waves.

- The reference case highlights the differences in terms of soot formation between the re-entrant and hybrid piston. A significant soot reduction, as well as a faster soot oxidation could be appreciated for the stepped lips and stepped lip-wave geometries in comparison with the re-entrant bowl.

Regarding the soot formation, it can be stated that:

- The reference case highlights the differences in terms of soot formation between the re-entrant and hybrid piston. A significant soot reduction, as well as a faster soot oxidation could be appreciated for the stepped lips and stepped lip-wave geometries in comparison with the re-entrant bowl.

- The sweep of SOE and EGR potentiated the effect of the waves. The mean KL and accumulated intensity curves always showed a faster

soot oxidation for the stepped lip-wave side. In addition, the 2D evolution maps show that the wave protrusions initially produce more soot. However, they promote a faster soot oxidation. Without regard to the region close to the bowl wall, the wave side presents lower KL values than the other side of the piston.

- At the final stages of combustion, the stepped lip-wave side always presents less area covered by soot than the side without waves.

Bibliography

[1] Xuan Tiemin, Pastor José V., García-Oliver José M., García Antonio, He Zhixia, Wang Qian and Reyes Miriam. "In-flame soot quantification of diesel sprays under sooting/non-sooting critical conditions in an optical engine". *Applied Thermal Engineering*, Vol. 149 n^o 301, pp. 1–10, 2019.

[2] Pastor José V., García Antonio, Micó Carlos, Möller Sebastian and García-Oliver José M. "Application of optical diagnostics to the quantification of soot in n -alkane flames under diesel conditions". *Combustion and Flame*, Vol. 164, pp. 212–223, 2015.

[3] Kurtz Eric M. and Styron Joshua. "An Assessment of Two Piston Bowl Concepts in a Medium-Duty Diesel Engine". *SAE International Journal of Engines*, Vol. 5 n^o 2, pp. 344–352, 2012.

[4] Zha Kan, Busch Stephen, Warey Alok, Peterson Richard C. and Kurtz Eric. "A Study of Piston Geometry Effects on Late-Stage Combustion in a Light-Duty Optical Diesel Engine Using Combustion Image Velocimetry". *SAE International Journal of Engines*, Vol. 11 n^o 6, pp. 783–804, 2018.

[5] Dolak Jonathan George, Shi Yu and Reitz Rolf. "A computational investigation of stepped-bowl piston geometry for a light duty engine operating at low load". *SAE Technical Papers*, 2010.

[6] Busch Stephen, Zha Kan, Perini Federico, Reitz Rolf, Kurtz Eric, Warey Alok and Peterson Richard. "Bowl Geometry Effects on Turbulent Flow Structure in a Direct Injection Diesel Engine". *SAE Technical Papers*, Vol. 2018-Septe, 2018.

[7] Dahlstrom Jessica, Andersson Oivind, Tuner Martin and Persson Håkan. "Experimental Comparison of Heat Losses in Stepped-Bowl and Re-Entrant Combustion Chambers in a Light Duty Diesel Engine". *SAE Technical Papers*, 2016.

[8] Eismark Jan, Andersson Mats, Christensen Magnus, Karlsson Anders and Denbratt Ingemar. "Role of Piston Bowl Shape to Enhance Late-Cycle Soot Oxidation in Low-Swirl Diesel Combustion". *SAE International Journal of Engines*, Vol. 12, apr 2019.

[9] Eismark Jan, Christensen Magnus, Andersson Mats, Karlsson Anders and Denbratt Ingemar. "Role of fuel properties and piston shape in influencing soot oxidation in heavy-duty low swirl diesel engine combustion". *Fuel*, Vol. 254 n^o December 2018, pp. 115568, 2019.

[10] Busch Stephen, Zha Kan, Kurtz Eric, Warey Alok and Peterson Richard. "Experimental and Numerical Studies of Bowl Geometry Impacts on Thermal Efficiency in a Light-Duty Diesel Engine". *SAE Technical Paper Series*, Vol. 1, pp. 1–12, 2018.

[11] Rochussen Jeremy, McTaggart-Cowan Gordon and Kirchen Patrick. "Parametric study of pilot-ignited direct-injection natural gas combustion in an optically accessible heavy-duty engine". *International Journal of Engine Research*, Vol. 21 n^o 3, pp. 497–513, mar 2019.

[12] Pastor José V., García-Oliver José M., García Antonio, Micó Carlos and Möller Sebastian. "Application of optical diagnostics to the quantification of soot in n-alkane flames under diesel conditions". *Combustion and Flame*, Vol. 164, pp. 212–223, 2016.

Chapter 6

Potential of e-fuels for fossil diesel replacing: An optical analysis

Contents

6.1 Introduction

This chapter is focused on applying e-fuels as the alternative for reducing the in-cylinder soot formation and achieving both cleaner combustion and fossil-fuel dependency reduction. Moreover, in this current thesis, e-fuels are

considered also a promising way for reducing the carbon dioxide footprint. In order to better understand the combustion process of e-fuels and evaluate their potential for soot reduction, an optical investigation in a single cylinder optical diesel engine together with different optical techniques was carried out.

The present study is divided into two parts. The first one has the objective of analysing the utilization of two different e-fuels types in pure form: neat Fischer-Tropsch (FT) diesel and Oxymethylene dimethyl ether (OME_X). In this case, three different optical techniques are applied simultaneously in the analysis. Natural luminosity and OH* chemiluminescence were used for the evaluation of the combustion process evolution and identification of zones where air/fuel ratio is close to the stoichiometric or not. Finally, 2C pyrometry is used for quantifying the soot formation inside the combustion chamber.

Once the test by using e-fuels in the pure form is done, the second part is performed. It aims firstly to identify if the flame radiation emitted by the OME_X comes from the soot incandescence or from the chemiluminescence of chemical species. Secondly, this part has the objective of defining an optimum substitution rate of diesel mass in OME_X without increasing or penalizing the soot formation. The blends considered in the work are 10 %, 20 %, 30 % and 50 % of diesel mass in OME_X. The pure form of each fuel, diesel and OME_X, was also tested. For this purpose, three optical techniques are employed: natural luminosity imaging, high-speed emissions spectroscopy and 2-color pyrometry. In addition for both parts of the study, a thermodynamic analysis was also performed.

6.2 FT diesel and OME_X potencial: An optical analysis

6.2.1 Optical Setup

For this first part of the study, a specific optical setup was mounted in the test cell of the optical engine, as is represented in figure 6.1. By using this array of cameras, the flame radiation that comes from the bottom piston (main optical access) can be registered by the three optical techniques (natural luminosity, OH* chemiluminescence and 2C pyrometry) simultaneously. In order to recover the light from the flame, a 45◦ mirror is positioned just below the optical access of the piston. It reflects all flame light from the combustion towards the optical system. To make possible the three optical systems to receive the flame light, a set of optical devices are employed. Firstly,

a dichroic mirror is positioned just before the cameras with the objective of transmitting the natural luminosity radiation (up to 750 nm) and reflecting the UV radiation. The UV radiation, which is reflected, goes toward the intensified camera, located at 180◦ relative to the engine crankshaft. This is the camera responsible for performing the measurements of the $OH*$ chemiluminescence. The portion of light transmitted by the dichroic mirror goes toward a beam splitter. This optical element is in charge of transmitting 50 % of the incident light and reflecting the other 50 %. In this way, the other two cameras of the optical setup receive the flame radiation that comes from the combustion chamber. One of them was equipped with a 660 nm filter, which is used for both 2-color measurements as well as for the natural luminosity imaging. The other one was equipped with a 550 nm filter, which was used for 2-color pyrometry.

In the OH* chemiluminescence measurements, an Andor Solis iStar ICCD intensified camera was employed. An UV objective with a 100 mm focal length f/2 lens and a 310 nm $\pm$ 10 nm bandpass filter is coupled in the camera. The spatial resolution was 8.75 pixel/mm. The gain used in the camera was kept the same for all fuels tested, allowing a direct comparison between them. The natural luminosity images were collected with a Photron SA-5 high speed CMOS camera. Different exposure time was set for each tested fuel due to the high differences in terms of flame radiation intensity. For fossil diesel and FT diesel an exposure time of 6.65 μs was used, while for OME_X, an exposure time of 35.5 μs was set. The images have a resolution of 512 x 512 pixels with a spatial resolution of 8.1 $pixels/mm$. By using this image resolution, the maximum frame rate allowed was 25 kfps and it was used for all tests performed. Finally, for the 2C measurements, two Photron SA-5 high speed CMOS cameras were employed. One of the cameras was equipped with an interference filter of 660 nm with 10 nm FWHM and another one with an interference filter of 550 nm with 10 nm FWHM as well. An objective with 100 mm focal length and f/2 was coupled in each camera. Images were recorded at 25 kfps with an exposure time of 6.65 μs for the 660 nm camera and 10.05 μs for the 550 nm camera.

6.2.2 Operating conditions

This first part of the work was performed for three different engine loads (1.5 bar, 4.5 bar and 7.5 bar IMEP) and a constant engine speed of 1200 rpm. For each IMEP, the intake pressure and intake temperature were changed and they are represented in table 6.1. For simulating the backpressure in

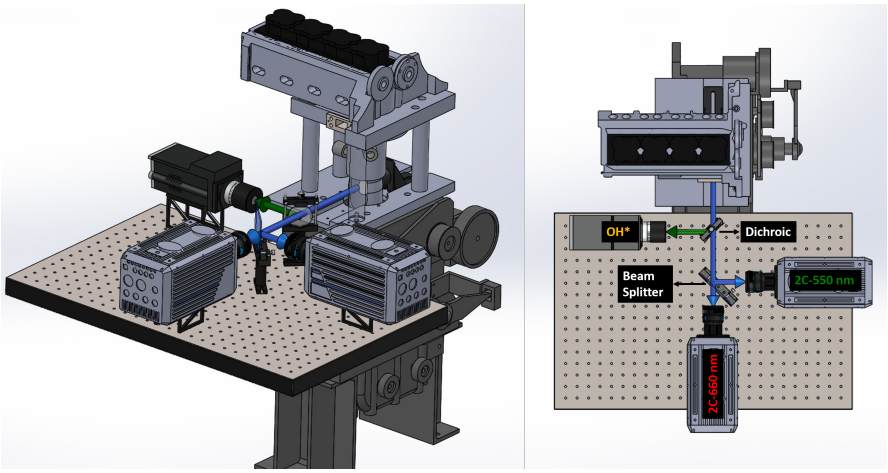

Figure 6.1. *Optical setup for analysing FT diesel and OME_X potential.*

Inj. Pattern	Engine Speed	IMEP (bar)	Pint (Bar)	Tint (◦C)	Toil (◦C)	Tcool (◦C).
Mult.	1250	1.5	1.5	100	60	15-25
		4.5	1.9	90		
		7.5	2.15	90		

Table 6.1. *Engine operating conditions.*

the exhaust system, the exhaust pressure was kept 0.2 bar higher than intake pressure.

For the present study, an injection strategy with 4 injection events, including 2 pilots, a main and a post injection was employed. This strategy is based on original equipment manufacturer (OEM), which is used for calibrating the metal version (GM 1.6 L) of this optical version. In addition, different authors have studied similar strategies. As the engine IMEP was increased, the injection pressure was increased as well (400, 670 and 800 bar). For all fuels tested, it was tried to keep the same IMEP and similar CA50. Considering that the fuel properties like LHV and cetane number are different, variations on the injection duration and timing were applied for each fuel. As already commented in previous chapters, the engine was run under skip fire mode, where one combustion cycle every twenty cycles was performed. In table 6.2 is represented the different injection timings used for each engine load and fuel.

Fuel	IMEP [bar]	Inj. Pressure [bar]	Injection timing [CAD]			
-	-	-	Pilot 1	Pilot 2	Main	Post
diesel	1.5	400	-14.65	6.36	-2.2	4.46
	4.5	670	-14.1	6.36	-2.2	7
	7.5	800	-16.55	-6.36	-2.2	8.06
FT diesel	1.5	400	-13.5	-6.15	-2.2	3.825
	4.5	670	-13.44	-6.7	-2.2	6.7
	7.5	800	-15.45	-6.66	-2.2	7.95
OMEX	1.5	400	-13.5	-6.15	-2.2	6.825
	4.5	670	13.44	-6.7	-2.2	9.18
	7.5	800	-15.45	-74	-2.2	10.5

Table 6.2. *Injection timings.*

6.2.3 Results

For the results of the first part of this current chapter, it will be presented the analysis of the three fuels based on the three optical techniques applied. In order not to become the explanation of results repetitive in this subsection, the discussion will be performed in detail for the conditions of 7.5 bar IMEP, where the images and conclusions will be compared with the previous results that have been found in the literature. The main results from the engine conditions of 1.5 and 4.5 bar IMEP will be summarized at the end of this subsection.

6.2.3.1 Injection rate measurements

The injection rate measurements for the condition at 7.5 bar IMEP can be seen in figure 6.2. In order to get a similar RoHR curve and consequent similar CA50 for the three fuels, the SOE of each fuel has been modified. For the FT diesel and OME_X, the injection of the pilot 1 was delayed in comparison with diesel with the objective of compensating the differences in the reactivity of the fuels. Regarding pilot 2, a slight delay of SOE is applied for the diesel. During the main injection, the same SOE is used for three fuels. The energizing time (ET) of the main is shorter for the FT diesel than the fossil diesel for keeping the same engine IMEP. In contrast, for the OME_X, due to its lower LHV, a larger ET is required (around two times the one used for the

other fuels). In addition, the behaviour of the injector seems to be different when using OME_X. In figure 6.2 can be seen that dwell time between the end of the main injection and the start of the post injection is kept always the same. This is the reason that the post injection for the OME_X occurs later in terms of CAD. Considering this, it is clear that once the ET for the OME_X injection has finished, the injector takes much more time for closing. The post injection seems to happen immediately after the main injection. The lower viscosity and higher density could be pointed out as the reason for this different behaviour. The sequence of natural images in figure 6.4, which are shown in the next section of the results, confirms this as well.

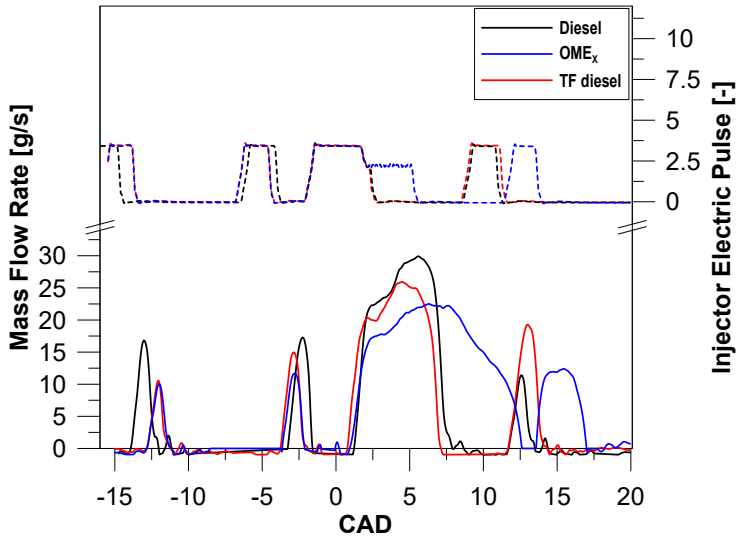

Figure 6.2. *Mass flow rate and injector electric pulse at 7.5 bar of IMEP.*

6.2.3.2 Natural luminosity and rate of heat release analysis

In figures 6.3 and 6.4 are shown the RoHR and natural luminosity images of the combustion evolution at 7.5 bar IMEP respectively. Regarding the figure of natural luminosity, it is important to highlight that the range of light intensity displayed for each fuel is different. The maximum light intensity for FT diesel and fossil diesel reaches 2500 while for OME_X the maximum is around 400. Moreover, during the tests with OME_X, it was necessary to remove the interference filter in front the camera to be possible to register some

radiation signals. This very low light intensity from the OME_X combustion, which will be discussed in detailed later, suggests less soot formation.

From the RoHR diagram, it is possible to appreciate that the pilot 1 starts to burn earlier when using FT diesel and OME_X, even if the injection event for both fuels occurred later than the injection for fossil diesel. The higher cetane number of these two fuels in comparison with diesel could be related with this shorter ignition delay. At -1.6 CAD, where the first natural luminosity images are shown, the pilot 2 injection has already started to burn for the three fuels, even if for the fossil diesel, the pilot 2 starts to burn slightly delayed. At this instant, no significant light radiation can be observed for the three fuels.

When the combustion of the main injection takes place, from 4 CAD until 6 CAD, the RoHR is similar for the three fuels. Looking the NL images for this time interval, there is no differences in terms of radiation intensity as well as flame distribution between FT diesel and fossil diesel, indicating the same combustion behaviour for both fuels. On the contrary, OME_X releases much less radiation in comparison with the other two fuels, as already commented in the previous paragraphs. In addition, the distribution of the flame light inside the piston bowl is more uniform for the case with OME_X. The lower viscosity of the OME_X causes an improvement of the spray atomization and a consequent improvement of the air/fuel mixture, as already reported in previous studies [1]. In the same way, the high oxygen content in the OME_X molecule acts improving the oxygen/carbon ratio inside the combustion chamber. These specific characteristics help in reducing the formation of rich zones of fuel, avoiding the existence of local high soot concentration inside the bowl.

Some dark regions can be appreciated inside the bowl at 9 CAD, when using fossil diesel. These same regions, close to the bowl wall, was already reported in previous work [2] as the cold soot (without light radiation) present in the flame. On the other hand, these dark zones can not be observed when FT diesel is burning, suggesting that the soot present inside the bowl is hotter than the case with fossil diesel. This part will be analysed later, in the results obtained from the 2C pyrometry measurements. At this instant (9 CAD), fossil diesel and FT diesel have already finished the main injection event, while OME_X continues injecting due to its larger ET. This can be noted in RoHR diagram, where the OME_X is still releasing a higher amount of energy in comparison with the other two fuels.

The post injection event and the late-cycle oxidation process is represented by the images from 13.5 CAD until 25 CAD. The most important thing that

can be highlighted during this period is that the FT diesel oxidises faster than fossil diesel as the decrease of the natural luminosity is faster.

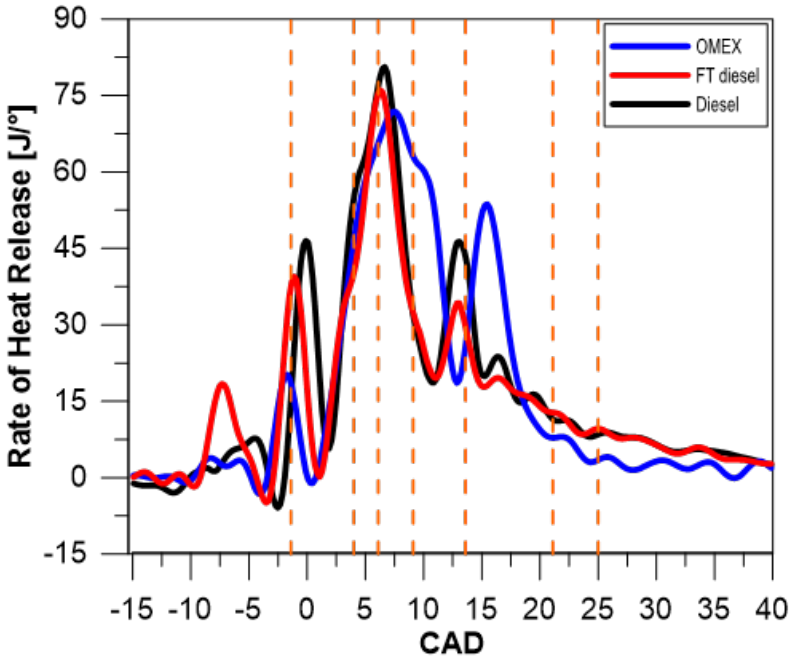

Figure 6.3. *RoHR diagram for each fuel at 7.5 bar IMEP.*

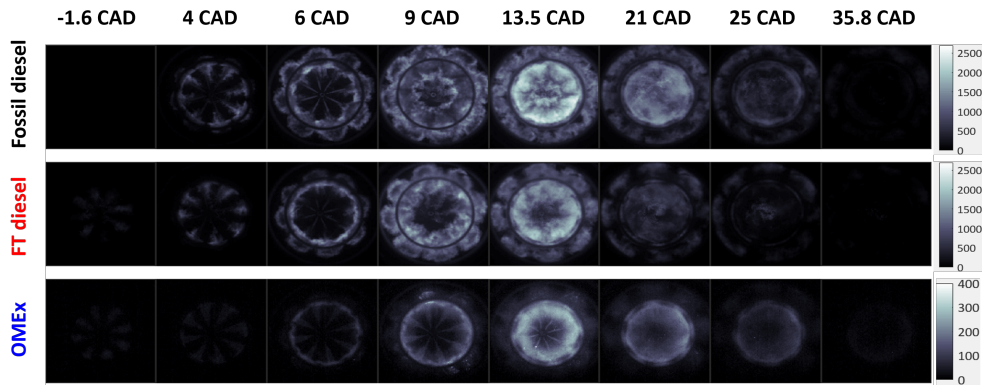

Figure 6.4. *NL images of the combustion evolution for different crank angle degrees and fuels at 7.5 bar IMEP.*

The accumulated intensity curves for the three fuels at 7.5 bar IMEP, which are shown in figure 6.5, represent the overall behaviour of each fuel tested. The faster oxidation for the FT diesel in comparison with fossil diesel

can be appreciated also in this image. In addition, the accumulated intensity curve of OME_X confirms that its radiation intensity is much lower than the other two fuels. Despite the largest injection duration for OME_X, the RoHR curve and the NL confirm that its combustion duration is shorter.

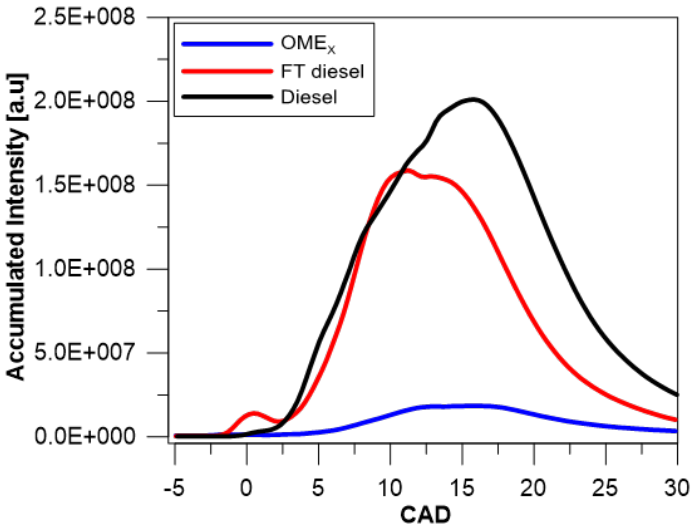

Figure 6.5. *Accumulated intensity for each fuel at 7.5 bar IMEP.*

6.2.3.3 OH* chemiluminescence analysis

The measurement of OH* chemiluminescence for the three fuels at specific times is shown in figure 6.6. Measurements were performed for six crank angle degrees and correspond to 7.5 bar IMEP. Even tough no natural luminosity radiation can be detected at -1.6 CAD, when is occurring the pilot 2 injection, it is possible to detect some OH^* radiation. At this period, the OH^* intensity is higher for the FT diesel, which corroborates with the higher RoHR diagram. Going forward in the combustion evolution, at 4 CAD, the high signal intensity of both OH* images and NL located in the periphery of the bowl indicates that in this regions both fuel rich and near-stoichiometric zones coexist, as already commented in previous work [3] and evidencing the importance of the OH^* for the process of soot oxidation [4].

In contrast, the differences between $OH*$ and NL images start to arise from 9 CAD. It is important to highlight that the dark zones cited previously in the NL images correspond also to low OH* radiation. It is well known that this radical, when in its excited state, is present only in high temperature reaction zones, where the fuel/air ratio is near stoichiometric. In this sense,

the lack of OH^* signal in these regions could indicate the presence of fuel rich zones with soot at lower temperatures. For the image at 13 CAD, high OH* intensity can be appreciated for the same regions, where previously were covered by dark regions. This increase of OH^* intensity is the result of the soot oxidation process forced by the post injection event.

When the comparison is performed between the three fuels, at 9 CAD the FT diesel presents a larger area covered by the OH^* radiation than the fossil diesel, which means fewer dark zones in the NL images. Moreover, the OME_X showed the highest intensity for the $OH*$ radiation, although it presented the NL images with the lowest intensity. As it has been mentioned previously, the higher presence of OH^* in excited stated when using OME_X can be directly related to high amount of oxygen present in the molecule of this fuel. This leads to a reduction of the fuel rich local zones, increasing the near-stoichiometric zones, where the OH^* is always present.

At the final stages of combustion (35.8 CAD), even if the injection duration of the OME_X is the longest between the three fuels, the absence of OH^* signal for this fuel confirms the combustion process ends earlier than the other two fuels. Furthermore, at this instant, the fossil diesel presents the highest OH^* intensity, indicating the slowest soot oxidation process among the fuels tested.

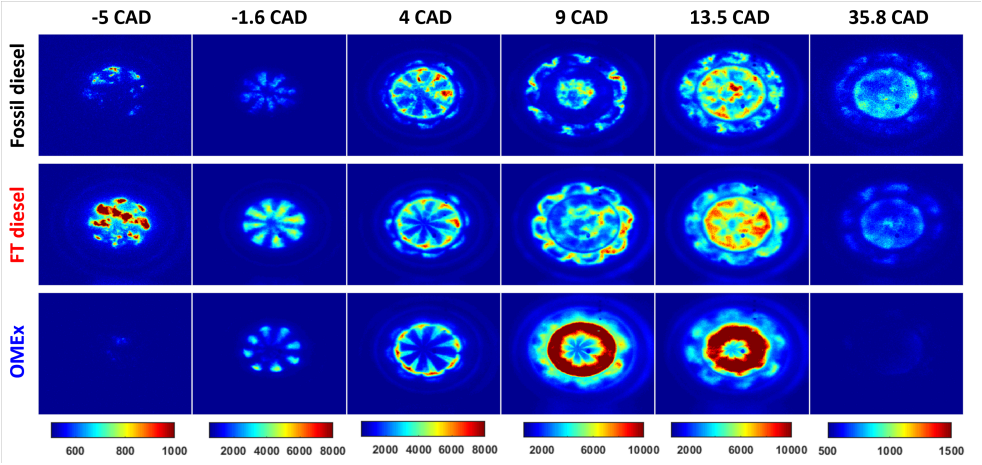

Figure 6.6. *OH^* chemiluminescence images for different crank angle degrees and fuels at 7.5 bar IMEP.*

6.2.3.4 2-color pyrometry - Soot analysis

From the 2-color technique it was possible to evaluate and quantify the soot formation when using the different fuels at 7.5 bar IMEP. Taking into account that when the interference filters (660 nm and 550 nm) were mounted in the cameras, the radiation intensity emitted by the OME_X flame was below the threshold of the camera detection, allowing only the measurements of soot for the FT diesel and fossil diesel. The 2-color images are presented in figure 6.7 for the same CAD's which were considered previously in the images of NL and OH*. The soot concentration is indicated by a parameter called KL_{2C}, which is represented in the color scale from 0 to 3.

A weak flame radiation is detected from -1.6 CAD until 1.6 CAD, which makes the KL_{2C} almost unmeasurable. The soot quantity (KL_{2C} value) starts to increase from 4 CAD until 6 CAD, when is occurring the main injection. The highest soot areas are localized in the bowl periphery where the NL and OH^* showed the highest intensity. There is no appreciable difference until 6 CAD between fossil diesel and FT diesel. At 9 CAD, the region where can be see the highest soot volume fraction for the fossil diesel in the 2-color measurements corresponds to the region where NL and OH^* signals for fossil diesel were weak or almost non-existent. The values of KL_{2C} for the FT diesel for this instant were slightly lower in comparison with fossil diesel, indicating less soot formation. The larger differences can be found for this instant in the squish zone.

From 13.5 CAD to 25 CAD, after the post-injection, the KL_{2C} images and NL images have a good agreement. Areas with high light intensity in the NL images correspond to areas with high KL_{2C}. In addition, FT diesel still shows lower KL_{2C} values than fossil diesel.

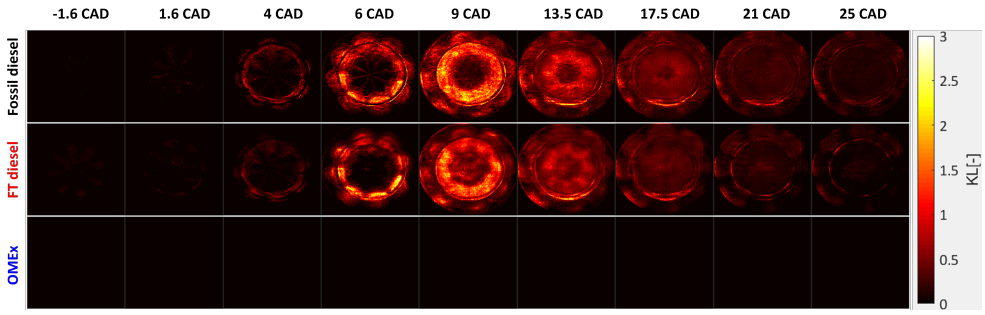

Figure 6.7. *KL values for different crank angle degrees and fuels at 7.5 bar IMEP.*

The figure 6.8 summarizes the soot evolution during the combustion process. The curves of mean KL is shown for the different fuels. The fossil

diesel starts to increase earlier in the cycle than FT diesel, as the figure clearly represents. Furthermore, the maximum KL value for the fossil diesel is slightly higher. Moreover, FT diesel seems to oxidize faster, corroborating with NL and $OH*$ results.

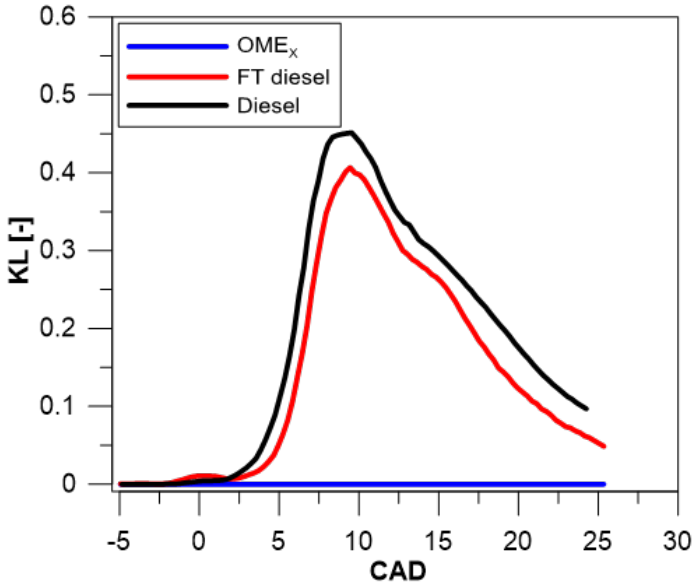

Figure 6.8. *Evolution of mean KL at 7.5 bar IMEP.*

The maps for the spatial and temporal soot evolution, which are based on sector and radial discretization, are shown in figure 6.9. The y-axis of the map represents the spatial resolution and the temporal resolution is represented in the x-axis. For the sectors map (Figure 6.9- left), the pink lines correspond to the spray axes. Thus, the combustion evolution for each spray can be visualized by separating the combustion chamber in small sectors.

The first point to be highlighted is the non-uniformity of soot formation in each spray of both FT diesel and fossil diesel fuels. The non-homogeneous temperature distribution inside the cylinder as well as the differences in the injector holes due to carbon deposition are some of experiments uncertainties that could lead to this effect. Furthermore, although the maps for each fuel are similar, they evidence that the higher soot formation for the fossil diesel is not concentrated in a specific region but along the whole combustion chamber. When analysing spray by spray, it is possible to see that fossil diesel presents larger areas with high KL values than FT diesel. Moreover, the map also indicates that FT diesel achieves lower KL values before than fossil diesel due to the less soot generated inside the cylinder and the faster oxidation.

The radial maps (figure 6.9-right) show where the highest soot concentrations are located and, in addition, how the soot evolves inside the combustion chamber while the combustion process is occurring. The highest soot KL can be found around 15 mm from the injector, in a region located at the periphery of the bowl. As the piston moves far from the TDC, the highest soot KL areas move toward the center of the piston while decreasing its value. During this decreasing of KL values, fossil diesel reaches low values (below 0.5) when the soot cloud (or flame) is closer to bowl center, while FT diesel achieves these same values earlier, at around of 6 mm of radius. This fact highlights again the faster soot oxidation for the FT diesel. For the region from 18 mm to 26 mm, where is located the squish region, FT diesel presents lower soot concentration than fossil diesel.

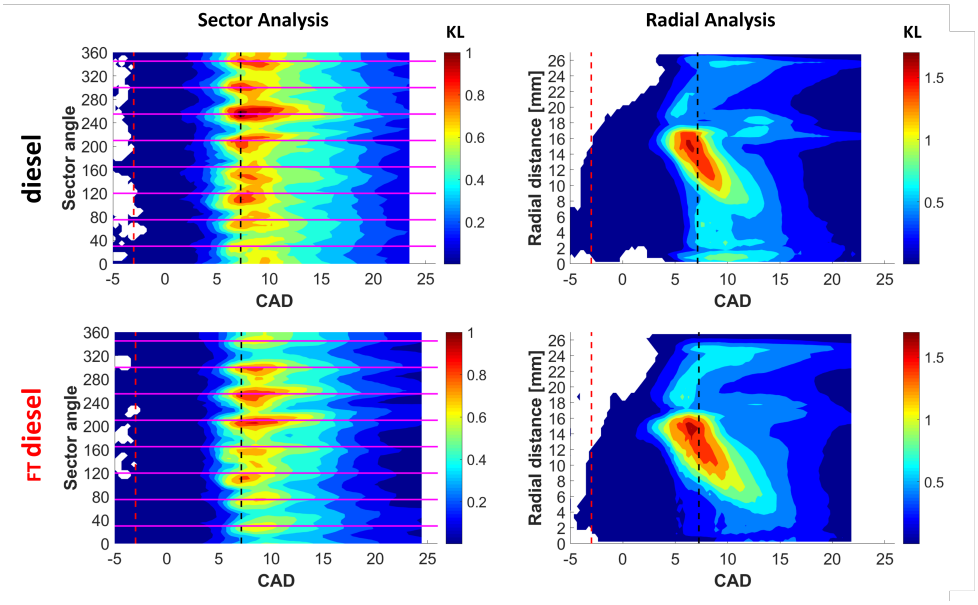

Figure 6.9. *Spatial and temporal soot volume fraction distribution for FT diesel and fossil diesel at 7.5 bar IMEP for the sector and radial analysis.*

6.2.3.5 4.5 bar and 1.5 bar IMEP analysis

The same sequence of tests and methodology was applied for other two conditions, 4.5 and 1.5 bar IMEP. In Figure 6.10, the accumulated intensity from the NL measurements for the three fuels and the two conditions is shown. It can be seen that OME_X, as it was described previously, presents the lowest radiation values for both conditions tested. In addition, at 1.5 bar IMEP,

accumulated intensity curve for the commercial diesel is higher than for FT diesel as it was already seen for 7.5 IMEP. However, a different trend is noted at 4.5 bar. In this case, the peak of accumulated intensity for FT diesel is slightly higher than for the commercial diesel.

The high quantity of cold soot at 4.5 bar IMEP for diesel could be the responsible of the weaker natural luminosity detected. A region of cold soot emits low-intensity radiation but absorbs large amounts of light. This is represented by the dark regions which are formed during the combustion process. They diminish the accumulated luminosity as shown in figure 6.10. At 4.5 bar IMEP this phenomena is more relevant than at 7.5 bar IMEP due to the lower injection pressure, which contributes to the formation of rich fuel zones.

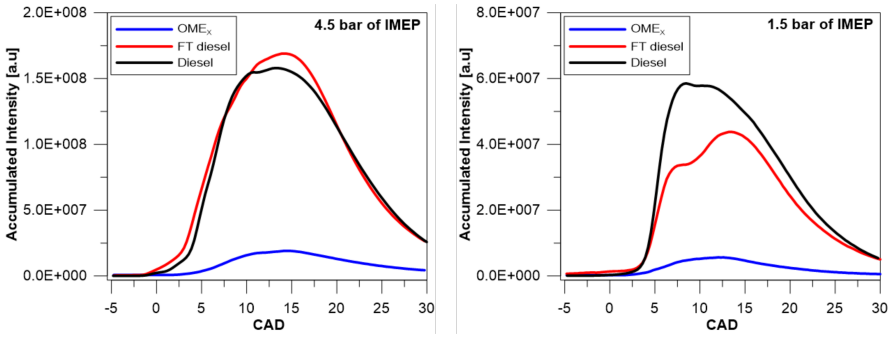

Figure 6.10. *Accumulate intensity for (a) 4.5 bar and (b) 1.5 bar IMEP.*

In figure 6.11, it is possible to see that this behavior is not followed by the KL measurements. The mean KL curve at 4.5 bar is indicating a higher soot production for the commercial diesel, as it was observed for the other operating conditions. This points out the limitations of soot formation analysis based only on natural luminosity measurements and the benefits of an additional technique like 2-color pyrometry.

6.3 OME_X-diesel blends: An analysis of soot evolution

6.3.1 Optical setup

For this second part of the study, the optical setup was mounted as it is represented in figure 6.12. For identifying the different species present during the neat OME_X as well as OME_X-diesel blend combustion process, the two

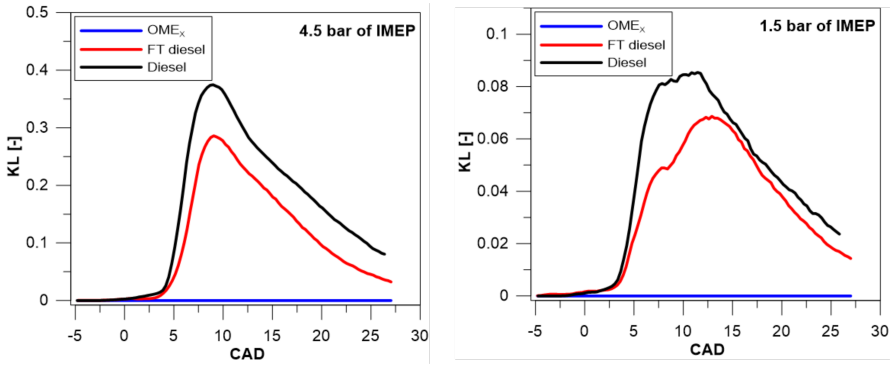

Figure 6.11. *Mean KL evolution for (a) 4.5 bar and (b) 1.5 bar of IMEP.*

optical techniques, spectroscopy in the UV-visible range and flame natural luminosity imaging, were applied simultaneously for the analysis of this current section. The flame radiation that comes from the combustion chamber goes through the transparent piston bowl and gets reflected by the 45° elliptical mirror. This 45° mirror offers a good reflection efficiency in the UV and the visible range due to its surface which is composed by an enhanced aluminum. The efficiency of reflection is above 85 % when using between 250 and 700 nm.

Once the flame radiation is reflected by the mirror, it reaches a neutral density filter. The filter has an optical density of 0.15 and its composition is basically fused silica. A small fraction of the incident light, around 15 %, is reflected by the neutral filter. This portion of the flame radiation reaches a high-speed camera, where the images of natural luminosity of the flame are recorded. The other portion of the incident light (around 70 %) is transmitted by the filter in the VIS-UV range to the spectrograph.

Regarding the devices for registering the natural luminosity images, a high speed CMOS camera (Photron Fastam Nova - S9) is employed for recording the flame luminosity. A Carl Zeiss Makro- Planar T 100 mm f/2 ZF2 lens is coupled to the camera. It was employed an image resolution of 640 x 944 pixels and a frame rate of 10.000 fps, which means approximately 0.5 CAD resolution at 1250 rpm of engine speed. In order to avoid the image saturation, it was applied different exposure times as represented in table 6.3. In this sense, it was necessary an intensity correction during the image post processing with the objective of normalizing the light intensity for the different fuels. The image acquisition was triggered with the injection electric pulse.

A Jobin Yvon Horiba 180 spectrograph assembled with a high speed CMOS camera (Photron SA5) and a Hamamatsu C10880-03F high-speed intensifier

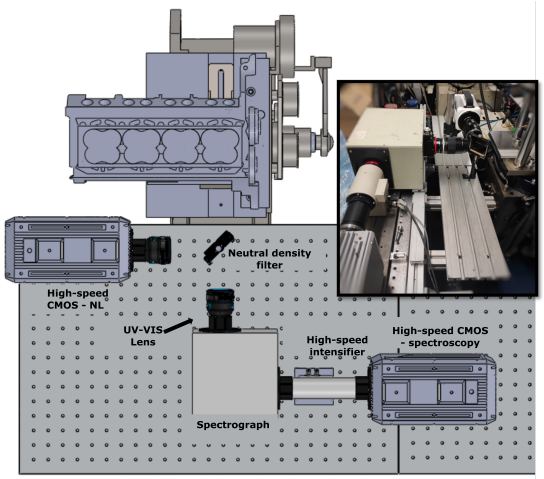

Figure 6.12. *Optical setup for spectroscopy analysis.*

were used for the high-speed spectroscopy acquisition. A grating with 600 groove/mm equips the spectrograph. The camera was set with an image size of 896 x 848 pixels and a frame rate of 10,000 fps. The table 6.3 shows the different exposure times and gain values used for the image acquisition. From this camera configuration, it was possible to obtain a wavelength bandwidth of 170 nm per image. Thus, in order to cover the desired spectrum range, measurements were performed with the grating centered at three different wavelengths: 330 nm (245−415), 400 nm (315−485) and 470 nm (385−555) respectively.

For a optimum combination between the spectral resolution and light intensity, the slit width was set to 0.1 mm. The flame radiation from the combustion chamber was focused with a UV Nikon objective (105 mm focal length), coupled to the entrance slit.

The figure 6.13 shows the field of view obtained when using the selected slit width. This region (highlighted) includes half of the bowl. An image from the field of view was acquired based on the zero order diffraction of the grating, where a conventional image is obtained due to the radiation is not decomposed per wavelengths. When radiation is decomposed, the spectrum is split along the horizontal axis of the image while the vertical axis corresponds to the vertical location within the field of view.

A calibration was performed by using a mercury-argon light source with a known discrete emission spectrum. During this first step, each horizontal pixel

Technique	Fuel	Shutter speed [μs]	Gain (999 max.)
Spectroscopy camera	O100	99.75	850
	O90D10	99.75	850
	O80D20	99.75	850
	O70D30	58.49	850
	O50D50	24.76	850
	D100	39.75	800
Natural Luminosity camera	O100	98	-
	O90D10	14.3	-
	O80D20	1.3	-
	O70D30	0.3	-
	O50D50	0.2	-
	D100	0.2	-

Table 6.3. *Shutter speed and gain used for the different fuel blends.*

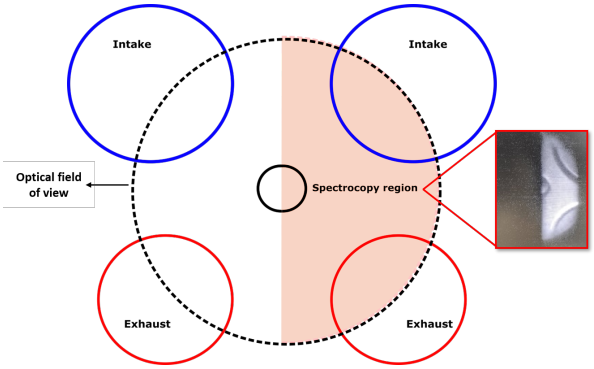

Figure 6.13. *Combustion chamber region considered for spectroscopy analysis.*

of the registered spectra was converted into a specific wavelength. In addition, as the grating efficiency varies with the wavelength, a second correction of the spectra intensity was performed to compensate this effect. As a reference, a tungsten-ribbon calibration lamp, with a known continuous emission spectrum [5], was used. For each recorded instant, a mean intensity value per wavelength (horizontal axis) was calculated considering only the pixels (in the vertical axis) corresponding to the measurement region shown in figure 6.13.

The tungsten-ribbon lamp allows also to calibrate the system to transform digital levels to light intensity of radiation ($W/(srm^2nm)$). This information has been used to perform a similar analysis to the one characteristic of 2-Color pyrometry [6]. By using the light intensity of two different wavelengths, the Planck law and the soot emissivity equations can be solved and the soot KL factor (optical density) as well as the soot temperature can be calculated. The wavelengths 450 and 530 nm were used for the 2C analysis. The first one is large enough to guarantee a small influence of the chemiluminescence radiation of the flame. The second one is separated from the grating edge, where the grating efficiency is poor (and correction is not reliable). The KL values are calculated from the mean intensity of radiation obtained for each wavelength.

6.3.2 Fuel blends and operating conditions

Commercial diesel and OMEx, as well as several blends of them, were studied in the current part of the work. The main fuel properties of each one were already shown in chapter 3. The blends are in mass and they were obtained by mixing different percentages of diesel in neat OMEX (10%, 20%, 30% and 50%). The miscibility of diesel and OME_X was analyzed for different percentages. For blends up to 50% of diesel the results were satisfactory. In addition, previous works have already been used the same ratio of diesel blended in OME_X [7, 8].

The test matrix and engine conditions used in this work are represented in table 6.4. Tests were performed at around 9.2 bar IMEP (figure 6.14) and a constant engine speed of 1250 rpm. The injection timing and duration were adjusted for each fuel, trying to keep the same IMEP and similar CA50. All IMEP values are around 9.2 bar with small variations (especially for neat Diesel). However, these conditions have been considered similar enough to perform the comparison of the different fuels tested. The intake pressure and temperature were the same for all tests. Thus, a different injection strategy for each fuel was necessary. In order to simulate more realistic operating conditions, an exhaust backpressure with 0.2 bar higher than intake pressure was employed. This could be achieved by means of an electronically controlled valve located at the exhaust system. The coolant of the cylinder wall was kept between 15 ◦C and 25 ◦C. A flat piston was used for this part of the study.

A multiple injection strategy with 4 pulses, including two pilot, one main and one post injection, was employed for the current work. In table 6.5 is presented the duration of each injection for each fuel blend. For all fuels tested, the injection pressure was kept at 800 bar. The strategy is based on

Fuel	Inj. Pattern	Engine Speed	Pint (Bar)	Pexh (Bar)	Tint (◦C)	Toil (◦C)	Tcool (◦C)
OMEX							
Diesel							
O90/D10	Mult.	1250	2.15	2.35	100	60	15-25
O80/D20							
O70/D30							
O50/D50							

Table 6.4. *Engine test conditions.*

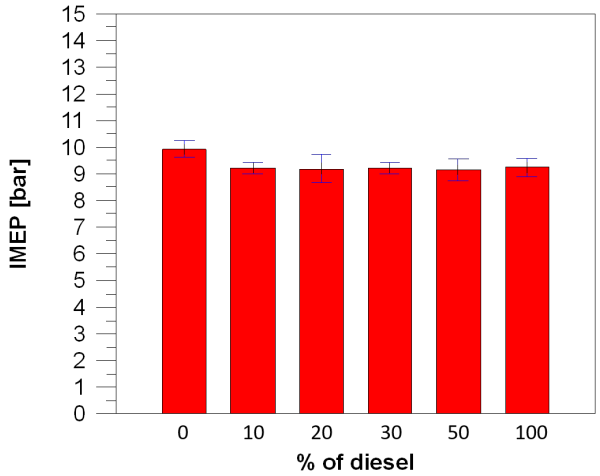

Figure 6.14. *IMEP for each fuel blend tested - % of diesel mass in OME_X.*

original equipment manufacturer (OEM) used for standard engine calibration. In order to compensate the lower OME_X's LHV and perform the tests under similar IMEP for all the blends, the energizing time of the main injection was adjusted for each of them. The Figure 6.15 represents the electric pulse only for the main and post injection, where the adjustment is performed.

6.3.3 Results

The results will be presented in this section following a specific sequence. Firstly, an analysis with the natural luminosity of the flame is presented and discussed in order to identify spatially the differences in the combustion process as diesel mass is added in pure OME_X. Later, the results regarding the high-speed spectroscopy and 2-color measurements are presented, where mainly the soot formation and oxidation for each blend is discussed.

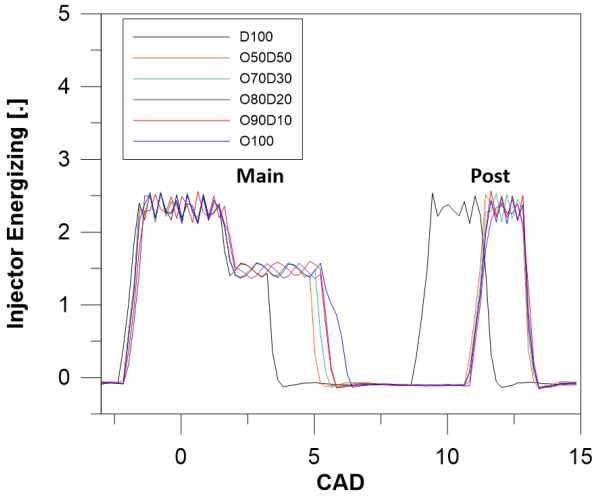

Figure 6.15. *Injector energizing strategies applied for each fuel blend.*

Fuel	Pilot 1 [μs]	Pilot 2 [μs]	Main [μs]	Post [μs]
O100	373	400	1146	373
O90D10	373	400	1065	373
O80D20	373	400	1065	373
O70D30	373	400	1040	373
O50D50	373	400	1013	373
D100	373	400	825	453

Table 6.5. *Injection durations.*

6.3.3.1 High speed flame natural luminosity

A first approach has been carried out, based on the flame natural luminosity. It provides less information than other more complex measuring techniques. However, it is still useful to identify differences in terms of flame evolution and radiation between blends. As already discussed by several studies [9, 10], the flame light intensity is one of the main indicator of soot concentration. The figures 6.16 and 6.17, where the RoHR and cumulative HR are shown, will be used to explain and reference the flame events represented in Figure 6.18. The RoHR curves were calculated by using a model based on the first law of thermodynamic [11]. In figure 6.18, the flame natural luminosity images for different crank angle degrees and different fuel blends

are represented. As it has been mentioned in the previous section, tests for each blend were performed with a different shutter speed configuration, due to the great variation on radiation intensity. Considering this, the measured intensity from each blend was corrected, taking the neat OME_X as reference. In this way, blends and pure fuels can be directly compared. The images at 3.4 CAD represent the premixed combustion phase, where the soot formation rate is low as it is represented by the low radiation intensity observed for all the blends. At 7.1 CAD, combustion achieves the diffusive phase, and the soot formation ratio increases, represented by an important increase of flame broadband radiation. From this point, the differences between blends arise. For all the cases, the highest intensity regions are in the periphery of the bowl, where the flame-flame and flame-wall interactions are occurring. At this instant, the maximum luminosity intensity increases significantly with diesel fraction, indicating that the soot formation is increasing as well. At 10.9 CAD, the main injection for the blends and neat diesel has finished (not for neat OME_X) and the soot formed begins to be oxidized. For the blends up to 20 % of diesel content, the soot generated during the main injection (observed at 7.1 CAD) seems to be oxidized as the radiation observed at 10.9 CAD decreases in comparison with previous instants. The high content of OME_X in the blend could be promoting a faster oxidation of previously formed soot. Above 20% of diesel, in contrast, the trend is the opposite. The radiation intensity is not decreasing and even the area covered by high intensity radiation grows, in comparison with the blends with less diesel fraction. This trend is clearer when moving to 14.6 CAD. At this instant, the blends with lower diesel content (even O70D30) show a clear reduction of radiation intensity in comparison to that measured at 7.1 CAD. However, for O50D50 and neat diesel it seems that soot concentration is still increasing as the high intensity radiation extends to almost the whole piston bowl. Besides, up to 30% of diesel, it is possible to see the jet of the post injection spreading in the flame due to the faster oxidation that occurs during the main injection. In contrast, for O50D50 and D100, the soot cloud remaining inside the bowl still covers the combustion chamber and hides the post injection jets. When the post injection enters in the main injection flame and burns, the light intensity increases considerably. The earlier post injection of D100 could cause a larger increase of the radiation intensity in comparison to the other fuels at 14.6 CAD, but it is considered that this will not alter the soot trend observed when fuels are compared. After that, during the late combustion stage, some differences can be highlighted.

Based on the above mentioned, it can be stated that as the fraction of diesel increases in the blend, the soot oxidation seems to worsen. If the cumulative heat release curve (figure 6.17) is observed, large differences are visible above

50% of total energy released (around 15 CAD). At this stage, the cumulative heat release increases faster for the fuels with high OME_X content and it extends up to the 80% of the total energy released. At first, this behaviour could be related to the different injection strategy of the blends in comparison to the one used for pure diesel. However, it is possible to see that O50D50 shows a heat release behaviour more similar to D100. Therefore, the higher energy released between 15 and 30 CAD (around 50 to 80% of the total energy released) by blends with diesel content below 50% and pure OME_X cannot be explained by the different injection strategy. For this reason, it has been related with a higher soot oxidation rate during this stage, which is coherent with a faster burnout observed in the images and related to a faster decrease of soot concentration. It means that when diesel increases above 30%, the soot oxidation is worsened and the burnout process slowed down, which is confirmed by both natural luminosity and process combustion heat release.

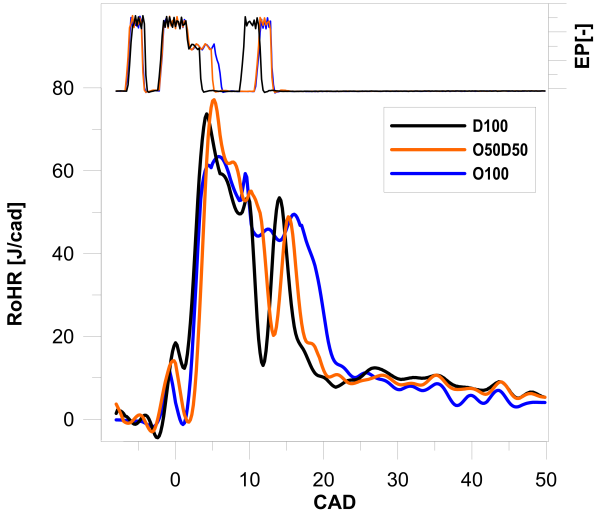

Figure 6.16. *RoHR for neat OME_X, O50D50 and neat diesel.*

The increase of luminosity intensity due to the addition of diesel was evaluated by calculating and comparing the total accumulated radiation intensity of each blend at every measured CAD. The results are shown in figure 6.19. A logarithmic scale has been used to allow the comparison between all blends tested. The figure is representing a range of CADs where the maximum accumulated intensity is achieved. As it can be seen, only a 10 % of diesel is enough to increase one order of magnitude the light intensity emitted by the flame. This could be linked with the soot formation increase caused by

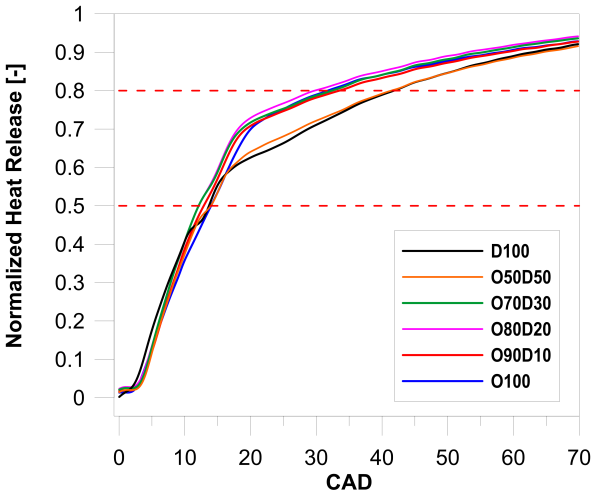

Figure 6.17. *Cumulative heat release for all fuel blends.*

the diesel addition. As the percent of diesel added in the blend rises, the differences in terms of radiation intensity become higher. This behavior is very clear up to 30 % of diesel blend, where the difference in terms of absolute value increases as diesel mass increases. However, for 50 % of diesel, the differences in comparison with neat diesel (D100) are reduced. This suggests that the potential of OME_X to promote less soot formation has a minimum effect when diesel fraction increases above 50 %. A similar behaviour when using different diesel substitution rates in OME_X was found by Garcia, et al [7] in a metal engine.

6.3.3.2 High speed spectroscopy

Despite it can be expected negligible soot formation by OME_X, in figure 6.18 and figure 6.19 it is possible to see that the combustion of this fuel emits broadband radiation. However, it must be highlighted that this signal includes the contribution of other sources different from soot. One of the most important is chemiluminescence. Although it is weak in comparison to soot thermal radiation, it becomes relevant when soot concentration is reduced, e.g. first or last stages of combustion or when using low sooting fuels like OME_X. Thus, based on natural luminosity imaging, it is difficult to state whether the radiation observed for this fuel is chemiluminescence or includes soot emission contributions.

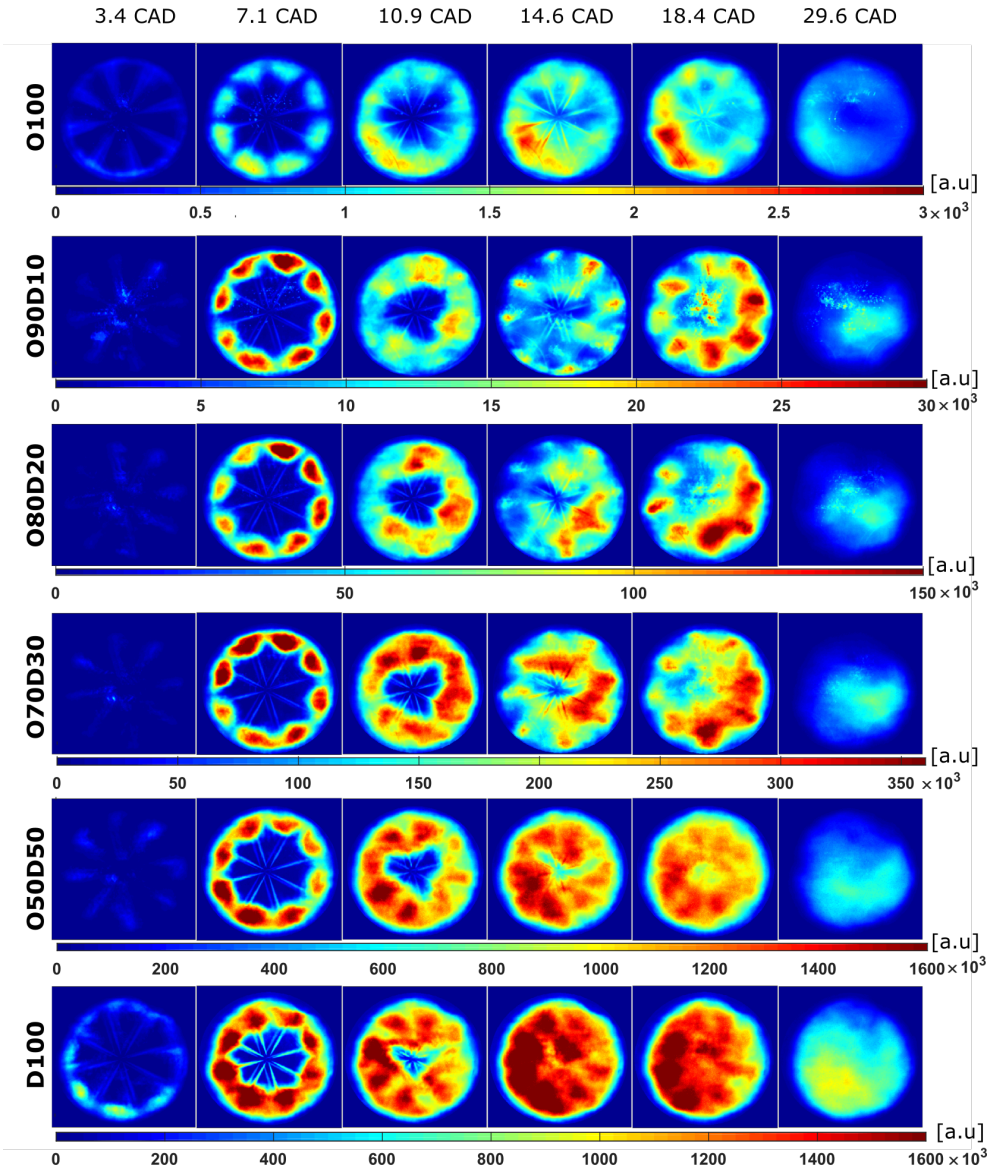

Figure 6.18. *Flame natural luminosity for each blend tested.*

These uncertainties affect not only pure OME_X but also the blends with low diesel content (specially O90D10). In order to properly identify the dominating radiation source for each fuel tested, the use of high-speed spectroscopy is proposed. In contrast with natural luminosity imaging, it is a

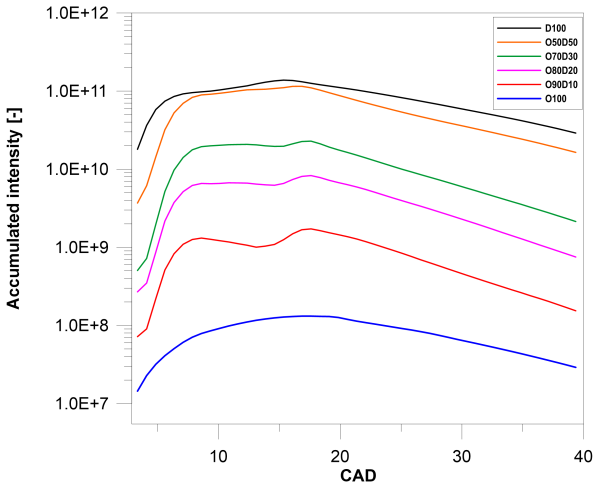

Figure 6.19. *Accumulated intensity for the different fuel blends (logarithmic scale).*

spectrally resolved technique which allows to characterize not only radiation intensity but also the spectrum characteristics.

In order to highlight the differences among fuels, the spectra of the combustion process at 10 CAD are shown in figure 6.20, for all them. As it can be observed, O100 presents a completely different spectrum in comparison with the other blends. The maximum intensity in the spectrum comes from the OH^* emissions. The peak of $OH*$ is broad due to the presence of several optics between flame and camera and the large spectrograph slit aperture used for the tests, which was necessary to achieve enough sensitivity. From 420 nm, the light intensity starts to decrease rapidly, which confirms the non-soot formation. Up to 30% of diesel, the OH^* chemiluminescence contribution can be identified in the spectra. From O50D50, the high soot formation increases and the OH^* chemiluminescence signal disappears. In general, the light intensity and the slope of the curve increases in the visible range (450-500 nm) as the diesel concentration increases. This is a consequence of the higher soot formation.

The maps presented in figure 6.21 show the temporal evolution of the radiation spectrum during the combustion process of the different blends. Each map represents the wavelengths in the x-axis, from 290 nm to 530 nm. The y-axis represents the CAD evolution. The first thing that can be confirmed with this technique is the absence of soot during pure OME_X combustion. Soot thermal radiation is characterized by an exponential increase of the intensity towards higher wavelengths (in the range considered in this work). Thus, as

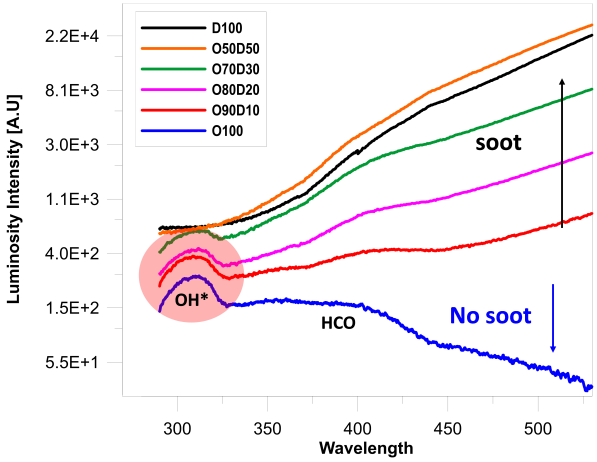

Figure 6.20. *Spectrum at 10 CAD for the different blends.*

this behavior is not observed for OME_X, it can be stated that no soot thermal radiation is detected. In contrast, it is possible to see at around 310 nm that the OH^* chemiluminescence radiation is very intense during all combustion duration, from the earlier to the late combustion stages. During the first stages of the combustion process, the OH-radicals brake the precursors of the soot formation. In addition, the high oxygen content could increase the near-stoichiometric zones, increasing the concentration of OH^*. Additionally, a continuum band, centered around 380 nm, is visible. It can be associated with the HCO radical (Vayda bands from 270 to 410 nm) [12], which represents the transition from the low to high temperatures reactions [13]. Therefore, based on the spectrum analysis, it can be stated that natural luminosity images represent mainly HCO emissions in the visible range (above 400 nm).

When diesel is mixed with OME_X, characteristic soot thermal radiation appears as it can be observed that the intensity increases with wavelength in the visible range. A 10% of diesel blended in OME_X is enough to generate soot. However, its concentration is low as its radiation is not dominating the emission spectrum. Additionally, it can be observed that thermal radiation disappears quickly (before 25 CAD) which suggests a fast soot oxidation. As the diesel content increases, more soot is generated and more difficult becomes its oxidation. Up to 20% of diesel, the soot formed during main and post injection can be easily distinguished. As it was observed with natural luminosity images, the soot radiation generated during the main injection drastically decreases. This suggesting a fast oxidation process before the start of the post injection event. From 30% of diesel, soot emission increases.

Furthermore, when the post injection starts, the main injection radiation slightly decreases, evidencing a clear reduction of the oxidation rate at this stage of the combustion process. For O70D30, it is still possible to see an important $OH*$ emission, which can be related with a high concentration of this radical. It helps on completely oxidizing soot before the piston achieves the 40 CAD.

When diesel fraction is increased to 50%, the behaviour drastically changes. The characteristic OH^* intensity peak observable in the blends until 30% of diesel cannot be identified for O50D50 and D100. This could be associated with two main factors. The first one is related with the intensifier settings used for these two fuels. The configuration guaranteed no saturation in the visible range (where soot thermal radiation is more intense) but the sensitivity in the UV-range was reduced. Therefore, the lower intensity of the OH^* was not registered by the camera. The second factor is related with the attenuation of the OH^* signal due to the high soot concentration during the diffusion phase. The spectra of O50D50 and D100 also shows a similar soot formation and oxidation behaviour. The radiation intensity levels are similar, and, in both cases, it is possible to see soot radiation up to 60 CAD. This confirms the trend observed with natural luminosity (figure 6.18) and the HR curve (figure 6.17). The higher slope of the curves for O50D50 and D100 suggest a higher chemical activity in comparison to the other blends late in the cycle. It can be concluded that the benefits of using OME_X seems to be reduce significantly when it represents less than 50% of the mixture.

As it has been described in the methodology section, the spectrograph information can be used to evaluate soot concentration. For this purpose, a 2-color pyrometry algorithm is applied to the radiation intensity at 450 and 530 nm, for all the blends and D100 (pure OME_X was excluded). Thus, an average soot KL evolution is calculated. Results are summarized in figure 6.22. For O90D10, the KL values were lower than the inferior limit (0.001) set for the calculation, confirming very low soot formation. For O80D20, the soot formed during de combustion process is higher and measurable. Nevertheless, it is still very low if compared with the remaining blends. The first remarkable KL increment is found between O80D20 and O70D30. Thus, it can be stated that above 20% of diesel fraction its effect on soot formation is relevant.

When comparing O50D50 and O70D30, it can be seen that, until 20 CAD, main differences are focused on the high peaks which correspond to the combustion of the main and post injection. These peaks are also visible for D100 but not for the blends with less diesel content. Additionally, a great difference can be noted during the oxidation phase, after 20 CAD. The soot of

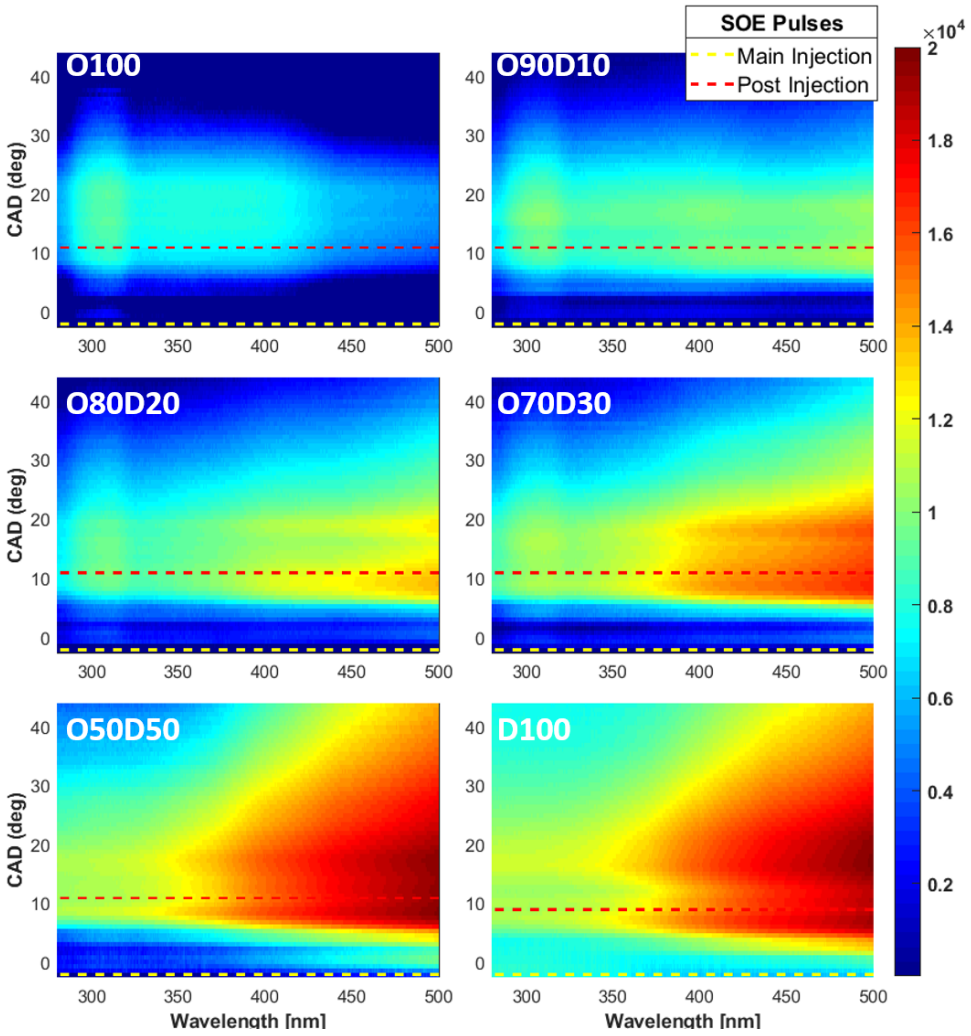

Figure 6.21. *Maps of the high-speed spectroscopy analysis for the different blends.*

O70D30 oxidizes much faster than O50D50 as the KL values decreases faster. In fact, it is notorious that the blend with the highest diesel fraction O50D50 presents clear difficulties to oxidize soot.

When O50D50 is compared to D100, there are some important points to be highlighted. First of all, as shown in figure 6.15, the longer injection duration results in longer oxidation time for the blend in comparison to D100. In this case, although the soot formed during main and post-injection combustion is higher, the injection duration is much shorter and the oxidation process begins

earlier. Additionally, it must be pointed out that as long as we move later in the cycle, temperature and pressure decrease which hinders the oxidation process. Another consideration is related with the similar light intensity presented in the spectroscopy and natural luminosity analysis between the two fuels. In a first approach, results suggested similar soot formation for both fuels. However, it must be kept in mind that soot thermal radiation intensity is related with its concentration but also with its temperature. In this sense, the 2-color pyrometry shows that soot formed by O50D50 is lower than D100. This indicates that the high light intensity of radiation is also caused by a higher temperature. The higher peak of RoHR, as shown in Figure 6, could be increasing the temperature inside the combustion chamber in relation to the 100D.

The 2-color pyrometry allows to establish a relative comparison between blends. Based on these results, it can be stated that diesel can be added up to 20% of mass substitution rate without significantly increasing soot formation. An important soot reduction as well as an efficient oxidation process is still possible to obtain with 30% of diesel in comparison to pure diesel. However, above 50% of diesel, although soot formation is still lower than for 100D, higher soot levels reach later stages of the cycle as a consequence of the longer injections required. Thus, the potential benefits of improving soot oxidation disappear. To keep the same engine load, a trade-off exists between the capacity of OME_X to reduce soot formation and improve soot oxidation and the necessity of longer injection durations due to its lower LHV.

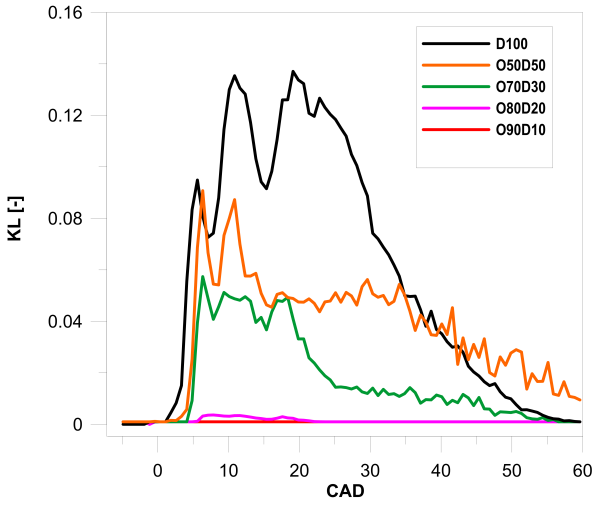

Figure 6.22. *KL values for the different OME_X-diesel blends.*

6.4 Summary & conclusions

The current chapter focused in studying as well as evaluating the potential of efuels in replacing the fossil diesel. For this purpose, specific optical techniques were employed in an optical engine with the objective of better understanding the combustion process and the soot production when burning these different efuels. The analysis was split into two main parts, where the first one is centred in evaluating the potential of using both OME_X and FT diesel in pure form. The second part aimed to identify the limits of diesel mass blended in OME_X, while keeping low soot formation and an efficient soot oxidation process. In addition, this second part have also been used for answering some questions that have arisen in the first part, when analysing the natural luminosity emitted by the OME_X combustion.

Regarding the fist part, FT diesel and OME_X combustion were evaluated by using three optical techniques (Natural luminosity, OH^* chemiluminescence and 2-color pyrometry) and the results were compared with commercial diesel. The main conclusion of this first part can be summarized as follows:

- In the RoHR curve is evidenced the higher cetane number of FT diesel. Although the pilot 1 is delayed for the FT diesel in relation to the commercial diesel, the combustion is starting earlier.
- Although OME_X has a larger main injection duration than the other two fuels, RoHR curve is indicating that the combustion ends earlier.
- OME_X presented a much lower natural luminosity intensity than FT diesel and commercial diesel for the three conditions tested, reinforcing the idea that it could be a non-sooting fuel.
- In terms of maximum natural luminosity intensity, FT diesel has showed lower values than diesel. However, dark regions were observed for the commercial diesel which are related with high concentration of cold soot.
- FT diesel light intensity reduces faster than commercial diesel, indicating that the soot oxidation seems to finish earlier.
- The highest peak for the FT diesel in the RoHR curve during the pilot 1 is confirmed by the OH^* images, where the intensity is higher as well.
- The dark zones, which were visualized previously in the NL images at 9.1 CAD, in the OH^* measurements are represented by the ring with low intensity. This is due to the high concentration of soot is blocking the

OH^* chemiluminescence signal or there is no chemical reaction occurring in this zone. In this case, the OH^* intensity signal of FT diesel is higher than commercial diesel.

- Although the NL intensity for the OME_X is lowest between the three fuels, it presents the highest OH^* intensity. The high amount of oxygen can increase the local zones near of stoichiometric conditions and increases the OH^* intensity. Furthermore, the very low soot formation permits a better visualization of the $OH*$ chemiluminescence that is not possible to see for the case with FT diesel and fossil diesel.

- The images at 35.8 CAD prove the shortest combustion duration for the OME_X. Furthermore, it is clear that FT diesel presents a faster oxidation than commercial diesel.

- FT diesel presents lower soot emissions than commercial diesel for the three conditions tested.

- At 9 CAD, the dark zones in the NL images correspond to the highest soot concentration zones in the 2 color images.

- Faster oxidation for the FT diesel in relation to the commercial diesel is evidenced again in the 2 color technique.

- No correlation of NL images and 2 color images at 9 CAD. Dark zones (low intensity) in NL images represents high soot concentration in 2 color images. From 13.5 until 25 CAD, the highest NL intensity corroborates with the highest KL values.

- Radial map presents lower KL values in the squish zone when FT diesel was used. Furthermore, the FT diesel flame oxidises the soot farther from the center than commercial diesel.

Regarding the study involving OME_X-diesel blends, three different optical techniques were used to analyse the influence of diesel substitution rate in OME_X: natural luminosity, spectroscopy and 2-color pyrometry. From the main results, it is possible to state that:

- The cumulative heat release curves showed that above 30% of diesel content, the oxidation velocity considerably decreases and extends the burnout process.

- A 10% of diesel blend is enough for increasing in one order of magnitude the natural light intensity emitted by the flame. Up to 30% of diesel blend, the light intensity increases as the diesel mass quantity increases. Above 50% of diesel mass, the increment in terms of light intensity reduced significantly.
- The spectroscopy measurements have proven the absence of soot during pure OME_X combustion. As diesel mass is increased in the blend, the radiation for higher wavelengths (related to soot thermal radiation) increases as well.
- Significant OH^* emission could be appreciated for the blends with up to 30% of diesel mass. This can be related with a high concentration of this radical which helps oxidizing soot and its precursors before 40 CAD.
- 2C pyrometry shows that the soot formation can be kept very low up to 20% of diesel mass substitution rate. For 50% of diesel content, the soot reduction is still remarkable. However, the longer injection duration in comparison to pure diesel extends the late soot oxidation.

6.A Spectroscopy image calibration

The signal registered by the high-speed camera that is coupled to the spectrograph needs to be calibrated in terms of wavelength and intensity of radiation to obtain an accurate emission spectrum. In this work, a procedure was developed which is described in the following lines. The figure 6.23 shows an example of the signal acquired, which corresponds to one of the tests performed in this work. For each image, the pixel coordinate in the x-axis is translated to the corresponding wavelength value (thanks to the calibration procedure). Additionally, for each column, all pixels are averaged to obtain a unique averaged intensity value per wavelength.

The first step of the process consists of translating the x-axis of each image capture by the high-speed camera to the corresponding wavelength value. For this purpose, the discrete emission spectrum of a Mercury-Argon was used. The emission bands of this equipment allow to stablish the correspondence between the x-axis position in the images and the corresponding wavelength, for all the grating positions used in this work. An example of this procedure is shown in figure 6.23, where the image registered by the high-speed camera (top) is compared with the spectrum obtained by averaging the pixel intensity in the y-axis and identifying the wavelength of the main peaks of the image.

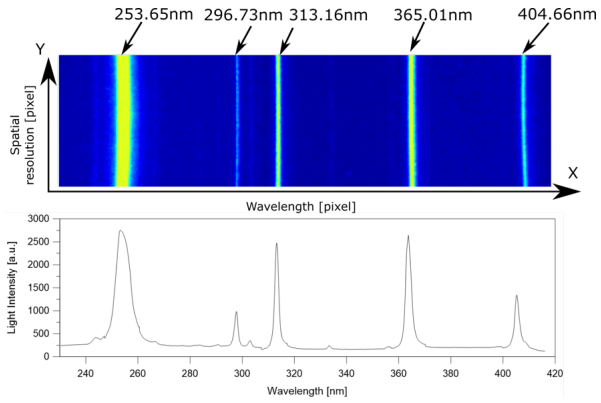

Figure 6.23. *Image of the emission spectrum of a calibration mercury-argon lamp (top) and the corresponding spectrum obtained by applying the first step of the calibration procedure. Information corresponds to the grating centred at 330nm.*

The second step of the calibration procedure is focused on compensating the wavelength-dependent efficiency of the different optical elements and the grating. For this purpose, a tungsten-ribbon calibration lamp was used as reference [14]. This device presents thermal continuous emission spectrum, which was calibrated in laboratory providing the intensity of radiation ($W/(srm^2nm)$ per wavelength. The signal registered by the high-speed camera corresponding to this device is compared to its calibrated spectrum, to define a wavelength-dependent correction factor. It is assumed that the efficiency at the central wavelength (where the grating is centered) is maximum. Then, the ratio between the signal at this wavelength and at any other wavelength must be equal to the ratio between the intensity of radiation of the lamp at the same wavelengths. Based on this, a calibration factor is calculated and applied to the registered spectrum. In figure 6.24, a comparison between the registered spectrum and the corrected one are shown. The real lamp emission spectrum has been included as reference, which has been normalized to be comparable with the measured spectrum. Data corresponds to a grating configuration centered at 470nm. As it can be seen, the optical set-up efficiency is constant up to 450 nm. After this, the efficiency starts to decrease. However, the calibration procedure can compensate this change of behavior and the corrected spectrum is close to the reference one.

For each acquisition configuration (grating position, intensifier gain and shutter time), a specific wavelength-dependent correction factor needs to be calculated. Besides, it must be obtained using the same optical set-up as the one used in experiments. Otherwise, the efficiency of the optical elements not

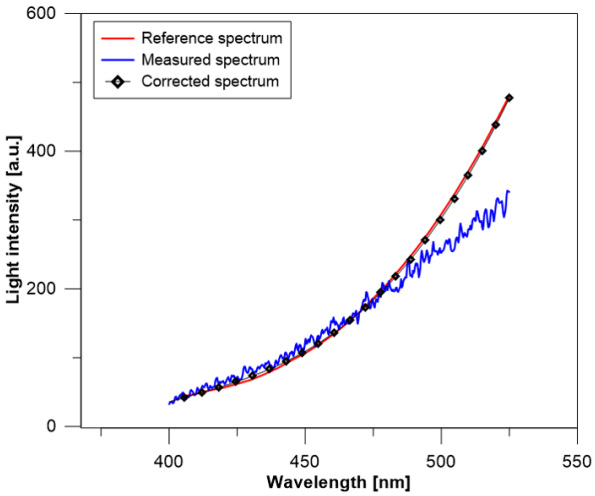

Figure 6.24. *Comparison between the tungsten-ribbon lamp measured spectrum (blue) with the grating centred at 470nm, the one obtained after calibration (black) and the real spectrum (red).*

used in this procedure will not be considered in the correction factor and it will affect its accuracy. In figure 6.25 it is shown an example of the calibration procedure applied to experimental data. It corresponds to pure diesel with the grating centered at 470nm. The signal registered (top) is converted into an emission spectrum (bottom) applying the first step described in this appendix. Then, the correction coefficient calculated based on the tungsten-ribbon lamp (second step) is applied to compensate for the efficiency of each optical element including the spectrograph, the intensifier, and the camera (bottom).

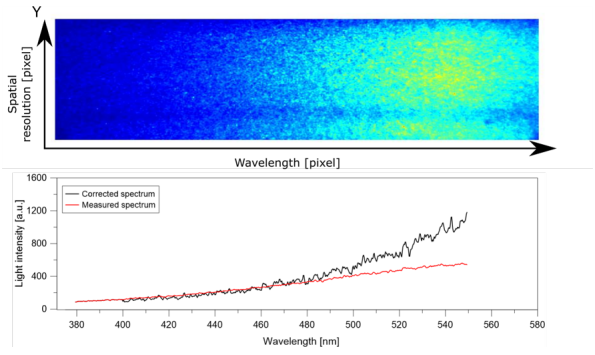

Figure 6.25. *Emission registered for pure Diesel with the grating centered at 470nm (top) and the resulting spectrum (bottom) before and after the calibration procedure.*

The final step is to calculate a correlation between the intensity of radiation of the tungsten-ribbon lamp and the corresponding digital levels obtained by the optical set-up and the correction procedure described above. This correlation is applied to experimentally measured combustion spectra to transform them form digital levels to intensity of radiation and apply the 2C pyrometry algorithm.

Bibliography

[1] Liu Haoye, Wang Zhi, Li Yanfei, Zheng Yanyan, He Tanjin and Wang Jianxin. "Recent progress in the application in compression ignition engines and the synthesis technologies of polyoxymethylene dimethyl ethers". *Applied Energy*, Vol. 233-234 n^o October 2018, pp. 599–611, 2019.

[2] Roberts Gregory, Lind Ted, Eagle W., Musculus Mark PB, Andersson Öivind and Rousselle Christine. "Mechanisms of Post-Injection Soot-Reduction Revealed by Visible and Diffused Back-Illumination Soot Extinction Imaging". *SAE Technical Paper Series*, Vol. 1, pp. 1–20, 2018.

[3] Jakob Markus, Hülser Thomas, Janssen Andreas, Adomeit Philipp, Pischinger Stefan and Grünefeld Gerd. "Simultaneous high-speed visualization of soot luminosity and OH * chemiluminescence of alternative-fuel combustion in a HSDI diesel engine under realistic operating conditions". *Combustion and Flame*, Vol. 159 n^o 7, pp. 2516–2529, 2012.

[4] Kosaka Hidenori, Nishigaki Takahiro, Kamimoto Takeyuki, Sano Takashi, Matsutani Akira and Harada Shinichi. "Simultaneous 2-D Imaging of OH Radicals and Soot in a Diesel Flame by Laser Sheet Techniques". *SAE Technical Paper Series*, Vol. 1 n^o 412, 2010.

[5] Hwang Wontae, Dec John and Sjöberg Magnus. "Spectroscopic and chemical-kinetic analysis of the phases of HCCI autoignition and combustion for single- and two-stage ignition fuels". *Combustion and Flame*, Vol. 154, pp. 387–409, 2008.

[6] Pastor José V., García Antonio, Micó Carlos, Möller Sebastian and García-Oliver José M. "Application of optical diagnostics to the quantification of soot in n -alkane flames under diesel conditions". *Combustion and Flame*, Vol. 164, pp. 212–223, 2015.

[7] García Antonio, Gil Antonio, Monsalve-serrano Javier and Sari Rafael Lago. "OMEx-diesel blends as high reactivity fuel for ultra-low NOx and soot emissions in the dual-mode dual-fuel combustion strategy". *Fuel*, Vol. 275 n^o April, pp. 117898, 2020.

[8] García Antonio, Monsalve-serrano Javier, Villalta David, Lago Rafael, Gordillo Victor and Gaillard Patrick. "Potential of e-Fischer Tropsch diesel and oxymethyl-ether (OMEx) as fuels for the dual-mode dual-fuel concept". *Applied Energy*, Vol. 253 n^o July, pp. 113622, 2019.

[9] Pellegrini Leonardo, Marchionna Mario, Patrini Renata, Beatrice Carlo, Del Giacomo Nicola and Guido Chiara. "Combustion Behaviour and Emission Performance of Neat and Blended Polyoxymethylene Dimethyl Ethers in a Light-Duty Diesel Engine". *SAE Technical Paper Series*, Vol. 1, 2012.

[10] Rao Lingzhe, Zhang Yilong, Kim Dongchan, Su Hu Chien, Kook Sanghoon, Kim Kenneth S. and Kweon Chol Bum. "Effect of after injections on late cycle soot oxidation in a small-bore diesel engine". *Combustion and Flame*, Vol. 191, pp. 513–526, 2018.

[11] Pastor José, Olmeda Pablo, Martín Jaime and Lewiski Felipe. "Methodology for Optical Engine Characterization by Means of the Combination of Experimental and Modeling Techniques". *Applied Sciences*, Vol. 8 n^o 12, pp. 2571, 2018.

[12] Mancaruso Ezio and Vaglieco Bianca M. "Spectroscopic measurements of premixed combustion in diesel engine". *Fuel*, Vol. 90 n^o 2, pp. 511–520, 2011.

[13] Pastor J. V., García-Oliver J. M., García A., Micó C. and Durrett R. "A spectroscopy study of gasoline partially premixed compression ignition spark assisted combustion". *Applied Energy*, Vol. 104, pp. 568–575, 2013.

[14] Xuan Tiemin, Pastor José V., García-Oliver José M., García Antonio, He Zhixia, Wang Qian and Reyes Miriam. "In-flame soot quantification of diesel sprays under sooting/non-sooting critical conditions in an optical engine". *Applied Thermal Engineering*, Vol. 149 n^o 301, pp. 1–10, 2019.

Chapter 7

Conclusions and future work

Contents

The aim of this chapter is to summarize the main findings reported in the previous chapters. The conclusions of the different works carried out throughout the thesis are included in this summary. In addition, in the last part of the chapter is discussed and presented the future works. This last part has the objective of tracing new possibilities that can potentially contribute to improve the knowledge about soot production (formation and oxidation process) and ways for its reduction in internal combustion engines.

7.1 Conclusions

As already previously discussed in the *Introduction* chapter, the main goal of this thesis is to test and to evaluate new technologies with the potential

of reducing the soot produced inside the combustion chamber during the combustion process. For this purpose, an optical engine with real piston bowl shapes completely transparent was employed in the study. This optical engine allowed the application of several optical techniques, which provided all informations necessary for understanding the different phenomena involved in the study.

In the chapter 2, the literature review put in evidence the necessity of finding new strategies for reducing the pollutant emissions in diesel engines as well as the potential of using new piston geometries and fuels for this same purpose. A new concept of piston for heavy-duty vehicles, where wave protrusions are distributed around the piston bowl circumference, has been demonstrated a significant decrease in soot production. However, there were no studies involving this new technology in swirl-supported light duty engines. In the same way, it was also seen that some recent studies showed the great potential of e-fuels for both soot reduction and diesel replacing. Among these e-fuels, FT diesel and OME_X have been received special attention. The first one due to the similar properties with fossil diesel. The second one due to the potential of low soot production when used in diesel engines. In contrast, very few studies in optical engines using these e-fuels could be found in the literature. Thus, these both alternatives, wave protrusions piston and e-fuels, opened up a new field of research to be explored in light-duty diesel engines for reducing the soot emissions.

In this way, the current work has been developed in three main parts, which were grouped into three chapters of results. The first one was focused on understanding the in-cylinder flow movement induced by the shape of a real piston geometry. The second and third ones were directly centred in the utilization of new hardware and fuels for the reduction of the soot produced during the combustion process. The important conclusions of each study are summarized in the following subsections.

7.1.1 In-cylinder flow characterization of the optical engine

In the first chapter of results, a preliminary study involving the in-cylinder movement when using a real piston bowl shape was carried out. This first part was extremely useful to characterize the in-cylinder flow pattern of the optical engine used for this thesis. The study was performed by using the PIV technique under motored and non-reactive engine conditions. The effect of the spray on the air flow field as well as the turbulent kinetic distribution inside the piston bowl were evaluated. A special methodology for correcting the

optical distortions induced by the piston shape was also applied. In addition, a special study involving ray-tracing methodology was applied for improving the laser illumination inside the bowl.

The first important achievement of this first part of the work was the well-succeed employment of a real bowl piston shape in an optical engine, which was for the first time in the CMT institute. This allowed to replicate in an optical engine, as much as possible, the real conditions used in a metal engine. In addition, this first part of the study strongly contributed for understanding the issues and optical limitations involved when using pistons with complex geometries. Moreover, it also contributed for the development of specific post-processing methodologies, which were applied for all analysis developed in this thesis.

For the tests performed under motored conditions it was possible to identify the typical behaviour of the air motion inside of a re-entrant bowl as already reported by some similar studies. As the piston approaches to TDC, the velocity inside the bowl decreases. When the piston is closer to the cylinder head, it was appreciated a deflection of the PIV vectors, indicating the typical movement of the flow from the squish region to the bowl, it is known as squish-bowl interaction. Another specific characteristic of re-entrant bowls in swirl-supported engines, which is also clearly present in the measurements, is the location of higher velocities at the periphery of the bowl. This is a result of the squish-swirl interaction. When the piston is located at TDC, the field of view was limited by the window, allowing to visualize just a small portion of the bowl. Once the piston starts to goes down, the effect of squish expansion, where the air floes out of the bowl towards the squish zone, has been noted.

When the fuel was injected in a inert ambient, the flow pattern has changed. A deceleration was appreciated in the flow while the injection event was still occurring. Another fact that corroborates with the velocity deceleration is the moment when the injection event ends. At this same instant under motored conditions the flow velocity was higher. Although the velocities were lower in terms of magnitude for the measurements with injection, more recirculation zones appeared inside the bowl.

Finally, the turbulent kinetic energy analysis showed the distribution of the turbulence and its evolution inside the bowl when the fuel is injected. Taking into account the methodology applied for the analysis, it is possible to see an increase of TKE around the regions of the spray. As the spray penetrates inside the bowl, the TKE increases in the same direction, from the center to the periphery (bowl lip). When injection ends, a decrease of TKE is perceived.

As a general conclusion from this first part of results, it was possible to characterize the flow pattern of the optical engine as well as define strategies and create methodologies for carrying out the experiments that were performed in the subsequent chapters. In addition, the challenge of measuring the velocity field inside a real piston geometry by means PIV technique, although with some limitations, has been successfully overcome.

7.1.2 Combustion behaviour and soot formation analysis of the optical engine by using different bowl templates

The second chapter of results was already focused on the study and application of solutions for reducing in-cylinder soot formation by means innovative piston bowl geometries. Three different piston geometries (re-entrant, stepped lip and stepped lip-wave) at different engine loads, engine conditions and injection strategies were evaluated. The soot formation and oxidation, flame movement and combustion evolution for each piston geometry were analysed by applying OH^* chemiluminescence, 2-color pyrometry, CIV and natural luminosity optical techniques. In addition, an in-cylinder pressure analysis was also performed for each piston.

First of all, the in-cylinder pressure analysis allowed to fit the same in-cylinder conditions for the different piston geometries. In addition, a comparison of the RoHR between hybrid and re-entrant piston was performed, identifying the differences in terms of combustion evolution and how the fuel burns in each piston. In general, the RoHR analysis showed that the hybrid piston enhanced fuel combustion, in particular for the pilot 1. Moreover, for all engine conditions tested, the hybrid piston finished the combustion earlier than the re-entrant piston. The late cycle oxidation process is accelerated when the hybrid piston was used.

From the CIV technique, it was possible to clearly identify the differences of the flame movement that are induced by the different geometries tested. The role of the wave protrusions was evidenced by the CIV analysis, where a reverse flow of the flames towards the bowl center has been appreciated. This reverser flow, which comprehends to the side where the waves and stepped lip geometries coexist, presented a higher velocity field than the side with just the stepped lip shape. However, both sides of hybrid piston had lower velocity field when compared with the re-entrant piston. This is explained by the effect of the stepped lip geometry (present in both sides of hybrid piston), which splits the spray into two parts and reduces the kinetic energy available inside the bowl. Although the stepped lip collaborated to reduce the flow

velocity, can be stated that the wave protrusions partially compensated this loss of kinetic energy, as the velocity of flow increased for the side where the waves are present.

The OH^* chemiluminescence measurements confirmed the shorter combustion duration when using the hybrid piston, as the OH^* signal extinguishes earlier in comparison with re-entrant piston. Moreover, as the combustion evolved, specially after the post injection, the intensity of the OH^* was higher for the hybrid piston than the re-entrant one, which evidences a better air-fuel mixture in the hybrid piston. When making an analysis only for the hybrid piston during the late cycle oxidation process, higher OH^* intensity close to the piston center is promoted by the waves protrusions when compared with the side without them. This confirms the capability of the waves protrusions in facilitating the flame reaches the fresh air available in the piston center.

Finally, by means of the 2 color technique it was possible to analyse and estimate the soot formed and oxidized in each piston geometry, from the beginning to the end of the combustion process. The technique allowed to get the temporal evolution of the soot production (formation and oxidation) and its spatial distribution inside the piston for each instant measured. Once the technique provided the temporal and spatial information of the soot, it was possible to exactly identify for each bowl geometry, the moment during the combustion when the soot formation started, when the soot formation reached its maximum formation rate and when the most part of the soot was oxidized. Moreover, it was also possible to know where was located the regions with more soot concentration inside of each bowl geometry tested. From this, the first important conclusion is the significant reduction of soot formation as well as a faster soot oxidation for both stepped lip and stepped lip-wave geometries when compared with the re-entrant bowl. The effect of wave protrusions were enhanced by the sweep of EGR and SOE conditions. In this case, the difference between the stepped lip ans stepped lip-wave sides were even more evidenced. The side composed by the waves initially formed slightly more soot than the other side. However, the oxidation process was faster for the side with waves in comparison with the side without them. In addition, during the final stages of the combustion and for all conditions tested, the side with waves presented less area covered by the soot cloud than the other side.

7.1.3 Potential of e-fuels for fossil diesel replacing: An optical analysis

The last chapter was centred in the analysis and evaluation of the e-fuels as a potential alternative for fossil diesel replacing as well as for reducing the in-cylinder soot production. Two different e-fuels (FT diesel and OME_X) were tested in the same optical engine already employed for the previous studies and the results were compared with the fossil diesel. The studies carried out in the chapter 6 was split into two parts. In the first one, the potential of using FT diesel and OME_X in a pure form were evaluated by using three optical techniques (NL, OH^* and 2 color pyrometry). Once this first part was concluded, it was evidenced the low tendency for OME_X generating soot. In addition, some questions regarding the natural luminosity emitted by the OME_X combustion were raised. Taking into account the findings in the this first part, a second part of the study was proposed. This second part aimed to fulfil two goals: The first one was focused on identifying if the source of OME_X radiation comes from the soot formation or from the chemiluminescence of chemical species. The second goal was centred in finding an optimum blend ratio for the OME_X and diesel that keeps low the soot formation, while the LHV of the fuel blend is higher than pure OME_X. Based on these goals, a specific technique named spectroscopy was employed simultaneously with the natural luminosity technique. An innovative way for using the spectroscopy technique was applied in this setup. A high-speed camera coupled with a high-speed intensifier and a spectrograph provided temporal resolution for the measurements. From the spectroscopy measurements it was also possible to apply the 2-color technique.

From the analysis of the e-fuel in a pure form, it is possible to state that FT diesel presented similar combustion behaviour to the fossil diesel. The maximum soot formation for the FT diesel was slightly lower and the oxidation process faster than fossil diesel. The OH^* chemiluminescence and natural luminosity measurements confirmed for the fossil diesel the existence of a larger area covered by cold soot in comparison with FT diesel. On the other hand a huge difference was observed for OME_X, in terms of combustion behavior and soot formation/oxidation in comparison with the other two fuels. First of all, the low radiation intensity of the OME_X flame in the NL measurements indicated the low tendency of soot formation. In addition, the $OH*$ signal was higher than FT diesel and fossil diesel. As OME_X is a fuel with a high concentration of oxygen, the local zones near the stoichiometric can increase, which consequently increase the OH^* intensity. In addition, the problem of the soot cloud blocks the OH^* signal, which was appreciated in the FT diesel and

fossil diesel measurements, was not present in the case of this fuel. The soot quantification for the OME_X was not possible due to the 2 color pyrometry was not able to measure the very low radiation intensity emitted by the flame. Then, in this fist part of the study, the results cannot confirm if OME_X is a non-sooting fuel or if some small portion of soot is produced during the OME_X combustion.

Until the end of this first part of the study some important conclusions were obtained, but it was not possible to state anything about the production or not of soot from the OME_X combustion. Thus, the second part of the study aimed to search answers for the questions that were raised previously. In this sense, the application of high-speed spectroscopy technique allowed to confirm the existence or not of soot when using pure OME_X as well as defining the maximum diesel mass that can be blended in OME_X, while keeping low the soot production. 2-color technique was also used by using the data obtained from the spectroscopy analysis. In addition, the natural luminosity provided the spatial information of the flame inside the bowl for each OME_X-diesel blend tested. From the spectroscopy analysis, it is possible to state the absence of soot during the pure OME_X combustion. In addition, up to 30 % of diesel mass blended in pure OME_X, a remarkable presence of OH^* signal could be appreciated during the most part of the combustion process. From 50 % of diesel, this characteristic peak of OH^* cannot be identified, probably due to the high soot radiation intensity. The addition of 10 % of diesel in OME_X was enough for increasing in one order of magnitude the natural luminosity emitted by the flame. From the 2-color analysis, it was possible to conclude that up to 20 % of diesel, the soot formation can be kept very low. From 50 % of diesel, the soot formation is still lower than pure diesel, but the longer injection duration in comparison with diesel extends the late oxidation process.

7.2 Future Works

The present thesis has evaluated the potential of new piston geometries as well as new alternative fuels with the objective of reducing the in-cylinder soot formation of a light-duty diesel engine in an optical version. Even though the study has provided interesting results regarding the potential of new technologies for reducing the soot emissions and replacing the fossil diesel, certain features have a extensive field to be investigated and better understood. Some suggestions for future works are provided in the following paragraphs.

7.2.1 CFD model of the optical engine

Although optical engines are able to provide many details regarding the combustion process, there are some specific informations, for example mixture formation and air-fuel ratio distribution, that the optical techniques cannot provide due to their limitations. Taking this into account, the development of CFD models, when well-validated with experimental data, can be used for complement the results obtained in the experimental part. In this sense, it must highlighted that the current thesis represents a complete database for future model developments. In the case specific of OME_X fuel for example, the CFD models could help in the comprehension of the high intensity of OH^* and its distribution inside the piston for different piston planes.

7.2.2 Studies of new piston templates in medium and heavy duty engines

All new technologies for soot reduction presented in this thesis were applied in a light-duty diesel engine. In this case, the soot formation and oxidation is also affected by the swirl motion, which is higher in small pistons. In contrast, in heavy-duty engines, the in-cylinder conditions are totally different and the pistons have a direct impact on the oxidation process. Considering that Volvo already tested a wave piston in heavy-duty engines but without the inclusion of the stepped lip shape, the evaluation of this join of stepped lip and wave piston geometries and its behaviour when applied in big engines appears as an interesting alternative to study.

7.2.3 Studies of e-fuels using advanced optical techniques

For a better comprehension of these new kind of fuels, there are a lot of studies and analysis regarding the flame structure and the different chemical species that are being formed during the combustion that still could be performed. For this, characterization of fuels with large oxygen concentration (i.e. OME_X) could be carried out in controlled ambient conditions by using advanced optical techniques. In specific, Planar Laser-Induced Fluorescence (PLIF) could be applied for analysing the spatial distribution of specific chemical species and its interaction in the flame. In this case, the OH^* PLIF, fuel tracers PLIF or formaldehyde PLIF could be very useful for identifying the flame structure, flame distribution, etc. Moreover, other techniques such NO_X PLIF could be used to study pollutant formations (which is not possible in optical engines).

Bibliography

-.
2018 Outlook for Energy: a view to 2040.
Vol. 49 n^o 11-12, pp. 23–25, 2018. (cited on pp. 33, 34)

ABB Automation Products GmbH and Analytics Measurement &.
Thermal Mass Flowmeter Sensyflow FMT700-P, 2017. (cited on p. 56)

Abdul Karim Z. A. and Khan Mohammed Yahaya.
Water-in-Diesel EmulsionsâFuel Characteristics.
pp. 53–64. Springer, 2018. (cited on p. 33)

Abu-Jrai A., Tsolakis A., Theinnoi K., Cracknell R., Megaritis A., Wyszynski M. L. and Golunski S. E.
Effect of gas-to-liquid diesel fuels on combustion characteristics, engine emissions, and exhaust gas fuel reforming. Comparative study.
Energy and Fuels, Vol. 20 n^o 6, pp. 2377–2384, 2006. (cited on p. 38)

Albrecht H.-E, Borys M., Damaschke N. and Tropea Cameron.
Laser Doppler and Phase Doppler Measurement Techniques.
01 2003. (cited on p. 24)

AVL.
Pressure sensor for combustion analysis.
2011. (cited on p. 55)

Bae Choongsik and Kim Jaeheun.
Alternative fuels for internal combustion engines.
Proceedings of the Combustion Institute, Vol. 36 n^o 3, pp. 3389–3413, 2017.
(cited on pp. 33, 35)

Basha Syed Ameer and Raja Gopal K.
In-cylinder fluid flow, turbulence and spray models-A review.
Renewable and Sustainable Energy Reviews, Vol. 13 n^o 6-7, pp. 1620–1627, 2009.
(cited on p. 20)

Benajes Jesús, García Antonio, Monsalve-Serrano Javier and Lago Sari Rafael.
Fuel consumption and engine-out emissions estimations of a light-duty engine running in dual-mode RCCI/CDC with different fuels and driving cycles.
Energy, Vol. 157, pp. 19–30, 2018. (cited on p. 4)

Bianchi G M and Pelloni P.
Numerical Study of the Combustion Chamber Shape for Common Rail H . S . D . I . Diesel Engines.
Society, n^o 724, 2010. (cited on p. 28)

Binjuwair Saud, Ibrahim Salah, Wigley Graham and Pitcher Graham.
In-Cylinder Flow Structure Analysis by Particle Image Velocimetry Under Steady State Condition.
SAE Technical Paper Series, Vol. 1 n^o Ic, 2012. (cited on p. 20)

Boccardo Giulio, Millo Federico, Piano Andrea, Arnone Luigi, Manelli Stefano, Fagg Simon, Gatti Paolo, Herrmann Olaf Erik, Queck Dirk and Weber Jost.
Experimental investigation on a 3000 bar fuel injection system for a SCR-free non-road diesel engine.
Fuel, Vol. 243 n^o October 2018, pp. 342–351, 2019. (cited on p. 4)

Bockhorn Henning.
Soot formation in Combustion, 1994. (cited on p. 19)

Bohl Thomas, Smallbone Andrew, Tian Guohong and Roskilly Anthony P.
Particulate number and NOx trade-off comparisons between HVO and mineral diesel in HD applications.
Fuel, Vol. 215 n^o March 2016, pp. 90–101, 2018. (cited on p. 37)

Bortel Ivan, Vávra JiÅí and Takáts Michal.
Effect of HVO fuel mixtures on emissions and performance of a passenger car size diesel engine.
Renewable Energy, Vol. 140, pp. 680–691, 2019. (cited on p. 37)

Bosch Wilhelm.
The Fuel Rate Indicator: A New Measuring Instrument For Display of the Characteristics of Individual Injection, 1966. (cited on p. 53)

Brossard C, Monnier J C, Barricau P, Vandernoot F X, Sant Y Le, Besnerais G Le, Brossard C, Monnier J C, Barricau P, Vandernoot F X and Sant Y Le.
Principles and applications of particle image velocimetry.
AerospaceLab, pp. 1–11, 2009. (cited on pp. 59, 60)

Busch Stephen, Zha Kan, Kurtz Eric, Warey Alok and Peterson Richard.
Experimental and Numerical Studies of Bowl Geometry Impacts on Thermal Efficiency in a Light-Duty Diesel Engine.
SAE Technical Paper Series, Vol. 1, pp. 1–12, 2018. (cited on pp. 31, 110, 115)

Busch Stephen, Zha Kan, Perini Federico, Reitz Rolf, Kurtz Eric, Warey Alok and Peterson Richard.
Bowl Geometry Effects on Turbulent Flow Structure in a Direct Injection Diesel Engine.
SAE Technical Papers, Vol. 2018-Septe, 2018. (cited on pp. 24, 27, 31, 104, 110)

Busch Steve, Zha Kan, Perini Federico and Reitz Rolf.
Piston Bowl Geometry Impacts on Late-Cycle Flow and Mixing in a Small-Bore Diesel Engine Outline â¢ Overview : piston bowl geometry project â¢ Computational study : bowl geometry impacts on late-cycle flow structure and turbulent mixing â¢ Results â¢ Bowl geo.
2017. (cited on pp. 24, 26, 29, 31)

CAESES.
Intake Port Design, 2018. (cited on p. 22)

Cartellieri Wolfgang P. and Herzog Peter L.
Swirl supported or quiescent combustion for 1990's heavy-duty di diesel engines - An analysis.
In *SAE Technical Papers*, feb 1988. (cited on p. 24)

Chen Hao, Su Xin, Li Junhui and Zhong Xianglin.
Effects of gasoline and polyoxymethylene dimethyl ethers blending in diesel on the combustion and emission of a common rail diesel engine.
Energy, Vol. 171, pp. 981–999, 2019. (cited on p. 71)

Colban W, Ekoto I, Kim D and Miles P C.
In-Cylinder PIV Measurements in an Optical Light-Duty Diesel at LTC Conditions.
THIESEL 2008 Conference on Thermo-and Fluid Dynamic Processes in Diesel Engines, pp. 1–24, 2008. (cited on pp. 80, 88, 89)

Cornwell Richard and Conicella Fabrizio.
DIRECT INJECTION DIESEL ENGINES, 2011. (cited on pp. 29, 30)

da Costa Roberto Berlini Rodrigues, Gomes Carlos Alberto, Valle Ramon Molina, Franco Rafael Lara and Huebner Rudolf.
PIV Measurements of In-Cylinder Tumble Flow in a Motored Single Cylinder Optical Research Engine.
SAE Technical Paper Series, Vol. 1, 2016. (cited on p. 78)

Dahlstrom Jessica, Andersson Oivind, Tuner Martin and Persson Håkan.
Experimental Comparison of Heat Losses in Stepped-Bowl and Re-Entrant Combustion Chambers in a Light Duty Diesel Engine.
SAE Technical Papers, 2016. (cited on pp. 29, 104, 109)

Dannemann J., Pielhop K., Klaas M. and Schröder W.
Cycle resolved multi-planar flow measurements in a four-valve combustion engine.
Experiments in Fluids, Vol. 50 n^o 4, pp. 961–976, 2011. (cited on p. 80)

Dec John E.
A conceptual model of di diesel combustion based on laser-sheet imaging.
SAE Technical Papers, 1997. (cited on pp. 17, 18)

Dec John E. and Coy Edward B.
OH radical imaging in a di diesel engine and the structure of the early diffusion flame.
SAE Technical Papers, n^o 412, 1996. (cited on p. 18)

Dembinski Henrik W R.
In-cylinder Flow Characterisation of Heavy Duty Diesel Engines Using Combustion Image Velocimetry.
Doctoral Thesis, 2013. (cited on pp. 22, 61)

Dimitriadis Athanasios, Seljak Tine, Vihar Rok, Žvar Baškovič Urban, Dimaratos Athanasios, Bezergianni Stella, Samaras Zissis and Katrašnik Tomaž.
Improving PM-NOx trade-off with paraffinic fuels: A study towards diesel engine optimization with HVO.
Fuel, Vol. 265 n^o December 2019, 2020. (cited on p. 37)

Dolak Jonathan George, Shi Yu and Reitz Rolf.
A computational investigation of stepped-bowl piston geometry for a light duty engine operating at low load.
SAE Technical Papers, 2010. (cited on pp. 29, 104)

Dumouchel Christophe.
On the experimental investigation on primary atomization of liquid streams.
Experiments in Fluids, Vol. 45 n^o 3, pp. 371–422, 2008. (cited on p. 15)

Eder Torsten, Lückert Peter, Kemmner Markus and Sass Heiko.
OM 654 â Launch of a New Engine Family by Mercedes-Benz.
MTZ worldwide, Vol. 77 n^o 3, pp. 60–67, 2016. (cited on p. 29)

Edinburgh Instruments.
What is a Spectrometer? (cited on p. 64)

Eismark Jan, Andersson Mats, Christensen Magnus, Karlsson Anders and Denbratt Ingemar.
Role of Piston Bowl Shape to Enhance Late-Cycle Soot Oxidation in Low-Swirl Diesel Combustion.
SAE International Journal of Engines, Vol. 12, apr 2019.
(cited on pp. 32, 33, 105, 106, 111, 122)

Eismark Jan and Balthasar Michael.
Device for reducing emissions in a vehicle combustion engine, 2013. (cited on p. 31)

Eismark Jan, Christensen Magnus, Andersson Mats, Karlsson Anders and Denbratt Ingemar.
Role of fuel properties and piston shape in influencing soot oxidation in heavy-duty low swirl diesel engine combustion.
Fuel, Vol. 254 n^o December 2018, pp. 115568, 2019.
(cited on pp. 31, 32, 105, 106, 110, 111)

European Co.
European Partnership under Horizon Europe Towards zero emission road transport.
Technical Report May, European Comission, 2020. (cited on p. 4)

Gamma Technologies.
Engine Performance Application Manual.
Technical report, 2016. (cited on p. 58)

García Antonio, Gil Antonio, Monsalve-serrano Javier and Sari Rafael Lago.
OMEx-diesel blends as high reactivity fuel for ultra-low NOx and soot emissions in the dual-mode dual-fuel combustion strategy.
Fuel, Vol. 275 n^o April, pp. 117898, 2020. (cited on pp. 148, 153)

García Antonio, Monsalve-serrano Javier, Villalta David, Lago Rafael, Gordillo Victor and Gaillard Patrick.
Potential of e-Fischer Tropsch diesel and oxymethyl-ether (OMEx) as fuels for the dual-mode dual-fuel concept.
Applied Energy, Vol. 253 n^o July, pp. 113622, 2019. (cited on p. 148)

Garcia-Oliver Jose M, Garcia Antonio, Gil Antonio and Pachano Leonardo.
Study of Air Flow Interaction with Pilot Injections in a Diesel Engine by Means of PIV Measurements.
SAE International Journal of Engines, Vol. 10 n^o 3, 2017. (cited on pp. 24, 89)

Gaydon A. G.
The Spectroscopy of Flames, volume 53.
Springer Netherlands, Dordrecht, 1974. (cited on p. 61)

Gill S. S., Tsolakis A., Dearn K. D. and Rodríguez-Fernández J.
Combustion characteristics and emissions of Fischer-Tropsch diesel fuels in IC engines.
Progress in Energy and Combustion Science, Vol. 37 n^o 4, pp. 503–523, 2011.
(cited on p. 38)

Glassman Irvin and Yetter Richard A.
Combustion.
Elsevier Inc., Burlington, fourth edition edition, 2008. (cited on p. 17)

Group Kistler.
Piezoresistive Absolute Pressure Sensors.
n^o 4053, pp. 1–7, 2009. (cited on p. 55)

Hao Bin, Song Chonglin, Lv Gang, Li Bo, Liu Xiaofang, Wang Kan and Liu Yaowu.
Evaluation of the reduction in carbonyl emissions from a diesel engine using Fischer-Tropsch fuel synthesized from coal.
Fuel, Vol. 133, pp. 115–122, 2014. (cited on p. 37)

Härtl Martin, Seidenspinner Philipp, Jacob Eberhard and Wachtmeister Georg.
Oxygenate screening on a heavy-duty diesel engine and emission characteristics of highly oxygenated oxymethylene ether fuel OME1.
Fuel, Vol. 153, pp. 328–335, 2015. (cited on pp. 38, 39)

Heraeus-Quartzglass.
SUPRASIL 1, 2, 3 and SUPRASIL Standard 1. (cited on p. 68)

HEYWOOD J. B.
Internal Combustion Engine Fundamentals.
McGraw-Hill, New York, 1 edition, 1988. (cited on pp. 12, 15, 17, 20, 21, 24, 25)

Higgins Brian, Siebers Dennis and Aradi Allen.
SAE TECHNICAL Diesel-Spray Ignition and Premixed-Burn Behavior.
n^o 724, 2014. (cited on p. 16)

Hsu Bertrand.
Practical Diesel-Engine Combustion Analysis.
SAE International, oct 2002. (cited on pp. 12, 17)

Hwang Wontae, Dec John and Sjöberg Magnus.
Spectroscopic and chemical-kinetic analysis of the phases of HCCI autoignition and combustion for single- and two-stage ignition fuels.
Combustion and Flame, Vol. 154, pp. 387–409, 2008. (cited on p. 147)

Iannuzzi Stefano Emanuele, Barro Christophe, Boulouchos Konstantinos and Burger Jakob.
Combustion behavior and soot formation/oxidation of oxygenated fuels in a cylindrical constant volume chamber.
Fuel, Vol. 167, pp. 49–59, 2016. (cited on pp. 38, 39)

Iikubo Shotaro, Adachi Yusuke and Shimokawa Kiyohiro.
COMBUSTION CHAMBER STRUCTURE FOR DIRECT NUECTION DESEL ENGINE, 2012. (cited on p. 29)

Jakob Markus, Hülser Thomas, Janssen Andreas, Adomeit Philipp, Pischinger Stefan and Grünefeld Gerd.
Simultaneous high-speed visualization of soot luminosity and OH * chemiluminescence of alternative-fuel combustion in a HSDI diesel engine under realistic operating conditions.
Combustion and Flame, Vol. 159 n^o 7, pp. 2516–2529, 2012. (cited on p. 139)

Jiao Yufei, Liu Ruilin, Zhang Zhongjie, Yang Chunhao, Zhou Guangmeng, Dong Surong and Liu Wuquan.
Comparison of combustion and emission characteristics of a diesel engine fueled with diesel and methanol-Fischer-Tropsch diesel-biodiesel-diesel blends at various altitudes.
Fuel, Vol. 243 n^o July 2018, pp. 52–59, 2019. (cited on p. 38)

Johansson Bengt.
Influence of the velocity near the spark plug on early flame development.
SAE Technical Papers, 1993. (cited on p. 24)

JOSÉ MARÍA GARCÍA OLIVER.
Aportaciones al estudio del proceso de combustión turbulenta de chorros en motores diesel de inyección directa.
Doctoral Thesis, 2004. (cited on p. 62)

Kaario Ossi, Lendormy Eric, Sarjovaara Teemu, Larmi Martti and Rantanen Pekka.
In-cylinder flow field of a diesel engine.
SAE Technical Papers, n^o 724, 2007. (cited on p. 20)

Kalghatgi Gautam.
Is it really the end of internal combustion engines and petroleum in transport?
Applied Energy, Vol. 225 n^o April, pp. 965–974, 2018. (cited on p. 2)

König Andrea, Marquardt Wolfgang, Mitsos Alexander, Viell Jörn and Dahmen Manuel.
Integrated design of renewable fuels and their production processes: recent advances and challenges.
Current Opinion in Chemical Engineering, Vol. 27, pp. 45–50, 2020. (cited on p. 33)

Kook Sanghoon and Pickett Lyle M.
Liquid length and vapor penetration of conventional, Fischer-Tropsch, coal-derived, and surrogate fuel sprays at high-temperature and high-pressure ambient conditions.
Fuel, Vol. 93, pp. 539–548, 2012. (cited on p. 38)

Kosaka Hidenori, Nishigaki Takahiro, Kamimoto Takeyuki, Sano Takashi, Matsutani Akira and Harada Shinichi.
Simultaneous 2-D Imaging of OH Radicals and Soot in a Diesel Flame by Laser Sheet Techniques.
SAE Technical Paper Series, Vol. 1 n^o 412, 2010. (cited on p. 139)

Kurtz Eric M. and Styron Joshua.
An Assessment of Two Piston Bowl Concepts in a Medium-Duty Diesel Engine.
SAE International Journal of Engines, Vol. 5 n^o 2, pp. 344–352, 2012.
(cited on pp. 28, 29, 104)

Lapuerta Magín, Armas Octavio, Hernández Juan José and Tsolakis Athanasios.
Potential for reducing emissions in a diesel engine by fuelling with conventional biodiesel and Fischer-Tropsch diesel.
Fuel, Vol. 89 n^o 10, pp. 3106–3113, 2010. (cited on p. 38)

Leach Felix, Ismail Riyaz, Davy Martin, Weall Adam and Cooper Brian.
The e ff ect of a stepped lip piston design on performance and emissions from a high-speed diesel engine.
Applied Energy, Vol. 215 n^o November 2017, pp. 679–689, 2018. (cited on p. 29)

Leach Felix, Kalghatgi Gautam, Stone Richard and Miles Paul.
The scope for improving the efficiency and environmental impact of internal combustion engines.
Transportation Engineering, Vol. 1 n^o April, pp. 100005, 2020. (cited on p. 2)

Lee Jongyoon, Lee Sangyul, Kim Jungho and Kim Duksang.
Bowl Shape Design Optimization for Engine-Out PM Reduction in Heavy Duty Diesel Engine.
SAE Technical Papers, Vol. 2015-April n^o April, 2015. (cited on p. 28)

Liu Haoye, Wang Zhi, Li Yanfei, Zheng Yanyan, He Tanjin and Wang Jianxin.
Recent progress in the application in compression ignition engines and the synthesis technologies of polyoxymethylene dimethyl ethers.
Applied Energy, Vol. 233-234 n^o October 2018, pp. 599–611, 2019. (cited on pp. 38, 137)

Liu Haoye, Wang Zhi, Wang Jianxin and He Xin.
Improvement of emission characteristics and thermal efficiency in diesel engines by fueling gasoline/diesel/PODEn blends.
Energy, Vol. 97, pp. 105–112, 2016. (cited on p. 71)

Liu Haoye, Wang Zhi, Zhang Jun, Wang Jianxin and Shuai Shijin.
Study on combustion and emission characteristics of Polyoxymethylene Dimethyl Ethers/diesel blends in light-duty and heavy-duty diesel engines.
Applied Energy, Vol. 185, pp. 1393–1402, 2017. (cited on p. 39)

Liu Yao, Tan Jianguo, Wan Minggang, Zhang Lang and Yao Xiao.
Quantitative Measurement of OHâ and CHâ Chemiluminescence in Jet Diffusion Flames.
ACS Omega, Vol. 5 n^o 26, pp. 15922–15930, 2020. (cited on p. 62)

Lumpp Björn, Rothe Dieter, Pastötter Christian, Lämmermann Reinhard and Jacob Eberhard.
OXYMETHYLENE ETHERS AS DIESEL FUEL ADDITIVES OF THE FUTURE.
MTZ worldwide eMagazine, Vol. 72 n^o 3, pp. 34–38, 2011. (cited on p. 39)

Ma Xiao, Ma Yue, Sun Shuaishuai, Shuai Shi-Jin, Wang Zhi and Wang Jian-Xin.
PLII-LEM and OH* Chemiluminescence Study on Soot Formation in Spray Combustion of PODEn-Diesel Blend Fuels in a Constant Volume Vessel.
SAE Technical Paper Series, Vol. 1 n^o 2329, 2017. (cited on p. 38)

Mancaruso Ezio and Vaglieco Bianca M.
Spectroscopic measurements of premixed combustion in diesel engine.
Fuel, Vol. 90 n^o 2, pp. 511–520, 2011. (cited on p. 156)

Miles Paul, Megerle Marcus, Sick Volker, Richards Keith, Nagel Zac and Reitz Rolf.
The evolution of flow structures and turbulence in a fired HSDI diesel engine.
SAE Technical Papers, n^o 724, 2001. (cited on p. 24)

Miles Paul C.
Turbulent Flow Structure in Direct-Injection, Swirl-Supported Diesel Engines, pp. 173–256.
Springer Berlin Heidelberg, Berlin, Heidelberg, 2009. (cited on pp. 22, 78, 93)

Miles Paul C., Collin Robert, Hildingsson Leif, Hultqvist Anders and Andersson Öivind.
Combined measurements of flow structure, partially oxidized fuel, and soot in a high-speed, direct-injection diesel engine.
Proceedings of the Combustion Institute, Vol. 31 II n^o x, pp. 2963–2970, 2007.
(cited on pp. 78, 89)

Miles Paul C., Hildingsson Leif and Hultqvist Anders.
The influence of fuel injection and heat release on bulk flow structures in a direct-injection, swirl-supported diesel engine.
Experiments in Fluids, Vol. 43 n^o 2-3, pp. 273–283, 2007. (cited on p. 89)

Mollenhauer Klaus and Tschöke Helmut.
Handbook of Diesel Engines.
Springer, Berlim, 2010. (cited on pp. 13, 14, 20, 21, 25)

Montajir Rahman M., Tsunemoto H., Ishitani H. and Minami T.
Fuel spray behavior in a small di diesel engine: Effect of combustion chamber geometry.
SAE Technical Papers, n^o 724, 2000. (cited on p. 28)

Mueller Charles J. and Martin Glen C.
Effects of Oxygenated Compounds on Combustion and Soot Evolution in a DI Diesel Engine:Broadband Natural Luminosity Imaging.
SAE Technical Paper Series, Vol. 1 n^o 724, 2002. (cited on p. 61)

Musculus Mark P.B., Singh Satbir and Reitz Rolf D.
Gradient effects on two-color soot optical pyrometry in a heavy-duty DI diesel engine.
Combustion and Flame, Vol. 153 n^o 1-2, pp. 216–227, 2008. (cited on p. 67)

Najafabadi Izadi.
Analyzing of in-cylinder flow structures and cyclic variations of partially premixed combustion in a light duty engineIzadi.
n^o 2016, 2017. (cited on p. 89)

Neely Gary D., Sasaki Shizuo and Sono Hiroshi.
Investigation of alternative combustion crossing stoichiometric air fuel ratio for clean diesels.
SAE Technical Papers, 2007. (cited on pp. 29, 30)

Nishida Kentaro, Hashizume Takeshi, Hasegawa Ryo and Ogawa Takashi.
Low Cooling Losses and Low Emission Analysis of Small Bore Diesel Engine Combustion.
SAE Technical Papers, Vol. 2015-September n^o September, pp. 1–7, 2015.
(cited on p. 29)

Omari Ahmad, Heuser Benedikt and Pischinger Stefan.
Potential of oxymethylenether-diesel blends for ultra-low emission engines.
Fuel, Vol. 209 n^o May, pp. 232–237, 2017. (cited on p. 38)

Pastor J. V., García-Oliver J. M., García A., Micó C. and Durrett R.
A spectroscopy study of gasoline partially premixed compression ignition spark assisted combustion.
Applied Energy, Vol. 104, pp. 568–575, 2013. (cited on p. 156)

Pastor José, Olmeda Pablo, Martín Jaime and Lewiski Felipe.
Methodology for Optical Engine Characterization by Means of the Combination of Experimental and Modeling Techniques.
Applied Sciences, Vol. 8 n^o 12, pp. 2571, 2018. (cited on p. 150)

Pastor José V., García A., Micó C. and García-Carrero Alba A.
Experimental study of influence of Liquefied Petroleum Gas addition in Hydrotreated Vegetable Oil fuel on ignition delay, flame lift off length and soot emission under diesel-like conditions.
Fuel, Vol. 260 n^o October 2019, pp. 116377, 2020. (cited on p. 37)

Pastor Jose V., Garcia Antonio, Micó Carlos, Lewiski Felipe, Vassallo Alberto and Pesce Francesco Concetto.
PIV and DBI Experimental Characterization of Air Flow-Spray Interaction and Soot Formation in a Single Cylinder Optical Diesel Engine Using a Real Bowl Geometry Piston.
SAE Technical Paper Series, Vol. 1 n^o Ld, pp. 1–14, 2019. (cited on p. 22)

Pastor José V., García Antonio, Micó Carlos, Möller Sebastian and García-Oliver José M.
Application of optical diagnostics to the quantification of soot in n -alkane flames under diesel conditions.
Combustion and Flame, Vol. 164, pp. 212–223, 2015. (cited on pp. 99, 148)

Pastor José V., García-Oliver José M., García Antonio, Micó Carlos and Möller Sebastian.
Application of optical diagnostics to the quantification of soot in n-alkane flames under diesel conditions.
Combustion and Flame, Vol. 164, pp. 212–223, 2016. (cited on pp. 64, 116)

Payri F., Margot X., Gil A. and Martin J.
Computational study of heat transfer to the walls of a di diesel engine.
SAE Technical Papers, Vol. 2005 n^o 724, 2005. (cited on p. 57)

Payri R., Salvador F. J., Gimeno J. and Bracho G.
A new methodology for correcting the signal cumulative phenomenon on injection rate measurements.
Experimental Techniques, Vol. 32 n^o 1, pp. 46–49, 2008. (cited on p. 53)

Pellegrini Leonardo, Marchionna Mario, Patrini Renata, Beatrice Carlo, Del Giacomo Nicola and Guido Chiara.
Combustion Behaviour and Emission Performance of Neat and Blended Polyoxymethylene Dimethyl Ethers in a Light-Duty Diesel Engine.
SAE Technical Paper Series, Vol. 1, 2012. (cited on pp. 38, 39, 150)

Pickett Lyle M.
Visualization of diesel spray penetration, cool-flame, ignition, high-temperature combustion, and soot formation using highspeed imaging.
Western States Section/Combustion Institute Fall Meeting 2007, Vol. 2 n^o 1, pp. 867–879, 2007. (cited on p. 17)

Pickett Lyle M., Siebers Dennis L. and Idicheria Cherian A.
Relationship between ignition processes and the lift-off length of diesel fuel jets.
SAE Technical Papers, n^o 724, 2005. (cited on pp. 17, 27)

Posada Francisco, Chambliss Sarah and Blumberg Kate.
Costs of Emission Reduction Technologies for Heavy-Duty Diesel Vehicles.
The International Council of Clean Transportation (ICCT), Vol. 1 n^o February, pp. 39, 2016. (cited on pp. 4, 5)

Pourfallah Mohsen.
Optimization of Intake port shape in a DI Diesel Engine Using CFD Flow Simulation.
n^o June 2010, 2018. (cited on pp. 22, 23)

Poussin Olivier, Gaillard Patrick, Garcia Antonio, Monsalve-Serrano Javier and Martinez-Boggio S.D.
Dual-Fuel RCCI Diesel-Gasoline Hybrid Truck Concept to Achieve the Future Emissions Targets.
10th Aachen Colloquium China Sustainable Mobility 2020, n^o Ci, 2020. (cited on p. 35)

Quoc Hoang Xuan, Vignon Jean Marc and Brun Maurice.
A new approach of the two-color method for determining local instantaneous soot concentration and temperature in a D.I. Diesel combustion chamber.
SAE Technical Papers, 1991. (cited on p. 19)

Rao Lingzhe, Zhang Yilong, Kim Dongchan, Su Hu Chien, Kook Sanghoon, Kim Kenneth S. and Kweon Chol Bum.
Effect of after injections on late cycle soot oxidation in a small-bore diesel engine.
Combustion and Flame, Vol. 191, pp. 513–526, 2018. (cited on p. 150)

Reitz R. D., Ogawa H., Payri R., Fansler T., Kokjohn S., Moriyoshi Y., Agarwal A. K., Arcoumanis D., Assanis D., Bae C., Boulouchos K., Canakci M., Curran S., Denbratt I., Gavaises M., Guenthner M., Hasse C., Huang Z., Ishiyama T., Johansson B., Johnson T. V., Kalghatgi G., Koike M., Kong S. C., Leipertz A., Miles P., Novella R., Onorati A., Richter M., Shuai S., Siebers D., Su W., Trujillo M., Uchida N., Vaglieco B. M., Wagner R. M. and Zhao H.
IJER editorial: The future of the internal combustion engine.
International Journal of Engine Research, Vol. 21 n^o 1, pp. 3–10, 2020. (cited on pp. 2, 35)

Rimkus Alfredas, Žaglinskis Justas, Rapalis Paulius and Skačkauskas Paulius.
Research on the combustion, energy and emission parameters of diesel fuel and a biomass-to-liquid (BTL) fuel blend in a compression-ignition engine.
Energy Conversion and Management, Vol. 106, pp. 1109–1117, 2015. (cited on p. 38)

Ritchie Hannah.
Energy.
Our World in Data, 2014.
https://ourworldindata.org/energy. (cited on p. 2)

Ritchie Hannah.
Sector by sector: where do global greenhouse gas emissions come from?, 2020. (cited on p. 2)

Roberts Gregory, Lind Ted, Eagle W., Musculus Mark PB, Andersson Öivind and Rousselle Christine.
Mechanisms of Post-Injection Soot-Reduction Revealed by Visible and Diffused Back-Illumination Soot Extinction Imaging.
SAE Technical Paper Series, Vol. 1, pp. 1–20, 2018. (cited on p. 137)

Rochussen Jeremy, McTaggart-Cowan Gordon and Kirchen Patrick.
Parametric study of pilot-ignited direct-injection natural gas combustion in an optically accessible heavy-duty engine.
International Journal of Engine Research, Vol. 21 n^o 3, pp. 497–513, mar 2019. (cited on p. 116)

Rounce P., Tsolakis A., Rodríguez-Fernández J., York A. P. E., Cracknell R. F. and Clark R. H.
Diesel Engine Performance and Emissions when First Generation Meets Next Generation Biodiesel.
SAE Technical Paper Series, Vol. 1, pp. 1–10, 2010. (cited on p. 38)

Ryan Tom.
Combustion Targets for Low Emissions and High Efficiency.
In *Diesel Engine Emissions Reduction (DEER) Conference*, 2005. (cited on p. 29)

Schaberg Paul, Botha Johan, Schnell Mark, Hermann Hans Otto, Pelz Norbert and Maly Rudolf.
Emissions performance of GTL diesel fuel and blends with optimized engine calibrations.
SAE Technical Papers, 2005. (cited on p. 38)

Schemme Steffen, Samsun Remzi Can, Peters Ralf and Stolten Detlef.
Power-to-fuel as a key to sustainable transport systems â An analysis of diesel fuels produced from CO 2 and renewable electricity.
Fuel, Vol. 205, pp. 198–221, 2017. (cited on p. 33)

Senecal P. K., Miles Paul C., Mitra Saurav, Busch Stephen, Wijeyakulasuriya Sameera and Zha Kan.
Characterization of Flow Asymmetry During the Compression Stroke Using Swirl-Plane PIV in a Light-Duty Optical Diesel Engine with the Re-entrant Piston Bowl Geometry.
SAE International Journal of Engines, Vol. 8 n^o 4, 2015. (cited on pp. 22, 24, 79)

Serrano José Ramón, Novella Ricardo and Piqueras Pedro.
Why the development of internal combustion engines is still necessary to fight against global climate change from the perspective of transportation.
Applied Sciences (Switzerland), Vol. 9 n^o 21, 2019. (cited on p. 3)

Siegemund Stefan, Trommler Marcus, Kolb Ole, Zinnecker Valentin, Schmidt Patrick, Weindorf Werner, Zittel Werner, Raksha Tetyana and Zerhusen Jan.
E-Fuels study. The potential of electricity-based fuels for low-emission transport in the EU.
Deutsche Energie-Agentur GmbH (dena), 2017. (cited on p. 37)

Skeen Scott, Manin Julien and Pickett Lyle M.
Visualization of Ignition Processes in High-Pressure Sprays with Multiple Injections of n-Dodecane.
SAE International Journal of Engines, Vol. 8 n^o 2, pp. 696–715, 2015. (cited on p. 17)

Smith Anthony.
Ricardo low emissions combustion technology helps JCB create the off-highway industry ' s cleanest engine.
Ricardo Press Release, n^o 222915, pp. 4–6, 2010. (cited on pp. 29, 30)

Suppes Galen J. and Storvick Truman S.
The New Electric Vehicle Society.
Sustainable Power Technologies and Infrastructure, pp. 161–190, 2016. (cited on p. 25)

Tanov Slavey, Johansson Bengt, Richter Mattias, Wang Zhenkan and Wang Hua.
Effects of Injection Strategies on Fluid Flow and Turbulence in Partially Premixed Combustion (PPC) in a Light Duty Engine.
SAE Technical Paper Series, Vol. 1 n^o Ldv, 2015. (cited on pp. 78, 89, 92)

Tanov Slavey, Pachano Leonardo, Andersson Öivind, Wang Zhenkan, Richter Mattias, Pastor José V., García-Oliver José M. and García Antonio.
Influence of spatial and temporal distribution of Turbulent Kinetic Energy on heat transfer coefficient in a light duty CI engine operating with Partially Premixed Combustion.
Applied Thermal Engineering, Vol. 129, pp. 31–40, 2018. (cited on pp. 86, 89, 93)

Tikar Sameer, Malkhede Dileep and Nandgaonkar Milankumar.
Design and Development of Intake Ports for 2-Valve & 4-Valve Configurations for Heavy Duty Off-Highway Diesel Engine.
SAE Technical Papers, n^o October, 2019. (cited on p. 23)

Tree Dale and I. Svensson Kenth.
Soot processes in compression ignition engines.
Progress in Energy and Combustion Science, Vol. 33, pp. 272–309, jun 2007.
(cited on pp. 18, 19, 20)

TSI Inc.
Particle Image Velocimetry INSIGHT 4G, 2011. (cited on p. 85)

Wang Guixin, Yu Wenbin, Li Xiaobo and Yang Rui.
Influence of fuel injection and intake port on combustion characteristics of controllable intake swirl diesel engine.
Fuel, Vol. 262 n^o November 2019, pp. 116548, 2020. (cited on p. 23)

Wang Zhenkan, Tanov Slavey, Wang Hua, Richter Mattias, Johansson Bengt and Alden Marcus.
High-Speed Particle Image Velocimetry Measurement of Partially Premixed Combustion (PPC) in a Light Duty Engine for Different Injection Strategies.
2015. (cited on pp. 24, 89)

Wickman D. D., Senecal P. K. and Reitz R. D.
Diesel engine combustion chamber geometry optimization using genetic algorithms and multi-dimensional spray and combustion modeling.
SAE Technical Papers, Vol. 2001 n^o 724, 2001. (cited on p. 28)

Xuan Tiemin.
Optical investigations on diesel spray dynamics and in-flame soot formation.
Doctoral Thesis, Universitat Politècnica de València, 2017. (cited on pp. 13, 15)

Xuan Tiemin, Pastor José V., García-Oliver José M., García Antonio, He Zhixia, Wang Qian and Reyes Miriam.
In-flame soot quantification of diesel sprays under sooting/non-sooting critical conditions in an optical engine.
Applied Thermal Engineering, Vol. 149 n^o 301, pp. 1–10, 2019. (cited on pp. 99, 163)

Yan Jingde and Borman Gary L.
Analysis and In-Cylinder Measurement of Particulate Radiant Emissions and Temperature in a Direct Injection Diesel Engine.
sep 1988. (cited on p. 19)

Yoo Dockoon, Kim Duksang, Jung Wook, Kim Nagin and Lee Dongin.
Optimization of diesel combustion system for reducing PM to meet tier4-final emission regulation without diesel particulate filter.
SAE Technical Papers, Vol. 11 n^o October 2013, 2013. (cited on pp. 29, 30)

Zha Kan, Busch Stephen, Warey Alok, Peterson Richard C. and Kurtz Eric.
A Study of Piston Geometry Effects on Late-Stage Combustion in a Light-Duty Optical Diesel Engine Using Combustion Image Velocimetry.
SAE International Journal of Engines, Vol. 11 n^o 6, pp. 783–804, 2018.
(cited on pp. 26, 29, 30, 61, 104, 106)

Zhang Tankai, Eismark Jan, Munch Karin and Denbratt Ingemar.
Effects of a wave-shaped piston bowl geometry on the performance of heavy duty Diesel engines fueled with alcohols and biodiesel blends.
Renewable Energy, Vol. 148 n^o x, pp. 512–522, 2020. (cited on p. 4)

Zhao H.
Laser Diagnostics and Optical Measurement Techniques in Internal Combustion Engines.
SAE International, 2012. (cited on pp. 58, 59, 60, 63, 64)

Zhao H. and Ladommatos N.
Optical diagnostics for soot and temperature measurement in diesel engines.
Progress in Energy and Combustion Science, Vol. 24 n^o 3, pp. 221–255, 1998.
(cited on pp. 19, 63)

Zhao Mengmeng, Buttsworth David and Choudhury Rishabh.
Experimental and numerical study of OH* chemiluminescence in hydrogen diffusion flames.
Combustion and Flame, Vol. 197, pp. 369–377, 2018. (cited on p. 62)

Zhu Y., Zhao H., Melas D. A. and Ladommatos N.
Computational study of the effects of the re-entrant lip shape and toroidal radii of piston bowl on a HSDI diesel engine's performance and emissions.
SAE Technical Papers, Vol. 2004 n^o 724, 2004. (cited on pp. 28, 29)